Optical fibre CO_2 sensing for monitoring the effects of tissue loading

Nadia Afroze, MSc

Thesis submitted to the University of Nottingham

for the degree of Doctor of Philosophy

November 2022



University of Nottingham

UK | CHINA | MALAYSIA

Abstract

The ultimate objective of this PhD thesis is to develop and characterise optical fibre sensors for carbon dioxide (CO_2) monitoring during tissue loading. CO_2 is a reliable marker for the early detection of pressure ulcers (PUs). In this thesis, a reflection mode optical fibre CO_2 sensor (OFCS) was developed for early prediction of PUs formation.

Transcutaneous CO_2 probes based on electrochemical sensing are commercially available for measurement of arterial partial pressure. It is therefore important to consider the advantages of OFCS in terms of device form and performance. The most important potential advantage is that an OFCS is very thin (core diameter, Ø 62.5 µm, cladding diameter, Ø 125 µm) and flexible and so could be used for continuous monitoring during patient treatment or during everyday life. Furthermore, electrochemical sensors require skin heating, temperature calibration and use of contact gel; OFCS can potentially monitor without. Therefore, if comparable performance to electrochemical sensing could be achieved, then there is an opportunity for OFCS to be widely adopted for monitoring tissue breakdown.

Skin damage is quite a slow process (1-2 hrs to develop a grade 3 or 4 PUs); a commercially available transcutaneous CO_2 probe (t_C Sensor 92) response time is around 78 seconds, which is acceptable to clinicians and requires no further improvement. Therefore, a response time of approximately 3 minutes would be acceptable for monitoring PUs. The t_C Sensor 92 probe measures the partial pressure of CO_2 (PCO_2) in units of mmHg or kPa. The measurement range varies according to the different loading amounts on the skin, such as the PCO_2 value of 36-44 mmHg (for 40 mmHg or 5.3 kPa loading), 50-60 mmHg (for 80 mmHg or 10.7 kPa loading), and > 80 mmHg (for 120 mmHg or 16 kPa loading). Therefore, an OFCS would need to be able to discriminate these ranges.

The optical fibre tip was coated with thymol blue (TB) using a sol-gel coating process. The highest absorption peak of the OFCS was achieved at a wavelength of around 600 nm. The OFCS had response and recovery times of 60 seconds and 413 seconds, respectively, in the range of 0 ppm (0% CO_2) to 50000 ppm (5% CO_2). Light from a halogen light source illuminated the optical fibre tip, and the reflected light (proportional to CO_2) was detected.

The OFCS has been calibrated in a gas chamber alongside the t_C Sensor 92 probe and a commercial CO_2 datalogger. The humidity effects on the OFCS were nullified using a polytetrafluoroethylene (PTFE) film as a barrier between the sensor and external environment.

Further characterisation of the sensing film has also been conducted. The dye characteristics such as transmission and absorption spectra of TB were observed by varying pH values and CO_2 flow. The highest absorption peak of TB (red), TB (yellow), and TB (blue) were achieved at a wavelength of 549, 452, and 606 nm, respectively. The different shapes of the spectrum of TB according to pH variation and CO_2 flow were illustrated using skewness and kurtosis as an alternative to attenuation measurements at a single detection wavelength.

The TB concentration was calculated from the film thickness of the dried film on the OFCS tip. This film thickness was measured using scanning electron microscope (SEM) images. These values were used as input parameters in a simulation of the fibre tip as a Fabry-Perot interferometer (FPI). The highest absorption peak of the FPI was achieved at a wavelength of around 600 nm, and the spectrum of TB contains interference fringes. The fringe visibility was calculated from the simulated reflection spectrum of the FPI. The relationship between fringe visibility and film thickness helped to choose 7.234 μm as the optimum film thickness.

All three CO_2 sensors have been used to measure the skin CO_2 with and without weight loading. The PCO_2 emitted from the human forearm has been measured using the t_C Sensor 92 probe without weight loading at sensor temperatures of 37 °C and 42 °C for 30 minutes. The developed 10 OFCSs (OFCS 1-10) and a commercial CO_2 sensor were validated on 10 volunteers' (Volunteer 1-10) forearms and measured the changes in CO_2 concentration during loading at a range of 32 °C and 43.4 °C for 20 minutes. The gas flow was stopped when the skin was loaded, which allowed CO_2 to build up in the tissue. The OFCS 1-6 measured the CO_2 changes on the volunteers' (Volunteer 1-6) skin and in the air successfully, but unfortunately, the OFCS 7-10 couldn't measure the CO_2 changes on the volunteers' (Volunteer 7-10) skin and in the air. The commercial CO_2 sensor also successfully measured the CO_2 changes on the volunteers' (Volunteer 1-10) skin and in the

air. The minimum and maximum achieved skin CO_2 concentration was 149 ppm and 429 ppm, respectively, over 3 trials.

In conclusion, promising results from the human forearm using the OFCS and commercial CO_2 sensor were achieved. Key improvements of the OFCS are identified which, with future work, will lead to improved performance for eventual deployment in the clinic.

Bismillah Hir Rahman Nir Rahim ("In the name of the Allah, The Most Gracious and The Most Merciful") and Allah can do all things [Surat Al-Baqarah (2:106) – The Noble Qur'an]

Acknowledgements

I would like to express my gratitude to everyone (my teachers, colleagues, family members, friends, and well-wishers) who encouraged me to do this PhD.

I would like to express my sincere gratitude to my supervisors, Prof Stephen P. Morgan, Prof Serhiy Korposh, Prof Barrie R. Hayes-Gill, and Dr Ricardo Goncalves Correia, for providing me with the opportunity to pursue my PhD. Undoubtedly, I am so fortunate to have them all as my mentors, and I thank them for their valuable advice, continuous guidance, and support during my PhD journey. It could be impossible to complete my PhD without their guidance and support.

I would like to thank my collaborator, Prof Peter R. Worsley, School of Health Sciences, University of Southampton, for providing the necessary information and equipment to measure PCO_2 from the skin during loading.

I would like to thank my internal assessor, Prof Amanda J. Wright, for her valuable feedback and inspiration for my research during annual reviews.

I would like to thank Prof Seung-Woo Lee, Department of Chemical and Environmental Engineering, The University of Kitakyushu, for helping me to develop my knowledge of the chemistry fundamentals of an optical fibre sensor.

I would like to thank my colleagues from Optics and Photonics Research Group: Dr Francisco Ulises Hernandez Ledezma, Dr Chalani Abeywardena, Dr Liangliang Liu, Dr Hattan Ballaji, Dr Mohammad Al Badri, Dr David Gomez, Dr Sandor Erdody, Dr Chenyang He, Dr Chong Liu, Dr Will Xing, Stuart Murray, Yasmine Saoud, Adam Garon, Peizhou Wu, James Bradbury, James Ell, Simon Stockwell, Brett Gadsby, Nat Limweshasin, Suvvi Kuppur Narayana Swamy, Itzel Avila Castro, Basem Basunaid, and Christina Shrees for their help, support, cooperation, and for gifting me the lovely memories.

I would like to acknowledge the Faculty of Engineering Research Excellence PhD Scholarship, University of Nottingham (UoN), for providing me with the financial support to pursue my PhD.

I would like to thank Donna Astill-Shipman, Senior Research Operations Officer, Faculty of Engineering, UoN, for managing and solving any issues regarding my scholarship matters and ethics applications of my experiments.

I would like to thank Dr Aled Jones and Mark Rose, Health and Safety Officer, Faculty of Engineering, UoN, for giving me valuable feedback and approval on the risk assessment of my experiments.

I would like to thank the Clinical Engineering Department at Queen's Medical Centre (QMC) for introducing me to Ray Stewart at Radiometer, who kindly lent us the t_C Sensor 92 probe and TCM TOSCA monitor for my experiment. I would like to thank Ray Stewart, Transcutaneous Monitoring Product Specialist, Radiometer Ltd, UK, for supplying me with the essential equipment to measure PCO_2 from the skin and guiding me in operating the transcutaneous monitoring systems.

I would like to thank Dr Sabrin Samad, Research Technician, Nanoscale and Microscale Research Centre (nmRC), UoN, for measuring the film thickness from the dried film on the OFCS tip using the SEM images.

Thanks to Mark Birkin, Alex Ottway, Edward Kujawinski, and Jonathan Pepper, Engineering/Electronics Technicians, Electronic Workshop, Faculty of Engineering, UoN, for providing me with electronics items and advising me on how to use them. Thanks to Nigel Lowe, Martin Carmichael, and Tom Wilson, Store Technicians, L2 Faculty Store, Faculty of Engineering, UoN, for providing me with the ordered necessary stuff for my experiment. Thanks to Andrew Plummer, Supervisor, Central Engineering Workshop, Faculty of Engineering, UoN, for printing a few Teflon based moulds for my experiment. Thanks to John Hinchliffe, Kevin Last, Guy Thompson, and Ian Medley, Mechanical Technicians, Power Electronics and Machines Centre (PEMC), Faculty of Engineering, UoN, for making holes in a custom-made gas chamber using a drilling machine and delivering the gas cylinders for my experiment.

Special thanks to Nourin Kadir (my best friend and colleague) for giving me continuous guidelines and encouragement since my PhD application periods till now. Also, special thanks to Nuzat Nuray Alam (my colleague) and Ritika Das (my junior friend) for providing me with the mental support to complete my PhD smoothly. Also, special thanks to Dr Athoy Nilima (my friend) and Dr Fairuza Faiz (my teacher and colleague) for guiding and helping me to understand the fundamentals of an optical fibre sensor at different stages of my PhD. Also, special thanks to Mosaruf Hussan (my colleague) and Kushal Khandelwal (my junior friend) for supporting me in learning various data processing techniques at the early stage of my PhD.

My deepest gratitude to Md. Hafiz Uddin (my father), Aleya Akter (my mother), and Md. Tusher Ahmed (my younger brother) for keeping the faith in me that I am capable enough to complete the PhD, for their unconditional love, care, support, and motivation throughout my entire PhD journey.

Above all, my immense gratitude to Allah for guiding and protecting me all the time and, making me capable, giving me the strength to complete the PhD. Alhamdulillah for everything.

Author's Publications

Conferences

1. N. Afroze, R. Correia, P.R. Worsley, B.R. Hayes-Gill, S.-W. Lee, S.P. Morgan, S. Korposh, "Skin CO_2 monitoring for early detection of pressure ulcers using an optical fibre CO_2 sensor," *28th International Conference on Optical Fibre Sensors (OFS-28),* Hamamatsu, Japan, November 2023, submitted manuscript.

Table of Contents

Abstract ii

Acknowledgements v

Author's Publications vii

Conferences vii

Table of Contents viii

List of Figures xv

List of Tables xxv

List of Acronyms xxvii

1. Chapter 1 1

Thesis Introduction 1

1.1 Introduction 1

1.2 Aims and Objectives 1

1.3 Motivation 2

1.4 Optical fibre sensors 3

1.4.1 OFS principles 3

1.4.1.1 Intrinsic OFS 3

1.4.1.2 Extrinsic OFS 4

1.4.2 Benefits of OFSs 5

1.4.3 Commercially available OFCSs 5

1.5 Monitoring T_CPCO_2 from skin 6

1.5.1 Skin structure 6

1.5.1.1 Epidermis 7

1.5.1.2 Dermis 7

1.5.1.3 Hypodermis 8
1.5.2 Overview of transcutaneous monitoring 8
1.5.2.1 Key factors for transcutaneous monitoring 9
1.5.2.2 A transcutaneous sensor on skin 9
1.6 OFCS on patients' skin 10
1.7 Thesis structure 11
2. Chapter 2 13
Literature Review 13
2.1 Introduction 13
2.2 CO_2 inside human body and Pressure ulcers relationship with transcutaneous CO_2 13
2.2.1 CO_2 transport to body 14
2.2.2 CO_2 release from skin 14
2.2.3 pH and CO_2 relationship 16
2.2.4 Transcutaneous CO_2 17
2.2.5 Pressure ulcers 19
2.3 Previously conducted research at different institutions 21
2.3.1 Research conducted by our collaborators at the University of Southampton 21
2.3.2 Research conducted by researchers at Beijing Chaoyang Hospital 24
2.4 T_CPCO_2 measurement using an optical miniaturized cell 27
2.5 Commercial devices for measuring CO_2 and T_CPCO_2 29
2.6 Comparison between a t_C Sensor 92 probe and an OFS 36
2.7 Overview of an OFS 36
2.7.1 General principle of designing an OFS 36

2.7.2 Classification of an OFS depending on operating principle 37
2.7.2.1 Intensity based optical fibre sensor 37
2.7.2.2 Wavelength modulated optical fibre sensor 39
2.7.2.3 Phase modulated optical fibre sensor 40
2.7.2.4 Polarisation modulated optical fibre sensor 41
2.7.3 Classification of an OFS depending on application 41
2.7.3.1 Physical optical fibre sensor 41
2.7.3.2 Chemical optical fibre sensor 42
2.8 Latest advances in OFpHSs 43
2.9 Sensing film coating techniques 46
2.10 OFCSs review 48
2.11 Background of the OFS developed in this research 53
2.11.1 Optical fibre structure 53
2.11.2 Refractive index 53
2.11.3 Critical angle, Total internal reflection, and Numerical aperture 54
2.11.4 Maxwell's equations 56
2.11.5 Optical fibre category 58
2.11.6 Optical attenuation and Bending losses 60
2.11.7 Types of fibre materials 61
2.12 Summary 61
3. Chapter 3 63
Optical Fibre CO_2 Sensor – Fabrication & Characterisation 63
3.1 Introduction 63
3.2 Sensor fabrication 63
3.2.1 Materials 63

3.2.2 Reason behind choosing materials 64
3.2.3 Absorption and Dye concentration relationship 65
3.2.4 Characteristics of dye according to pH variation 66
3.2.4.1 Characteristics of Thymol Blue 66
3.2.4.2 Experimental set-up for varying pH of Thymol Blue 68
3.2.4.3 Spectra of Thymol Blue according to pH variation 70
3.2.5 Film preparation 71
3.2.6 Selection process of optimum withdrawal speed 72
3.3 Sensor characterisation 74
3.3.1 Experiment set-up 74
3.3.2 Results 76
3.3.3 Discussion 86
3.4 Cross-sensitivity of an OFCS 89
3.4.1 Temperature cross-sensitivity of an OFCS 89
3.4.2 Humidity cross-sensitivity of an OFCS 90
3.4.3 Nullifying humidity effects on OFCS 93
3.5 Reducing film cracking 95
3.5.1 Cracking demonstrated on GS 95
3.5.2 Fibre sensor with and without Triton X-100 96
3.5.3 OFCS spectra with and without Triton X-100 97
3.6 Film thickness measurement of an OFCS from SEM images 101
3.7 Fibre-to-fibre variability 106
3.8 Summary 111
4. Chapter 4 114
Shape Analysis of Dye's Spectrum & Modelling of Fabry-Perot Interferometer 114

4.1 Introduction 114
4.2 Analysis of Thymol Blue spectrum shape 114
4.2.1 Relevant theory of skewness and kurtosis 114
4.2.2 CO_2 and pH relationship 116
4.2.3 Experimental set-up for adding CO_2 inside Thymol Blue solution 117
4.2.4 Spectrum of Thymol Blue according to pH variation with and without CO_2 118
4.3 Fabry-Perot interferometer 126
4.3.1 Principle of operation 126
4.3.2 Relevant formulas 127
4.4 Optimise film thickness according to fringe visibility 129
4.5 Summary 136
5. Chapter 5 137
Monitoring CO_2 Emitted from Human Skin 137
5.1 Introduction 137
5.2 Monitoring CO_2 emitted from human skin using a t_C Sensor 92 probe 137
5.2.1 Experimental set-up for monitoring CO_2 emitted from human skin using a t_C Sensor 92 probe 137
5.2.2 Calibration of PCO_2 and Temperature corrected PCO_2 values 140
5.2.3 Results from monitoring CO_2 emitted from human skin using a t_C Sensor 92 probe 143
5.3 Monitoring CO_2 emitted from human skin during loading using an OFCS and a commercial CO_2 sensor 145
5.3.1 Introduction to a loading machine 146
5.3.2 Experimental set-up for monitoring CO_2 emitted from human skin during loading using an OFCS and a commercial CO_2 sensor 147

5.3.3 Calibration of OFCSs (used for skin CO_2 measurement) 150

5.3.4 Results from monitoring CO_2 emitted from human skin during loading using an OFCS and a commercial CO_2 sensor 151

5.3.4.1 Signal to Noise Ratio 160

5.3.4.2 Percentage error 161

5.3.5 Discussion of obtained results from volunteer's skin CO_2 measurement. 164

5.4 Summary 167

6. Chapter 6 170

Summary, Conclusions & Future Work 170

6.1 Introduction 170

6.2 Summary and Conclusions 170

6.3 Future work 174

6.3.1 Guidelines to fabricate, store, and perform experiment with OFCSs 174

6.3.2 Steps to refine an FPI model 177

6.3.3 Design of a GCC on a fixation ring 178

6.3.4 Design of a prototype for skin CO_2 measurement 179

6.3.5 Design of a portable clinical unit for skin CO_2 measurement 181

References 185

A. Appendix A 201

Results from calibration of OFCSs (used for skin CO_2 measurement) 201

B. Appendix B 220

Results from monitoring CO_2 emitted from human skin using a t_C Sensor 92 probe ……..220

C. Appendix C 226

Results from monitoring CO_2 emitted from human skin during loading using an OFCS and a commercial CO_2 sensor 226

D. Appendix D 263

Experiment Ethics Approval 263

List of Figures

Figure 1.1: Basic block diagram of OFS system (adapted from [9]) 3
Figure 1.2: Block diagram of (a) intrinsic OFS (b) extrinsic OFS (adapted from [9]) 4
Figure 1.3: (a) Cross-section of human skin [14] Schematic structure of (b) epidermis layer (c) dermis layer and hypodermis layer [16] 6
Figure 1.4: Skin CO_2 measurement from PUs patient's skin using 4 OFCSs 11
Figure 2.1: Gas exchange in alveolus (adapted from [26]) 15
Figure 2.2: Relationship between pH and dissolved CO_2 concentrations in water [28] ... 16
Figure 2.3: Oxyhaemoglobin dissociation curve [26] 18
Figure 2.4: (a) Common locations of PUs [31] (b) Different stages of PUs [32] 19
Figure 2.5: Loading gantry utilised to provide pressure on sacrum [8] 21
Figure 2.6: T_CPCO_2 response after applying pressure on soft body tissues for 3 separate modes [8] 22
Figure 2.7: T_CPCO_2 skin response for 3 separate categories at sacrum [2] 23
Figure 2.8: Miniature EW sensor with spiral and straight waveguide [38] 27
Figure 2.9: Optical T_CPCO_2 monitoring method using optical miniaturized sampling cell [39] 28
Figure 2.10: Comparison in-vivo T_CPCO_2 monitoring achieved with MicroGas and optical microcell system [39] 28
Figure 2.11: IR gas analyser (Applied Physics Corporation) [46] 30
Figure 2.12: (a) Commercial CO_2 datalogger (CO2Meter.com, CM-0058) [48] (b) Commercial CO_2 sensor (CO2Meter.com, CM-0120) [49] (c) NDIR CO_2 sensor (adapted from [50]) 32
Figure 2.13: (a) t_C Sensor 92 probe (Radiometer) [1] (b) V-Sign™ Sensor 2 probe (SenTec) [51] 32
Figure 2.14: A Stow-Severinghaus electrode for measuring pH (adapted from [54]) 35
Figure 2.15: (a) Intensity based optical fibre sensor (adapted from [56]) (b) Wavelength modulated optical fibre sensor [57] (c) Phase modulated optical fibre sensor (adapted from [9]) (d) Polarisation modulated optical fibre sensor (adapted from [9]) 37

Figure 2.16: Film coating processing routes (a) LbL deposition [77] (b) Sol-gel coating [78] 47
Figure 2.17: Schematic diagram of set-up used for OFCS operating in (a) reflection mode (b) transmission mode (adapted from [83]) 48
Figure 2.18: Schematic diagram of LPG based CO_2 sensor [90] 51
Figure 2.19: (a) Basic structure (adapted from [91]) (b) Cross-sectional view of optical fibre (adapted from [92]) 53
Figure 2.20: Refraction of a beam of light is based on indices of refraction (n_1 and n_2) for each material (adapted from [92]) 54
Figure 2.21: (a) When incidence angle is equal to θ_C, refraction angle is equal to 90° (b) When incidence angle is greater than θ_C, light is reflected into core (adapted from [93]) 54
Figure 2.22: Schematic of the evanescent wave with ray theory approach [94] 56
Figure 2.23: An EM wave consisting of electric and magnetic oscillating fields [96] 57
Figure 2.24: Different characteristics of (a) multimode graded-index fibre (b) multimode step-index fibre (c) single-mode fibre (adapted from [91-92]) 58
Figure 3.1: Schematic diagram of light travelling through a solution (adapted from [104]) 66
Figure 3.2: Structural transitions of TB according to different pH values [105] 67
Figure 3.3: Absorption spectra, A_λ of TB for different pH values [105] 67
Figure 3.4: Experimental set-up for monitoring pH variation of TB 68
Figure 3.5: Ethanol and different colours of TB solutions in 1 cm pathlength cuvettes .. 69
Figure 3.6: (a) Transmission spectra (b) Absorption spectra (c) Molar absorption coefficient curve of TB for different pH values 70
Figure 3.7: Experimental set-up for coating process onto (a) optical fibre tip (b) glass substrate using commercial dip coating unit 71
Figure 3.8: Plot of the thickness versus withdrawal speed [108] 73
Figure 3.9: Observation of dried GS with 3 layers after 24 hours with different withdrawal speeds 73
Figure 3.10: Zoom view of dried GS without and with cracking 74
Figure 3.11: Experimental set-up for CO_2 calibration of OFCS 75
Figure 3.12: Reflection spectrum of OFCS after coating 77

Figure 3.13: (a) Reflection spectrum of OFCS including reflection spectrum of bare fibre (b) Absorption spectrum of OFCS with 4 layers after drying for 24 hours 77
Figure 3.14: (a) Reflection spectra of OFCS including reflection spectrum of bare fibre (b) Absorption spectra of OFCS with 4 layers for maximum and minimum CO_2 concentration 78
Figure 3.15: Reflection spectrum of bare fibre for (a) step up (b) step down response of OFCS..... 79
Figure 3.16: (a) Step up response w.r.t. reflection intensity (b) Step down response w.r.t. reflection intensity (c) Step up response w.r.t. absorbance (d) Step down response w.r.t. absorbance response of OFCS modified with sol-gel coating to different CO_2 concentrations with changing PCO_2 values at wavelength 600 nm..... 80
Figure 3.17: Reflection spectrum of bare fibre for reversibility of OFCS..... 81
Figure 3.18: Reversibility ((a) w.r.t. reflection intensity (b) w.r.t. absorbance) of OFCS different CO_2 concentrations with changing PCO_2 values at wavelength 600 nm 81
Figure 3.19: Polynomial fitting of (a) reflection intensities of OFCS to different CO_2 concentrations (b) reflection intensities of OFCS to different PCO_2 values (c) absorbances of OFCS to different CO_2 concentrations (d) absorbances of OFCS to different PCO_2 values and (e) PCO_2 values of t_C Sensor 92 probe to different CO_2 concentrations at wavelength 600 nm 84
Figure 3.20: Response and recovery times measurement of OFCS for 5% CO_2 at wavelength 600 nm 85
Figure 3.21: Experimental set-up for temperature calibration of OFCS [109]..... 89
Figure 3.22: Average normalised intensity value of OFCS to different CO_2 concentrations with changing temperature values at wavelengths 595-617 nm [109] 90
Figure 3.23: Experimental set-up for RH calibration of OFCS 91
Figure 3.24: (a) Reflection spectrum of bare fibre (b) Reflection spectra (c) Absorption spectra of OFCS to different RH values 91
Figure 3.25: (a) Reflection intensity (b) Absorbance of OFCS to different RH values at wavelength 600 nm 92
Figure 3.26: (a) Dimension of GCC (b) Experimental set-up for RH calibration of OFCS inside GCC with PTFE film..... 93

Figure 3.27: (a) Reflection intensity (b) Absorbance of OFCS inside GCC sandwiched with PTFE film and commercial CO_2 sensor to different RH values at wavelength 600 nm... 94
Figure 3.28: (a) Dimension of GS (b) Observation of coated GS with 1, 2, and 3 layers and dried GS with 3 layers after 24 hours 95
Figure 3.29: Images of PtOEP immobilised in silica matrices (a) without (b) with Triton X-100 [117]..... 97
Figure 3.30: (a) Reflection spectra (b) Absorption spectra of OFCSs with 3 layers after coating on that day (c) Reflection spectra (d) Absorption spectra of OFCSs with 3 layers coating after drying for 24 hours on next day..... 98
Figure 3.31: (a) Reflection spectra (b) Absorption spectra of OFCSs with 3 layers coating after storing for 9 days (c) Reflection spectra (d) Absorption spectra of OFCSs with 3 layers coating after storing for 16 days (e) Reflection spectra (f) Absorption spectra of OFCSs with 3 layers coating after storing for 35 days..... 99
Figure 3.32: (a) Reflection spectra (b) Absorption spectra of OFCSs after drying for 24 hours..... 101
Figure 3.33: Schematic diagram of fibre tips on specimen holder 102
Figure 3.34: SEM images of bare fibre's tip..... 102
Figure 3.35: SEM images of OFCS 1's tip with (a) 1 layer (b) film thickness measurement 103
Figure 3.36: SEM images of OFCS 2's tip with (a) 2 layers (b) film thickness measurement 103
Figure 3.37: SEM images of OFCS 3's tip with (a) 3 layers (b) film thickness measurement 103
Figure 3.38: Experimental set-up for CO_2 calibration of OFCS for skin CO_2 measurement 106
Figure 3.39: Reflection spectrum of bare fibre for fibre to fibre variability..... 107
Figure 3.40: Response (a) Reflection Intensity (b) Absorbance of OFCS 1 for different CO_2 concentrations at wavelength 600 nm..... 108
Figure 3.41: Linear fitting of variation in response (reflection intensity and absorbance) of OFCS 1 to different CO_2 concentrations at wavelength 600 nm..... 110
Figure 4.1: Illustration of skewness and kurtosis (adapted from [125])..... 116

Figure 4.2: A process of adding CO_2 with DI water 117
Figure 4.3: pH test strips (P4786, Sigma-Aldrich, UK) [126] 117
Figure 4.4: Experimental set-up for monitoring pH variation of TB with CO_2 118
Figure 4.5: Monitoring pH variation of TB with CO_2 using pH strip 118
Figure 4.6: Transmission spectra of Ethanol without CO_2 flow 119
Figure 4.7: (a) Transmission spectra (b) Absorption spectra (c) MAC curve of TB (red) without CO_2 flow 119
Figure 4.8: (a) Transmission spectra (b) Absorption spectra (c) MAC curve of TB (yellow) without CO_2 flow 120
Figure 4.9: (a) Transmission spectra (b) Absorption spectra (c) MAC curve of TB (blue) without CO_2 flow 120
Figure 4.10: Transmission spectra of Ethanol with CO_2 flow 121
Figure 4.11: (a) Transmission spectra (b) Absorption spectra (c) MAC curve of TB (red) with CO_2 flow 121
Figure 4.12: (a) Transmission spectra (b) Absorption spectra (c) MAC curve of TB (yellow) with CO_2 flow 122
Figure 4.13: (a) Transmission spectra (b) Absorption spectra (c) MAC curve of TB (blue) with CO_2 flow 122
Figure 4.14: (a) Mean Intensity (b) Mean Absorbance (c) Mean MAC of TB with and without CO_2 flow 124
Figure 4.15: Mean Skewness of (a) Intensity (b) Absorbance and MAC of TB with and without CO_2 flow 124
Figure 4.16: Mean Kurtosis of (a) Intensity (b) Absorbance and MAC of TB with and without CO_2 flow 125
Figure 4.17: Schematic diagram of fibre-tip FPI sensor (adapted from [127]) 126
Figure 4.18: (a) Constructive (b) Destructive interference occurs when 2 waves meet [130] 127
Figure 4.19: MAC curve of TB (blue) 130
Figure 4.20: Simulated (a) Reflection spectrum (b) Absorption spectrum of FPI for film thickness 4.888 μm 131

Figure 4.21: Simulated (a) Reflection spectrum (b) Absorption spectrum of FPI for film thickness 5.690 µm 131
Figure 4.22: Simulated (a) Reflection spectrum (b) Absorption spectrum of FPI for film thickness 7.234 µm 132
Figure 4.23: The maximum and minimum intensity detection from simulated reflection spectrum of FPI for film thickness 4.888 µm at wavelengths 586-598 nm..... 132
Figure 4.24: The maximum and minimum intensity detection from simulated reflection spectrum of FPI for film thickness 5.690 µm at wavelengths 586-598 nm..... 133
Figure 4.25: The maximum and minimum intensity detection from simulated reflection spectrum of FPI for film thickness 7.234 µm at wavelengths 586-598 nm..... 133
Figure 4.26: Fringe visibility of FPI by varying film thickness at wavelengths 586-598 nm 134
Figure 4.27: The maximum and minimum intensity detection from reflection spectrum of OFCS for film thickness 3.835 µm and 6.259 µm at wavelengths 525-567 nm 135
Figure 5.1: Experimental set-up for monitoring PCO_2 from human skin using t_C Sensor 92 probe 139
Figure 5.2: Calibration process of t_C Sensor 92 probe using TCM TOSCA monitor..... 139
Figure 5.3: PCO_2 measurement using t_C Sensor 92 probe for different temperatures when temperature correction factor is turned on..... 143
Figure 5.4: Average PCO_2 measurement using t_C Sensor 92 probe from Volunteer 1's forearm (5 trials) 144
Figure 5.5: (a) Schematic diagram of loading machine (b) Dimension of empty weight holder with steel rod (c) Top view of empty weight holder (d) Top view of weight holder with 100 g slotted mass (e) Dimension of PLA based circular plate..... 146
Figure 5.6: Experimental set-up for monitoring CO_2 emitted from wrapped human skin during loading using OFCS and commercial CO_2 sensor..... 147
Figure 5.7: Different views of holder for simultaneous CO_2 measurement using OFCS and commercial CO_2 sensor..... 148
Figure 5.8: Hot & cold therapy disc and Foil blanket..... 148
Figure 5.9: (a) (c) (e) Reflection spectra and (b) (d) (f) Absorption spectra of OFCS 1. Each row represents a different Trial 1-3 for Volunteer 1..... 153

Figure 5.10: (a) (c) (e) Response (Reflection Intensity) of OFCS 1 at wavelength 600 nm and commercial CO_2 sensor on Volunteer 1's forearm (b) (d) (f) Volunteer 1's skin temperature while heated disc is on forearm for Trials 1-3, respectively 155
Figure 5.11: (a)-(c) Response (Absorbance) of OFCS 1 at wavelength 600 nm and commercial CO_2 sensor on Volunteer 1's forearm for Trials 1-3, respectively 156
Figure 5.12: (a)-(c) Response (Raw Reflection Intensity) of OFCS 1 at wavelength 600 nm in the air for Trials 1-3, respectively 159
Figure 5.13: Response (Raw and Smooth Reflection Intensity) of OFCS 1 at wavelength 600 nm in the air for Trial 1 160
Figure 5.14: (a) PLA based holder containing OFCS tip and commercial CO_2 sensor (b) OFCS is placed in air without bending (c) OFCS is placed in air with bending 165
Figure 6.1: Experimental set-up for a simultaneous coating process onto multiple optical fibre tips during (a) coating (b) drying intervals using commercial dip coating unit 175
Figure 6.2: Coating of optical fibre tip for (a) lower (b) higher immersed length 176
Figure 6.3: (a) Front (b) Back view of fixation ring 178
Figure 6.4: Dimension of PLA based GCC on fixation ring 178
Figure 6.5: (a) Internal structure (b) Block diagram of prototype for skin CO_2 measurement using OFCS 179
Figure 6.6: Experimental set-up for monitoring CO_2 emitted from human skin during loading using OFCS and prototype 181
Figure 6.7: (a) Internal structure (b) Block diagram of portable clinical unit for skin CO_2 measurement using 4 OFCSs 182
Figure 6.8: Experimental set-up for monitoring CO_2 emitted from human skin during loading using 4 OFCSs and portable clinical unit 184
Figure B.1: Average PCO_2 measurement using t_C Sensor 92 probe from Volunteer 2's forearm 221
Figure B.2: Average PCO_2 measurement using t_C Sensor 92 probe from Volunteer 3's forearm 221
Figure B.3: Average PCO_2 measurement using t_C Sensor 92 probe from Volunteer 4's forearm 222

Figure B.4: Average PCO_2 measurement using t_C Sensor 92 probe from Volunteer 5's forearm 222
Figure B.5: Average PCO_2 measurement using t_C Sensor 92 probe from Volunteer 6's forearm 223
Figure B.6: Average PCO_2 measurement using t_C Sensor 92 probe from Volunteer 7's forearm 223
Figure B.7: Average PCO_2 measurement using t_C Sensor 92 probe from Volunteer 8's forearm 224
Figure B.8: Average PCO_2 measurement using t_C Sensor 92 probe from Volunteer 9's forearm 224
Figure B.9: Average PCO_2 measurement using t_C Sensor 92 probe from Volunteer 10's forearm 225
Figure C.1: (a) (c) (e) Reflection spectra and (b) (d) (f) Absorption spectra of OFCS 2. Each row represents a different Trial 1-3 for Volunteer 2 227
Figure C.2: (a) (c) (e) Reflection spectra and (b) (d) (f) Absorption spectra of OFCS 3. Each row represents a different Trial 1-3 for Volunteer 3 228
Figure C.3: (a) (c) (e) Reflection spectra and (b) (d) (f) Absorption spectra of OFCS 4. Each row represents a different Trial 1-3 for Volunteer 4 229
Figure C.4: (a) (c) (e) Reflection spectra and (b) (d) (f) Absorption spectra of OFCS 5. Each row represents a different Trial 1-3 for Volunteer 5 230
Figure C.5: (a) (c) (e) Reflection spectra and (b) (d) (f) Absorption spectra of OFCS 6. Each row represents a different Trial 1-3 for Volunteer 6 231
Figure C.6: (a) (c) (e) Reflection spectra and (b) (d) (f) Absorption spectra of OFCS 7. Each row represents a different Trial 1-3 for Volunteer 7 232
Figure C.7: (a) (c) (e) Reflection spectra and (b) (d) (f) Absorption spectra of OFCS 8. Each row represents a different Trial 1-3 for Volunteer 8 233
Figure C.8: (a) (c) (e) Reflection spectra and (b) (d) (f) Absorption spectra of OFCS 9. Each row represents a different Trial 1-3 for Volunteer 9 234
Figure C.9: (a) (c) (e) Reflection spectra and (b) (d) (f) Absorption spectra of OFCS 10. Each row represents a different Trial 1-3 for Volunteer 10 235

Figure C.10: (a) (c) (e) Response (Reflection Intensity) of OFCS 2 at wavelength 600 nm and commercial CO_2 sensor on Volunteer 2's forearm (b) (d) (f) Volunteer 2's skin temperature while heated disc is on forearm for Trials 1-3, respectively..... 236
Figure C.11: (a)-(c) Response (Absorbance) of OFCS 2 at wavelength 600 nm and commercial CO_2 sensor on Volunteer 2's forearm for Trials 1-3, respectively 237
Figure C.12: (a)-(c) Response (Raw Reflection Intensity) of OFCS 2 at wavelength 600 nm in the air for Trials 1-3, respectively..... 238
Figure C.13: (a) (c) (e) Response (Reflection Intensity) of OFCS 3 at wavelength 600 nm and commercial CO_2 sensor on Volunteer 3's forearm (b) (d) (f) Volunteer 3's skin temperature while heated disc is on forearm for Trials 1-3, respectively..... 239
Figure C.14: (a)-(c) Response (Absorbance) of OFCS 3 at wavelength 600 nm and commercial CO_2 sensor on Volunteer 3's forearm for Trials 1-3, respectively 240
Figure C.15: (a)-(c) Response (Raw Reflection Intensity) of OFCS 3 at wavelength 600 nm in the air for Trials 1-3, respectively..... 241
Figure C.16: (a) (c) (e) Response (Reflection Intensity) of OFCS 4 at wavelength 600 nm and commercial CO_2 sensor on Volunteer 4's forearm (b) (d) (f) Volunteer 4's skin temperature while heated disc is on forearm for Trials 1-3, respectively..... 242
Figure C.17: (a)-(c) Response (Absorbance) of OFCS 4 at wavelength 600 nm and commercial CO_2 sensor on Volunteer 4's forearm for Trials 1-3, respectively 243
Figure C.18: (a)-(c) Response (Raw Reflection Intensity) of OFCS 4 at wavelength 600 nm in the air for Trials 1-3, respectively..... 244
Figure C.19: (a) (c) (e) Response (Reflection Intensity) of OFCS 5 at wavelength 600 nm and commercial CO_2 sensor on Volunteer 5's forearm (b) (d) (f) Volunteer 5's skin temperature while heated disc is on forearm for Trials 1-3, respectively..... 245
Figure C.20: (a)-(c) Response (Absorbance) of OFCS 5 at wavelength 600 nm and commercial CO_2 sensor on Volunteer 5's forearm for Trials 1-3, respectively 246
Figure C.21: (a)-(c) Response (Raw Reflection Intensity) of OFCS 5 at wavelength 600 nm in the air for Trials 1-3, respectively..... 247
Figure C.22: (a) (c) (e) Response (Reflection Intensity) of OFCS 6 at wavelength 600 nm and commercial CO_2 sensor on Volunteer 6's forearm (b) (d) (f) Volunteer 6's skin temperature while heated disc is on forearm for Trials 1-3, respectively..... 248

Figure C.23: (a)-(c) Response (Absorbance) of OFCS 6 at wavelength 600 nm and commercial CO_2 sensor on Volunteer 6's forearm for Trials 1-3, respectively 249
Figure C.24: (a)-(c) Response (Raw Reflection Intensity) of OFCS 6 at wavelength 600 nm in the air for Trials 1-3, respectively..... 250
Figure C.25: (a) (c) (e) Response (Reflection Intensity) of OFCS 7 at wavelength 600 nm and commercial CO_2 sensor on Volunteer 7's forearm (b) (d) (f) Volunteer 7's skin temperature while heated disc is on forearm for Trials 1-3, respectively..... 251
Figure C.26: (a)-(c) Response (Absorbance) of OFCS 7 at wavelength 600 nm and commercial CO_2 sensor on Volunteer 7's forearm for Trials 1-3, respectively 252
Figure C.27: (a)-(c) Response (Raw Reflection Intensity) of OFCS 7 at wavelength 600 nm in the air for Trials 1-3, respectively..... 253
Figure C.28: (a) (c) (e) Response (Reflection Intensity) of OFCS 8 at wavelength 600 nm and commercial CO_2 sensor on Volunteer 8's forearm (b) (d) (f) Volunteer 8's skin temperature while heated disc is on forearm for Trials 1-3, respectively..... 254
Figure C.29: (a)-(c) Response (Absorbance) of OFCS 8 at wavelength 600 nm and commercial CO_2 sensor on Volunteer 8's forearm for Trials 1-3, respectively 255
Figure C.30: (a)-(c) Response (Raw Reflection Intensity) of OFCS 8 at wavelength 600 nm in the air for Trials 1-3, respectively..... 256
Figure C.31: (a) (c) (e) Response (Reflection Intensity) of OFCS 9 at wavelength 600 nm and commercial CO_2 sensor on Volunteer 9's forearm (b) (d) (f) Volunteer 9's skin temperature while heated disc is on forearm for Trials 1-3, respectively..... 257
Figure C.32: (a)-(c) Response (Absorbance) of OFCS 9 at wavelength 600 nm and commercial CO_2 sensor on Volunteer 9's forearm for Trials 1-3, respectively 258
Figure C.33: (a)-(c) Response (Raw Reflection Intensity) of OFCS 9 at wavelength 600 nm in the air for Trials 1-3, respectively..... 259
Figure C.34: (a) (c) (e) Response (Reflection Intensity) of OFCS 10 at wavelength 600 nm and commercial CO_2 sensor on Volunteer 10's forearm (b) (d) (f) Volunteer 10's skin temperature while heated disc is on forearm for Trials 1-3, respectively..... 260
Figure C.35: (a)-(c) Response (Absorbance) of OFCS 10 at wavelength 600 nm and commercial CO_2 sensor on Volunteer 10's forearm for Trials 1-3, respectively 261

Figure C.36: (a)-(c) Response (Raw Reflection Intensity) of OFCS 10 at wavelength 600 nm in the air for Trials 1-3, respectively 262
Figure D.1: Set-up for monitoring CO_2 emitted from wrapped human skin during loading using OFCS and commercial CO_2 Sensor 267
Figure D.2: Set-up for monitoring PCO_2 from human skin using t_C Sensor 92 probe ... 269

List of Tables

Table 2.1: Grading pattern of Braden scale [37] 24
Table 2.2: Variation in T_CPCO_2 values between chest in lateral position, sacrococcygeal region in lateral and supine position [36] 26
Table 2.3: Specifications of commercial devices for measuring CO_2 and T_CPCO_2 33
Table 2.4: OFCSs based on sol-gel films [81] 50
Table 3.1: Calculation of TB concentration according to pH variation 69
Table 3.2: Film Thickness of the layers from the fringes observed in Figure 3.12 87
Table 3.3: Preparation protocol of sol-gel solutions (Solution 1 and Solution 2) inside glass vial [103] 96
Table 3.4: Reflection intensity and absorbance of OFCS 1 and OFCS 2 and reflection intensity of bare fibre at wavelength 600 nm based on number of OFCSs' storing days100
Table 3.5: Average film thickness and TB concentration measurement from SEM images of OFCSs 105
Table 3.6: Variation of CO_2 concentration and response (reflection intensity and absorbance) of OFCS 1 at wavelength 600 nm for different time periods 109
Table 3.7: OFCS's sensitivity w.r.t. intensity and absorbance 111
Table 4.1: Interpretation of skewness values [123] 115
Table 4.2: Interpretation of kurtosis values [123] 115
Table 4.3: Interpretation of all spectra of TB for different pH values 123
Table 4.4: The necessary parameters' values for simulation of FPI 130
Table 5.1: PCO_2 value measurement for different CO_2 concentrations [obtained from Figures 3.16 (a) and (c), increasing trend (1.7% CO_2 to 4.6% CO_2) and Figures 3.16 (b) and (d), decreasing trend (5.3% CO_2 to 1.0% CO_2) respectively] 141

Table 5.2: Temperature correction factor for T_CPCO_2 measurement at different temperatures [55] 141
Table 5.3: Average PCO_2 values of 10 volunteers' at different sensor temperatures for 5 trials..... 144
Table 5.4: Nature of reflection and absorption spectra of OFCSs (OFCS 1-10)..... 154
Table 5.5: Nature of reflection intensity and absorbance of OFCSs (OFCS 1-10) 157
Table 5.6: Error and SNR calculation of 10 volunteers' for 3 trials..... 163
Table 5.7: Observation and possible reasons for variation in obtained results during skin CO_2 measurement 166
Table A.1: Variation of CO_2 concentration and response (reflection intensity and absorbance) of OFCS 2 at wavelength 600 nm for different time periods 203
Table A.2: Variation of CO_2 concentration and response (reflection intensity and absorbance) of OFCS 3 at wavelength 600 nm for different time periods 205
Table A.3: Variation of CO_2 concentration and response (reflection intensity and absorbance) of OFCS 4 at wavelength 600 nm for different time periods 207
Table A.4: Variation of CO_2 concentration and response (reflection intensity and absorbance) of OFCS 5 at wavelength 600 nm for different time periods 209
Table A.5: Variation of CO_2 concentration and response (reflection intensity and absorbance) of OFCS 6 at wavelength 600 nm for different time periods 211
Table A.6: Variation of CO_2 concentration and response (reflection intensity and absorbance) of OFCS 7 at wavelength 600 nm for different time periods 213
Table A.7: Variation of CO_2 concentration and response (reflection intensity and absorbance) of OFCS 8 at wavelength 600 nm for different time periods 215
Table A.8: Variation of CO_2 concentration and response (reflection intensity and absorbance) of OFCS 9 at wavelength 600 nm for different time periods 217
Table A.9: Variation of CO_2 concentration and response (reflection intensity and absorbance) of OFCS 10 at wavelength 600 nm for different time periods 219

List of Acronyms

2-3 diphosphoglycerate	(DPG)
3-Aminopropyltrioxysilane	(APTES)
8-hydroxypyrene-1,3,6-trisulfonic acid	(HPTS)
American Chemical Society	(ACS)
Alternating pressure air mattress	(APAM)
Ammonia	(NH_3)
Argon	(Ar)
Arterial partial pressure of carbon dioxide	(P_aCO_2)
Arterial partial pressure of oxygen	(P_aO_2)
Bare fibre	(BF)
Bicarbonate ions	(HCO_3^-)
Carbon dioxide	(CO_2)
Carbonic acid	(H_2CO_3)
Cetyltrimethylammonium bromide	(CTAB)
Chemical optical fibre sensor	(COFS)
Deionised	(DI)
Electromagnetic	(EM)
Electromagnetic interference	(EMI)
Ethanol	(EtOH)
Ethyltriethoxysliane	(ETES)
Evanescent wave	(EW)
Fabry-Perot	(FP)
Fabry-Perot interferometer	(FPI)
Fibre Bragg grating	(FBG)
Gas collection chamber	(GCC)
Glass substrate	(GS)
Hydrochloric acid	(HCl)
Hydrogen ions	(H^+)
Infrared	(IR)

Intensity based optical fibre sensor	(IBOFS)
Layer-by-Layer	(LbL)
Light emitting diode	(LED)
Linearly polarised	(LP)
Long Period grating	(LPG)
Magnetic resonance imaging	(MRI)
Metal organic framework	(MOF)
Methyltriethoxysilane	(MTES)
Methyltrimethoxysilane	(MTMS)
Microcentrifuge tube	(MT)
Molar absorption coefficient	(MAC)
Multimode	(MM)
Multimode fibre	(MMF)
Nanoparticles	(NPs)
Nanoscale and Microscale Research Centre	(nmRC)
National Health Service	(NHS)
Nitric acid	(HNO3)
Nitrogen	(N_2)
Nondispersive infrared	(NDIR)
No-core fibre	(NCF)
Oxygen saturation of arterial haemoglobin	(S_PO_2)
Optical density	(OD)
Optical fibre CO_2 sensor	(OFCS)
Optical fibre humidity sensor	(OFHS)
Optical fibre NH_3 sensor	(OFNS)
Optical fibre pH sensor	(OFpHS)
Optical fibre pressure sensor	(OFPS)
Optical fibre sensor	(OFS)
Optical fibre strain sensor	(OFSS)
Optical fibre temperature sensor	(OFTS)

Optical path difference	(OPD)
Organically modified silica	(Ormosil)
Orthosilicic acid	$Si(OR)_4$
Oxygen	(O_2)
Partial pressure of carbon dioxide	(PCO_2)
Partial pressure of oxygen	(PO_2)
Phase modulated optical fibre sensor	(PMOFS)
Physical optical fibre sensor	(POFS)
Plastic-clad silica	(PCS)
Platinum octaethylporphyrin	(PtOEP)
Polarisation modulated optical fibre sensor	(POMOFS)
Polyaniline	(PAni)
Poly allylamine hydrochloride	(PAH)
Poly(acrylic acid)	(PAA)
Poly(ethylene glycol) diacrylate	(PEGDA)
Polydimethylsiloxane	(PDMS)
Polylactic acid	(PLA)
Polytetrafluoroethylene	(PTFE)
Pressure ulcers	(PUs)
Pulse rate	(PR)
Queen's Medical Centre	(QMC)
Refractive index	(RI)
Room temperature vulcanizing	(RTV)
RU(II)-tris(4,7-diphenyl-1,10-phenanthroline)	($RU(dpp)_3$)
Scanning electron microscope	(SEM)
Signal-to-noise ratio	(SNR)
Silanol group	(Si-OH)
Silica	(SiO_2)
Silicon	(Si)
Silicon nitride	(Si_3N_4)

Silver	(Ag)
Silver chloride	(AgCl)
Single mode fibre	(SMF)
SMF-NCF-SMF	(SNS)
Sodium bicarbonate	($NaHCO_3$)
Sodium chloride	(NaCl)
Sodium hydroxide	(NaOH)
T_CPCO_2 probe	(TP)
Temperature-controlled heating mat	(TCHM)
Tetraethyl orthosilicate or Tetraethoxysilane	(TEOS)
Tetramethyl orthosilicate	(TMOS)
Tetramethylammonium hydroxide	(TMAH)
Tetraphenylporphyrin tetrasulfic acid	(TPPS)
Thymol Blue	(TB)
Total internal reflection	(TIR)
Transcutaneous carbon dioxide pressure	(T_CPCO_2)
Transcutaneous oxygen pressure	(T_CPO_2)
Triethoxymethylsilane	(MTEOS)
Ultraviolet	(UV)
Ultraviolet-Visible	(UV-Vis)
University of Nottingham	(UoN)
Water	(H_2O)
Wavelength modulated optical fibre sensor	(WMOFS)

1. Chapter 1

Thesis Introduction

1.1 Introduction

This chapter introduces the project goals and potential contribution of an optical fibre sensor (OFS) for monitoring tissue loading. Section 1.2 discusses the aims and objectives of this research. Section 1.3 explains the novelty of this research. Section 1.4 is focused on the classification, features, and applications of the OFS. Section 1.5 illustrates the skin properties and the relationship between transcutaneous CO_2, pressure, and the skin. Section 1.6 demonstrates how the optical fibre CO_2 sensor (OFCS) will be placed on the patients' skin in future. Finally, Section 1.7 provides an overview of the whole thesis.

1.2 Aims and Objectives

This research aims to develop an OFS that can be used to monitor skin biomarkers associated with tissue breakdown, such as CO_2. If successful, this could ultimately be used to prevent pressure ulcers (PUs) by alerting subjects or medical professionals at an early stage whether they are at risk of developing PUs.

The specific aims of this PhD thesis are:

1) To develop and fabricate an OFCS.
2) To apply the sensor to monitor transcutaneous CO_2, a known skin biomarker of tissue breakdown.

The specific objectives of this PhD thesis are:

1) To fabricate an OFCS to monitor emission of CO_2 from skin.
2) To compare the OFCS's response to that of a commercial transcutaneous CO_2 probe and commercial CO_2 datalogger.
3) To monitor CO_2 emitted from human skin during loading using the developed OFCS and a commercial CO_2 sensor.
4) To develop a Fabry-Perot interferometer (FPI) model of the optical cavity created at the fibre tip to simulate varying the sensing film thickness.

1.3 Motivation

Several commercial clinical devices exist to measure transcutaneous carbon dioxide pressure (T_CPCO_2); however, these devices are either expensive or unsuitable to be used for continuous monitoring in positions likely to be susceptible to PUs due mainly to the size of the sensor head (diameter and height of the t_C Sensor 92 probe is 15 mm and 8 mm, respectively [1]). However, T_CPCO_2 is a promising biomarker for early detection of PUs in such a setting [2]. The commercial electrode is a pH electrode that detects the blood's pH changes that are proportional to the concentration of dissolved blood CO_2 [3]. The working principle of a pH electrode is mentioned in Section 2.5. The main drawbacks of commercial T_CPCO_2 electrodes are they are bulky preventing use for long periods on vulnerable body areas; and the high electrode temperature (37-45 ℃) results in only short application times to reduce skin burning risks. The commercial T_CPCO_2 electrode attaches to the skin via a contact gel, preventing bias from ambient air between the electrode and tissue [4]. This contact gel comprises a small quantity of sensitising element, which may cause an allergic reaction on sensitive skin [5]. Alternatively, optical fibre technology offers a suitable, reasonable, secure, and viable approach for long term monitoring by analysing the output response of the sensor and has been utilised clinically since the early 1960s. OFSs, such as the fabricated OFCS presented in this thesis, are small (core diameter, Ø 62.5 µm, cladding diameter, Ø 125 µm), lightweight, passive, have low attenuation, are insusceptible to electromagnetic interference (EMI), have high sensitivity and the capability to adhere to harsh environmental conditions [6]. The OFCS doesn't require skin heating, contact gel, and temperature calibration compared to the commercial T_CPCO_2 electrode. Therefore, if comparable performance to electrochemical sensing could be achieved, then there is an opportunity for OFCS to be widely adopted for monitoring tissue breakdown.

Skin damage is quite a slow process (1-2 hrs to develop a grade 3 or 4 PUs [7]); a commercially available transcutaneous CO_2 probe (t_C Sensor 92) response time is around 78 seconds [4], which is acceptable to clinicians and requires no further improvement. Therefore, I estimate a response time of approximately 3 minutes would be acceptable for monitoring PUs. The t_C Sensor 92 probe measures the partial pressure of CO_2 (PCO_2) in

units of mmHg or kPa. The measurement range varies according to the different loading amounts on the skin, such as the PCO_2 value of 36-44 mmHg (for 40 mmHg or 5.3 kPa loading), 50-60 mmHg (for 80 mmHg or 10.7 kPa loading), and > 80 mmHg (for 120 mmHg or 16 kPa loading) [8]. Therefore, an OFCS would need to be able to discriminate these ranges. This project aims to measure T_CPCO_2 without interfering with the metabolism or tissue perfusion, resulting in a novel and non-invasive approach for the tissue CO_2 measurement.

1.4 Optical fibre sensors

Optical fibres with appropriate modifications can be used as sensors to effectively observe physical, biological, and chemical measurands [9].

1.4.1 OFS principles

The basic block diagram of an OFS is illustrated in Figure 1.1. It comprises a light source (laser or light emitting diode (LED)), an optical fibre as a measurement channel, a sensing element (which converts the measurands to an optical signal), an optical detector, and processing tools at the endpoint (oscilloscope or computer). Depending on the sensor's site, an OFS can be categorized into intrinsic or extrinsic [9].

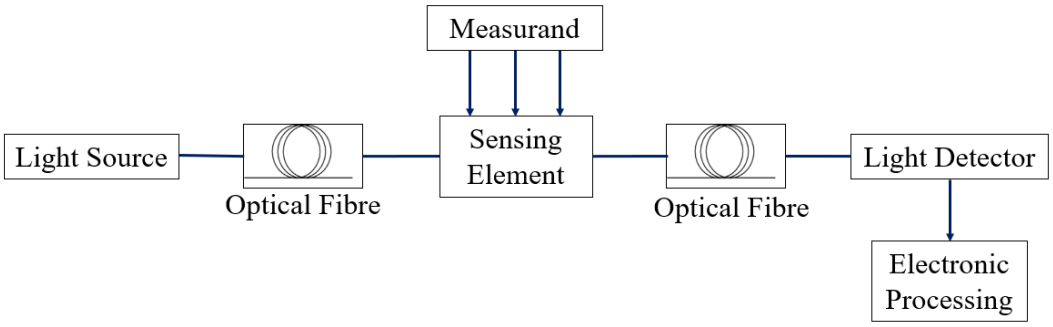


Figure 1.1: *Basic block diagram of OFS system (adapted from [9])*

1.4.1.1 Intrinsic OFS

Figure 1.2 (a) shows the fundamental concept of an intrinsic OFS in which the sensing mechanism is due to a change in the fibre itself. The optical fibre's internal property converts the environmental variations into a modulation of the optical signal. The intensity, phase, frequency, or polarisation are considered the light signal parameters [9].

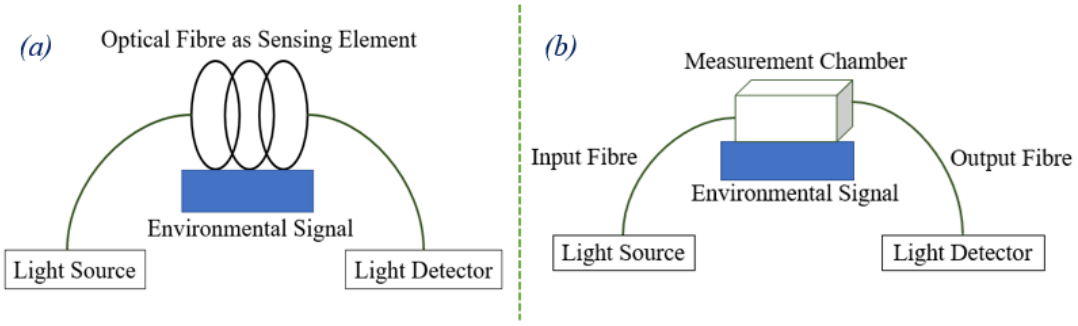


Figure 1.2: *Block diagram of (a) intrinsic OFS (b) extrinsic OFS (adapted from [9])*

1.4.1.2 Extrinsic OFS

Compared to intrinsic sensing, extrinsic sensing uses fibres to carry information to a measurement chamber, generating a light signal based on the data received in the measurement chamber. This measurement chamber could contain gas or liquid samples that will eventually produce an optical signal [9].

Figure 1.2 (b) illustrates the working principle of an extrinsic optical fibre sensing. In an extrinsic sensor the fibre itself is unchanged and sensing is undertaken by measuring a sensing element external to the fibre. The light travels from the light source to the black box attached to an input fibre, and the transmitted light is sent to the detector via an output fibre [10]. Also, the working principle of a reflection mode extrinsic OFS is mentioned in Section 2.10. The light travels from the light source to the sensor, and the optical detector receives the reflected light through an optical fibre coupler, according to Figure 2.16 (a).

The OFCS developed in this research is an extrinsic sensor because the fibre properties are not changing. The fibre tip is coated with a chemically sensitive layer (pH indicator dye, thymol blue, TB) and light is reflected from the fibre tip. The OFCS is placed inside different media (like air or CO_2 environment) to detect CO_2. The pH indicator dye changes its colour (blue to yellow), and the light intensity also varies within the absorbance band (around 500-700 nm) of the pH indicator dye due to the presence of CO_2. The change in light intensity is detected when the analyte interacts with the chemical coating on the fibre tip. The refractive index difference between the optical fibre core and chemically sensitive layer controls the reflected light intensity to the detector [11].

1.4.2 Benefits of OFSs

The OFSs give numerous benefits over typical electronics sensors. Such as [9],

I) Simple to implement in any form because of their small size and tubular geometry.

II) Lack of current flow reducing safety issues.

III) Fibres are chemically inert.

IV) Remote detecting capability.

V) Resistant to EMI and radio frequency interaction.

1.4.3 Commercially available OFCSs

Much progress has been made in the medical field with invasive and non-invasive OFSs. The sensor's small size permits insertion into tissue, and its non-voltaic behaviour means they are electrically safe. The functions of the OFSs are categorized within the several fields of usage, such as in-vitro (e.g., gas detection, body fluids, or ex-vivo tissue tests), non-invasive in-vivo, (e.g., optode placed on human skin), invasive in-vivo, (e.g., endoscopic devices or catheters), or in challenging situations where electronic devices are susceptible to the environment, such as during magnetic resonance imaging (MRI) [10].

Commercially available OFCSs have many functions in several areas. Two such companies are:

i) Intelligent Optical Systems, Inc., USA (https://www.intopsys.com) have developed a robust distributed fibre optic CO_2 sensor to measure the dissolved CO_2 from underground water. The whole length of the optical fibre functions as the sensor, able to cover a wide area and depths of hundreds of metres. A silica (SiO_2) glass core fibre is coated with a polymer [$(SiO_2)_n$] cladding consisting of a colorimetric pH indicator {8-hydroxypyrene-1,3,6-trisulfonic acid (HPTS) and Oregon Green 514 carboxylic acid}. During CO_2 exposure of any part of the optical fibre, CO_2 diffuses into the fibre cladding and immediately shifts the colour of the pH indicator. In this sensor, the evanescent field is utilised to interrogate the fibre cladding's properties. The light transmitted through the fibre

varies with the CO_2 concentration. The transmission spectrum of light (at a particular wavelength) rises with the dissolved CO_2 concentration in water [12].

ii) PreSens Precision Sensing GmbH, Germany (https://www.presens.de) developed a CO_2 dipping probe (DP-CD1) to measure and monitor the dissolved CO_2. Here, a 2 mm polymer optical fibre functions as the sensor where the fibre end is coated with a CO_2 sensitive material (HPTS). A high-grade steel tube covers and protects the fibre end containing CO_2 sensitive material. The response time is less than 3 minutes with a CO_2 measurement range from 10000 ppm to 250000 ppm and partial pressure of CO_2 (PCO_2) measurement range from 10 hPa to 250 hPa (8 mmHg to 180 mmHg) [13].

1.5 Monitoring T_CPCO_2 from skin

1.5.1 Skin structure

Skin is known as the human body's largest organ [14]. On average 1 square inch of skin comprises 650 sweat glands, 20 blood vessels, more than 1,000 nerve endings and 60000 pigment-producing cells and is typically 2 mm thick [15].

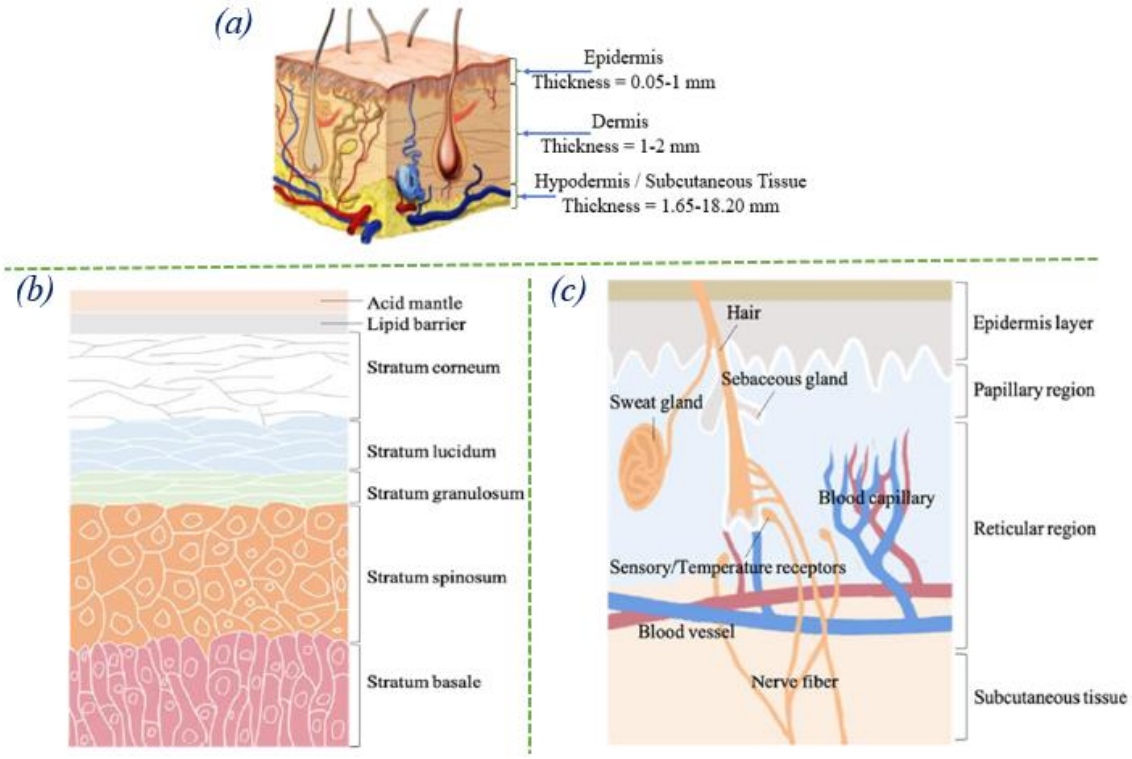


Figure 1.3: *(a) Cross-section of human skin [14] Schematic structure of (b) epidermis layer (c) dermis layer and hypodermis layer [16]*

Figure 1.3 demonstrates the cross-sectional view of human skin consisting of 2 main layers: the epidermis and dermis. Beneath the dermis is the hypodermis or subcutaneous greasy tissue [14].

1.5.1.1 Epidermis

The epidermis is the thinner and outermost layer of the skin containing 25-30 layers of dead cells. It functions as a defensive cover, waterproof barrier for skin, and contains the skin tone. It comprises keratinocytes, epithelial cells, which create hard, fibrous protein keratin. Keratinocytes give protection against parasites, bacteria, viruses, heat, fungi, ultraviolet (UV) radiation, and water loss by functioning as a barrier. No blood vessels exist in the epidermis. Diffusion from blood capillaries feeds the cells from the epidermis' lowest layers to the dermis' top layers [14-15] [17].

New cells are continually being formed in the epidermis' lowest layers. Naturally, these cells come up to the skin surface via the epidermis and remove the dead cells within 4 weeks. Melanin is a pigment generated by melanocytes inside the epidermis, and it protects the skin from UV light. Melanin is responsible for the skin's colour. The acid mantle and lipid barrier are located above the epidermis [16]. The epidermis is split into 5 sub-layers [14]:

I) stratum corneum – dead cells at the surface
II) stratum lucidum,
III) stratum granulosum,
IV) stratum spinosum,
V) stratum basale – sometimes called stratum germinativum.

1.5.1.2 Dermis

The dermis is the thickest and innermost layer of the skin, just beneath the epidermis. Sweat glands, tough connective tissue, lymphatic vessels, blood vessels, hair follicles, and sebaceous glands, which produce sebum (an oil that waterproofs hair) are inside the dermis. A basement membrane connects the dermis and epidermis firmly. The dermis gives the skin flexibility and strength and protects the skin from strain and stress by functioning as connective tissue [17]. The dermis' blood vessels eliminate wastes from its cells and the

epidermis's stratum basale (sometimes called stratum germinativum). Those blood vessels also feed to the cells and stratum basale [14].

The dermis contains 2 different regions, such as the papillary and reticular areas. Loose connective tissue can be found in the papillary region. The papillary area contains finger-like projections pressing into the epidermis, providing the dermis with a rough surface – this generates a person's fingerprint. The reticular area contains protein fibres that provide skin rigidity and elasticity and consist of dense, irregularly organised connective tissue [17].

1.5.1.3 Hypodermis

The subcutaneous tissue is the last and deepest layer of the skin, known as hypodermis or subcutis. The hypodermis is not considered a part of our skin. The hypodermis joins the skin to bone and muscle and connects the skin with nerve and blood vessels. The connective tissue, fat, and elastin can be found inside the hypodermis. Elastin (a flexible protein) returns the stretched tissue to its actual shape [14]. The large quantities of fat prevent excessive heat loss from the skin and protect our muscles and bones [17].

There are different types of skin injuries. They include cuts, lacerations, gashes, tears, scrapes, scratches, bruises, punctured skin, and pressure injuries [18]. PUs is caused by long periods of pressure over a bony part of the body (such as the hip and heel) [19].

Hulka and colleagues [20] defined biomarkers as biochemical alterations or an indicator that are measurable in biological media. Biomarker shows the whole scenario of disease from the initial symptoms through to the final stage [21]. For instance, the concentration of sweat lactate and T_CPCO_2 increased considerably in the presence of loading. Consequently, sweat lactate and T_CPCO_2 are considered potential biomarkers for PUs [2].

1.5.2 Overview of transcutaneous monitoring

The first appearance of commercial T_CPCO_2 examinations was in 1978. According to Bromley 2008 [22], 150 years ago, Physiologists discovered that human skin 'breathes' – that is it takes up O_2 and gives off CO_2 to the air. CO_2 diffuses through the skin surface faster than O_2: a transcutaneous sensor accurately shows the arterial partial pressure of CO_2 (P_aCO_2) value at sensor temperature $\simeq$ 37 °C considering the prolonged sensor's response

time. The membrane covered Severinghaus PCO_2 electrode are suitable for measuring T_CPCO_2 from newborns. The transcutaneous oxygen pressure (T_CPO_2) and T_CPCO_2 measuring technique were merged in 1979, and nowadays, this technique has become very popular [22].

1.5.2.1 Key factors for transcutaneous monitoring

A patient's respiratory and circulatory performance is monitored by a T_CPCO_2 probe (TP). The results obtained from T_CPCO_2 measurement develop the understanding of local skin variables (skin perfusion, diffusion path, and skin metabolism) [23].

Several factors have an influence on PCO_2 measurement using the TP. The essential factors are the following [23]:

i) The blood flow in the skin.

ii) The rate of O_2 absorption and CO_2 generation within dermal and epidermal tissue between the TP and skin capillaries.

iii) The temperature of the capillary blood.

iv) The diffusion resistance between the capillaries.

There are 2 reasons why local skin blood flow is significant. Firstly, the ratio between the blood flow and O_2 absorption and CO_2 generation controls the variances in arterial to venous O_2 and CO_2. As a result, capillary blood is not arterialised at minimal blood flow. Secondly, the skin capillaries contain the extended part of the diffusion gradient between the blood and TP. T_CPCO_2 measurement also depends on tissue metabolism. Because the O_2 and CO_2 binding curves of blood are highly temperature sensitive, knowing the temperature of capillary blood is essential for T_CPCO_2 measurement. Finally, the resistance between the TP and skin capillaries affects T_CPCO_2 measurement [23].

1.5.2.2 A transcutaneous sensor on skin

The transport of necessary nutrients to the tissue, which is directly related to its viability, is referred to as perfusion [24]. Good-quality skin perfusion areas are suitable for transcutaneous monitoring, especially the region having a uniform capillary bed with no large veins, hair, or skin defects. An incorrect result can be achieved when the TP is placed

on the top of the bone and has impaired perfusion. In addition, the TP can't be placed on the patient's skin having dermatological complications because those areas have lower local perfusion due to damaged tissue [4].

Even though the epidermis (outer layer) is avascular, tissue fluid is present in the lower dermal layers. Capillary loops run from the subcutaneous tissue to the skin surface. The body's temperature regulation system includes the skin structure. The TP's heat induces capillary loops to widen, and as a result, local skin blood flow increases, thus permitting CO_2 and O_2 to disperse up to 20 times more rapidly than at equilibrium from blood capillaries via the skin membrane [4] [22]. Increased tissue metabolism causes a significant rise in CO_2 production at this higher temperature. A "correction factor" can be used to eliminate this temperature effect. This correction factor adjusts the calibration values to provide a measurement nearly 30 % below the value predicted by the calibration gas. This correction factor must always be turned on and indicates "Corr." on a TCM monitor display. If the correction factor is turned off, the T_CPCO_2 values will overread by around 30 % [22].

1.6 OFCS on patients' skin

The future goal is to measure the skin CO_2 from an at-risk patient's skin using the OFCS. The process is described in detail in Sections 6.3.3 and 6.3.5, but this process is also briefly discussed here. The OFCS will be mounted by a fixation ring-based gas collection chamber (GCC) according to Figure 6.4. The size and shape of this kind of GCC are also mentioned in Figure 6.4. In Figure 1.4, four OFCSs (OFCS 1-4) are placed in different positions (such as the back of the head, shoulder blade, lower back, and heel) on the patient lying on a smart mattress. A grade 3 or 4 PUs can develop within 1 or 2 hours [7]. So, continuous monitoring of PUs is needed for the skin CO_2 measurement. Four OFCSs are placed inside the GCC based on the fixation ring, and the fixation ring with polyurethane foam is attached to the affected regions on the skin. If the skin CO_2 exceeds the normal range, the patient will be moved, or the cushion will be placed on the affected area to release the pressure from the skin.

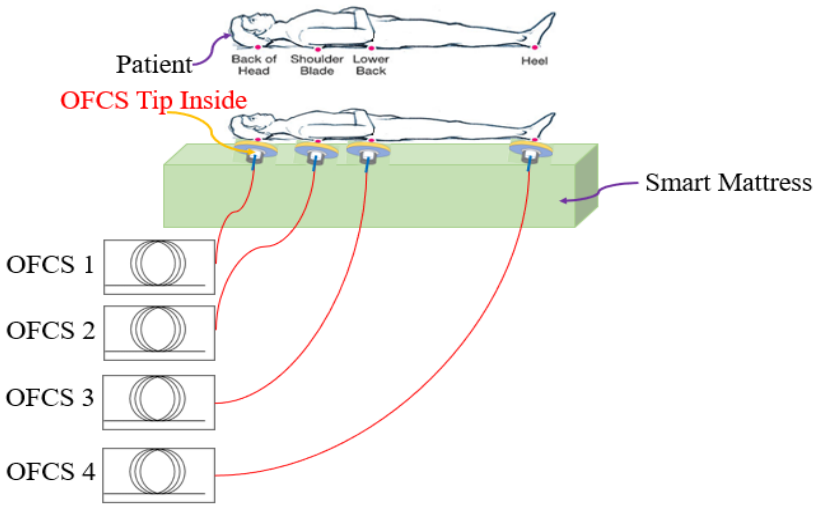


Figure 1.4: *Skin CO_2 measurement from PUs patient's skin using 4 OFCSs*

1.7 Thesis structure

This thesis is divided into 6 chapters that introduces OFS in healthcare; reviews literature; describes the fabrication and characterisation of the OFCS; describes the measurement of CO_2 emitted from human skin; observes dye (thymol blue) characteristics and develops an FPI simulation; summarises the present work and future directions of improving the OFCS in healthcare.

Chapter 1, as mentioned above, discusses the objectives and motivation for using the OFS to predict PUs. The principles, merits, usage of the OFS in the clinical field, various skin layers, and T_CPCO_2 measurement from the skin are also provided.

Chapter 2 contains the literature review relevant to this thesis and the background of this work. A review of the developed OFCS for monitoring CO_2 from human skin is described. A comparison of the benefits and drawbacks and healthcare applications of the literature is provided to demonstrate the novelty of the work developed in this thesis.

Chapter 3 describes the fabrication and characterisation of the developed OFCS. The results of in-vitro tests from the OFCS are compared to those of commercial devices. The method of reducing film cracking and the improved performance of the OFCS are also illustrated. The film thickness, dye (TB) concentration, absorption, and molar absorption

coefficient of dye (TB) are found. The fibre-to-fibre variability is achieved from the sensitivity of the 10 calibrated OFCSs (OFCS 1-10).

Chapter 4 reports on the modelling of an FPI on the optical fibre tip. Fringe visibility is calculated from experimental data and compared with simulated data. Also, the shape of the spectrum achieved from dye (TB) characteristics with and without CO_2 is discussed.

Chapter 5 shows the experimental set-up of monitoring CO_2 emitted from human skin using the TP, OFCS, and commercial CO_2 sensor during loading and unloading. The results of in-vivo tests from different volunteers are demonstrated.

Chapter 6 focuses on an overall summary and conclusion of the presented work with future directions proposed for the OFCS built for monitoring tissue loading.

2. Chapter 2

Literature Review

2.1 Introduction

A literature review delivers the necessary knowledge on the working principle and applications of a transcutaneous CO_2 sensor probe (t_C Sensor 92, Radiometer, UK), a commercial CO_2 sensor, and an optical fibre CO_2 sensor for designing the experiment using the devices. The previously done research with the t_C Sensor 92 probe provides guidelines for setting the experiment protocol using the devices. Section 2.2 illustrates the mechanism of CO_2 transport and CO_2 release from the skin and explains the relationship between pH and CO_2, pressure ulcers and transcutaneous CO_2. Section 2.3 demonstrates the previously conducted research at the University of Southampton and Beijing Chaoyang Hospital. Section 2.4 presents the optical methods for measuring T_CPCO_2. Section 2.5 is focused on the operating principle and available features of existing commercial devices for measuring CO_2 and T_CPCO_2. Section 2.6 discusses how an OFS is beneficial to measure T_CPCO_2 instead of using a t_C Sensor 92 probe. Section 2.7 includes the general principle and classification of an OFS. Section 2.8 is based on the latest advances in optical fibre pH sensors. Section 2.9 shows the sensing film coating techniques. Section 2.10 describes the working principle of different optical fibre CO_2 sensors. Section 2.11 mentions the fundamentals of optical fibres, and Section 2.12 concludes with a summary of this chapter.

2.2 CO_2 inside human body and Pressure ulcers relationship with transcutaneous CO_2

CO_2 is a non-flammable and colourless gas at normal pressure and temperature. CO_2 is produced in the body's tissue due to the cellular breathing method because of bicarbonates with buffering protons due to the metabolic acidosis resulting ischemia [25].

2.2.1 CO_2 transport to body

CO_2 is the outcome of cellular respiration and is moved from the tissues' cells in the body to the lung's alveoli through the bloodstream. CO_2 is moved in the blood via 3 separate paths [26]:

(I) Dissolved in the plasma: Only 5 % of CO_2 is moved in the blood's plasma as dissolved CO_2 molecules. CO_2 has a greater solubility than O_2; that is why a moderately larger CO_2 amount is dispersed in the blood's plasma compared to O_2 [26].

(II) Bound to haemoglobin: While O_2 attaches to the iron substance in haemoglobin, CO_2 can attach to the amino acid chains on haemoglobin. When CO_2 sticks to haemoglobin, it builds carbaminohaemoglobin. Around 10 % of CO_2 in the human body is transported using this approach. Carbaminohaemoglobin provides a bluish colour in red blood cells; that is why the veins containing deoxygenated blood seem to be blue [26].

(III) Bicarbonate ions: Most (i.e. 85 %) of CO_2 moves in the bloodstream as bicarbonate ions. The chemical reaction that explains the bicarbonate ion's formation in the blood is provided in Eq. (2.1) [26].

$$CO_2 + H_2O \rightleftharpoons H_2CO_3 \rightleftharpoons H^+ + HCO_3^- \qquad (2.1)$$

This equation illustrates that CO_2 reacts with water (H_2O) to develop carbonic acid (H_2CO_3), which detaches in solution to produce bicarbonate ions (HCO_3^-) and hydrogen ions (H^+). The major effect of this method is that the blood's pH becomes a pathway of finding the CO_2 amount in the blood. Bicarbonate ions (HCO_3^-) perform as a buffer for the blood's pH so that blood's pH level will be neutral (i.e. pH = 7) assuming that hydrogen and bicarbonate ions are stable [26].

2.2.2 CO_2 release from skin

External respiration or gas interchange happens in our lung's alveoli, which consist of capillaries. It appears in the alveoli so that O_2 is inserted into the bloodstream and CO_2 is extracted from the bloodstream. O_2 is transported to the heart's left side through the pulmonary vein, which drives it into the systemic flow [27]. Red blood cells transport O_2

into the tissues' capillaries of the human body. O_2 circulates into the tissues' cells, while CO_2 spreads out of the tissues' cells and into the blood capillary [26].

A partial pressure gradient stands for variation in a gas concentration inside a mixture of different gases, in which the gas is at a greater pressure in one site and a smaller pressure in another site. A gas will disperse from greater pressure to a smaller pressure down the gradient [27]. In Figure 2.1, partial pressure gradients permit the loading of O_2 into the blood capillary and the unloading of CO_2 out of the blood capillary. These 2 methods take place at the same moment [26].

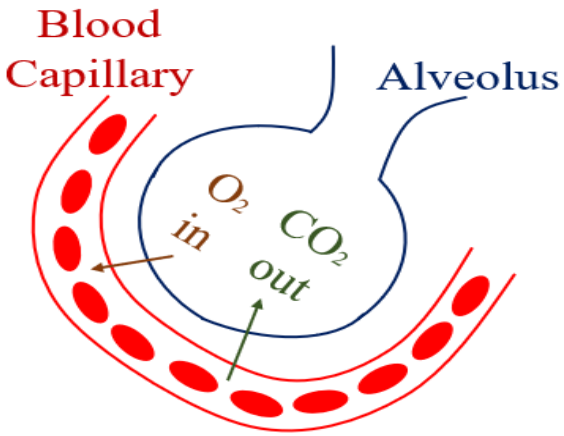


Figure 2.1: *Gas exchange in alveolus (adapted from [26])*

Partial pressure gradients in the systemic capillaries: – the arterial partial pressure of O_2 (P_aO_2) has a value of 100 mmHg, and P_aCO_2 has a value of 40 mmHg within the blood capillary. P_aO_2 value of 40 mmHg and P_aCO_2 value of 45 mmHg inside the tissues' cells permit gas interchange [26]. PO_2 is larger in ambient air than in the blood capillaries, so O_2 disperses into the blood capillaries (PO_2 in the air is about 159 mmHg). PCO_2 is larger inside the blood capillaries than in ambient air, so CO_2 spreads out of the blood capillaries. CO_2 within the skin tissue diffuses through the skin barrier to the air under the drive of the partial pressure difference (PCO_2 in the air is about 0.3 mmHg). The CO_2 starts to diffuse from the blood plasma into the alveoli under the drive of differential partial pressure (45 mmHg to 0.3 mmHg) [27].

2.2.3 pH and CO_2 relationship

Eq. (2.1) shows how CO_2 is mixed with H_2O and makes H_2CO_3 (a weak acid that decreases the water's pH). Reference [28] provides a standard curve determining the relationship between pH and CO_2 in water. The CO_2 flow rate was 1 L/min, and CO_2 concentrations were monitored using pH sensors placed inside a water tank. Here the x-axis represents the pH of the water, and the y-axis represents the CO_2 concentration inside the water [28].

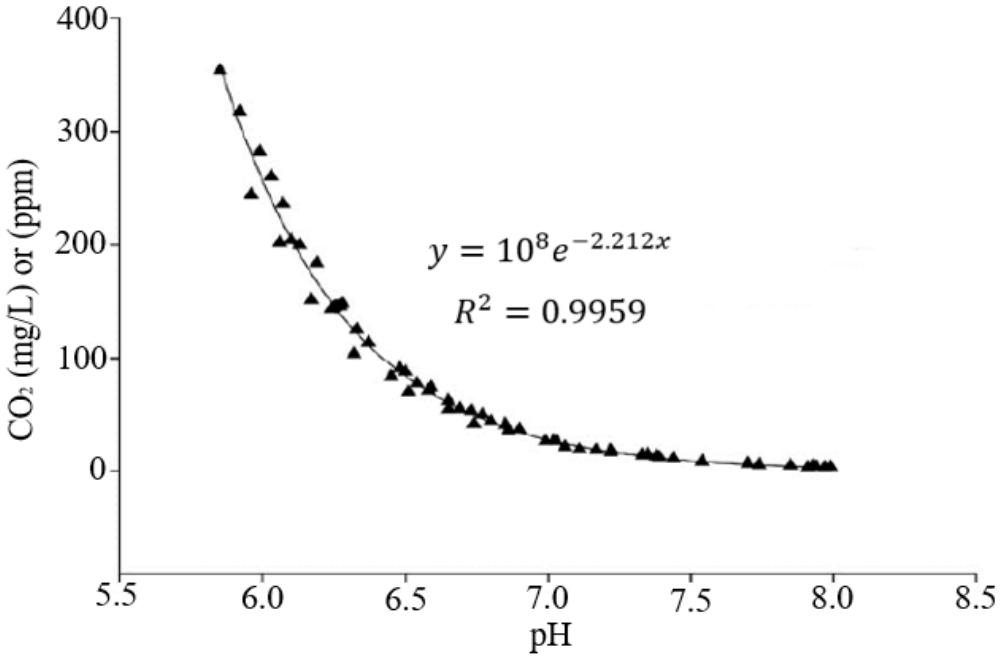


Figure 2.2: *Relationship between pH and dissolved CO_2 concentrations in water [28]*

The skin surface pH varies due to different factors such as age, ethnicity, sebum, sweat, detergents, cosmetic products, soaps, and occlusive dressing. The pH value of the normal skin surface is 4.5-6.0 [16]. The skin pH can't be related directly to water pH in Figure 2.2 and measurements of skin pH and CO_2 haven't been performed previously. Moreover, the skin pH cannot be directly related to the internal tissue pH due to the different factors described, hence a measurement of CO_2 emitted from the tissue via the skin is potentially a valuable biomarker.

However, healthy skin CO_2 measurement range is from 149 ppm to 429 ppm, obtained from the healthy 10 volunteers' skin over 3 trials during the skin CO_2 measurement test in

Section 5.3.4. However, as the human body is 60 % water [29], we can assume that Figure 2.2 is approximately valid, corresponding to a pH range of 5.5-6.25.

CO_2 can be calculated using the formula from Figure 2.2, $y = 10^8 e^{-2.212x}$

CO_2 (pH = 5.5) = $10^8 \times e^{-(2.212 \times 5.5)} = 520.443$ ppm ≈ 520 ppm

CO_2 (pH = 6.25) = $10^8 \times e^{-(2.212 \times 6.25)} = 99.056$ ppm ≈ 99 ppm

The OFCS will be able to detect the CO_2 range of 99 ppm to 520 ppm corresponding to the pH range of 5.5 to 6.25.

2.2.4 Transcutaneous CO_2

Transcutaneous monitoring is an advanced and precise technology that gives constant, non-invasive measuring of CO_2. They are popular because a non-invasive sensor is employed on the body, blood gases diffusing through the skin can be detected and measured [1]. T_CPCO_2 is a measurement of the level of CO_2 released from the skin that has a good correlation with P_aCO_2 [25]. PCO_2 indicates the CO_2 concentration dispersed in the blood and the interchange of this gas via lungs to outside as well [30]. PCO_2 of tissue is defined by the balance between P_aCO_2, blood flow and its circulation in tissue, the combination of anaerobic and aerobic metabolism, lactate variations in the body's tissue, and venous O_2 saturation. The amount of dissolved gas [from Eq. (2.2)] in the fluid (blood) is governed by Henry's law, namely [2],

$$PCO_2 = K_H [CO_2] \qquad (2.2)$$

where K_H is Henry's coefficient which depends on the CO_2 solubility in the body's tissue and its temperature [2].

PCO_2 rises with enhanced CO_2 concentrations. The level of expired CO_2 level from the human body is around 4 %, whereas the CO_2 range in the body's tissue is around 5-6 %. The existence of CO_2 aids the O_2 release from haemoglobin. This method, recognized as the Bohr effect, described as a move to the right of the oxyhaemoglobin dissociation curve (shown in Figure 2.3), indicates that a rise in plasma CO_2 diminishes the stability of haemoglobin saturation [2].

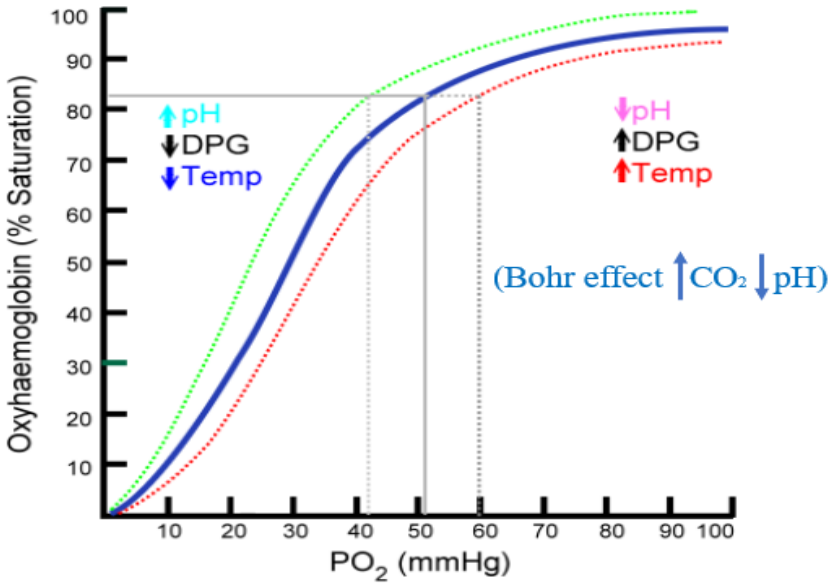


Figure 2.3: *Oxyhaemoglobin dissociation curve [26]*

The oxyhaemoglobin dissociation curve can shift in terms of different parameters. A change in the P_{50} of the curve is an indication that the dissociation curve has moved. P_{50} means PO_2 value at which 50 % haemoglobin, is saturated with O_2. Rightward shifts indicate a reduced affinity for the binding of haemoglobin, so that less O_2 binds to haemoglobin, and more O_2 is unloaded from it into the tissues. The curve moves right due to reduced blood pH (called the Bohr effect), boosted temperature, increased concentration of 2-3 diphosphoglycerate (DPG) and PCO_2. Red blood cells produce a substance called DPG which regulates the O_2 movement from red blood cells to body tissues. Leftward shifts indicate a raised affinity for the binding of haemoglobin, so that more O_2 binds to haemoglobin, but less O_2 is unloaded from it into the tissues. The curve moves left due to boosted blood pH, reduced temperature, decreased concentration of DPG and PCO_2 [26].

Rising CO_2 may add more molecules to haemoglobin to move away the extra amount of CO_2. Thus, large rises of PCO_2 in the body's tissue over normal rates shows both an immobility of blood flow and a move to anaerobic metabolism [2]. As the tissue is under pressure, the systemic capillary beneath the skin is occluded. So, the gas exchange is cut off, resulting in the accumulation of CO_2 in the tissue. CO_2 easily circulates into the extracellular area; localised tissue acidosis may arise. Indeed, CO_2 may disperse out of the

cells and be found at the tissue's surface. As a result, T_CPCO_2 increases. As a result, CO_2 detected from the skin is a valid marker for early PUs detection [2].

2.2.5 Pressure ulcers

PUs occurs when the skin is under high pressure for a short duration, or it is under moderate pressure for a long duration. The skin stops the blood flow due to the pressure on the skin, and the skin does not get enough O_2 and nutrients. Finally, the skin breaks down because of not receiving sufficient blood flow. These are recognized as PUs, pressure injuries, bed sores, and decubitus ulcers [31-32].

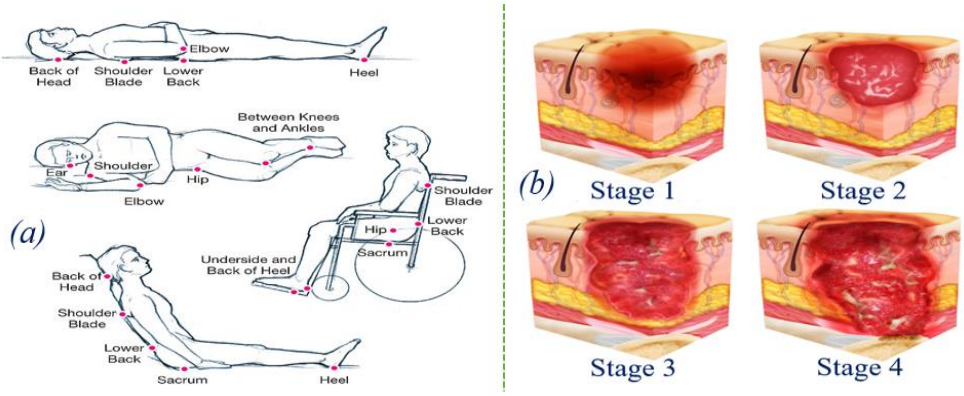


Figure 2.4: *(a) Common locations of PUs [31] (b) Different stages of PUs [32]*

PUs appears over the body areas with minimum body fat or muscle between bone and skin, such as at the tailbone, spine, hips, shoulder blades, elbows, and heels, as shown in Figure 2.4 (a) [34]. Figure 2.4 (b) demonstrates 4 stages of PUs:

(I) Stage 1: Skin may look red or a bruise. The outer side of the skin remains unbroken, but the body area is at extreme risk of future tissue breakdown. These sores can heal within 60 days with proper treatment if the affected area is identified rapidly [32].

(II) Stage 2: Skin starts to break open and create an ulcer [32].

(III) Stage 3: The sores worsen and expand below the skin side, creating a tiny crater. The risks of skin infection and tissue death are high [32].

(IV) Stage 4: The sores make progress, with massive damage to a deeper level of tissues (bones, tendons, and muscles). Major problems, such as osteomyelitis (bone infection) or sepsis (infection conducted via the blood), can arise [32].

It is not fully understood how observed CO_2 changes relate to PU formation. Clinically the t_C Sensor 92 probe is used to measure P_aCO_2 from the skin to gain a better understanding. As discussed in Section 2.3.1, T_CPCO_2 has the potential to be used as a biomarker in a diagnostic test; and it is recommended that $T_CPCO_2 > 80$ mmHg [8], the patient needs to be switched positions or a cushion needs to be used to relieve the pressure [8].

The most crucial part of treating and preventing PUs is recognizing symptoms rapidly and requiring regular care to prevent the sores from becoming unmanageable [34]. The following actions are available as a treatment of PUs:

(I) (Re) Positioning: Frequent position changes within every couple of hours or 15 minutes ease pressure and permit sufficient blood flow to the skin [34].

(II) Pressure relieving devices: Cushions, air mattresses, and other pressure-easing devices ease pressure points [34].

(III) Wound cleaning process: Tiny wounds requires cleaning gently with clean water and soap. Broken sores need to be cleansed with a saline solution with every dressing [34].

(III) Nutrition: Especially protein keeps the skin healthy and repairs wounds. Adequate nutrition prevents and heals the sores [34].

(IV) Dressings and topical treatments: Barrier creams, gels, and ointments protect wounds from infection and promote healing [34].

(V) Antibiotics: Topical, oral, or IV, antibiotics stop infections before developing systematic infections or even sepsis [34].

(VI) Surgical debridement: Debridement means removing dead tissue using different techniques, such as rinsing dead tissue with a heavy water flow and or taking off dead tissue with laser [34].

(VII) Vacuum treatments: Negative pressure therapy provides vacuum pressure on the skin injured area, removes moisture, and eliminates infection risk [34].

(VIII) Surgery: When PUs is in Stage 3 or 4, surgery may be required to block the wound, minimise fluid loss, and reduce the risk of future difficulties [34].

PUs treatment cost ranges from £ 1,064 (Stage 1) to £ 10,551 (Stage 4). Treatment costs rise with the associated PUs stage because the healing time is extended, and difficulties are greater in more serious situations. The total treatment cost in the UK is yearly £ 1.4-2.1 billion (around 4 % of total National Health Service (NHS) budget) where the nursing time is the most expensive part of this treatment [35].

2.3 Previously conducted research at different institutions

2.3.1 Research conducted by our collaborators at the University of Southampton

Skin ischemia will change the soft tissue's status leading to their ultimate tissue breakdown. The outcome of various loading regimes, comprising repetitive and prolonged loading, on the normal T_CPCO_2 value, at locations alongside bony prominences of 14 healthy participants were monitored using a transcutaneous electrochemical sensor by our collaborators at the University of Southampton. The device deployed was a combined O_2 and CO_2 tension electrode (model D841, Radiometer A/S, Denmark) with the TCM3 device (Radiometer A/S, Denmark). The correlation between the tissue breakdown and tissue CO_2 for a fixed duration was observed [8].

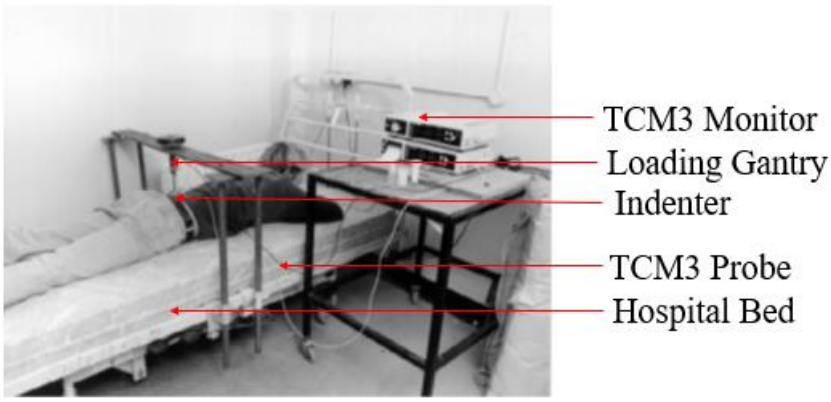


Figure 2.5: *Loading gantry utilised to provide pressure on sacrum [8]*

The pressure was applied generally between the volunteer's support and soft body tissues. Loads were placed on the test location through a 40 mm Perspex indenter and bed-mounted loading jig, as shown in Figure 2.5. Three nominal mode ranges for applied pressures were chosen 40 mmHg (5.3 kPa), 80 mmHg (10.7 kPa), and 120 mmHg (16 kPa) for the loading or unloading procedure. The changes in gas levels were evaluated continuously at the sacrum during the test interval (20 minutes) [8].

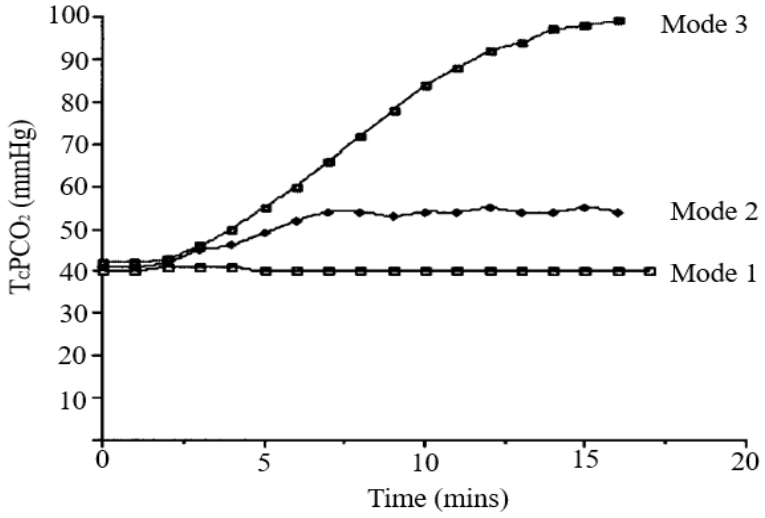


Figure 2.6: *T_CPCO_2 response after applying pressure on soft body tissues for 3 separate modes [8]*

The normal range of P_aCO_2 is 36-44 mmHg (4.8-5.9 kPa) in healthy soft tissues. The normal range was slightly exceeded (50 mmHg) in this test. The threshold T_CPCO_2 value was fixed at 50 mmHg (6.7 kPa) during this test period [8]. Figure 2.5 shows the sensor on the sacrum with loading (t = 0 mins defines the point when loading is first applied). The analysis was suitably split into 3 separate pressure modes [Mode 1 (40 mmHg or 5.3 kPa), Mode 2 (80 mmHg or 10.7 kPa), and Mode 3 (120 mmHg or 16 kPa)] as shown in Figure 2.6. The achieved T_CPCO_2 value range was 36-44 mmHg, 50-60 mmHg, and > 80 mmHg for Modes 1, 2, and 3, respectively. The resulting response based on these different modes is given below [8]:

(I) Mode 1 (40 mmHg or 5.3 kPa): Steady T_CPCO_2 values that are the same as base values for soft body tissues [8].

(II) Mode 2 (80 mmHg or 10.7 kPa): The significant CO_2 accumulation in the localised body tissues [8].

(III) Mode 3 (120 mmHg or 16 kPa): A blocking of both lymphatic drainage and blood supply [8].

The increment in tissue T_CPCO_2 was monitored during the test [8]. The impaired oxygenation combined with an excess of tissue T_CPCO_2, termed hypercapnia, would influence cell apoptosis [2]. The measure of T_CPCO_2 is consequently a potential marker to determine the viability of the tissue [8].

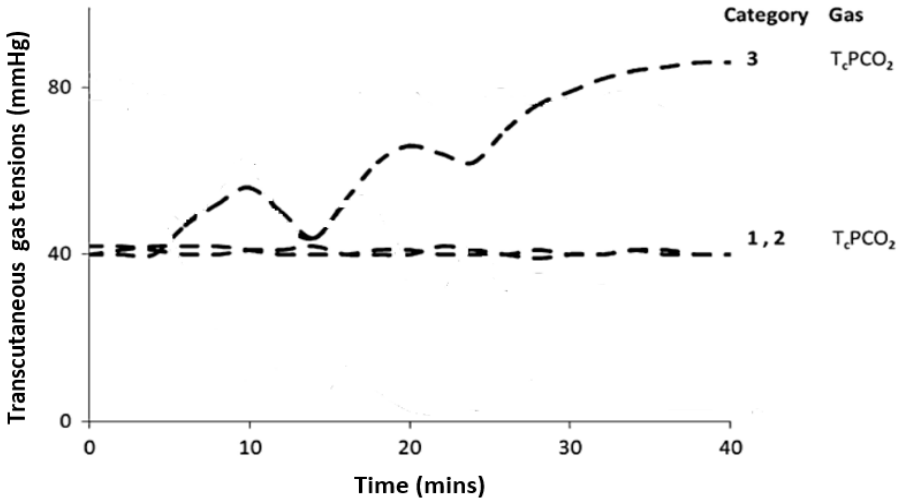


Figure 2.7: *T_CPCO_2 skin response for 3 separate categories at sacrum [2]*

The performance of an alternating pressure air mattress (APAM) was also observed with work from the University of Southampton, regarding its capacity to keep skin status on 12 healthy participants lying in a supine position. The APAM consists of a sacral segment assisted with alternating low pressure, with inner pressure rates adapted to body mass index and subject morphology, which act as a natural pressure sensor. Inner mattress pressure, interface pressure, and transcutaneous gas values at the sacrum were all measured. The measured skin response at the sacrum due to the alternating support pressures was presented in 3 separate groups and identified as Categories 1, 2, and 3, as shown in Figure 2.7. Figure 2.7 shows that associated T_CPCO_2 levels remained within the normal range (around 40 mmHg) for Category 1 and 2. However, Category 3 showed an increased value in CO_2 above base levels. In all cases, the maximum interface pressure at the sacrum was

60 mmHg (8 kPa). The researchers indicated that Category 3 had the possible threat of having PUs and thus required comfortable cushions with strict observance to a pressure release scheme. The conclusion being that T_CPCO_2 has again proved as a reliable marker to determine the status of tissue [2].

2.3.2 Research conducted by researchers at Beijing Chaoyang Hospital

PUs brings mental and physical discomfort to patients whilst, additionally increasing clinical expenditure (£ 1,064 (Grade 1) to £ 10,551 (Grade 4) [35]). The incidence of PUs is possible to avoid only by detection and prevention at the early stage of PUs. The link between T_CPCO_2 and Braden score was explored by researchers at the Beijing Chaoyang Hospital, an affiliated hospital of Capital Medical University, Beijing, China, to measure the tissue's activity after being pressed. The Braden scale is generally used in the medical care of PUs now. The T_CPCO_2 values were measured at the anterior chest in a lateral position and sacrococcygeal regions in lateral and supine positions using a TCM CombiM device (Radiometer A/S, Denmark) [36].

Braden and Bergstrom developed the Braden scale in 1984. The Braden scale evaluates PUs risk in patients from 6 aspects: sensory perception, moisture; activity; mobility; nutrition; friction force, and shear force (also related to the patient's ability of movement). The lower the Braden score, the greater the risk [36]. Table 2.1 provides the grading system of the Braden scale.

Table 2.1: *Grading pattern of Braden scale [37]*

Sensor Perception		Moisture		Activity		Mobility		Nutrition		Friction and Shear	
No Impairment	4	Rarely Moist	4	Walks Frequently	4	No Limitations	4	Excellent	4		
Slightly Limited	3	Occasionally Moist	3	Walks Occasionally	3	Slightly Limited	3	Adequate	3	No Apparent Problem	3
Very Limited	2	Very Moist	2	Chair Bound	2	Very Limited	2	Probably Inadequate	2	Potential Problem	2
Completely Limited	1	Completely Moist	1	Bedbound	1	Completely Immobile	1	Very Poor	1	Problem	1

80 volunteers with no PUs were recruited from 1 February 2017 to 31 May 2017 in Beijing Chaoyang Hospital. A balanced approach was adopted to identify a PUs risk status defined into 2 classes, a high-risk class (i.e., volunteers with a maximum Braden score of 12 points) and a low-risk class (i.e., volunteers with a Braden score range 15-22 points). By considering, the Braden score's inaccuracies, volunteers with a Braden score range of 12-15 were not classified in terms of high or low risk classification [36].

This analysis contained 31 subjects (25 men, 6 women, aged 41~88 years old) in the high-risk class and 49 subjects (32 men and 17 women, aged 40~87 years old) in the low-risk class [36].

T_CPCO_2 was monitored with the following procedure for both classes [36].

(i) After turning on the device, the probe temperature was fixed at 44 ℃ and prewarmed for 20 minutes allowing the widening of blood vessels. Initially, with the subject in the lateral position, the researchers placed the probe on the volunteer's sacrococcygeal region. T_CPCO_2 was measured for around 20 minutes after stabilising the values [36].

(ii) Next, volunteers switched to the supine position from the lateral position. Then T_CPCO_2 was measured for nearly 20 minutes after stabilising the values [36].

(iii) The researcher then placed the probe on the volunteer's anterior chest in the lateral position. Then T_CPCO_2 was measured for about 20 minutes after stabilising the values [36].

The relationships between the Braden Scale and T_CPCO_2 were assessed using correlation analysis [36].

The obtained results are provided below:

(i) Comparison of T_CPCO_2 between the chest and sacrococcygeal areas in lateral posture [36]:

The outcomes are presented in Table 2.2, which reveals no remarkable change in T_CPCO_2 values between the chest and sacrococcygeal areas in lateral posture both in low and high-risk class [36].

Table 2.2: *Variation in T_CPCO_2 values between chest in lateral position, sacrococcygeal region in lateral and supine position [36]*

Volunteer class	T_CPCO_2 in chest [lateral posture] (mmHg)	T_CPCO_2 in sacrococcygeal region [lateral posture] (mmHg)	T_CPCO_2 in sacrococcygeal region [supine posture] (mmHg)	$\triangle T_CPCO_2$ from lateral posture to supine posture in sacrococcygeal region (mmHg)
High risk	41.78 ± 10.91	41.63 ± 10.88	72.81 ± 28.23	31.19 ± 9.92
Low risk	40.84 ± 9.82	39.14 ± 7.93	48.47 ± 17.61	9.33 ± 2.66

(ii) T_CPCO_2 values in supine posture are sensitive to the risk level of PUs [36]:

Table 2.2 shows that T_CPCO_2 values in the high-risk class are considerably greater than those in the low-risk class in supine posture. These results indicate a remarkable increase in T_CPCO_2 when the volunteer switches from lateral to supine posture. This outcome shows that T_CPCO_2 values are delicate to the variation of pressure applied on the assessed zone [36].

The magnitudes of changes T_CPCO_2 are sensitive to the risk level of PUs [36]:

Table 2.2 illustrates that T_CPCO_2 magnitude rise in the high-risk class is considerably greater than in the low-risk class. This outcome indicates that the variations for T_CPCO_2 magnitude are sensitive to the risk level of PUs [36].

The accumulation of toxic metabolites causes elevated T_CPCO_2, which is not beneficial for tissue activity. When T_CPCO_2 continues to affect local tissue, the blood flow of the tissue will be blocked entirely. T_CPCO_2 is greater for a high-risk class than for a low-risk class. The results show that T_CPCO_2 increases by 75 % in the high-risk class after the sacrococcygeal regions are pressed, and T_CPCO_2 increases by 24 % in the low-risk class. T_CPCO_2 is used as a method to assess the risk of damage to a patient's soft tissue. T_CPCO_2 serves as an active metric in evaluating the threat of PUs [36].

2.4 T_CPCO_2 measurement using an optical miniaturized cell

The Institute of Applied Optics researchers, École Polytechnique Fédérale de Lausanne (EPFL), Switzerland, propose the following method as a substitute for electrochemical CO_2 measurement. CO_2 is estimated by identifying its optical absorption from the sensor's surface using the evanescent wave (EW). The sensor's surface consists of a spiral and straight waveguide established on silicon nitride (Si_3N_4) using the modulation spectroscopy method. The waveguide is designed in a shrunk spiral less than 5 mm in diameter. Figure 2.8 illustrates the spiral implemented on-chip of 6 mm x 6 mm and waveguide length are 16 cm. The propagation loss of -0.4 dB/cm is achieved, over 50 cm of detecting length [38].

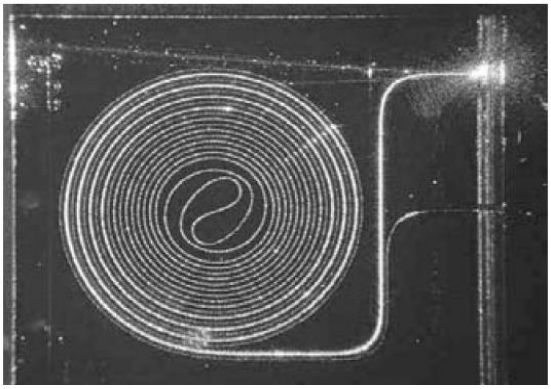


Figure 2.8: *Miniature EW sensor with spiral and straight waveguide [38]*

In Figure 2.9, elevated selectivity is achieved by adjusting the laser source's narrow spectral width in a certain molecule absorption line. A near-infrared light (a wavelength of 1580 nm) is used as a light source. Alternatively, a micro-optics-type miniaturized sampling cell is used for measuring CO_2. The sample volume adjoining to the skin surface is nearly 1 mm^3 permitting less than 1 minute response time. This experiment was executed on a volunteer with the microcell optical sensor placed on the human forearm and warmed at 42 °C. Figure 2.10 presents comparable results achieved with a commercial electrochemical T_CPCO_2 sensor (MicroGas 7650, Radiometer-Basel, Switzerland) [39].

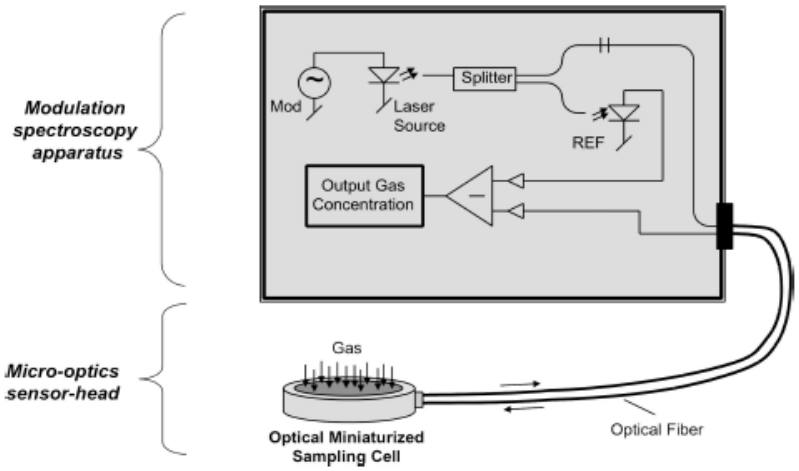


Figure 2.9: *Optical T_CPCO_2 monitoring method using optical miniaturized sampling cell [39]*

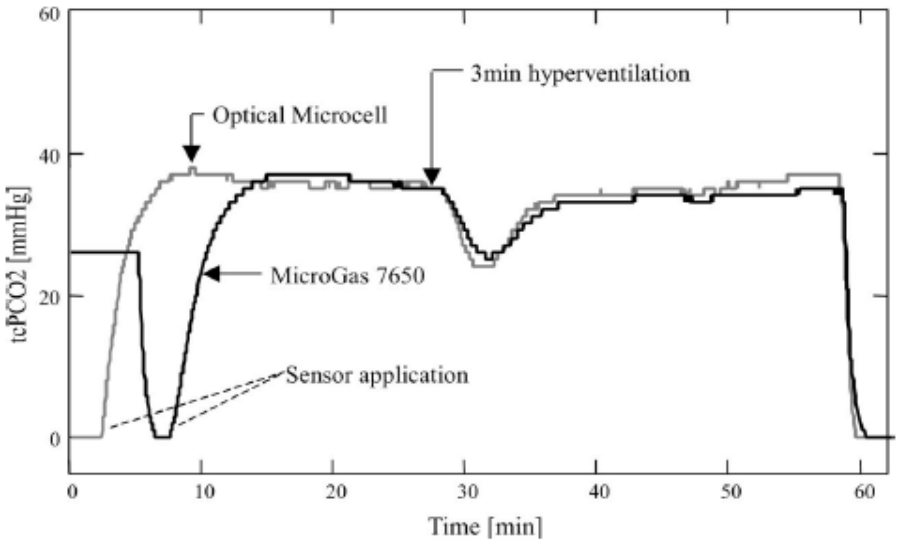


Figure 2.10: *Comparison in-vivo T_CPCO_2 monitoring achieved with MicroGas and optical microcell system [39]*

A list of researcher group and company are mentioned below who is working on optical fibre CO_2 sensors.

a) Researchers from City University London (School of Computer Science, Mathematics, and Engineering), UK, fabricated a fibre optic multi-sensor for detecting partial pressure of CO_2 and O_2 [40].

b) Researchers from University of Nottingham (Optics and Photonics Research Group and Department of Chemical and Environmental Engineering), UK and Charles University

(Institute for Environmental Studies), Czech Republic, fabricated long period grating optical fibre CO_2 sensor coated with metal organic framework HKUST-1 [41].

c) Researchers from the Northwest University (School of Physics), China, fabricated 2 different optical fibre CO_2 sensors based on the Fabry-Perot interferometer [42-43].

d) Researchers from the Ming Chi University of Technology (Department of Mechanical Engineering), Taiwan, fabricated optical fibre CO_2 sensor based on colorimetric change of pH indicator dye and quantum dots [44].

The summary of these above mentioned works is mentioned in Section 2.10.

(e) Also, two commercial optical fibre CO_2 sensors are mentioned in Section 1.4.3. Intelligent Optical Systems, Inc., USA, made one of them [12] and PreSens Precision Sensing GmbH, Germany, made another one [13].

The sensor from EPFL is not based on optical fibre; here, the researchers from EPFL built the CO_2 sensor using a waveguide or micro-optics-type miniaturized sampling cell. A modulation spectroscopy technique is used to measure CO_2 by detecting the optical absorption in the evanescent wave at the surface of a transcutaneous sensor [39].

In this thesis, a developed OFCS utilises the intensity response of guided light in a multimode fibre. Here, the absorbance of a sensitive film at the optical fibre tip is used for monitoring CO_2 in the intensity based OFS configuration and is relatively easy to fabricate. The transmission of intensity modulated signal in typical commercial optical fibres is stable [45].

2.5 Commercial devices for measuring CO_2 and T_CPCO_2

Existing commercial devices are available to measure CO_2 from the environment and T_CPCO_2 from human skin, such as infrared (IR) gas analyser (Applied Physics Corporation); commercial CO_2 datalogger and CO_2 sensor (CO2Meter.com); t_C Sensor 92 probe (Radiometer); and V-Sign™ Sensor 2 probe (SenTec).

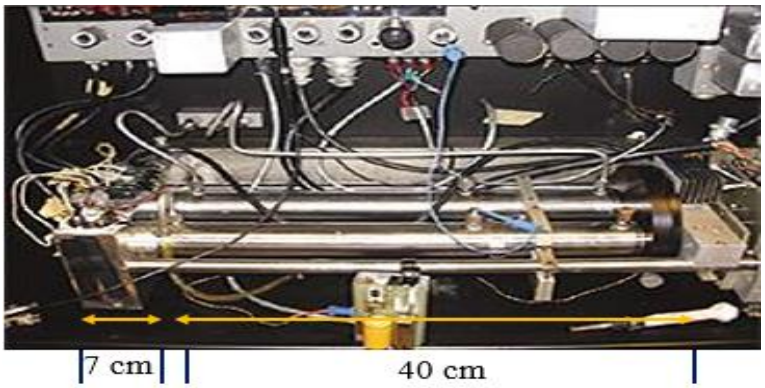


Figure 2.11: *IR gas analyser (Applied Physics Corporation) [46]*

Since the 1750s, when Joseph Black, a Scottish physicist and chemist, first discovered CO_2, a mercury manometer was initially used to measure CO_2 levels. Manometers contain a U-shaped glass tube loaded with mercury to estimate gas pressure. If volume, pressure, and temperature of a dry gas sample including CO_2 molecules are recognized, the number of CO_2 moles can be determined utilising the Boyle's ideal gas law ($PV = nRT$), where P is the pressure, V is the volume, n is the number of moles, R is the gas constant, and T is the temperature in Kelvin [47].

The method of estimating CO_2 in atmospheric air samples requires several recording hours allowing mercury manometers to increase accuracy. CO2Meter.com website provides the following information about early CO_2 sensor technologies [47]:

> 'That is why Charles Keeling used an IR gas analyser, which was calibrated along with his manometer when the US weather office called to begin hourly ambient air CO_2 testing on the Maura Loa volcano in Hawaii. The earliest IR gas analyser (Applied Physics Corporation) functioned on Mauna Loa between 1958 to 2006. Like each IR gas sensor, the analyser at Mauna Loa utilised a similar simple principle for CO_2 measurement.'

Figure 2.11 shows the IR gas analyser with vacuum tube electronics. The 2 prominent steel tubes are the reference and sample cells. The earliest IR gas analyser was precise, but it was very large, with a 40 cm long sample tube. The IR source is attached to the right of the

tubes, and detectors are attached to the left of the tubes [46]. The CO_2 absorption band is quite near to the IR band. Therefore, the amount of light absorbed by the CO_2 molecules is proportional to the CO_2 levels in the gas sample. Since low CO_2 levels do not consume too much light, the effect can be calculated by requiring an extended tubing [47].

Another example is a nondispersive infrared (NDIR) CO_2 sensor. Figure 2.12 (a) illustrates such a commercial CO_2 datalogger (K33 ICB 10% CO_2 Sensor, CO2Meter.com, USA) with a measurement range of 0-100000 ppm (0-10% CO_2) and a response time of nearly 20 seconds [48]. Figure 2.12 (b) demonstrates a commercial CO_2 sensor (CozIR-A 10,000 ppm CO_2 Sensor, CO2Meter.com, USA) with a measurement range of 0-10000 ppm (0-1% CO_2) and a response time of around 30 seconds. The diameter of the external body of CO_2 sensor, Cozir (C_1) is 43 mm and the diameter of CO_2 sensor, Cozir's sensing head (C_2) is 18 mm [49].

The measuring principle of NDIR at a known wavelength is established on gas absorption of radiation. Figure 2.12 (c) shows the NDIR module part, which includes a gas measuring chamber, a wavelength filter, a far IR source, and a far IR detector. Every CO_2 molecule inside the gas chamber absorbs the IR-radiated light at a particular wavelength. The filter permits movement across it only with a wavelength of 4.3 μm. The detector's light intensity is proportional to the amount of CO_2 molecules provided inside the gas chamber and follows Lambert-Beer law [50]:

$$I = I_0 \, e^{-kl[CO_2]} \qquad (2.3)$$

where I is the light intensity at the detector after CO_2 absorption, I_0 is the light intensity at the source (Wm^{-2}), k is the absorption index of CO_2 at 4.3 μm, l is the absorption path length, and $[CO_2]$ is the CO_2 concentration [50].

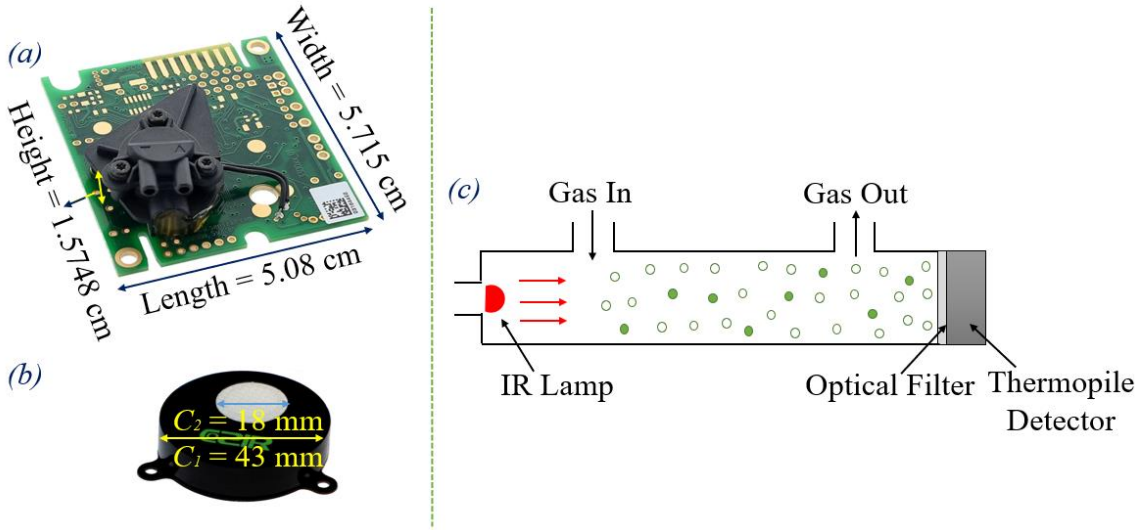


Figure 2.12: *(a) Commercial CO_2 datalogger* (CO2Meter.com, CM-0058) *[48] (b) Commercial CO_2 sensor* (CO2Meter.com, CM-0120*) [49] (c) NDIR CO_2 sensor (adapted from [50])*

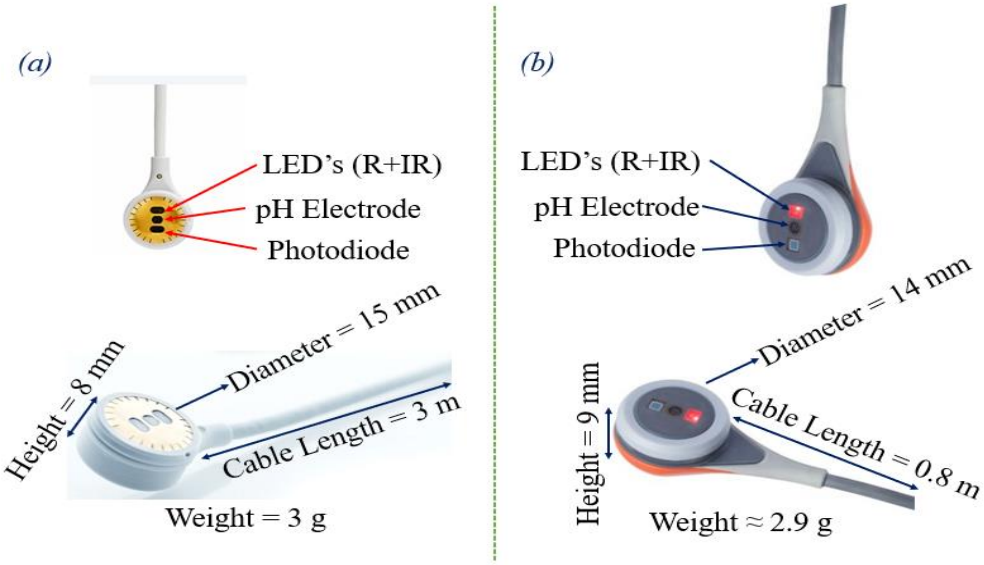


Figure 2.13: *(a) t_C Sensor 92 probe* (Radiometer) *[1] (b) V-Sign™ Sensor 2 probe* (SenTec) *[51]*

Table 2.3: *Specifications of commercial devices for measuring CO_2 and T_CPCO_2*

Device	CO_2 Sensor	Range	Resolution	Accuracy	Response Time	Drift	Temperature	Reference
K33 ICB 10% CO_2 Sensor	NDIR	0-100000 ppm	0.001 %/10 ppm	± 100 ppm vol ± 1 % of measured value	< 20 seconds	–	0-50 °C	[48]
CozIR-A 10,000 ppm CO_2 Sensor	NDIR	0-10000 ppm	1 ppm	± 50 ppm ± 3 % of reading	30 seconds	–	0-50 °C	[49]
t_C Sensor 92	Stow-Severinghaus Electrode	5-100 mmHg	–	± 5 mmHg over the measurement range	26 seconds (measured at 43 ºC)	± 10 % over calibration interval	37-45 ºC	[52]
V-Sign™ Sensor 2	Stow-Severinghaus Electrode	0-200 mmHg	0.1 mmHg below 100 mmHg / 1 mmHg above 100 mmHg	–	< 75 seconds	< 0.5 %/hour	37-44.5 ºC	[51]

Radiometer Ltd. offers a complete range of the TCM monitors, such as a TCM TOSCA monitor. This monitoring system is intended for continuous monitoring of PCO_2, oxygen

saturation of arterial haemoglobin (S_PO_2), and pulse rate (PR). SenTec Ltd. also offers the SenTec Digital monitor with V-Sign™ Sensor 2 probe for monitoring T_CPCO_2, S_PO_2, and PR. It is indicated for use on neonatal, paediatrics, and adults [1]. Both the t_C Sensor 92 probe (Radiometer, UK) and V-Sign™ Sensor 2 probe (SenTec, UK) contains a red LED, an IR LED, and a photodiode to measure S_PO_2 and PR along with a pH electrode to measure T_CPCO_2, as shown in Figure 2.13 (a) and (b), respectively. The characteristics of commercial devices for assessing CO_2 and T_CPCO_2 are presented in Table 2.3.

In both the t_C Sensor 92 probe and V-Sign™ Sensor 2 probe, CO_2 is estimated using a Stow-Severinghaus-type electrode (as shown in Figure 2.14), which is a modified glass electrode. This technique contains a pH electrode in an electrolyte buffer including sodium bicarbonate ($NaHCO_3$) which reacts with CO_2, wrapped by a gas-permeable membrane. CO_2 disperses from the skin across the membrane, where it produces a carbonic acid dissociation reaction. The reaction changes the pH of the solution, causing a measured potential difference between the pH electrode and the reference silver/silver chloride (Ag/AgCl). The change in pH is proportional to the concentration of dissolved blood CO_2 [3].

As HCO_3^- in the electrolyte solution is held at a stable level, the H^+ concentration variations will be almost the same as the pH variations according to Eq. (2.1). The estimated pH is therefore transformed into CO_2 values by the Henderson-Hasselbalch equation and presented as a T_CPCO_2 value in mmHg or kPa [53]:

$$pH = pK_{a\,H_2CO_3} + log_{10}\frac{[HCO_3^-]}{[H_2CO_3]} \qquad (2.4)$$

where *pH* is the blood's acidity, $pK_{a\,H_2CO_3}$ (= 6.1) is the negative logarithm (base 10) of the acid dissociation constant of carbonic acid. $[HCO_3^-]$ is the bicarbonate concentration in the blood, in mmol/L. $[H_2CO_3]$ is the carbonic acid concentration in the blood [53]:

$$[H_2CO_3] = k_{H\,CO_2} \times PCO_2 \qquad (2.5)$$

where $k_{H\,CO_2}$ (~ 0.03 (mmol/L)/mmHg) is a constant, including the solubility of CO_2 in blood. PCO_2 is the partial pressure of CO_2 in the blood in mmHg. The modified Henderson-Hasselbalch equation is found after substituting the value of $pK_{a\,H_2CO_3}$ and $[H_2CO_3]$ in Eq. (2.6) [53] resulting in:

$$pH = 6.1 + log_{10}\frac{[HCO_3^-]}{0.03 \times PCO_2} \quad (2.6)$$

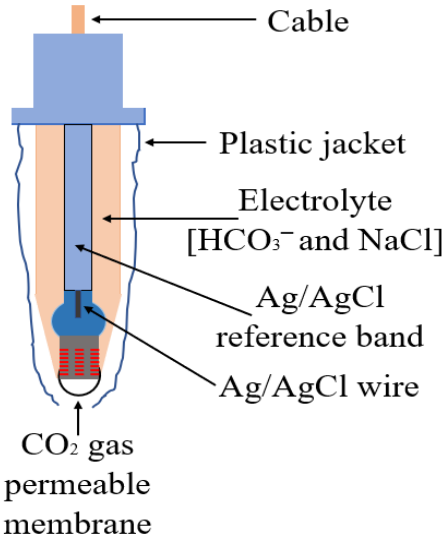


Figure 2.14: *A Stow-Severinghaus electrode for measuring pH (adapted from [54])*

The t_C Sensor 92 probe and V-Sign™ Sensor 2 probe are transcutaneous sensors. The sensors are placed on the skin, and the skin is heated. The suitable transcutaneous monitoring temperature is 42-45 °C. This sort of temperature is applied to rise the rate at which the reading can be performed and to 'arterialise' or raise perfusion to this area. The sensors must contact the skin through the contact gel, which is used to prevent bias from ambient air between the tissue and sensor. It requires around 3-7 minutes after the sensors have been put on the skin for estimating T_CPCO_2 values to become stable, and it may require a further 10-17 minutes to achieve consistent T_CPCO_2 values. The 90 % response time of a T_CPCO_2 electrode typically is 78 seconds. A shorter response time of these sensors is possible to be achieved for higher values of sensor temperature. Also, it is possible to reduce the risk of skin burns by changing location regularly and/or using a lower level of sensor temperature [4].

The t_C Sensor 92 probe (TCM4, Radiometer, UK) has been chosen to measure T_CPCO_2 from human skin during the experiments in this thesis. Previously our collaborators at the University of Southampton conducted their experiment using also the TCM devices (TCM3, Radiometer, UK) [8]. So, the obtained results from our experiment can be compared to the achieved results from our collaborators.

2.6 Comparison between a t_C Sensor 92 probe and an OFS

The t_C Sensor 92 probe and associated TCM TOSCA monitor require other accessories to measure T_CPCO_2 from human skin. These are [55]:

a) Adhesive Fixation Ring (Diameter = 32 mm) Kits with 1 Contact Gel (10 ml of Propylene Glycol)
b) Membraning Kits (12 Preparators) with 1 Electrolyte (10 ml of Ethylene Glycol)
c) Calibration Gas Cylinder (7.5% CO_2, 20.9% O_2, balance nitrogen (N_2))

The fixation ring is used to attach the probe to the skin. The fixation ring needs to be changed for every measurement because it loses its adhesion after removal from the skin. Patients who experience allergic reactions should not use the adhesive tapes of the fixation rings and are often excluded. The membrane of the probe needs to be changed every 2 weeks. The calibration gas cylinder needs to be changed when the monitor indicates less than 10 % gas remaining [55].

The main drawback of this probe, as mentioned in Section 1.3, are: the operating temperature of 37-45 ℃ may burn the skin; the contact gel may cause allergic skin reactions, and the TCM TOSCA monitor is relatively large and heavy (around 4 kg) [52].

An OFS is potentially a better method to measure CO_2 instead of using a t_C Sensor 92 probe. The features and benefits of an OFS are mentioned in Sections 1.3 and 1.4.2, respectively. The optical fibre is compact in size and lightweight and there are no skin burning and negligible skin irritations. In operation the intensity of the OFS at a specific wavelength changes due to the level of CO_2 concentrations.

2.7 Overview of an OFS

2.7.1 General principle of designing an OFS

The 4 components of an OFS are a light source, an optical fibre, a sensing element, and a detector. The general working principle of an OFS is described in Section 1.4.1 according to the schematic diagram in Figure 1.1. Those 4 components are used to make an OFS system, and the final step is a data processing to achieve the OFS's response.

2.7.2 Classification of an OFS depending on operating principle

An OFS can be categorised as an intensity (Figure 2.15 (a)), wavelength (Figure 2.15 (b)), phase (Figure 2.15 (c)), or polarisation (Figure 2.15 (d)) sensor depending on the operating principle [56]. These 4 different categories of OFSs are described below.

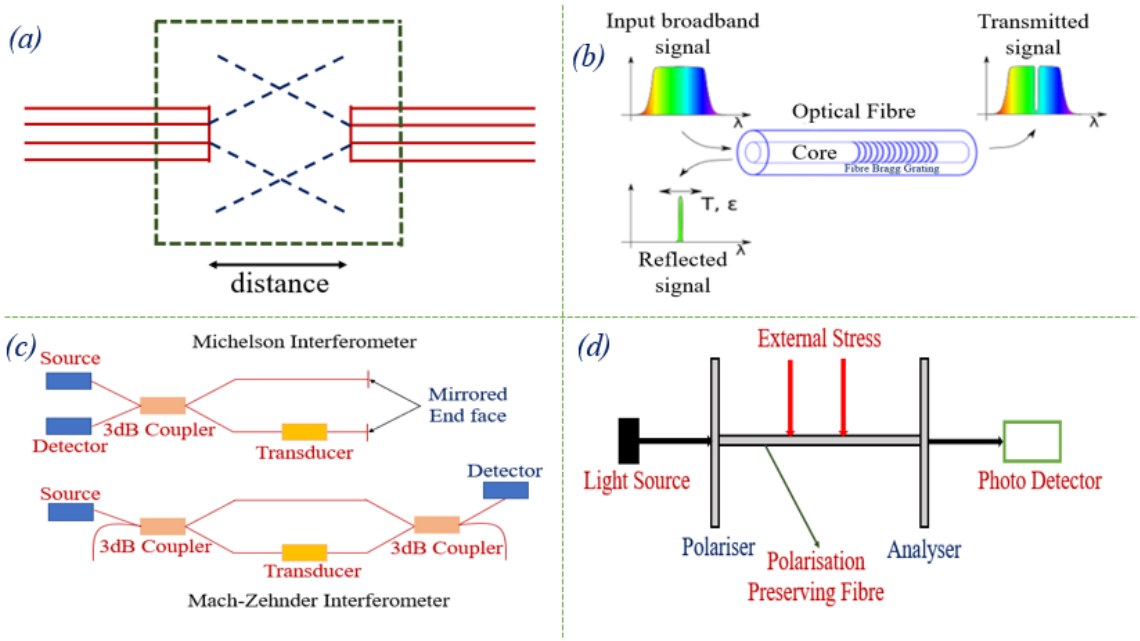


Figure 2.15: *(a) Intensity based optical fibre sensor (adapted from [56]) (b) Wavelength modulated optical fibre sensor [57] (c) Phase modulated optical fibre sensor (adapted from [9]) (d) Polarisation modulated optical fibre sensor (adapted from [9])*

2.7.2.1 Intensity based optical fibre sensor

The intensity based optical fibre sensor (IBOFS) depends on a signal that experiences some signal loss. They are created using equipment which converts the measured value into a force that bends the fibre and attenuates the signal. The signal can also be attenuated by a target's absorption or scattering. The IBOFS works as a transmission sensor which needs more light compared to other types of sensors, and multimode large core fibres are often used. A measurand induced variation in the optical intensity conveyed by an optical fibre can be brought on by several phenomena, including attenuation, microbending loss, and evanescent fields [56]. IBOFS are the simplest to implement, reliable, and low cost. However, source intensity variations, variable losses in fibres and connectors, and changes

in detector sensitivity can all cause drift in IBOFSs. So, a reference technique is required to prevent signal corruption [58].

The example of an IBOFS is a microbend sensor. This sensor's working principle is based on how the energy of guided modes is coupled to radiation modes by use of mechanical periodic micro bends. The transmitted light is attenuated as a result. The sensor is made up of 2 grooved plates with an optical fibre pass in between them, as shown in Figure 2.15 (a). The top plate may shift due to the applied pressure. When the fibre's bend radius exceeds the critical angle required to restrict the light to the core region light starts to leak into the cladding, causing an intensity modulation. [56].

Suppose we consider an optical fibre humidity sensor that comprises 2 optical fibres. One fibre with a thin film of poly(allylamine hydrochloride) (PAH)/silica nanoparticles (SiO_2 NPs) on its distal end for relative humidity (RH) measurement. A second, bare fibre (BF) is placed alongside the first fibre. Water vapour does not cling to the uncoated BF's smooth perpendicular fibre tip surface; hence it can be used to reduce the effect of bending losses [59] seen in the signal obtained from the sensor as both fibres. If 2 fibres are identical, they will suffer equal bending losses.

IBOFSs are typically used as chemical sensors using a sensitive film on the optical fibre tip. The sensing is achieved by utilising a light source with a wavelength absorbed by the chemical to be sensed. The resulting light intensity variation measures the chemical concentration inside a solution [60].

Absorption based OFSs are based on the property that the chosen analyte affects the intensity of the light propagating along the optical fibre. The Lambert-Beer law can be used to describe the intensity loss according to Eq. (2.20). For example, graphene-based thin films can be used to fabricate OFSs [61]. Adsorption of molecules on the surface of graphene can change the electrical conductivity and the complex refractive index (RI) value, which affects the absorption spectrum. Thus, by only measuring the absorption spectrum, different elements can be detected, and their concentrations can be determined [62]. The conductivity of graphene is significantly influenced by the ambient temperature,

humidity, and UV light, which can change the material's effective RI, which may be measured in the transmitted optical power [61].

The microfibre [63] and side-polished [64] optical fibre structures have been used to create graphene coated optical fibre temperature sensors. Highly birefringent fibre coated with graphene oxide and tapered single mode microfibres in contact with methylene-blue functionalised reduced graphene oxide has been used to fabricate optical fibre UV light exposure sensors [65]. The side-polished single mode fibres coated with reduced graphene oxide are used to fabricate optical fibre humidity sensors [66]. Light modulation of reduced graphene oxide affects by a high RH range from 70% RH to 90% RH [67].

2.7.2.2 Wavelength modulated optical fibre sensor

A wavelength modulated optical fibre sensor (WMOFS) uses changes in the wavelength of light for detection. The most widely used WMOFSs are the Fibre Bragg Grating (FBG) and Long Period Grating (LPG) sensor. An FBG is developed by making periodic changes in the refractive index (RI) of the core of a single mode fibre [9]. The fibre core is exposed to an intense interference pattern of an UV or a femtosecond laser to create this periodic change in RI. The RI variation created in this way creates an interference pattern functioning as a grating. FBG has a period of around 1 μm for a resonance wavelength of 1550 nm [68]. The working principle of a WMOFS using an FBG is represented in Figure 2.15 (b). An FBG sensor essentially reflects a portion of the incoming probe light spectrum corresponding to the Bragg wavelength and allows the rest of the spectrum to pass, almost undistorted. The Bragg wavelength depends on the RI of the fibre and grating pitch, defined when the sensor is manufactured, but both change with external environmental effects [57]. The reflected Bragg wavelength, λ_B, is defined by the following formula [69]:

$$\lambda_B = 2\, n_{eff}\, \Lambda \qquad (2.7)$$

where Λ is the grating pitch and n_{eff} is the effective RI [69].

FBGs can be deployed to determine pressure, temperature, strain, and slow vibration. These, parameters are monitored by directly measuring the Bragg shift [57]. The FBGs have high accuracy, high sensitivity, and a wide dynamic range. The drawbacks of FBGs are temperature sensitivity and difficulty in demodulating wavelength shifts [69].

An LPG has a period range from 100 μm to 1 mm. LPG transmits light from the core mode to a specific group of co-propagating cladding modes. A series of resonance bands characterise the transmission spectrum of an LPG; each corresponds to coupling to a different cladding mode due to the high attenuation in the cladding modes. The resonance wavelength of LPG is calculated using Eq. (2.8) [68].

$$\lambda_i = \left(n_c - n^i{}_{clad}\, \Lambda\right) \qquad (2.8)$$

where Λ is the period of the grating, n_c is the RI of the mode propagating in the core, and $n^i{}_{clad}$ is the effective RI of the ith axially symmetric and linearly polarised (LP) cladding mode. The surrounding RI's variation and optical thickness of nanoscale coatings deposited onto the cladding change the resonance wavelength because the cladding mode's EW interacts with the surrounding medium. LPG sensors are an excellent option for developing refractometers and biosensors [68].

2.7.2.3 Phase modulated optical fibre sensor

A phase modulated optical fibre sensor (PMOFS) compares the phase of light in a single fibre to a reference fibre. Figure 2.15 (c) illustrates the technique deployed in both a Michelson and Mach-Zehnder interferometer. When a light beam passes through an interferometer, the light is divided into 2 beams, one of the beams is exposed to the sensing environment and hence goes through a phase change whilst the second beam, doesn't pass through the sensing environment and is utilised as a reference. The beams interfere with each other when the beams are recombined. The available interferometers are Fabry-Perot (FP), Mach-Zehnder, Sagnac, Michelson, grating and polarimetric interferometer [9] – only the Michelson and Mach-Zehnder are illustrated in Figure 2.15 (c).

The PMOFS technique is widely used for acoustic sensing (Mach-Zehnder interferometer), temperature sensing (Michelson interferometer), and rotation sensing (Sagnac interferometer). Compared to IBOFSs, PMOFSs are more complex. Firstly, a wavelength variation of the source can be the reason for an unwanted phase shift. In a Mach-Zehnder interferometer, a wavelength shift of the source would affect both the sensing and reference arm equally, and the source variation would cancel out. So sensing is possible because one arm is exposed whilst another is, creating different optical path lengths. Secondly, the output signal may be uncertain due to the interferometer's sinusoidal output. Finally,

PMOFSs can only be operated when the optical path difference between the sensing and reference arm is less than the source's coherence length [58].

2.7.2.4 Polarisation modulated optical fibre sensor

The polarisation state of the light field acts as a sensing mechanism in a polarisation modulated optical fibre sensor (POMOFS). Whenever a fibre is in contact with any strain or stress, the RI will be varied. The RI's variation due to strain or stress is called an induced RI. So, different polarisation directions have an induced RI. Figure 2.15 (d) illustrates the set-up for the POMOFS, where a polariser generates polarising light that can be a polarisation-preserving fibre's length. There are several states of polarisation, such as circular, linear, and elliptical. In linear, during the light propagation, the electric field's direction remains in the same line. Whereas in elliptical polarisation state, the electric field's direction fluctuates during the light propagation, and in circular polarisation state, it rotates at a constant rate in a line perpendicular to the direction of the light propagation [9].

POMOFS are used as temperature sensors because the birefringence differs with temperature. Low birefringence fibres are utilised to develop the Faraday effect for current and magnetic field sensing application [58].

2.7.3 Classification of an OFS depending on application

An OFS can be categorized as a physical or chemical sensor depending on the application [56].

2.7.3.1 Physical optical fibre sensor

Physical optical fibre sensors (POFSs) are used to measure physical properties like temperature, pressure, strain etc. [56]. The examples of POFSs are given below:

Optical fibre temperature sensors (OFTSs) make use of a variety of transduction mechanisms, including Rayleigh scattering, temperature-dependent fluorescence lifetime, the thermo-optic effect, and thermal expansion in FPIs, LPGs, and FBGs. Body temperature can be measured with OFTSs [68].

Pressure can be measured using several OFS, including intensity modulated, FBGs, and FPIs. Optical fibre pressure sensors (OFPSs) are employed in neurology, cardiology, gastrointestinal, and urodynamics [68].

Optical fibre strain sensors (OFSSs) are based on FBGs or LPGs. OFSSs can measure the respiratory rate where chest movement causes a strain [68].

For instance, FBG is one kind of OFS to measure the pressure, temperature, and strain by using the following formula [68]:

$$\Delta\lambda = \lambda_B [(1 - P_e)\, \Delta\varepsilon + ((1 - P_e)\, \alpha + \xi)\Delta T] \qquad (2.9)$$

where $\Delta\lambda$ is the wavelength shift, ΔT is the temperature change, $\Delta\varepsilon$ is the strain change, P_e is the effective elasto-optical coefficient (theoretical value 0.22) of the FBG, α is the thermal expansion coefficient, and ξ is the thermo-optical coefficient [70].

The reflected centre wavelength is affected by the grating period and effective RI. The centre wavelength variation depends on temperature and strain. Strain variation has a linear relation with the FBG centre wavelength shift at a fixed temperature according to Eq. (2.9). The applied pressure on the FBG is correlated with the centre wavelength shift [70].

2.7.3.2 Chemical optical fibre sensor

Chemical optical fibre sensors (COFSs) are used to measure like biomarkers in gases, humidity, and pH, etc. [56]. The examples of COFSs are given below:

The breath biomarkers ammonia (NH_3) and CO_2 are essential for the detection of renal and respiratory illnesses [71]. The OFCS described in this thesis consists of an optical fibre tip coated with organically modified silica (Ormosil) films containing colorimetric dye, thymol blue (114545, Sigma-Aldrich, UK) enabling measurement of CO_2.

The optical fibre NH_3 sensor (OFNS) is coated with tetraphenylporphyrin tetrasulfic acid (TPPS) on the optical fibre tip. The intensity of the optical fibre NH_3 and CO_2 sensor is found at a particular wavelength window, which changes due to the different NH_3 and CO_2 concentrations, respectively [71].

Optical fibre humidity sensors (OFHSs) are fabricated using a few OFS configurations such as FBGs or FPIs that use humidity-sensitive thin films. For example, the FPI OFHS

works based on detecting the RI fluctuation brought on by water molecules absorbing into a humidity-sensitive film and reacting quickly according to different humidity levels. One of the most important factors in wound healing is humidity [68].

Optical fibre pH sensors (OFpHSs) are coated with dye indicators or fluorophores on the optical fibre tip. The OFpHS works based on detecting the colour change of the pH indicator dyes and the fluorophore's lifetime or fluorescent intensity. For instance, the FPI OFpHS is coated with PAH and the polymer poly(acrylic acid) (PAA) on the optical fibre tip to detect pH. The OFpHS can be used to monitor pH levels in human samples [68].

2.8 Latest advances in OFpHSs

A list of research groups is mentioned below who are actively working on optical fibre pH sensors.

a) Researchers from Wuhan University of Technology (National Engineering Research Centre of Fibre Optic Sensing Technology and Networks), China fabricated a no-core fibre optic sensor coated with PAni/PAA layer for pH detection. An optical fibre pH sensor is fabricated by combining 2 pieces of single mode fibre (SMF) and 1 section of no-core fibre (NCF), which is coated by pH-sensitive polyaniline/polyacrylic acid (PAni/PAA) using a layer-by-layer (LBL) method [72].

Firstly, a section of NCF (length ~ 3 cm) is spliced with 2 sections of SMFs by a fusion splicer, and the SNS (SMF-NCF-SMF) probe is created. After that, the PAni/PAA-sensitive film is deposited onto the NCF surface. A light source with a central wavelength of 1550 nm is used. This pH sensor is tested inside solution of hydrochloric acid (HCl) or sodium hydroxide (NaOH) in DI water with a pH range of 2-12. The NCF and surrounding medium act as the core and cladding during the RI sensing. The higher-order modes excite when the light enters from the input SMF to the NCF, resulting in a multimode interface. The pH variations of the sample affect the RI of the coated pH-sensitive film because the thickness of the film changes with pH. The ionic cross-linking between PAni and PAA will increase as the pH rises, leading to the sensitive film's shrinking. The amount of water molecules in the sensitive film gradually reduces as its thickness declines, which results in

a rise in the sensitive film's effective RI. The RI of the PAni/PAA-sensitive film increases due to the pH increment, resulting in a red shift of the resonance wavelength [72].

This sensor has cross-sensitivity to temperature because the pH of the solution rises due to the temperature increment. The temperature sensitivity is found to be about 0.01 nm/°C. The response and recovery times of this sensor are measured at < 10 secs. The sensor's sensitivity is achieved at 0.985 nm/pH for a pH range of 2-12 [72].

b) Researchers from City University London (School of Mathematics, Computer Science, and Engineering), UK and Technische Hochschule Mittelhessen University of Applied Sciences, Germany fabricated a fibre optic sensor coated with fluorescent monomer for pH detection. A fibre tip is coated with a pH indicator dye, fluorescein O-methacrylate doped hydrogel matrix, to make an optical fibre pH sensor for detecting a pH range of 5-8.5. Fluorescein is polymerizable; it makes covalent bonding with hydrogel matrix to prevent the dye leaching. Also, fluorescein contains the least negative charges compared to other fluorescent dyes (HPTS) [73].

The sensing mechanism is based on the changes in luminescence intensity due to the pH variation in the samples. A 470 nm wavelength LED is used as a light source for coupling light into the optical fibre. This pH sensor is tested inside 5 different pH buffers (at pH 5, 6, 7, 8, and 8.5, respectively). A maximum absorbance and a peak emission wavelength are achieved at 490 nm and 520 nm, respectively. An LED with an optical filter is used to keep the effect of stray light to a minimum. The relative intensity increases due to the pH increment. This pH sensor showed a stable response over a long-duration measurement (12 hours at pH 7) with continuous irradiation. A low signal drift is achieved at < 2.42 %/hr with a negligible effect of stray light. The response time of this sensor is measured at < 5 secs. The sensor's accuracy is achieved at around ± 0.04 pH units (at pH-7) [73].

c) Researchers from Jinan University (Institute of Photonics Technology), China and Hong Kong Polytechnic University (Photonics Research Centre), Hong Kong fabricated an all-polymer fibre optic sensor coated with hydrogel for pH detection. A single mode polymer fibre inscribed with a Bragg grating is coated with a UV-cured pH-sensitive hydrogel, poly(ethylene glycol) diacrylate (PEGDA) to make an optical fibre pH sensor. The pH of

the surrounding fluid affected the volume of the PEGDA, which caused lateral stress to develop in the Bragg grating [74].

An FBG array is created utilising the phase mask technology with a 325 nm He-Cd laser. This pH sensor is tested inside an aqueous solution of HCl with a pH range of 0-6.5. The resonance wavelength is found at around 1555 nm. The peak wavelength moves to a longer wavelength due to the pH decrement (6.5 to 3). This occurs because the HCl solution contains higher H^+ ions with lower pH values, which permits more H^+ ions to bind with O_2 atoms in the PEGDA. No peak wavelength shift is observed for the pH range of 0-2 [74].

This sensor has cross-sensitivity to temperature because the solidified PEGDA shows a thermal expansion coefficient of around 1.56×10^{-4}. This pH sensor shows a red shift of the resonance wavelength due to the temperature variation. The temperature sensitivity is found to be about 10 pm/°C. The response of this sensor is measured at 30 secs. The sensor's sensitivity is achieved at -0.34 nm/pH for a pH range of 3-6.5 [74].

d) Researchers from the Indian Institute of Technology, Dhanbad (Department of Applied Physics), India fabricated a no-core fibre optic sensor coated with bromophenol blue, cresol red, and chlorophenol red for pH measurement. An NCF with a bulge at the end of a single-mode fibre is coated with different pH indicator dyes (bromophenol blue, cresol red, and chlorophenol red) by dip-coating to develop an optical fibre pH sensor [75].

A small portion of the NCF is spliced with single mode fibre using a fusion splicer, and the NCF acts as a sensing probe. The eigenmodes excite when the light enters from the single mode fibre to the NCF. The surrounding environment has a significant impact on the RI of modes. A broadband light source with an operating wavelength of 1400-2000 nm is used. This pH sensor is tested inside a solution of HCl or nitric acid (HNO_3) in DI water with a pH range of 2-13. The resonance wavelength is found at around 1527 nm. The resonance wavelength moves towards a shorter wavelength (blue shift) due to pH increment for alkaline solutions. Oppositely, the resonance wavelength moves to a longer wavelength (red shift) due to pH increment for acid solutions [75].

The pH variation can be determined by observing the transition of indicators on the surface of the fibre probe from protonated to deprotonated forms. As a result, the electron density varies due to the cladding's RI increase. The effective RI of the cladding mode is

influenced, but the fundamental mode is unaffected after immersing this pH sensor in solutions of different pH values. The external RI affects the effective RI of the cladding mode. Consequently, when the external RI varies, the resonance wavelength moves towards the shorter or longer wavelength [75].

This sensor has cross-sensitivity to temperature because the thermal expansion of pH-sensitive film increases its volume and declines RI. This pH sensor shows a blue shift of the resonance wavelength due to the temperature variation. High temperature for either acidic or alkaline solutions increase H^+ ions, and as a result the pH value drops. So, the temperature sensitivity is found to be about 0.0018 nm/°C. The sensor's sensitivity is 1.02 nm/pH and -0.93 nm/pH for acidic solutions (pH = 2-7) and alkaline solutions (pH = 8-13), respectively [75].

2.9 Sensing film coating techniques

Two techniques commonly used for coating the pH indicator dyes onto the optical fibre tip are Layer-by-Layer (LbL) deposition and sol-gel process.

(a) LbL deposition: The LbL deposition process is used for thin-film fabrication procedures, illustrated in Figure 2.16 (a). The films are created by adding alternating multilayers of oppositely charged substances with solvent wash steps in between the layers. LbL can be completed using numerous methods such as spin, spray, immersion, electromagnetism, or fluidics [76]. The whole process of multilayer structures build-up by LbL usually consists of the following 4 steps: polycation, deionised (DI) water wash, polyanion, and DI water wash, as shown in Figure 2.16 (a). The substrate is immersed in the polycation and polyanion solutions, and then the substrate is cleaned with DI water between these 2 stages. These deposition techniques are then cycled to achieve the required number of paired layers called bilayers, and the multi-layered films are finally dried in N_2 gas after fabrication [77].

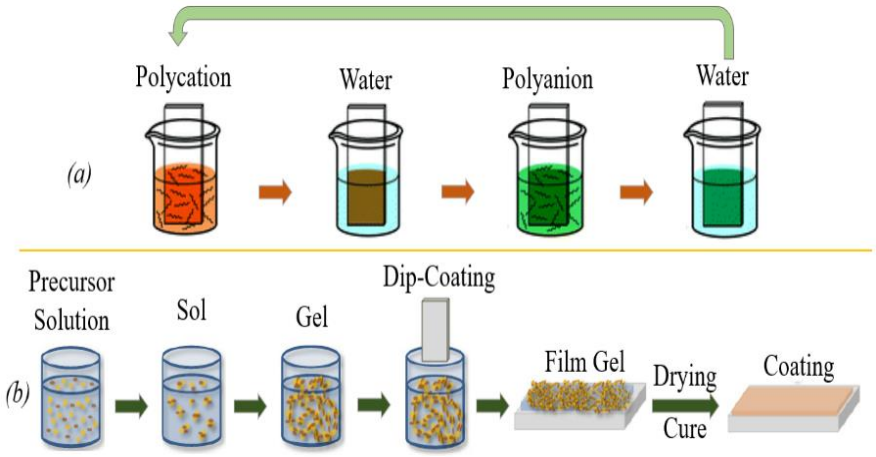


Figure 2.16: *Film coating processing routes (a) LbL deposition [77] (b) Sol-gel coating [78]*

(b) Sol-gel process: It is derived from the solution-gelation process. This term was described as a solution method that primarily created a colloid generated by a gel stage. The sol-gel method, illustrated in Figure 2.16 (b), comprises 4 steps: hydrolysis, condensation or polymerisation of monomers, particle growth, and gel creation. The precursor solution (an inorganic salt like metal chlorides or metal alkoxide solution) is chemically prepared to create hydrous metal oxides called hydroxides (hydrolysate). Colloidal dispersions (sols) of the hydrolysate are made by peptization, a gel is created by dehydration or pH control, and the resulting body calcined to create a fixed oxide product [78]. As sol is a liquid, it can be poured into a mould or be applied on a surface using the dip-coating method to create the layer on the fibre tip. The last and critical step in the sol-gel process is drying in N_2 environment for around 24 hours [79].

pH indicator dyes are commonly trapped in a solid matrix such as sol-gel developed materials or a polymer [80]. Such matrices expose selectivity and give flexibility and permeability, providing chemical and mechanical stability. The LbL method is ideal for fabricating thin polymer or polymetric NPs multilayers. The dip-LbL method is useful, but the overall prolonged deposition time and rinsing stages and the risk of cross-contamination make it a very time-consuming technique [77]. However, the sol-gel coating is a simple and very low-cost method to make metal oxides and permits control over the doping method or addition of transition metals with a high-level of purity and homogeneity as compared to other techniques. Sol-gel based materials have been chosen for fabricating

the OFCS because compared to polymers, sol-gel provides better optical transparency and are more flexible in terms of their fabrication. Ormosil is a reliable class of sol-gel substances containing features like porosity, flexibility, hydrophobicity, hardness, and stability, and fabricated under room temperature situations. In addition, polymers can resist autoclaving being superior to sol-gel based substances [80].

2.10 OFCSs review

The analytical signal is generated in a sensing element using electromagnetic (EM) radiation for the chemical optical fibre sensors. These sensors are based on optical principles such as reflectance, absorbance, fluorescence, or RI [81]. The chemical optical fibre sensors detect CO_2 using sensitive layers based on polymer or sol-gel that contains an organic pH indicator dye such as HPTS, thymol blue, methyl red, and phenol red. Colorimetric or fluorescent indicator dyes are possible to use for sensing CO_2 [82]. The operating principle of a reflection mode OFCS is shown in Figure 2.17 (a). The sensing material can be coated on the optical fibre tip, and it forms the film. The light travels from the source to the sensor and then from the sensor to the receiver by the optical fibre coupler. Also, the operating principle of a transmission mode OFCS is shown in Figure 2.17 (b). The light source and receiver are connected via a direct optical path. The amount of transmitted light depends on different interactions between the sensitive coating and input light [83].

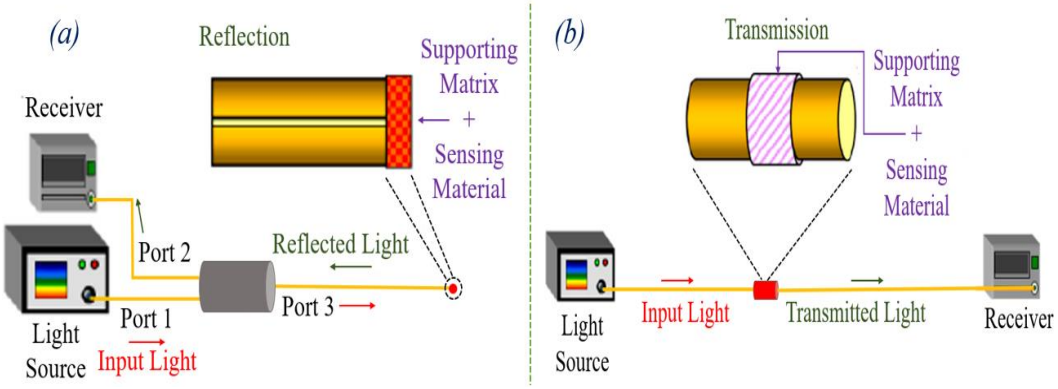


Figure 2.17: *Schematic diagram of set-up used for OFCS operating in (a) reflection mode (b) transmission mode (adapted from [83])*

Reference [42] discusses RI based OFCS. Here, a single mode fibre tip is coated with a sensitive layer of polyhexamethylene biguanide (PHMB) using the dip-coating method.

This PHMB micro-hemisphere layer forms a Fabry-Perot (FP) cavity on the fibre tip, which is highly sensitive to CO_2. The RI of the functionalisation layers varies due to the environmental CO_2 concentration. PHMB is a member of the guanidine polymer family, and basic amide-bearing functional groups are present in PHMB. Guanidine derivatives absorb and release CO_2 molecules, which results in RI variations in the material. PHMB is a suitable material for the functionalisation polymer layer, which is sensitive and selective to low CO_2 concentrations at ambient temperature and atmospheric pressure. A spectrum analyser (wavelength range of 1510-1590 nm) is used to record the reflection spectrum. The resonance wavelength is found at around 1570 nm. The resonance wavelengths of interference fringes moved toward shorter wavelengths due to increase in CO_2 concentration. The sensor's sensitivity is 1.22 pm/ppm for a CO_2 concentration range of 0-700 ppm [42].

The fluorescent pH indicator dyes (such as HPTS) are used in fluorescence type OFCSs. For instance, a blue light (470 nm) is used for excitation and fluorescent peak at 515 nm (green) is used for measuring PCO_2. The presence of CO_2 decreases the intensity of the fluorescence type OFCSs at 515 nm [84]. The colorimetric pH indicator dyes (such as thymol blue) are used in reflectance and absorption type OFCSs. The sensing methods that rely on fluorescence offer greater detection selectivity and sensitivity than other optical techniques formed on absorption estimations [80]. . The limitation of these sensors is that the indicator dyes suffer from leaching or photobleaching effects [85].

The different types of OFCSs based on sol-gel films and their special features are presented in Table 2.4.

Table 2.4: *OFCSs based on sol-gel films [81]*

Reagent	Sol-gel precursors	Linear range	Response time	Lifetime	Sensing Method	Comments	Reference
Pyranine	MTES/ETES, basic catalysis	0-20 %	< 1 minute	6 months (stored ambient)	Fluorescence	–	[86]
HPTS	TEOS+PDMS+APTES	0.023 % (gas)/6.6 % (dissolved)	8 seconds (gas)/1-2 minutes (dissolved)	12 months (stored dry)	Fluorescence	–	[87]
HPTS+RU $(dpp)_3$	MTES+CTAB	0.08 %	20-30 seconds	> 7 months	Fluorescence	Modified atmosphere packaging applications	[88]
Thymol Blue	MTMS	Full range, except 0.02-0.1 %	2 minutes	–	Absorption	–	[89]

APTES: 3-Aminopropyltrioxysilane, CTAB: cetyltrimethylammonium bromide, ETES: ethyltriethoxysliane, MTES: methyltriethoxysilane, HPTS: 8-hydroxypyrene-1,3,6-trisulfonic acid, RU$(dpp)_3$: RU(II)-tris(4,7-diphenyl-1,10-phenanthroline), MTMS: methyltrimethoxysilane, TEOS: tetraethyl orthosilicate, PDMS: polydimethylsiloxane

A few important parameters need to be considered before selecting materials and methods for OFS fabrication. The choice of material and methods depends on the response time, storage stability, gas sensing phase, gas measurement range, and applications for Table 2.4.

a) The fluorescence-based OFCS from Reference [86] is coated with pH indicator dye ‘pyranine’. This can be a good choice for fabricating thin film waveguide sensors for mass production with a CO_2 measurement range of 0-20% CO_2.

b) The fluorescence-based OFCS from Reference [87] is coated with pH indicator dye 'HTPS'. This can be a suitable option for CO_2 detection in both phases (gaseous and aqueous) with long shelf life (at least 12 months).

c) The fluorescence-based OFCS from Reference [88] is coated with pH indicator dye 'HTPS and $RU_{(dpp)3}$'. This can be a wise choice for CO_2 measurement in Modified Atmosphere Packaging applications with quite a long shelf life (at least 7 months).

d) The absorption-based OFCS from Reference [89] is coated with pH indicator dye 'thymol blue' This can be an appropriate choice for detecting the full range of CO_2 (100% CO_2) within only 2 minutes.

An optical fibre LPG based CO_2 sensor is coated with HKUST-1 (a material that belongs to the metal organic framework (MOF) family) using the LbL method. The measuring of the coating's RI variation, which is brought on by the entry of CO_2 molecules into the HKUST-1 pores, serves as the basis for the sensing mechanism. MOFs is a part of the crystalline materials with enormous internal surface areas, variable internal porosity, and organic activity. The materials have exceptional thermal and chemical stabilities due to the strong metal-oxygen-carbon linkages [90].

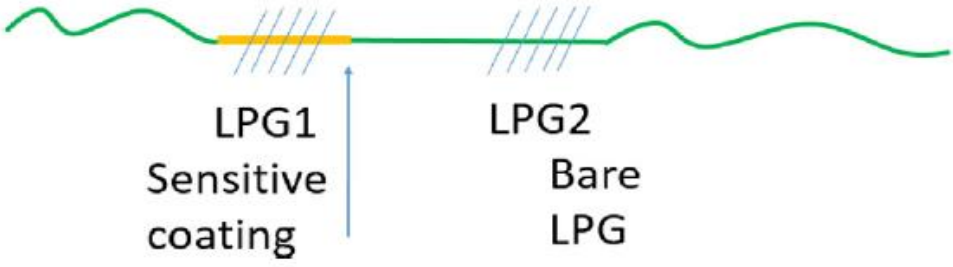


Figure 2.18: *Schematic diagram of LPG based CO_2 sensor [90]*

An LPG array of 30 mm long LPGs with periods of 109.5 µm and 110.5 µm is created by utilising an UV laser illumination and an amplitude mask. In Figure 2.18, the coated LPG1 with HKUST-1 can detect CO_2, but both LPGs have temperature sensitivity. Only a response to CO_2 may explain any variations in the separation between the centre wavelengths related to the bare and coated LPGs [90].

An alternative approach uses a single mode fibre with its tip coated with a sensitive layer of poly (ethyleneimine) (PEI)/poly (vinyl alcohol) (PVA). A Fabry-Perot interferometer

(FPI) cavity is created, which is sensitive to variations of CO_2 concentrations. PEI acts as a carrier molecule for the CO_2 reaction, and PVA serves as a base material for film formation. PEI/PVA blend membrane is a type of dense polymer film with many amino groups. At room temperature and normal atmospheric pressure, the dense polymer membrane can interact with CO_2 molecules due to the amino groups present in the polymer. A swept laser based optical spectrum analyser (resolution = 5 pm) is used to record the reflection spectrum. The wavelength shift of an interference fringe pattern can be used to measure CO_2 concentration. The tracing wavelength is chosen at around 1527 nm, and this wavelength moves to longer wavelengths due to increase in CO_2 concentration. RI variation in PEI/PVA film is 0.0509 for a CO_2 concentration range of 7.6-86.9% CO_2. The sensor's sensitivity is achieved at 0.281 pm/% CO_2 for a CO_2 concentration range of 7.6-86.9% CO_2. Multiple gas channels on the outer surface of PEI/PVA hybrid film make it easier for CO_2 to be transported. This sensor has a cross-sensitivity of humidity and temperature due to the properties of the PEI/PVA film [43].

Other research has developed a plastic optical fibre CO_2 sensor with a tip coated with $CuInS_2$/ZnS quantum dots (CIS/ZnS QDs) and α-naphtholphthalein-doped polymer matrix. The sensing mechanism is based on the fluorescence emission wavelength and colorimetric change of the CIS/ZnS QDs due to the variation in absorption of the pH-sensitive dye, α-naphtholphthalein, with changing CO_2 concentration. A UV LED light source with a central wavelength of 375 nm is used. The α-naphtholphthalein has an absorption wavelength of around 600 nm, and the absorbance declines as the CO_2 concentration rises. CIS/ZnS QDs have an emission wavelength of nearly 578 nm; as CO_2 concentration rises, the CIS/ZnS QDs fluorescence intensity increases due to the absorbance variation of the α-naphtholphthalein. Also, the CIS/ZnS QDs peak red emission wavelength moves to longer wavelengths due to the CO_2 concentrations increment. This red emission of the CIS/ZnS QDs as a wavelength shift detects a CO_2 concentration range of 0-100% CO_2. The sensitivity achieved is 630 pm/% CO_2 for a CO_2 concentration range of 0-100% CO_2. CIS/QDs can be a promising candidate for optical imaging and sensing due to their improved photoluminescence properties. However, the fluorescence intensity of this sensor reduces by around 65 % as the temperature increases from 25.3 °C to 54.8 °C [44].

2.11 Background of the OFS developed in this research

The basic information of an optical fibre is provided below:

2.11.1 Optical fibre structure

An optical fibre structure shown in Figure 2.19 contains 3 parts: the core, cladding, and buffer coating [91].

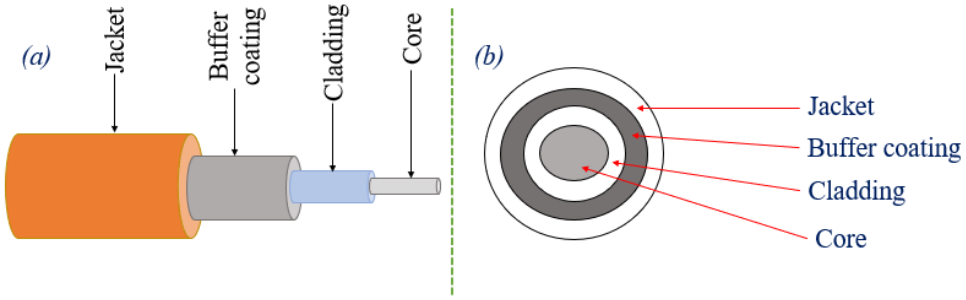


Figure 2.19: *(a) Basic structure (adapted from [91]) (b) Cross-sectional view of optical fibre (adapted from [92])*

The core is a rod-shaped dielectric material made of glass through which light propagates. A layer of dielectric material encloses the core called the cladding, whose RI is less than that of the core. The cladding reduces the light loss from the core into ambient air, minimises scattering loss at the core's surface, safeguards the fibre from absorbing surface contaminants such as dust and enhances mechanical robustness. The cladding is covered in an extra plastic soft layer labelled the buffer coating to protect the fibre from physical damage caused by micro bends [91]. The jacket is a layer of material around the buffer coating, usually made of plastic [92].

2.11.2 Refractive index

The ratio of the light velocity in the free space to the light velocity in material is defined as a material's refractive index. Thus, the refractive index, *n*, is defined as [92]:

$$n = \frac{c}{v} \qquad (2.10)$$

where *v* represents the light's speed in a medium and *c* is the light velocity in free space. Since *v* is always less than *c*, the RI is a dimensionless number greater than or equal to unity. Figure 2.20 illustrates the light bending as it passes between 2 media with different RI's according to Snell's law [92].

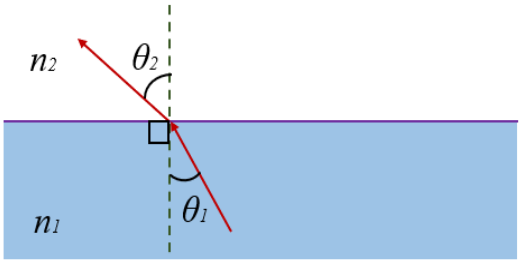


Figure 2.20: *Refraction of a beam of light is based on indices of refraction (n_1 and n_2) for each material (adapted from [92])*

Snell's law formula is developed from Fermat's principle. Fermat's theory states that "light travels in the shortest path that takes the least time". The formula is given below [92].

$$n_1 \sin\theta_1 = n_2 \sin\theta_2 \qquad (2.11)$$

where n_1 and n_2 represent the RI of material 1 and 2 correspondingly, and θ_1 and θ_2 represent the incidence angle and the refraction angle, respectively [92].

2.11.3 Critical angle, Total internal reflection, and Numerical aperture

When a ray of light hits the juncture between the core and cladding, the light beam will be entirely refracted back to the core if the beam's angle to the juncture is higher than a specific value called the critical angle. This incident is called total internal reflection (TIR); it is called total as virtually 100 % of the beam is reflected [92]. The critical angle is the incidence angle, where the refraction angle is 90°. The light must travel from a medium optically thick to a medium which is less dense, as shown in Figure 2.21 (a).

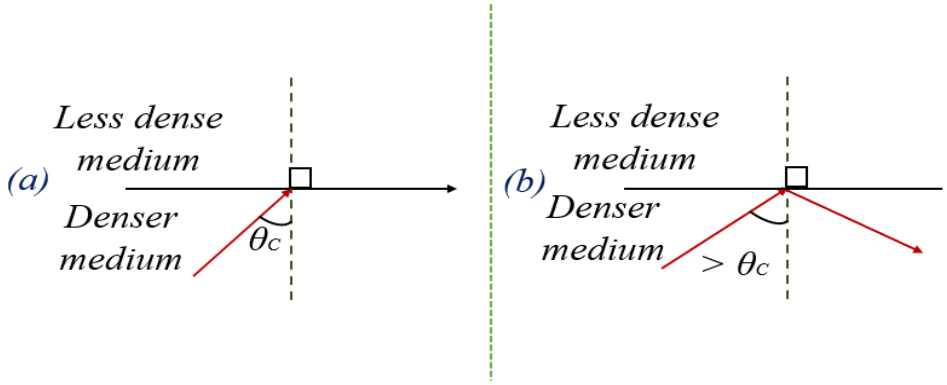


Figure 2.21: *(a) When incidence angle is equal to θ_C, refraction angle is equal to 90° (b) When incidence angle is greater than θ_C, light is reflected into core (adapted from [93])*

Snell's law is used to measure the critical angle at the surface between different media [Eq. (2.11)].

For TIR, the incidence angle is equal to critical angle. So, $\theta_1 = \theta_C$

The refraction angle at the critical angle is equal to 90°. So, $\theta_2 = 90°$

Solving for θ_C using Eq. (2.11)

$$n_1 \sin\theta_C = n_2 \sin 90°$$

$$\sin\theta_C = \left(\frac{n_2}{n_1}\right)(1)$$

$$\theta_C = sin^{-1}\left(\frac{n_2}{n_1}\right) \qquad (2.12)$$

In Figure 2.21 (b), this critical angle is smaller than the incidence angle; the refracted beam is not reflected in the medium but is referred to as TIR. The 2 conditions for TIR are a) light is passing through from an optically denser medium (larger RI) to a less dense medium (smaller RI) and b) the incidence angle is higher than the critical angle. To obtain TIR, the core's RI, n_{core} > the cladding's RI, $n_{cladding}$ [92].

An evanescent wave (EW) is created when a small portion of the guided electromagnetic wave's energy penetrates past the reflective interface, as shown in Figure 2.22. Numerous factors, including physical, optical, and geometrical variables, affect the EW. Among these factors, the EW is highly sensitive to changes in the medium's RI at the core-cladding interface in optical fibre sensors. The EW is absorbed by the medium surrounding the fibre core, including any molecules existing within the penetration depth of the EW which, in turn, causes attenuation of the guided wave's amplitude. The electromagnetic field's amplitude at the core-cladding interface diminishes exponentially to *1/e* of its starting value at a distance known as the penetration depth (d_p) of the EW. It can be expressed in Eq. (2.13) [94].

$$d_p = \frac{\lambda}{2\pi\sqrt{n^2{}_{core}\sin(\theta_i) - n^2{}_{cladding}}} \qquad (2.13)$$

where θ_i is the incident angle (with respect to the normal at the core-cladding interface), n_{core} is the core RI, $n_{cladding}$ is the cladding RI, and λ is the wavelength of the light. From Eq. (2.13), it can be seen that the incident wave angle, θ_i affects the penetration depth. Moreover, a lower refractive index contrast at the core-cladding interface produces a higher penetration depth. As a result, there is an increase in the interaction of light with the surrounding medium [94].

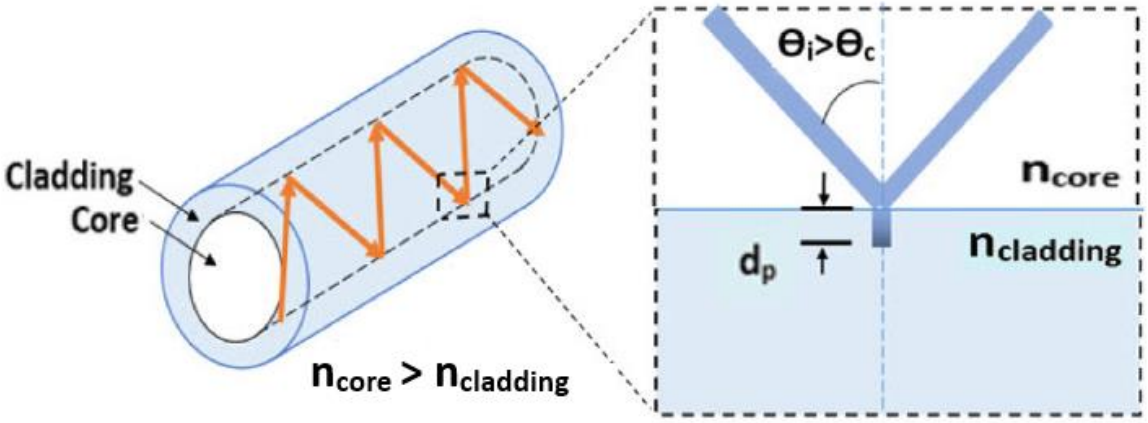


Figure 2.22: *Schematic of the evanescent wave with ray theory approach [94]*

An optical fibre's numerical aperture (NA) gives a measurement of the fibre's capacity to gather light. Mathematically, the *NA* reflects the RI's variation of the core, n_{core} and cladding, $n_{cladding}$ as follows [92]:

$$NA = \sqrt{n^2{}_{core} - n^2{}_{cladding}} \qquad (2.14)$$

The optical fibre allows more light to be coupled as the value of NA rises.

2.11.4 Maxwell's equations

Maxwell's 4 equations describe the light propagation. The equations are provided below [95]:

1st Law,

$$\nabla \cdot \vec{E} = \frac{\rho}{\epsilon_0} \qquad (2.15)$$

where E is the electric field, ρ is the electric charge density, and ε_0 is the permittivity of free space (8.854×10^{-12} F/m) [95].

1st law [Eq. (2.15)] is based on Gauss's law of electricity which means that "the divergence of the electric field in a specific region of space is proportional to the charge density in that region" [95].

2nd Law,

$$\nabla . \vec{B} = 0 \qquad (2.16)$$

where *B* is the electric field [95].

2nd law [Eq. (2.16)] is based on Gauss's law of magnetism which means that "the divergence of the magnetic field is zero" [95].

3rd Law,

$$\nabla x \vec{E} = \frac{-\partial \vec{B}}{\partial t} \qquad (2.17)$$

3rd law [Eq. (2.17)] is based on Faraday's law of induction which means "a closed loop of electric field lines will exist when the magnetic field varies with time" [95].

4th Law,

$$\nabla x \vec{B} = \mu_0 \vec{J} + \epsilon_0 \mu_0 \frac{\partial \vec{E}}{\partial t} \qquad (2.18)$$

where *J* is the current density and μ_0 is the permeability of free space ($4\pi \times 10^{-7}$ H/m) [95]. 4th law [Eq. (2.18)] is based on Ampere's circuital law which means "a closed loop of magnetic field lines will exist in the presence of a current and/or time varying electric field" [95].

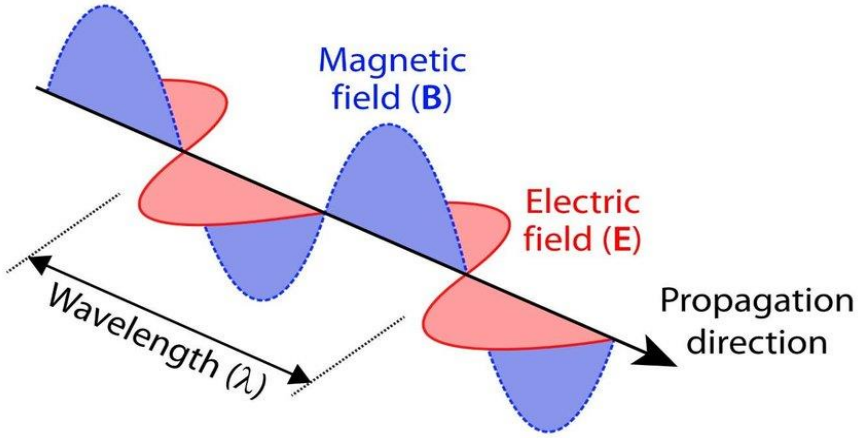


Figure 2.23: *An EM wave consisting of electric and magnetic oscillating fields [96]*

According to 3rd and 4th law of Maxwell's equations a variable magnetic field causes a variable electric field, and a variable electric field causes a variable magnetic field. Sinusoidal fields can propagate by themselves once they have been generated. Another name of propagating fields is electromagnetic waves. EM waves can propagate through the

vacuum according to Eq. (2.19). Figure 2.23 shows the EM waves (combination of orthogonal electric and magnetic waves) propagates through the vacuum with a wavelength (λ) [95-96].

The speed of light or EM waves is related to and electric and magnetic vacuum constants according to Eq. (2.19). The speed of light is calculated a 3 x 10^8 ms^{-1} using the values of permittivity and permeability of free space. So, light propagates as an EM wave through the vacuum [95].

Speed of Light,

$$c = \frac{1}{\sqrt{\epsilon_0 \mu_0}} \tag{2.19}$$

2.11.5 Optical fibre category

There are 2 general types of optical fibre: single mode fibre (SMF) and multimode fibre (MMF). MMF's core is significantly bigger than SMF's, numerous light rays or modes can go through the fibre at once. Light propagates through the core due to reflections at the core-cladding boundary [92]. Light propagates as an EM wave inside the optical fibre. SMF can only transmit the fundamental LP01 mode. However, MMF enables the propagation of more than one mode of the light wave (for instance, up to the LP21 mode) [97]. LP modes of an optical fibre have radially symmetric refractive index profiles (subscript denotes the radial and azimuthal symmetry) [98]. There are 2 types of MMF: step-index and graded-index.

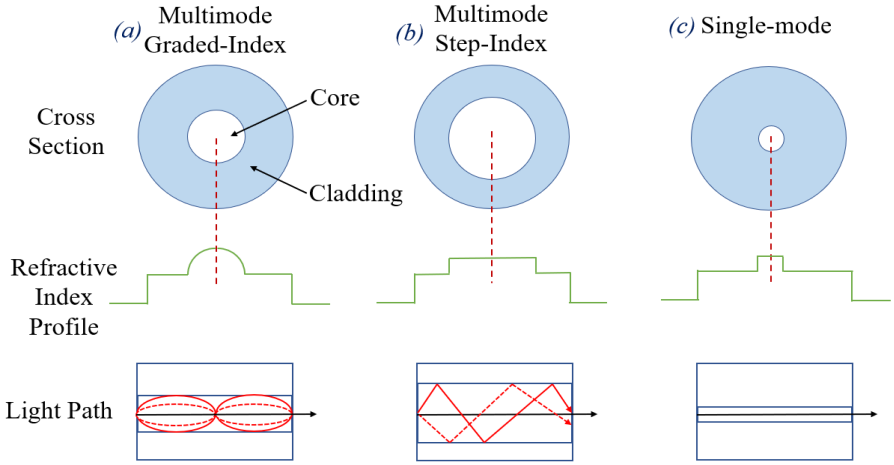


Figure 2.24: *Different characteristics of (a) multimode graded-index fibre (b) multimode step-index fibre (c) single-mode fibre (adapted from [91-92])*

In Figure 2.24 (a), a multimode graded-index fibre comprises a core in which the RI slowly reduces from the core centre outward towards the cladding. The light rays travel with different velocity in various paths because of the RI's variation. Light rays travel along the axis more slowly than those that go close to the cladding because of the higher RI at the core centre. Also, the light path is helical, and the attenuation is less than the multimode step-index fibre because of the graded-index. The set of rays arrive to the receiver at nearly the same moment due to the reduced path and increased speed made possible by the lower index towards the cladding; thus, it diminishes modal dispersion. Compared to a multimode step-index fibre, it can provide a faster data transfer rate [92].

In Figure 2.24 (b), a multimode step index fibre consists of a core with uniform RI and a core-cladding interface with a sharply decreased RI because cladding has a lower RI. The path of light rays is zig-zag in manner. Some of the light rays that make up a light pulse can follow a direct path from beginning to end and are referred to as direct rays. On the other hand, other rays pass through the cladding and arrive at the fibre's end. The dispersion is more than a multimode graded-index fibre because light travels through different paths inside the fibre, which makes a difference in the propagation time of light rays, resulting in a broadened light pulse at the fibre's end [92].

In Figure 2.24 (c), the SMF's core diameter is smaller and permits only one mode to propagate, so no modal dispersion occurs. As a result, an optical signal can travel farther distances. In addition, the distance between pulses can be narrowed with an optical transmitter when the SMF is used because of the lack of pulse spreading. This facilitates a greater operating rate by enabling the use of quicker pulsating light sources. The ray of light is transmitted through an SMF according to Figure 2.24 (c) [92]. The cut-off wavelength of an SMF is the wavelength above which the fibre propagates only with the fundamental mode. Under the cut-off wavelength, the light passes through more than one mode at a time [99]. The core of an SMF is typically 8-10 µm, compared to 50-200 µm for an MMF [92].

The outer cladding diameter of most SMFs and MMFs is 125 µm. Thus, standard size specifications indicate 8/125 µm (core/cladding) or 10/125 µm for a typical SMF and 50/125 µm or 62.5/125 µm for an MMF [92].

MMF with a diameter of 62.5/125 µm has been used for fabricating the OFCS in this thesis. Here, the operating wavelength for the OFCS is around 600 nm (visible wavelength). The reason for selecting an MMF over an SMF is because the MMF has a wide bandwidth. Either a LED or an incandescent light source (halogen light source) can be used with MMF. However, an SMF has a narrow bandwidth, and the price of the SMF in the visible wavelength range is high. In addition, a laser light source can be used with SMF.

2.11.6 Optical attenuation and Bending losses

There are many causes whereby an optical signal can be attenuated. For example, when photons travel through an optical fibre, they may collide with impurities and be absorbed, or they may scatter and lose energy. Attenuation must be expressed in decibels per kilometre (dB/km) at a particular wavelength since each wavelength travels differently through an optical fibre [92]. Lambert-Beer law describes how the intensity of a light beam exponentially decreases as it travels through a purely absorbing medium and is expressed as [100]:

$$I_t = I_0 10^{-\alpha c l} = I_0 10^{-A} \quad (2.20)$$

$$A = \alpha c l \quad (2.21)$$

where I_t and I_0 are the transmitted intensities and incident light beams intensities, respectively, α is the medium's absorption coefficient ($M^{-1}cm^{-1}$), c is its concentration (M), and l is the path length that the beam traverses (cm). The αcl term gives the absorbance (A), or optical density (OD) of the sample, with an OD of one, meaning that a tenth of the incident light passes through the sample [100].

Bending losses occur when an optical fibre is bent. The fibre mode becomes substantially smaller and then very lossy as the light is coupled out into the cladding. There are 2 types of bending losses: microbend loss and macrobend loss.

Microbend loss occurs because of microscopic fibre bends in the core-cladding boundary, generally caused by weak cable design and fabrication. Non-uniform horizontal stresses throughout the cabling establish micro bends [101].

Macrobends mean when a fibre has a large curvature (bend) radius or diameter, *r* relative to the fibre core diameter, *r>>a*. When a fibre has been bent in this manner, the incident angle is compromised, TIR fails, and thus the fibre's core no longer effectively confines and directs light. Macrobend losses are normally encountered throughout the installation process of the optical fibre [101].

The detected intensity of the OFCS used in this research therefore drops due to the bending effect and hence the fibre is kept as straight as possible during the experiment to avoid such bending losses.

2.11.7 Types of fibre materials

An optical fibre can be made from 3 different types of materials: glass, plastic, and plastic-clad silica [92].

Glass fibre is made of a glass core and cladding with impurities added to achieve the required indices of refraction needed to transmit light through the fibre. Glass fibre has the lowest attenuation [92].

Plastic fibre has a relatively thick plastic core and cladding. Plastic fibre has the highest attenuation and is relatively cheap [92].

Plastic-clad silica (PCS) fibre combines a glass core and a plastic cladding. Transparent silica makes up the glass core, while the plastic cladding has a lower RI than the core. A PCS fibre's composition places its attenuation in the middle of glass fibre and plastic fibre. Connecting or splicing PCS fibres can be challenging due to the significant plasticity in this fibre [92].

2.12 Summary

This chapter has illustrated the importance of CO_2 as a biomarker for PUs and presents a possible early treatment indicator. One way to measure the skin CO_2 is with T_CPCO_2 and different researchers in the field have been expanded upon. The process of measuring T_CPCO_2 using an optical miniaturized sampling cell has been presented with a list of commercial devices for monitoring CO_2 and T_CPCO_2 along with their operating principle. The overarching message is that the OFCS offers tremendous opportunities to monitor CO_2

giving an early warning sign with an unobtrusive, very small footprint. Optical fibre CO_2 sensors are frequently used in various environmental, industrial, and biological applications depending on the detection range and moisture insensitivity requirements. Optical fibre CO_2 sensors are developed by coating a fluorescent or colorimetric pH indicator dye on the optical fibre, which is sensitive to CO_2. pH indicator dyes are entrapped within a solid matrix such as polymer or sol-gel-based materials. The sensing film can be deposited on the optical fibre using several methods, such as dip-coating or spin-coating. The performance of the OFCSs depends on the selected materials and techniques. A drawback is that OFCSs suffer from leaching or photobleaching effects, which degrade the sensor performance (stability) and shelf life. The fabrication and characterisation of an OFCS will be discussed in Chapter 3.

3. Chapter 3

Optical Fibre CO_2 Sensor – Fabrication & Characterisation

3.1 Introduction

To understand the characteristics of an optical fibre CO_2 sensor properly, it is essential to fabricate the OFCS using the recipe and protocol from previous research and to calibrate the OFCS alongside the commercial CO_2 datalogger and t_C Sensor 92 probe. Section 3.2 lists materials used in this process and describes the reasons behind choosing these materials, the dye characteristics (changes in transmission and absorption spectra due to pH variation), the CO_2 sensing mechanism, and film preparation techniques. Section 3.3 focuses on the characteristics of the OFCS, such as the experimental set-up for calibration, the obtained results from the fabrication and calibration method along with stability of the OFCS. Section 3.4 shows the negligible temperature cross-sensitivity of the OFCS and how to nullify humidity cross-sensitivity. Section 3.5 illustrates the improved performance of the OFCS using Triton X-100 with sol-gel. Section 3.6 discusses the film thickness measurement and dye concentration calculation from the OFCS tip using the scanning electron microscope. Section 3.7 is based on the calibration results of 10 OFCSs and the sensitivity variation on the OFCSs. Finally, Section 3.8 summarises this chapter.

3.2 Sensor fabrication

It is essential to know the name of the materials and understand the dye characteristics for fabricating the OFCS. This section provides that information about the OFCS fabrication, including the film preparation method.

3.2.1 Materials

The materials used for the OFCS fabrication are as follows:

- Tetraethyl orthosilicate or tetraethoxysilane (TEOS), triethoxymethylsilane (MTEOS), ethanol, thymol blue (TB), tetramethylammonium hydroxide (TMAH) (10 wt. % in H_2O), and Triton X-100 are all obtained from Sigma-Aldrich, UK;

- Isopropyl alcohol (IPA) or 2-Propanol, ≥ 99.5% is obtained from Fisher Chemical, UK;
- CO_2 (5% Argon (Ar) mixture) is obtained from Ryvalgas, UK;
- N_2 (O_2 free) is obtained from BOC, UK;
- OM1 Multimode (MM) silica core, silica cladding (core diameter, *Ø* 62.5 µm, cladding diameter, *Ø* 125 µm) optical fibre and Pigtail Easystrip (ST, Length 1.5 m) are purchased from all4fiber GmbH, Austria.

3.2.2 Reason behind choosing materials

The sol-gel process has been selected for fabricating the OFCS. TEOS and tetramethyl orthosilicate (TMOS) are the most popular orthosilicates used as precursors. An orthosilicate is any salt of orthosilicic acid, $Si(OR)_4$. Both silicates function as inorganic crosslinking agents. They are uncoloured and crystal-clear liquids. When TMOS is hydrolysed, hazardous methanol is released, whereas ethanol is released from TEOS, therefore, TEOS is preferred as a silicon (Si) source [102]. H_2CO_3 is an acid which develops when CO_2 reacts with H_2O, according to Eq. (2.1). H_2CO_3 needs to be mixed with a base catalyst, TMAH to balance the acid-base equilibrium.

The precursor, TEOS is often combined with water and a co-solvent (commonly ethanol) to produce a homogeneous sol. The use of an adequate acid or base catalyst can speed up hydrolysis and polycondensation. TB is a suitable pH indicator dye entrapped in a sol-gel matrix for CO_2 detection. During the reaction, the viscosity of the solution gradually rises, forming a hard, porous, interconnected gel. The reaction occurs when monomeric alkoxysilanes are hydrolysed [Eq. (3.1)] and then condensed [Eq. (3.2)] [81]:

$$\equiv Si - OR + H_2O \rightarrow \equiv Si - OH + ROH \qquad (3.1)$$

$$\equiv Si - OR + OH - Si \equiv \rightarrow \equiv Si - O - Si \equiv + ROH \qquad (3.2)$$

where $R = C_2H_5$ is an alkyl group [81].

Two detectable ranges are available for TB as a pH indicator dye. Its colour changes from red to yellow at pH levels of 1.2 to 2.8 and from yellow to blue at pH levels of 8.0 to 9.2. The gas exchange between film and environment is controlled by the prepared sol-gel film doped with TB and TMAH. The colour change that occurs during the CO_2 reaction can be explained as follows [103]:

$$QOH + HT\ (red) \rightleftharpoons Q^{+}T^{-}.xH_2O \quad (3.3)$$

$$CO_2\ (g) \rightleftharpoons CO_2\ (aq) \quad (3.4)$$

$$\{Q^{+}T^{-}.xH_2O\ (blue)\} + CO_2\ (aq) \rightleftharpoons Q^{+}HCO_3{}^{-}.(x-1)H_2O + HT\ (yellow) \quad (3.5)$$

where *QOH* is TMAH, *HT* is the acidic version of TB, T^- is the deprotonated TB ion and Q^+ is a tetramethylammonium ion. $Q^+T^-.\ xH_2O$ is the ion pair formed within the sol-gel film by acidic TB and TMAH, which causes the colour shift from red to blue when the protonation state of TB changes [Eq. (3.3)]. Gaseous CO_2 moves to aqueous CO_2 once it infuses from the exterior into the sol-gel film. The hydrated water molecule combines with CO_2 to produce a hydrogen ion, which transforms from T^- to *HT*, as shown in Eq. (3.5), and the colour changes from blue to yellow [103].

3.2.3 Absorption and Dye concentration relationship

The amount of light that may travel through a material is known as its transmittance. The amount of light that a material absorbs is known as its absorbance. Figure 3.1 shows how the light travels through the dye solution. It is possible to identify the wavelength or range of wavelengths at which a solution absorbs light by exposing it to broadband light. If the light of a specific wavelength is not absorbed, the incident beam's intensity, which is directed at the solution (I_0), would be equal to the transmitted beam's intensity (I_t). If any of the light is absorbed, the beam's intensity as it passes through the solution will be lower than its original intensity. The proportion of incoming light which is absorbed by the solution can be calculated from the ratio of I_t to I_0. This is known as the transmittance *(T*) [104].

$$T = \frac{I_t}{I_0} \quad (3.6)$$

Absorbance (*A*) is defined in terms of the transmittance or another form of Eq. (2.20) [104].

$$A = -log_{10}\ (T) \quad (3.7)$$

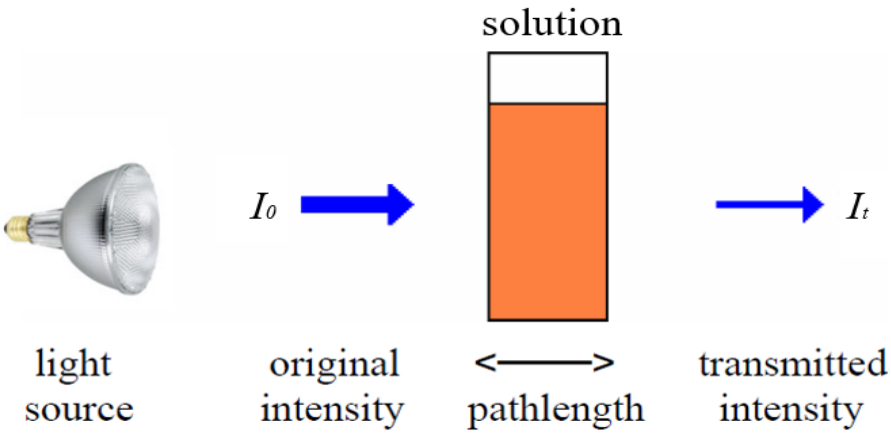


Figure 3.1: *Schematic diagram of light travelling through a solution (adapted from [104])*

The transmittance of a solution decreases with increasing light absorbance. A maximum wavelength (λ_{max}) is the wavelength at the highest absorption peak, which changes due to dye concentrations. In the absence of light scattering, a solution's absorbance is influenced by 3 different factors: the molar absorption coefficient (ε), concentration (c), and optical pathlength (l). The substance, solvent, and wavelength affect the molar absorption coefficient. Eq. (2.21) can be expressed as a function of a wavelength [104].

$$A_\lambda = \varepsilon_\lambda cl \qquad (3.8)$$

3.2.4 Characteristics of dye according to pH variation

The OFCS was coated with TB on the optical fibre tip to detect CO_2. TB is a pH indicator dye.

3.2.4.1 Characteristics of Thymol Blue

TB changes its colour from red (pH = 1.2) to yellow (pH = 2.8) and again from yellow (pH = 8) to blue (pH = 9.2). The pH transformation and structural transitions are illustrated in Figure 3.2. TB (red) deprotonates and becomes TB (yellow). After that, TB (yellow) deprotonates and becomes TB (blue). Conversely, TB (blue) protonates and becomes TB (yellow). After that, TB (yellow) protonates and becomes TB (red). Ultraviolet-visible (UV/vis) spectroscopy measured the transition from yellow to blue at a wavelength of 595 nm [105].

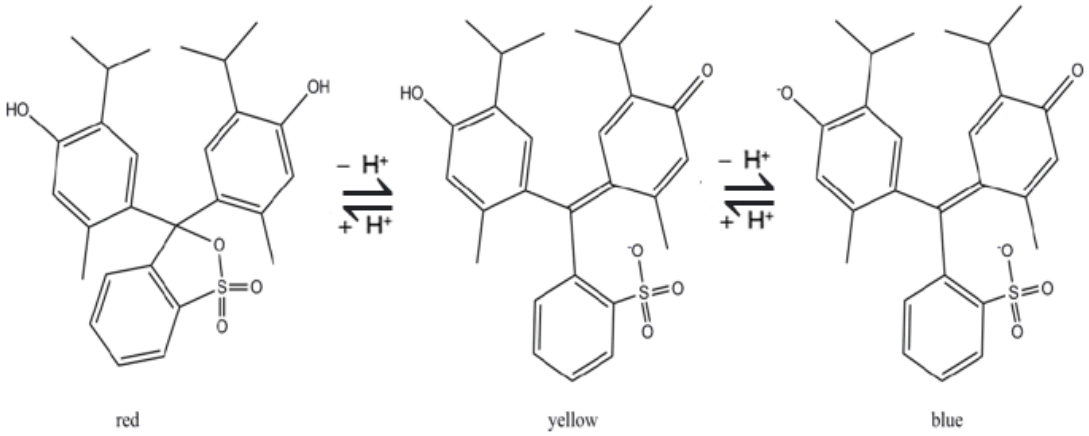


Figure 3.2: *Structural transitions of TB according to different pH values [105]*

The obtained calibration curves of TB from other research [105] are displayed in Figure 3.3. Two peaks can be seen in the absorption spectra of TB at wavelengths of 420 nm and 595 nm which are particularly noticeable in the pH range of 8-9. The absorbance at a wavelength of 595 nm ($A_{595\ nm}$) rises strongly at a pH value of 7.7-9 approximately following a sigmoidal curve [105].

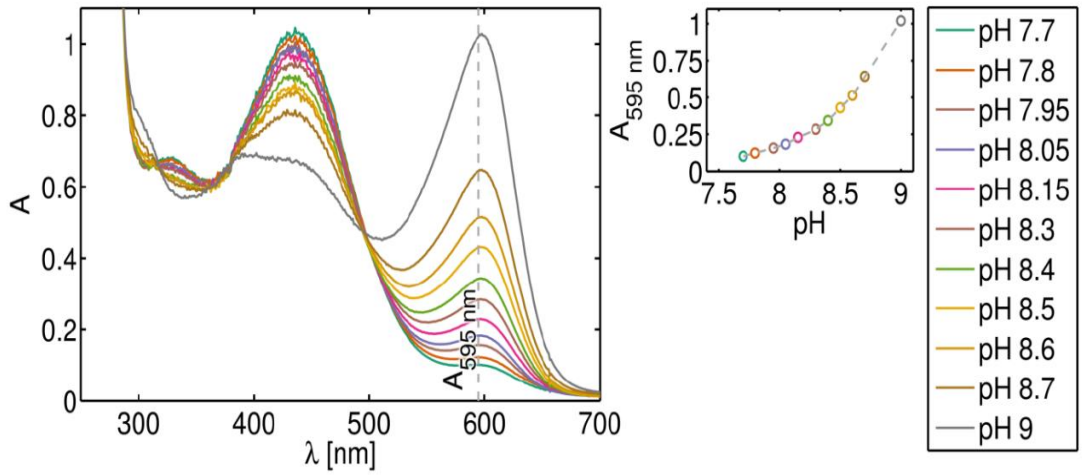


Figure 3.3: *Absorption spectra, A_λ of TB for different pH values [105]*

On the other hand, the absorption at a wavelength of 420 nm decreases slowly at a pH value of 7.7-9 as shown in Figure 3.3. The absorption peak at 420 nm gradually declines with rising pH values which means $A_{420\ nm}$ is less sensitive to pH variation. The changes in absorbance values at 595 nm can be used for pH measurements [105].

3.2.4.2 Experimental set-up for varying pH of Thymol Blue

In Figure 3.4, a krypton halogen light source (ecoVis, Ocean Insight, UK) illuminates a solution via a 1 x 2 MM coupler 50/50 (core diameter, Ø 62.5 µm, cladding diameter, Ø 125 µm, ideal loss/port 3 dB, Lightel, USA) and the transmitted light is detected using a spectrometer (FLAME-S-VIS-NIR-ES, optical resolution ~ 0.1-10 nm, Ocean Insight, UK) which is connected to a computer for data analysis. The coupler acts as a crude attenuator in this set-up. The ecoVis light source has a built-in cuvette holder. The cuvette (length = 1 cm) contains 2 ml of solution (TB with ethanol).

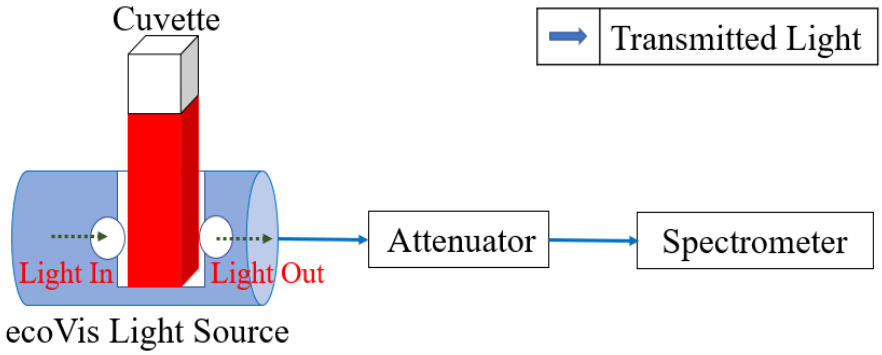


Figure 3.4: *Experimental set-up for monitoring pH variation of TB*

TB was purchased in powder form, and it is soluble in ethanol [106]. The TB solution became red after mixing TB with ethanol. To confirm the spectral response of TB in solution, sodium hydroxide (NaOH) and DI water were used to change the pH. The concentration of TB was also changed due to mixing NaOH and DI water into TB (red). In Figure 3.5, the ethanol and different colours of TB are poured inside the cuvette for further measurement. Eq. (5.4) is used to calculate an unknown concentration where 2 solutions are proportional. The concentration of TB is calculated from yellow and blue solutions using Eq. (3.9) [107].

$$C_i V_i = C_f V_f \qquad (3.9)$$

where C_i is the TB concentration (initial), V_i is the solution's volume (initial), C_f is the TB concentration (final), and V_f is the solution's volume (final) [107].

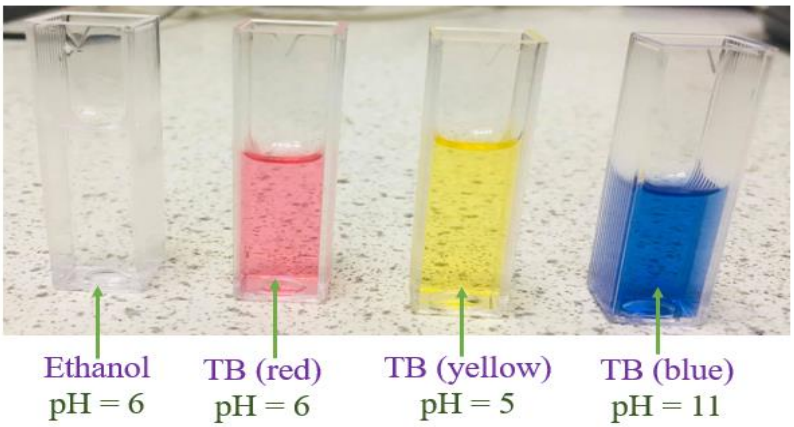


Figure 3.5: *Ethanol and different colours of TB solutions in 1 cm pathlength cuvettes*

The protocol of changing pH of TB is shown in Table 3.1. Thymol blue was purchased from Sigma-Aldrich and was of an American Chemical Society (ACS) grade and used without further purification.

Table 3.1: *Calculation of TB concentration according to pH variation*

pH = 6, Red colour solution [130 ml Ethanol (EtOH) + 2.51 mg TB] Molar weight of TB = 466.6 g/mol = 466600 mg/mol Concentration (*C*) of TB in EtOH = [(2.51 mg) / (130 ml)] = 0.019307692 mg/ml Conversion from mg/ml to M C_{red} = [(0.019307692 mg/ml) / (466600 mg/mol)] = 0.000000041379 mol/ml = 0.000041379 mol/litre = 0.000041379 M
Base (NaOH) preparation: 545.08 mg NaOH + 1.4 ml DI water Molar weight of NaOH = 39.997 g/mol Concentration of NaOH in DI water = [(0.54508 g) / (0.0014 l)] = 389.343 g/l Conversion from mg/ml to M C_{NaOH} = [(389.343 g/l) / (39.997 g/mol)] = 9.7343 mol/l = 9.7343 M
pH = 5, Yellow colour solution [2 ml Red colour solution + 0.2 ml DI water] $C_{fY} = C_i V_i / V_f$ C_{fY} = (0.000041379 M x 2 ml) / 2.2 ml = 0.000037617 M
pH = 11, Blue colour solution [2 ml Red colour solution + 0.5 µl NaOH solution] $C_{fB} = C_i V_i / V_f$ C_{fB} = (0.000041379 M x 2 ml) / 2.0005 ml = 0.000041368 M

3.2.4.3 Spectra of Thymol Blue according to pH variation

Figure 3.6 (a) shows the transmission spectra of the ethanol, TB (red), TB (yellow), and TB (blue) solutions. The transmission spectrum of ethanol is used as a reference signal. The transmission spectra of TB (red) and TB (blue) contains troughs at around 549 nm and 606 nm, respectively. The transmission spectrum of TB (yellow) doesn't contain a trough at any wavelengths.

Figure 3.6 (b) demonstrates the absorption spectra of the TB (red), TB (yellow), and TB (blue) solutions. The absorbance is calculated using Eq. (3.7). The highest absorption peak is found at around 549, 452, and 606 nm for TB (red), TB (yellow), and TB (blue) solutions, respectively.

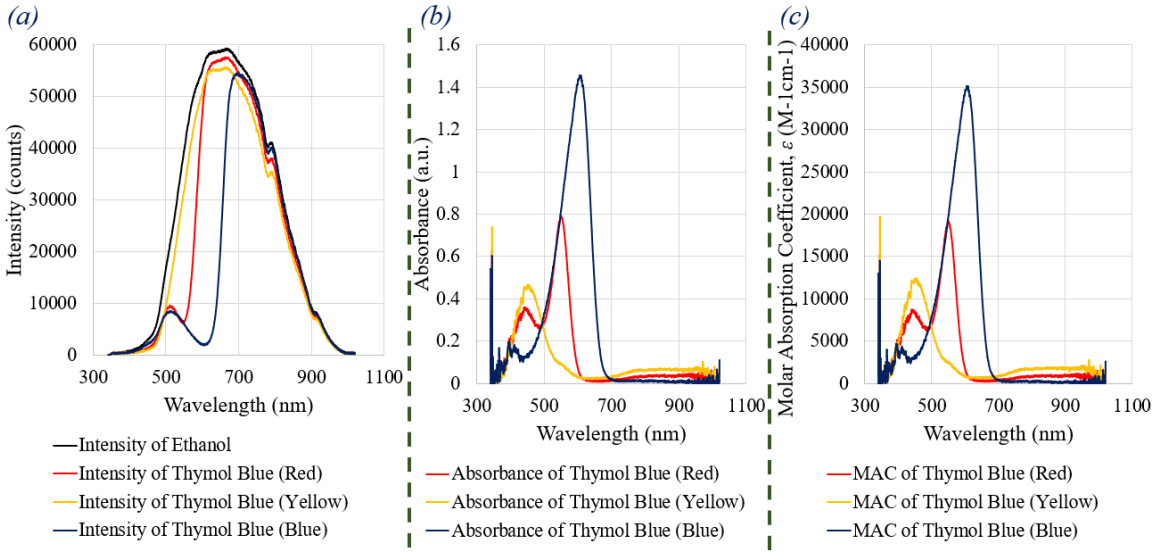


Figure 3.6: *(a) Transmission spectra (b) Absorption spectra (c) Molar absorption coefficient curve of TB for different pH values*

Figure 3.6 (c) illustrates the molar absorption coefficient (MAC) of the TB (red), TB (yellow), and TB (blue) solutions. The MAC is calculated using Eq. (3.8), Lambert-Beer law ($\varepsilon_\lambda = A_\lambda/cl$). The absorbance value is taken from Figure 3.6 (b), and the concentration value is obtained from Table 3.1. The pathlength of the cuvette is assumed to be 1 cm. To the author's knowledge, Lambert-Beer law is the best way to calculate the MAC. The MAC is 19188 $M^{-1}cm^{-1}$ at around 549 nm for TB (red). The MAC is 12439 $M^{-1}cm^{-1}$ at about 452 nm for TB (yellow). The MAC is 35144 $M^{-1}cm^{-1}$ at nearly 606 nm for TB (blue). The MAC

is ≥ 30000 $M^{-1}cm^{-1}$ at a wavelength range of 595-599 nm for TB, according to TB specification sheet [106]. The MAC value from the datasheet is close to the obtained MAC value from TB (blue). The observed MAC values are different from the specification sheet due to the experimental error. The MAC was calculated through the experiment performed in ambient conditions (room temperature), and the liquid was in a plastic (polystyrene) cuvette cell. Plastic absorbs UV light. The specification sheet of TB was taken from Sigma-Aldrich. It is not specified, but Sigma-Aldrich may calculate the MAC in standard conditions (fixed temperature), and the liquid may be in a quartz cuvette cell. Quartz doesn't absorb any light; it has greater transparency which doesn't affect measurements.

3.2.5 Film preparation

A stirrer (Stuart Hotplate Stirrer, US152, Cole-Parmer, UK) was used to mix the chemicals on each occasion. The mixture was prepared at room temperature (around 20 °C), and the heat-controlled knob of the plate was turned off during this mixing process. The speed was chosen at an arbitrary value of 1, equivalent to nearly 220 rpm, while mixing the chemicals. 1.8 ml MTEOS was stirred with 200 µl TEOS for 10 minutes in a 20 ml glass vial for preparing Ormosil solution. Next, 6 mL ethanol was added to the solution and stirred for another 10 minutes. TB powder (22 mg) was then added to the solution and stirred for another 15 minutes. Finally, 500 µl of TMAH was added to the solution, and the glass vial was covered and stirred for 1 hour using above mentioned automated stirrer before the dip-coating method [103].

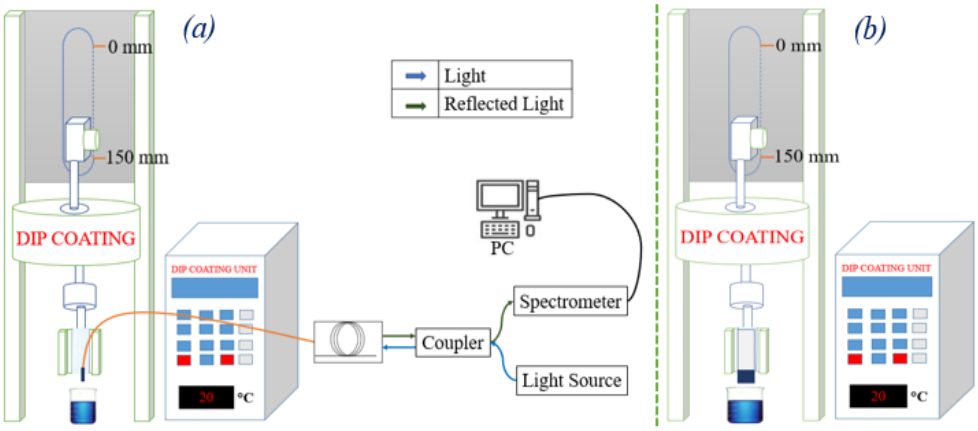


Figure 3.7: *Experimental set-up for coating process onto (a) optical fibre tip (b) glass substrate using commercial dip coating unit*

The jacket and buffer coating of the optical fibre was removed using a fibre optic stripper (JIC 375, Jonards Tools, USA). The optical fibre cladding was cleaned using IPA alcohol and clean wipes (Stickler Benchtop, MCC-WFW, Thorlabs, UK). The optical fibre tip was cleaved at 90º using a fibre-optic precision cleaver (VF-15H, Inno Instrument, Germany) and then dip-coated 4 times employing a commercial dip-coating unit (HO-TH-02, Holmarc Opto-Mechatronics Pvt. Ltd., India) with withdrawal speed of 3 mm/s, as shown in Figure 3.7 (a). The drying interval was 2 minutes between each coating layer in ambient air. Before use, the coated fibres were placed inside the pure N_2 (CO_2 and humidity free) environment for around 24 hours [103].

3.2.6 Selection process of optimum withdrawal speed

An optical fibre is made of silica (glass materials). In order to select the optimum withdrawal speed in the experimental set-up of Figure 3.7 (b), a glass substrate (GS) is deployed in place of the silica optical fibre. A GS (75 mm x 10 mm x 1 mm) also contains similar glass properties to an optical fibre. GS is transparent, and the size and shape are larger than the optical fibre tip. The fabrication process of GS doped with Ormosil is technically simple. It is much easier to observe the cracking on Ormosil coated GS during the drying process compared to the optical fibre tip.

A cleaning solution was prepared by mixing 20 ml of water with 20 ml of ethanol in a 100 ml volume glass beaker. The GS was put inside the cleaning solution. The glass beaker containing the cleaning solution was placed in an ultrasonic water bath (U50, Ultrawave, UK) for 3 minutes. The GS was cleaned by water and ethanol through this same process. Finally, the GS was left to dry in ambient air (for around 30 minutes), resulting in layer fixation. The preparation process (Section 3.2.5) of sol-gel solutions inside the glass vial was used for this experiment. In order to obtain samples with different thicknesses, the GS was dip-coated employing the commercial dip-coating unit with withdrawal speeds of 1, 2, 3, 4, 5, 6, 7, 8, and 9 mm/s 3 times, as shown in Figure 3.7 (b). The drying interval was 2 minutes between each coating layer in ambient air.

Figure 3.8 shows the thickness versus withdrawal speed curve for a precursor solution system consisting of TEOS, triethyl methyl orthosilicate, and Pluronic F-127 in ethanol on

a glass slide. The curve illustrates a minimum thickness for the withdrawal speed range of 0.1-1 mm/s when overlapping draining and capillarity regions. Thickness depends on the 2 opposing film thickness evolution regions (draining and capillarity) that were observed in this curve. If the withdrawal speed (normal range of ~ 1-10 mm/s) increases, the film thickness also rises [108]. The thick film creates the cracking, so reducing the withdrawal speed is one of the ways to remove the film cracking.

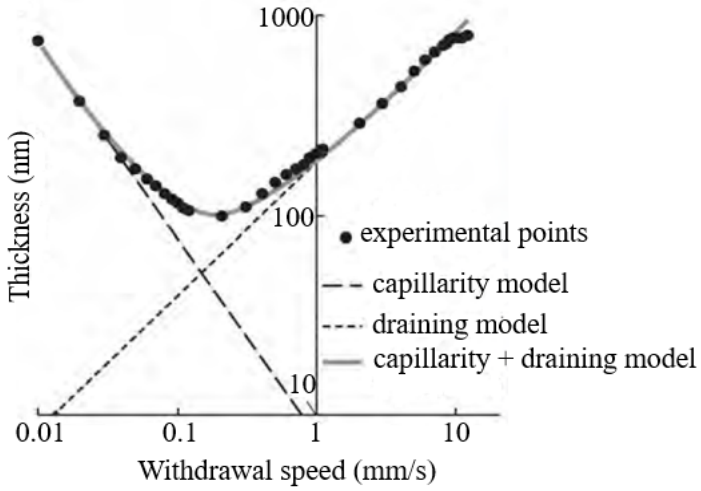


Figure 3.8: *Plot of the thickness versus withdrawal speed [108]*

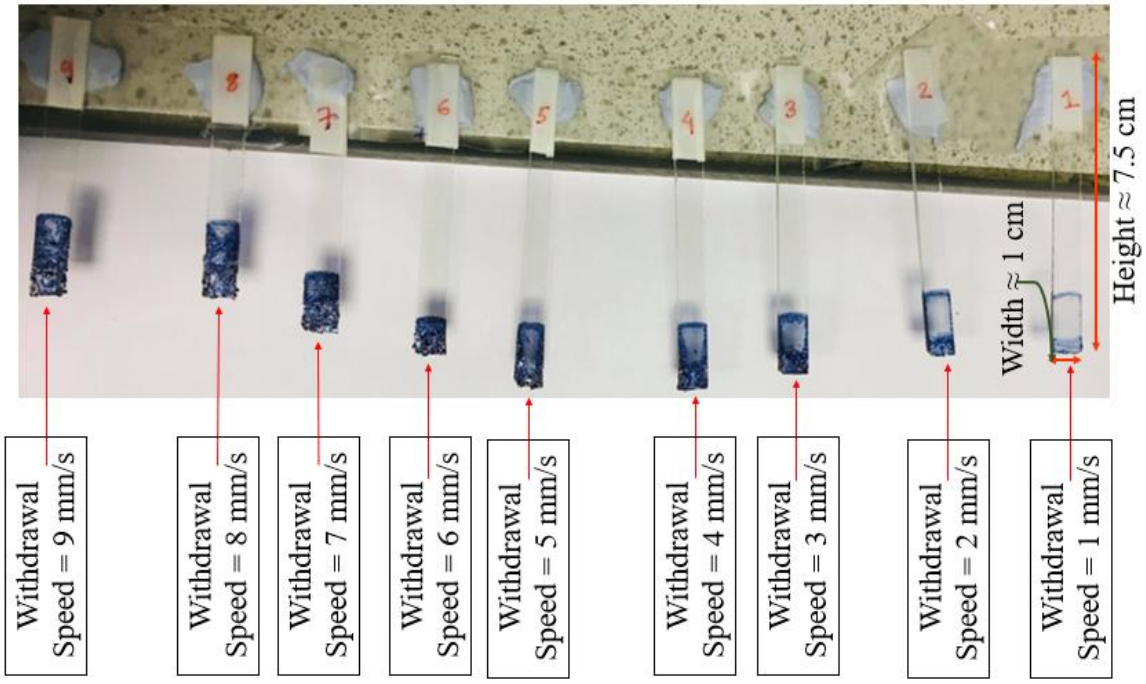


Figure 3.9: *Observation of dried GS with 3 layers after 24 hours with different withdrawal speeds*

When 1 mm/s and 2 mm/s are used for creating thin films, the thin film loses absorbance by around 24 hours. Figure 3.9 shows the effect after the drying process in ambient air for about 24 hours after coating with different withdrawal speeds. Cracking appeared on the GS the day after coating with the withdrawal speed 4, 5, 6, 7, 8, and 9 mm/s. So, 3 mm/s is chosen as an optimum withdrawal speed enabling a thick film while minimising cracking.

Figure 3.10 illustrates the images of dried GS without and with cracking, where it is visible that the bottom part of GS suffers from cracking. The purpose of Figure 3.10 is to show how the GS looks like with and without cracking. Both GSs have a withdrawal speed 3 mm/s. GS without cracking was observed from the coated GS with 3 layers on the coating day. Oppositely, GS with cracking was observed from the dried GS with 3 layers after 24 hours.

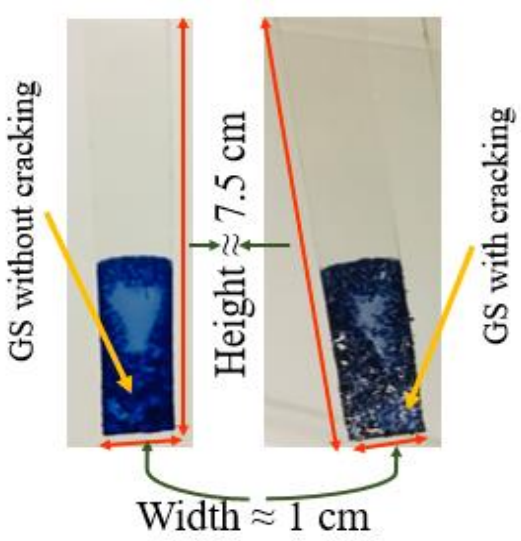


Figure 3.10: *Zoom view of dried GS without and with cracking*

3.3 Sensor characterisation

3.3.1 Experiment set-up

In Figure 3.11, a halogen light source (HL-2000, Ocean Insight, UK) is linked to a MM fibre optic attenuator (Fixed / Variable, Thorlabs, UK) through an SMA fibre optic patch cable (M92L01, core diameter, Ø 200 µm, cladding diameter, Ø 220 µm, Thorlabs, UK). The OFCS tip is illuminated by a halogen light source through a 1 x 2 MM Coupler 50/50

(core diameter, Ø 62.5 µm, cladding diameter, Ø 125 µm, ideal loss/port 3 dB, Lightel, USA) and the reflected light is captured using an optical spectrometer (FLAME-S-VIS-NIR-ES, optical resolution ~ 0.1-10 nm, Ocean Insight, UK) which is linked to a computer for data analysis.

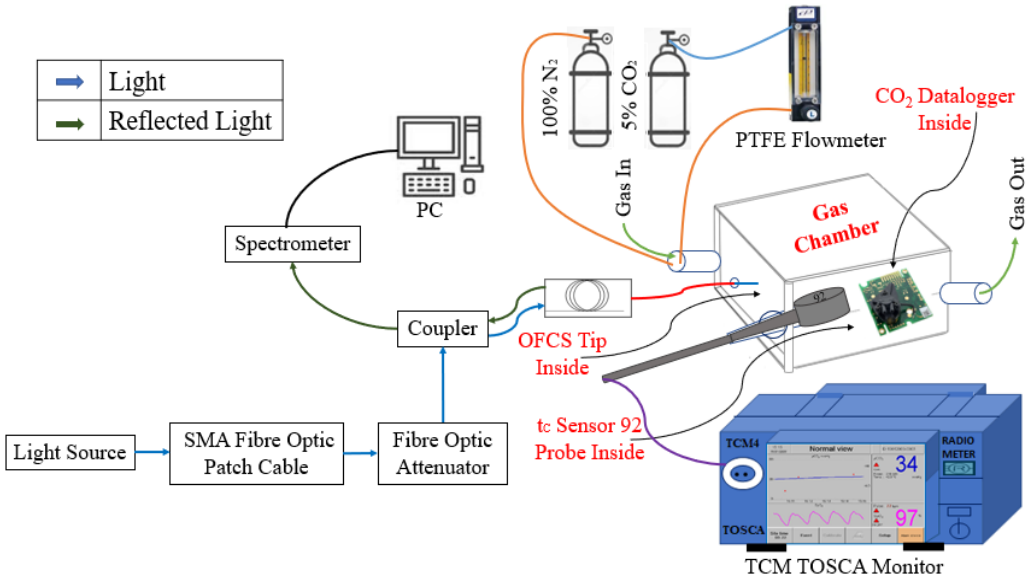


Figure 3.11: *Experimental set-up for CO_2 calibration of OFCS*

The t_C Sensor 92 probe and commercial CO_2 datalogger independently measure the PCO_2 values and CO_2 concentrations in the gas chamber. The t_C Sensor 92 probe is connected to the TCM TOSCA monitor, which is used to visualise the data and obtain the results. The OFCS, t_C Sensor 92 probe, and commercial CO_2 datalogger are housed inside a custom-made gas chamber (270 mm (L) x 195 mm (W) x 105 mm (H), BPA free plastic airtight container, Nisbets Plc., UK) with an input route and output route for gas inclusion and exclusion. N_2 and CO_2 gas mixture controlled the CO_2 concentration inside the gas chamber. The reflection intensity of the OFCS, CO_2 concentration (from the commercial CO_2 datalogger), and PCO_2 value (from the t_C Sensor 92 probe) were recorded using SpectraSuite Software, Gaslab Software, and the TCM TOSCA monitor, respectively during the experiment.

Pure N_2 gas was flushed inside the gas chamber until the CO_2 concentration becomes 0 ppm before the experiment commences. A polytetrafluoroethylene (PTFE) flowmeter (WZ-03216-52, Cole-Parmer, UK) was used to control the step-by-step variation of CO_2 concentration inside the gas chamber via the "gas-in" route. At least 10 minutes was needed

for the CO_2 concentration inside the gas chamber to stabilise. The reflection spectrum of the OFCS, CO_2 concentrations, and PCO_2 values (used for reference purposes) were recorded with a frequency of 1, 0.05, and 0.1 Hz, respectively. The minimum data recording interval was 20 seconds for the commercial CO_2 datalogger and 10 seconds for the t_C Sensor 92 probe. The integration time and data recording interval were chosen for the OFCS as 1 second to get enough data to plot the OFCS's response.

The formula of Absorbance, *A* is given below [103]:

$$A = 2 - log_{10}\left[\left(\frac{I_r}{I_0}\right) \times 100\right] \qquad (3.10)$$

where I_0 is the light intensity reflected from the optical fibre tip without any film, and I_r is the light intensity after interaction with the coated film [103].

3.3.2 Results

Figure 3.12 demonstrates a typical reflection spectrum after each coating cycle on the optical fibre tip during the coating process. Interference fringes for 1 layer and 2 layers of coating can be seen. The coated layer on the optical fibre tip creates an FPI cavity. FPI fringes can be visible due to the differential phase of reflected light between the optical fibre interface to the coated thin film and the interface of the coated thin film to ambient air. The absorption window was selected from 500 nm to 700 nm according to TB's absorption characteristics [109]. The fringes become less visible for 3 layers and 4 layers of coating, as shown in Figure 3.12. The interference fringes disappear when the thicker sol-gel coating or layers make the large path difference between the fibre and film. A continuous distribution of inference fringes with a range of phase differences that "average" to zero will generate due to the large path difference. As a result, the fringe visibility decreases [110]. Due to the increased absorption value induced by the thick film based on Eq. (3.10), the reflected intensity at a wavelength of around 600 nm diminishes as each layer is deposited [103].

Figure 3.13 (a) shows the reflection spectrum of a BF and the 4th layer coated optical fibre tip for drying in the pure N_2 (CO_2 and humidity free) environment after around 24 hours. During the drying process, the walls of the pores combine, and the pore size minimises due to the capillary forces on the pores' walls. As a result, a structural collapse occurs due to

the normal drying of the gel [111]. As the cavity length (film thickness) rises, the number of fringes increases after each layer coating. At the 4th layer, the fringe visibility diminishes, and the fringes will disappear due to the further increment number of coating cycles [108]. In Figure 3.13 (b), the absorbance is calculated by putting the reference signal (from the reflection spectrum of the BF) in Eq. (3.10), and the highest absorption peak is achieved at a wavelength of around 600 nm.

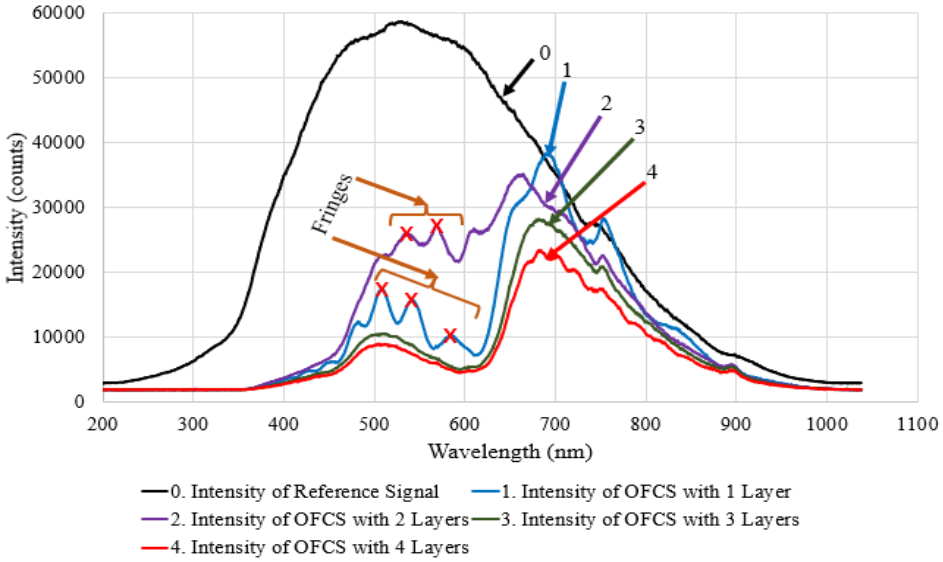


Figure 3.12: *Reflection spectrum of OFCS after coating*

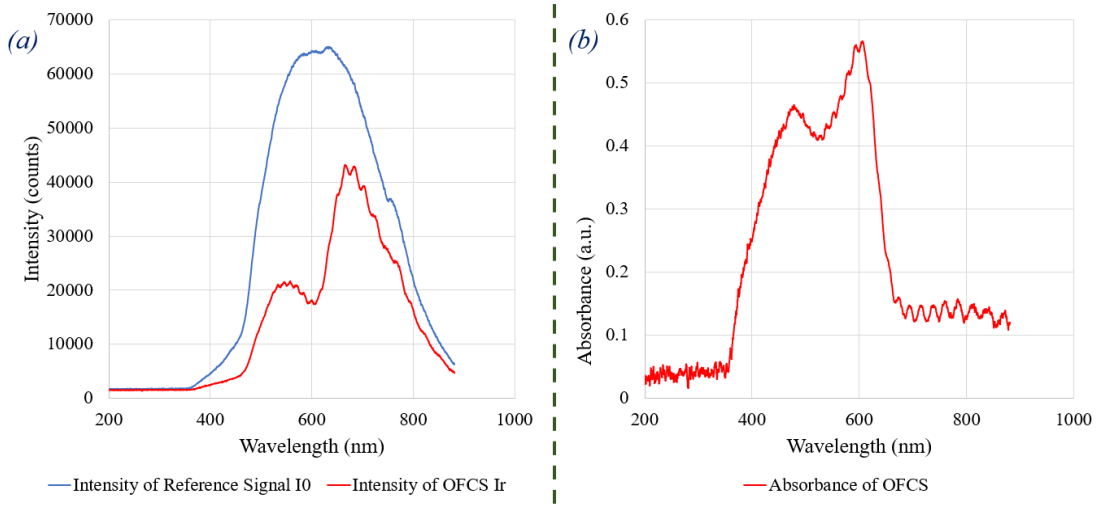


Figure 3.13: *(a) Reflection spectrum of OFCS including reflection spectrum of bare fibre (b) Absorption spectrum of OFCS with 4 layers after drying for 24 hours*

An example of calculating the absorbance from the OFCS w.r.t. BF (Figure 3.13) using Eq. (3.10) is as follows:

Reflection intensity of OFCS at wavelength 600 nm = 18122 counts

Reflection intensity of BF at wavelength 600 nm = 64217 counts

Absorbance at 600 nm, $A_{600\ nm} = 2 - \log_{10}[(18122 \text{ counts} / 64217 \text{ counts}) \times 100] = 0.549$

Figures 3.14 (a) and (b) illustrate the reflection spectrum of the BF, the reflection and absorption spectra of the OFCS for maximum (45000 ppm or 4.5% CO_2) and minimum (0 ppm or 0% CO_2) CO_2 concentration, respectively. The highest absorption peak due to the changes for CO_2 concentrations is achieved at a wavelength of around 600 nm, as shown in Figure 3.14 (b). A noticeable change in reflection intensity and absorbance at a wavelength of around 600 nm is observed and hence about 600 nm has been used for CO_2 detection and measurement.

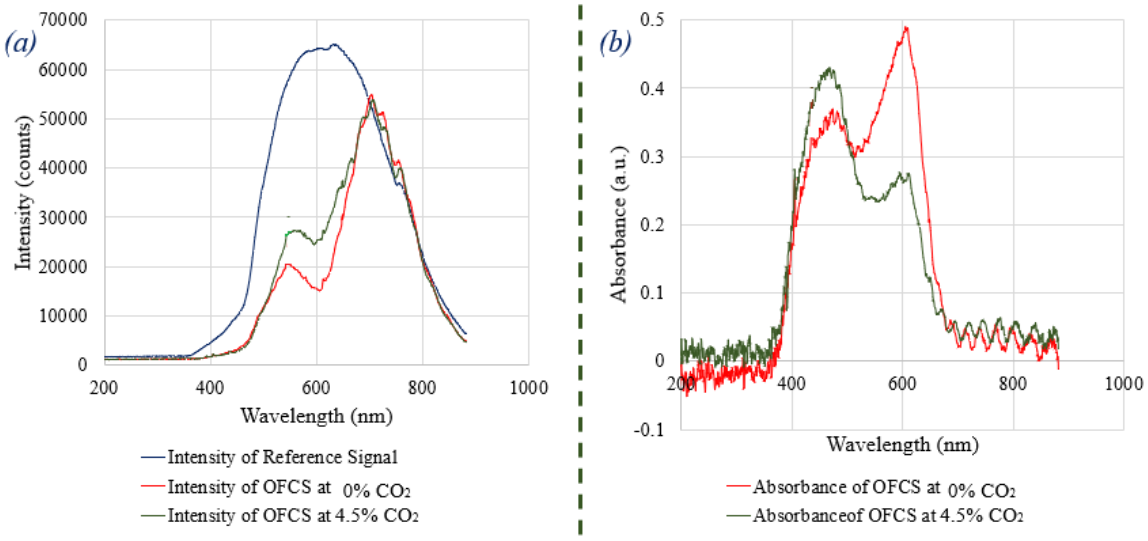


Figure 3.14: *(a) Reflection spectra of OFCS including reflection spectrum of bare fibre (b) Absorption spectra of OFCS with 4 layers for maximum and minimum CO_2 concentration*

Figures 3.15 (a) and (b) show the reference signals, which are reflected from the BFs' tip for the step up and step down response, respectively and those reference signals were used to calculate the absorbance using Eq. (3.10). The intensity of one BF is 61700 counts for step up response and the intensity of another BF is 54814 counts for step down response at a wavelength of 600 nm. Those responses of the BFs are achieved using the same experimental set-up with the same equipment, as detailed in Section 3.3.1. The reflection

spectrum of the BF was recorded with an integration time of 1 second using SpectraSuite Software.

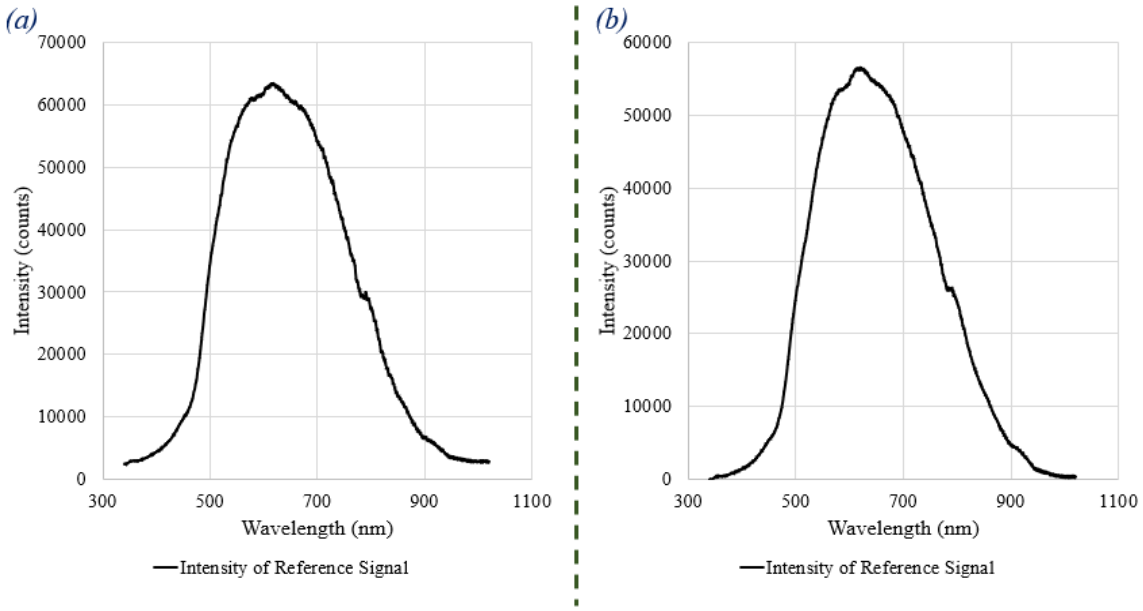


Figure 3.15: *Reflection spectrum of bare fibre for (a) step up (b) step down response of OFCS*

Figures 3.16 (a)-(d) show the step up and step down response of the OFCS to the CO_2 concentration and PCO_2 value measured (from the commercial CO_2 datalogger and t_C Sensor 92 probe, respectively) using the set-up, as shown in Figure 3.11, respectively. The reflection intensity of the OFCS at a wavelength of around 600 nm varies according to the variation of CO_2 concentrations from the commercial CO_2 datalogger and the shift of PCO_2 value from the t_C Sensor 92 probe. In Figures 3.16 (a) and (c), the reflection intensity and absorbance of OFCS increases and decreases with rising CO_2 concentration from 0 ppm (0% CO_2) to around 46000 ppm (4.6% CO_2), respectively. The PCO_2 value changes from 0 mmHg to 31.5 mmHg during the CO_2 measurement inside the gas chamber. In Figures 3.16 (b) and (d), the reflection intensity of the OFCS and absorbance decreases and increases with falling CO_2 concentration from around 53000 ppm (5.3% CO_2) to 0 ppm (0% CO_2), respectively. The PCO_2 value changes from 44 mmHg to 0 mmHg during the CO_2 measurement inside the gas chamber.

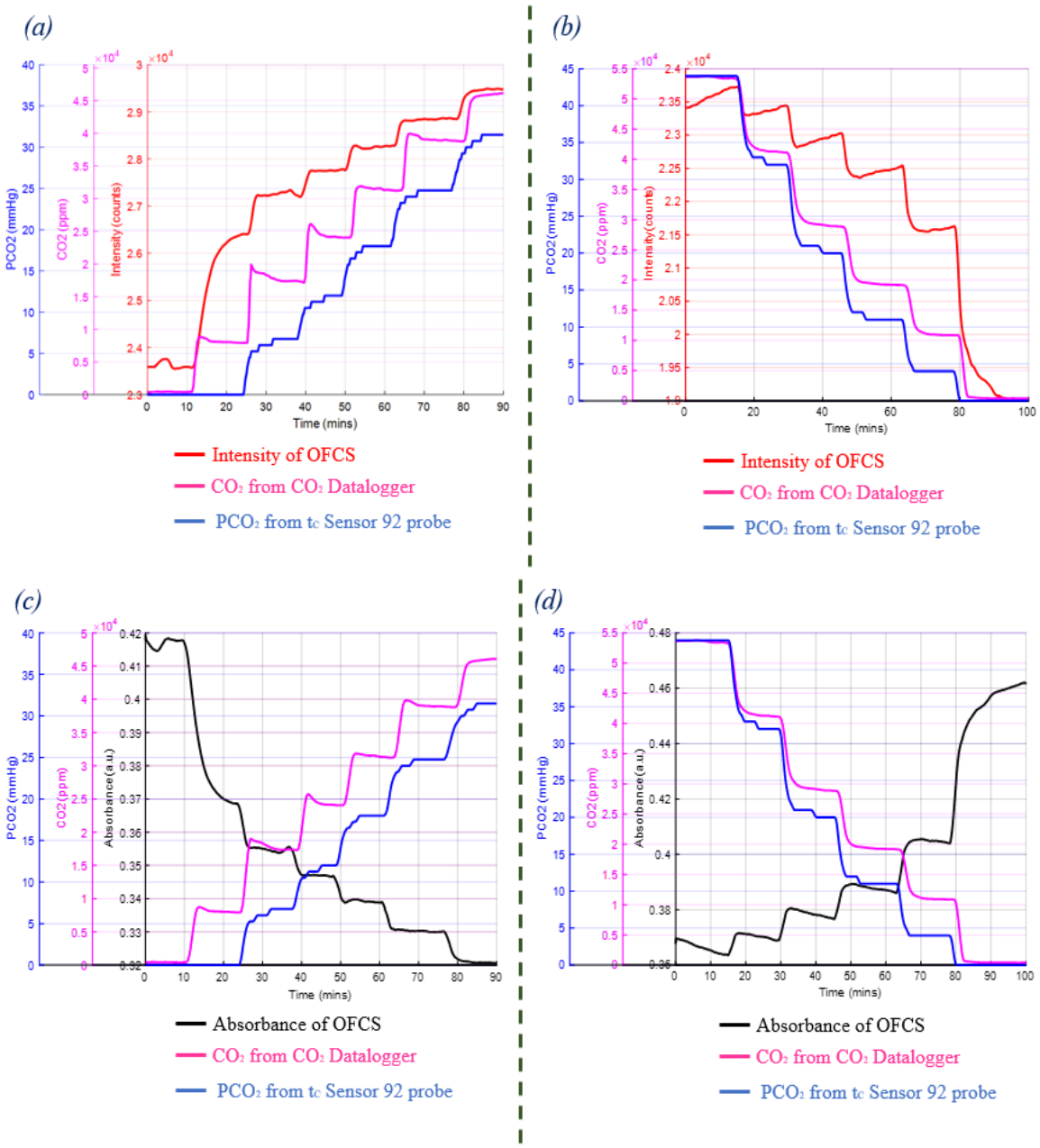


Figure 3.16: *(a) Step up response w.r.t. reflection intensity (b) Step down response w.r.t. reflection intensity (c) Step up response w.r.t. absorbance (d) Step down response w.r.t. absorbance response of OFCS modified with sol-gel coating to different CO_2 concentrations with changing PCO_2 values at wavelength 600 nm*

Figure 3.17 shows the reference signal, which is reflected from the BF's tip for the reversibility of OFCS and this reference signal was used to calculate the absorbance using Eq. (3.10). The intensity of the BF is 56995 counts at a wavelength of 600 nm. This response of the BF is achieved using the same experimental set-up, as detailed in Section 3.3.1. The reflection spectrum of the BF was recorded with an integration time of 1 second using SpectraSuite Software.

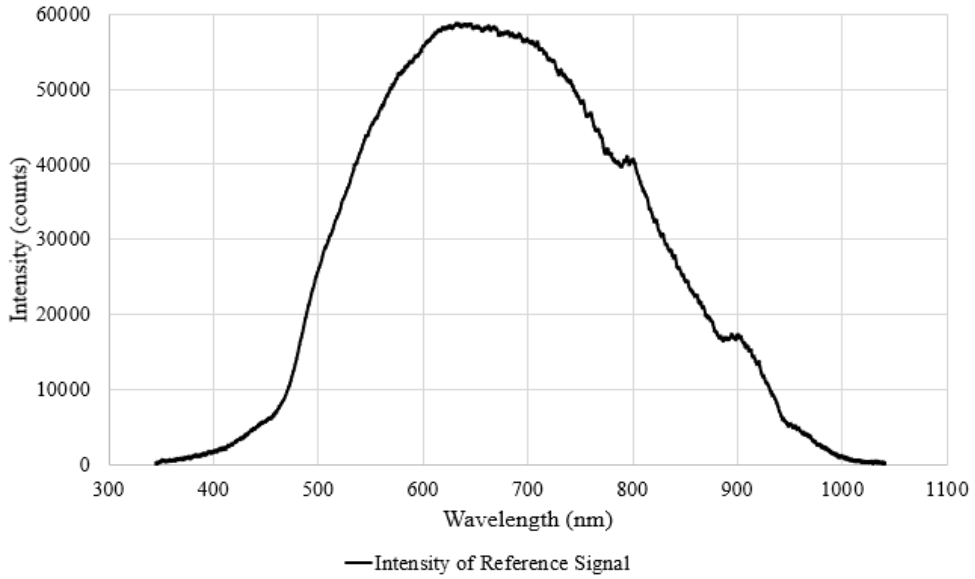


Figure 3.17: *Reflection spectrum of bare fibre for reversibility of OFCS*

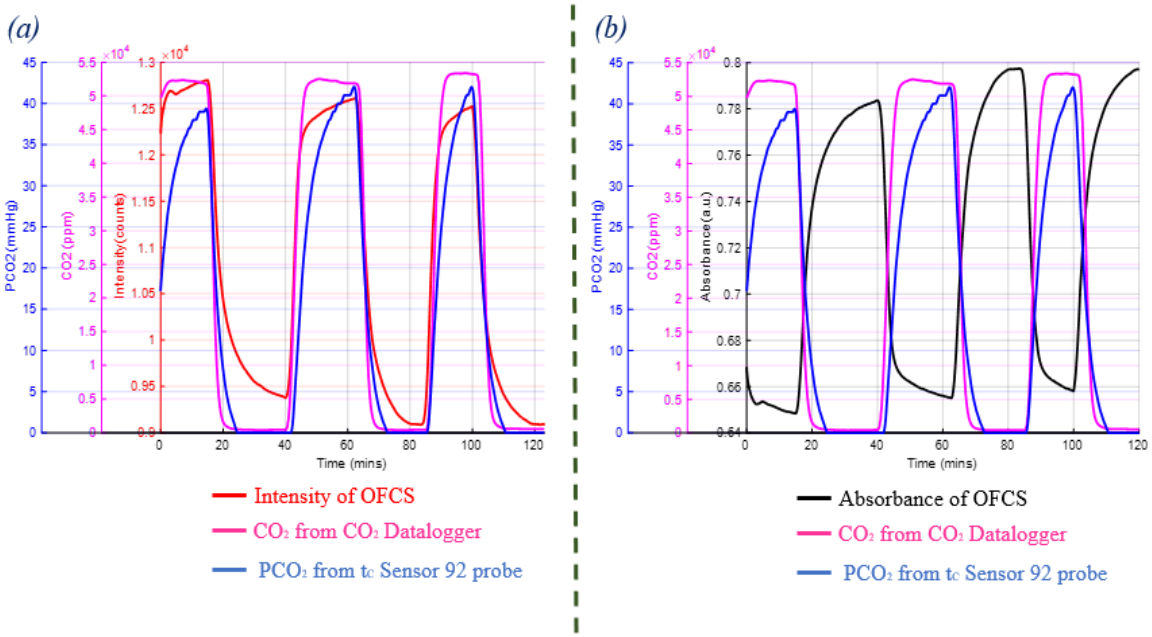
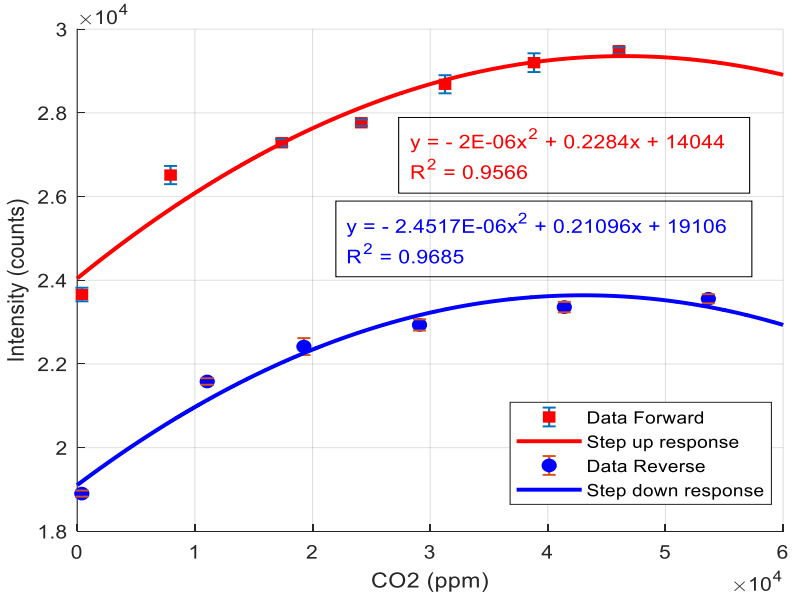


Figure 3.18: *Reversibility ((a) w.r.t. reflection intensity (b) w.r.t. absorbance) of OFCS different CO_2 concentrations with changing PCO_2 values at wavelength 600 nm*

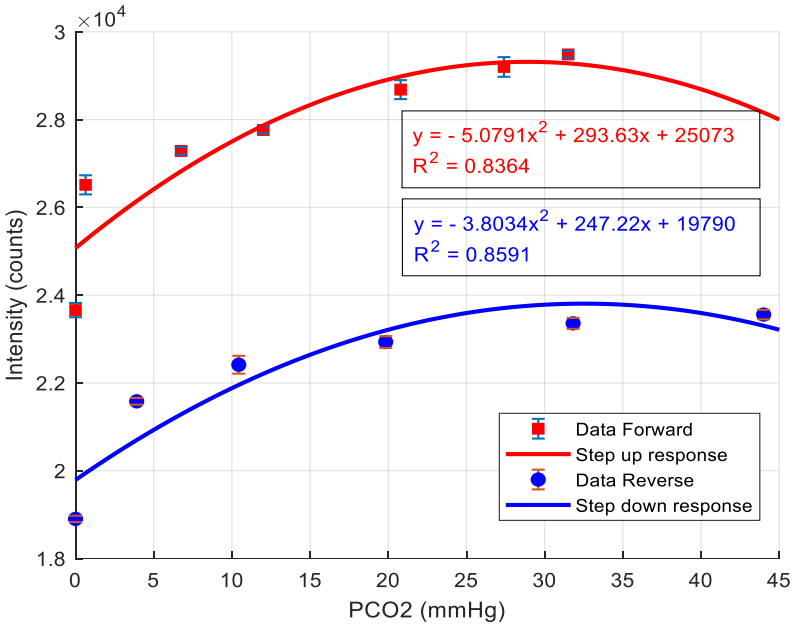
The reflection intensity and absorbance of the OFCS declines and rises with decreasing CO_2 concentration from nearly 50000 ppm (5% CO_2) to 0 ppm (0% CO_2), respectively. The reflection intensity and absorbance of the OFCS rises and declines with increasing CO_2 concentration from 0 ppm (0% CO_2) to almost 50000 ppm (5% CO_2) again, respectively. The PCO_2 value varies between the window of 0 mmHg and around 40 mmHg. The repeatability and reversibility of the response (reflection intensity and absorbance) of the OFCS at a wavelength of around 600 nm are shown in Figures 3.18 (a) and (b).

Figures 3.19 (a) and (b) show how the average reflection intensity is related to the average value of CO_2 concentration and PCO_2 via a polynomial fitting curve, respectively. Next, Figures 3.19 (c) and (d) illustrate how the average absorbance is associated with the average value of CO_2 concentration and PCO_2 via a polynomial fitting curve, respectively. Similarly, Figure 3.19 (e) demonstrates how the average value of PCO_2 is associated with the average value of CO_2 concentration via a polynomial fitting curve.

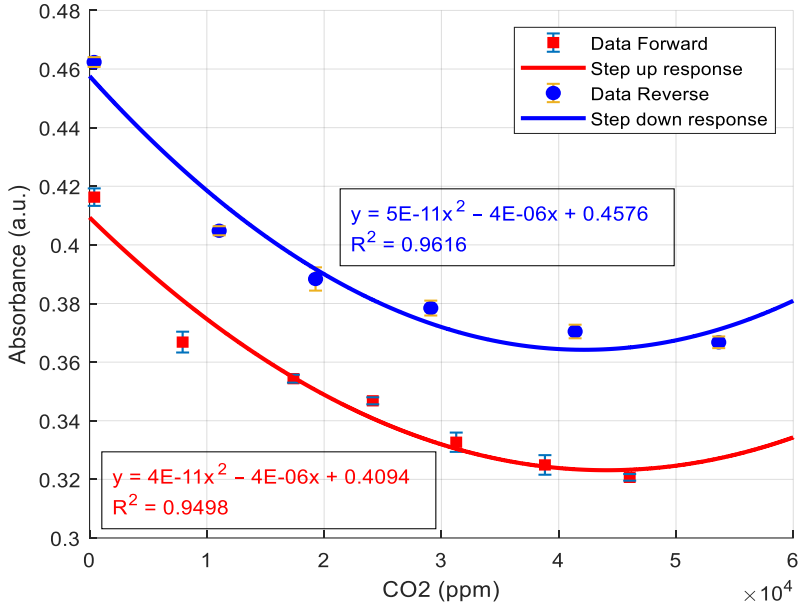
(a)



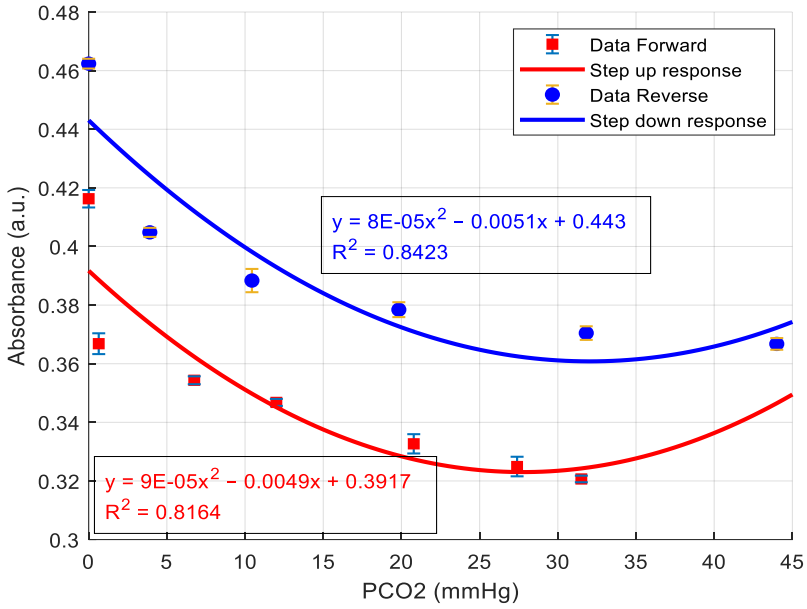
(b)


×10^4
3
2.8
2.6
2.4
2.2
2
1.8
Intensity (counts)
0
5
10
15
20
25
30
35
40
45
PCO2 (mmHg)
y = - 5.0791x^2 + 293.63x + 25073
R^2 = 0.8364
y = - 3.8034x^2 + 247.22x + 19790
R^2 = 0.8591
Data Forward
Step up response
Data Reverse
Step down response

(c)


0.48
0.46
0.44
0.42
0.4
0.38
0.36
0.34
0.32
0.3
Absorbance (a.u.)
0
1
2
3
4
5
6
CO2 (ppm)
×10^4
Data Forward
Step up response
Data Reverse
Step down response
y = 5E-11x^2 – 4E-06x + 0.4576
R^2 = 0.9616
y = 4E-11x^2 – 4E-06x + 0.4094
R^2 = 0.9498

(d)



(e)

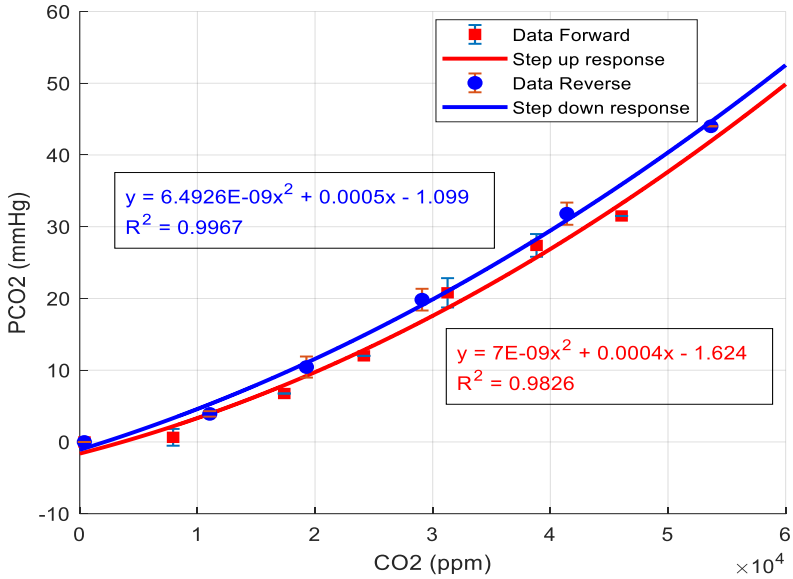


Figure 3.19: *Polynomial fitting of (a) reflection intensities of OFCS to different CO_2 concentrations (b) reflection intensities of OFCS to different PCO_2 values (c) absorbances of OFCS to different CO_2 concentrations (d) absorbances of OFCS to different PCO_2 values and (e) PCO_2 values of t_C Sensor 92 probe to different CO_2 concentrations at wavelength 600 nm*

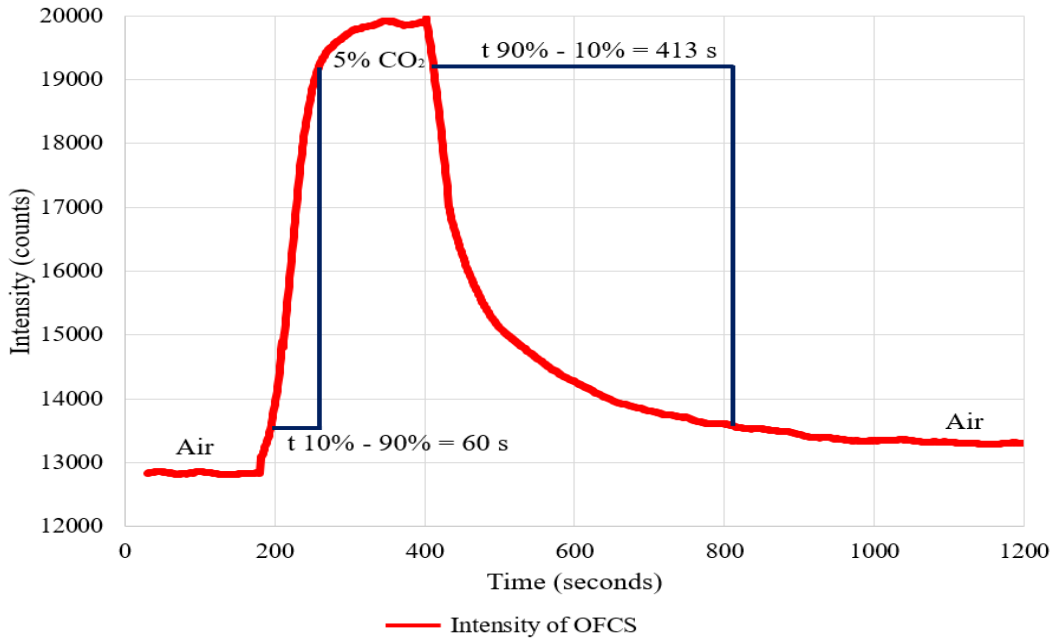


Figure 3.20: *Response and recovery times measurement of OFCS for 5% CO_2 at wavelength 600 nm*

The calculation of response and recovery times of the OFCS at a wavelength of around 600 nm is illustrated in Figure 3.20. The response time was calculated when the OFCS was inserted into gas chamber with 50000 ppm (5% CO_2) from ambient air (around 400 ppm). The recovery time was measured when the OFCS was taken out from the gas chamber 50000 ppm (5% CO_2) to ambient air (nearly 400 ppm). The response time of the OFCS is 60 seconds, which is the time required to rise from 10 % to 90 % of the final value of reflection intensity. However, the recovery time of the OFCS is 413 seconds which is the time required to drop from 90 % to 10 % of the final value of reflection intensity.

The response time is shorter than the recovery time as there are more active binding sites before measuring CO_2. CO_2 molecules quickly bind with the absorbing sites from lower to higher CO_2 concentrations. On the other hand, CO_2 molecules diffuse for a long time through the membrane surface (depending on film thickness and pore size) from higher to lower CO_2 concentrations [43]. Removing the sensor to ambient created a step change in CO_2, in future this could be flushed in an N_2 environment to achieve close to 0 ppm, but care would need to be taken to ensure rapid flushing so that the recovery time is not overestimated.

3.3.3 Discussion

To optimise the signal return from the OFCS, it is important that the absorbance is high enough to create measurable signal changes proportional to CO_2 but not too high to leave the reflected light undetectable. It is beneficial to consider the reflection intensity of the coated film after each layer of coating. When the number of layers increases, film thickness rises; consequently, the reflected intensity at a wavelength of around 600 nm declines, as shown in Figure 3.12. The absorbance will increase due to film thickness increment, according to Eq. (3.10). It was observed that if the film thickness increases too much (> 12 µm), the reflection intensity at a wavelength of 600 nm is below the detection threshold. Another visual observation is that if the film thickness increases too much (> 12 µm), the film starts cracking, and the absorbance band at 600 nm is lost. So, the optimum film thickness selection is based on observing the lowest reflection intensity (above 0 counts) while avoiding film cracking.

Still, the dip coating method is a suitable option for fabricating the OFCS. The thicker film can be achieved while avoiding cracking by raising the dye concentration and reducing the withdrawal speed using the dip coating method [108] [112]. Different additives, such as ethylene glycol, can be used in the sol-gel recipe, preventing the evaporation of base catalyst (TMAH is volatile) from sol-gel coatings. In my work, the minimum time (2 minutes) was chosen for curing between each layer.

Another layer may be put on the next day (after 24 hours) once the previous layer has dried, but there is a risk of reducing the layer's sensitivity. If the curing time chosen between each layer is long (such as 24 hours or the next day), TMAH will decompose, and the pH of the sensing layer will decrease. The OFCS containing TB on the fibre tip initially has a blue active layer, which first turns green and then yellow, and this colour change is related to the decrement of the layer's sensitivity to CO_2. This way, the coated layer will react with CO_2 and decrease the layer's sensitivity. TMAH will also evaporate from the layer of the sol-gel coating, and there will be an interaction between the layer and other chemicals in the ambient air [112].

The film thickness can be calculated from the fringes using the following expression [113]:

$$d = \frac{\Delta m}{2\sqrt{n^2 - sin^2\theta}} \times \frac{1}{(\lambda_1 - \lambda_2)} \quad (3.11)$$

$sin^2\theta$ can be expressed using Eq. (2.14):

$$NA = sin\theta = \sqrt{n^2{}_{core} - n^2{}_{cladding}}$$

$$\Longrightarrow sin^2\theta = n^2{}_{core} - n^2{}_{cladding}$$

By placing ($n^2{}_{core}$ - $n^2{}_{cladding}$) instead of $sin^2\theta$ in Eq. (3.11)

$$\Longrightarrow d = \frac{\Delta m}{2\sqrt{n^2{}_{film} - (n^2{}_{core} - n^2{}_{cladding})}} \times \frac{1}{(\lambda_1 - \lambda_2)}$$

$$\Longrightarrow d = \frac{\Delta m}{2\sqrt{n^2{}_{film} - n^2{}_{core} + n^2{}_{cladding}}} \times \frac{1}{(\lambda_1 - \lambda_2)} \quad (3.12)$$

where d is the film thickness, Δm is the number of peaks in the wavelength range used for calculation, n is the refractive index of the film (n_{film}), n_{core} is the refractive index of the fibre core, $n_{cladding}$ is the refractive index of the fibre cladding, θ is the angle of incidence, and λ_1 and λ_2 are the start and end wavelengths in the wavelength range used for calculation [92] [113]. The value of the parameter which is used in Eq. (3.12) is provided in Table 3.2.

Table 3.2: *Film Thickness of the layers from the fringes observed in Figure 3.12*

Layer number	Number of peaks or fringes, Δm	Start wavelength, λ_1 (nm)	End wavelength, λ_2 (nm)	Film thickness (μm)	Refractive Index, n		
					n_{film}	n_{core}	$n_{cladding}$
1	3	508	587	3.835	1.501 [109]	1.475 [114]	1.45 [115]
2	2	536	569	6.259			

The film thickness is extracted from the number of fringes from 1 layer and 2 layers of OFCS from Figure 3.12. The film thickness of 3 and 4 layers can't be extracted from Figure 3.12 due to no visible fringes in those layers at a wavelength range of 508-587 nm. The film thickness obtained from the SEM images of other OFCSs is used in an FPI simulation. In Figure 3.12, the OFCS of 1 layer and 2 layers have a film thickness of 3.835 μm and 6.259 μm, respectively. Conversely, in Figures 3.35-3.37, the SEM images of the 3 OFCSs

(OFCS 1-3) of 1, 2, and 3 layers have a film thickness of 4.888, 5.690, and 7.234 µm. Those film thickness values have differences from each other because they all are different sensors (OFCSs).

The responses (reflection intensity and absorbance) are different from the step up and step down response of Figures 3.16 (a)-(d) because this is the response from 2 different OFCSs fabricated on different days. Figures 3.16 (a) and (c) are obtained from one OFCS, and Figures 3.16 (b) and (d) are obtained from another OFCS. The polynomial equation and R^2 are almost the same for the increasing and decreasing trend, according to Figures 3.19 (a)-(e). So, the OFCSs worked in the same way because using the same fabrication method, but the reflection intensity values are different because of the changes (such as dye concentration increases due to the sol-gel matrix's volume shrinks) in film properties after drying. It is worth noting that although the polynomial fitting provides a good fit it does result in an ill-conditioned relationship i.e. 1 value of intensity correspond to 2 values of CO_2.

The OFCS reveals a moderate diminution in reflection intensity with every single day after the OFCS is fabricated. The OFCS loses its capability for sensing CO_2 within 10-15 days when stored in ambient air because of the decomposition of the base catalyst (TMAH) inside the film; the air toxicity to the sensing film and pH of the sensing film decreases slowly. The OFCS's shelf life (> 15 days) and stability in reflectivity may be considerably increased by storing the OFCS in pure N_2 [103].

The shaped glass and ceramics are fabricated using the sol-gel process. Although the sol-gel process is a lower-temperature preparation method and very appealing compared to traditional melting approach it still has drawbacks. For example, the emergence of cracks in the monolithic gel during the drying period is regarded as the most problematic [116]. The physical property of the gel varies during the ageing and drying process [117]. The thin film is created by Ormosil on the optical fibre tip using the sol-gel method. Sometimes the severe cracks appear from dried gel and defects during the storage period. This cracking caused the OFCS absorbance feature to be lost within a few days.

3.4 Cross-sensitivity of an OFCS

Temperature or humidity may affect the performance of an OFCS. So, it is essential to perform different tests to observe the response of an OFCS for temperature and humidity levels.

3.4.1 Temperature cross-sensitivity of an OFCS

Temperature cross-sensitivity of an OFCS was performed previously in Reference [109]. The average normalised intensity of a wavelength range of 595-617 nm was used for measuring CO_2 by varying different temperatures [109]. The following characterisation experiments follow this methodology.

In Figure 3.21, an OFCS is placed inside a gas chamber (15 cm (L) × 13 cm (W) × 8 cm (H)) with a humidity and temperature sensor (K33, CO2Meter.com, USA) and a temperature-controlled heating mat (TCHM). The TCHM was prepared by combining a heating mat (diameter = 50 mm), a J-type thermocouple, and a controller (IR33, Carol, UK). The OFCS was placed on the top of the heating mat and put inside the gas chamber for performing temperature calibration of the OFCS. The spectral information of the OFCS was obtained using a halogen light (HL-2000, Ocean Insight, UK) and a spectrometer (USB 2000, Ocean Insight, UK). N_2 and CO_2 gas mixture controlled the CO_2 concentration inside the gas chamber with the help of the PTFE flowmeter [109].

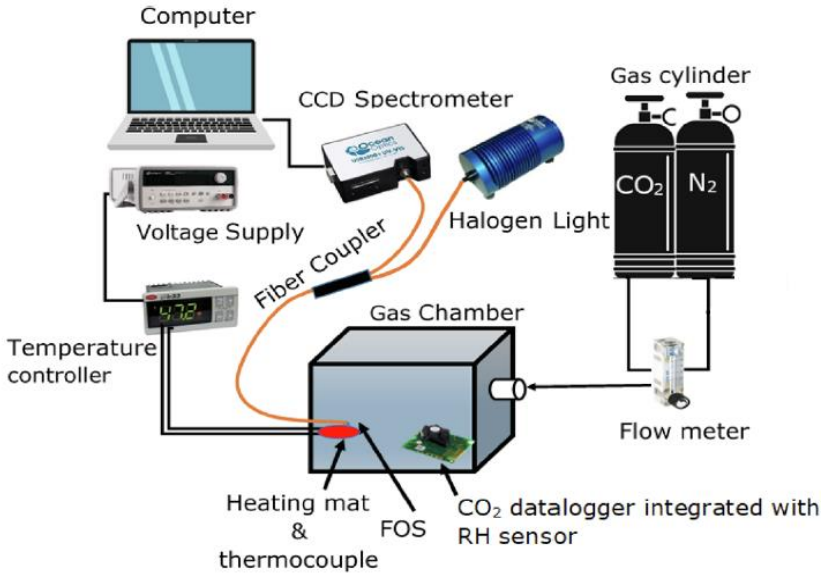


Figure 3.21: *Experimental set-up for temperature calibration of OFCS [109]*

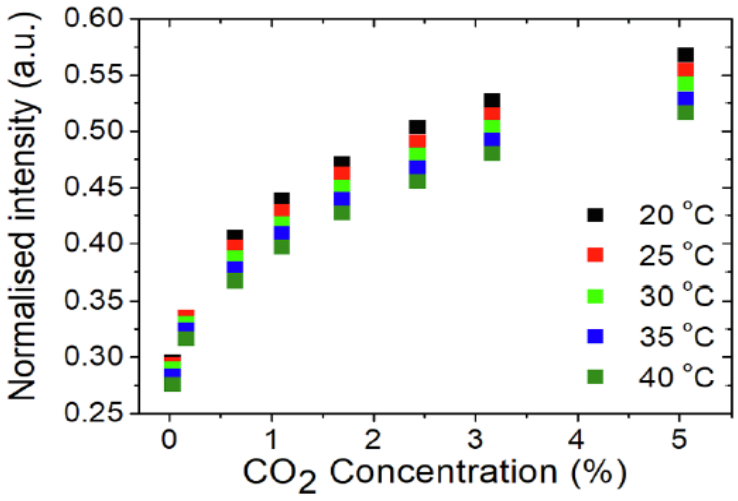


Figure 3.22: *Average normalised intensity value of OFCS to different CO_2 concentrations with changing temperature values at wavelengths 595-617 nm [109]*

In Figure 3.22, the changes in average normalised intensity value between wavelengths of 596-617 nm of the dye (thymol blue) were observed at varying temperatures (20 °C to 40 °C) and the CO_2 concentrations. The normalised intensity decreases by approximately 6 % at 0.03% CO_2, and the normalised intensity drops by about 9 % at 5% CO_2 when the temperature increases from 20 °C to 40 °C. The temperature effect depends on the CO_2 concentrations. Generally, the temperature effect is negligible at a stable room temperature [109].

3.4.2 Humidity cross-sensitivity of an OFCS

The response of an OFCS is affected by relative humidity. The OFCS is used for measuring the skin CO_2 due to the skin being a high area of humidity on the body. The ideal RH for human skin is around 50 % [118]. The OFCS is tested inside an environmental chamber to observe the response of the OFCS due to the RH variation.

In Figure 3.23, the same experimental set-up is used with the same equipment, as detailed in Section 3.3.1. The OFCS was placed inside an environmental chamber (Bench Top, C-TH40-20/1, CVMS Climatic, UK) for RH calibration (up to 90% RH). The environmental chamber can be controlled manually for step-by-step variation from 50 % to 90 %. The reflection spectrum of the OFCS was recorded with an integration time of 1 second using

SpectraSuite Software. The RH values were noted down manually every 1 minute from the environmental chamber during the experiment. The temperature inside the environmental chamber was controlled at 35 °C (similar to normal human body temperature).

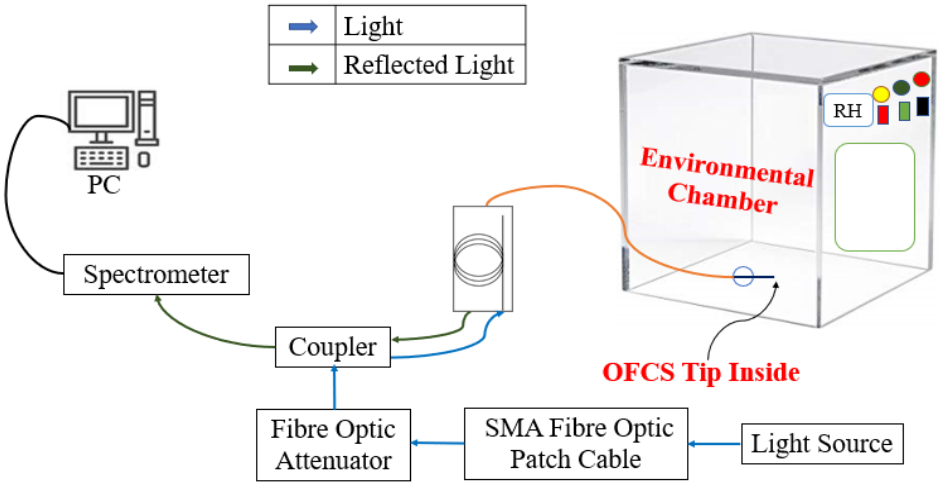


Figure 3.23: *Experimental set-up for RH calibration of OFCS*

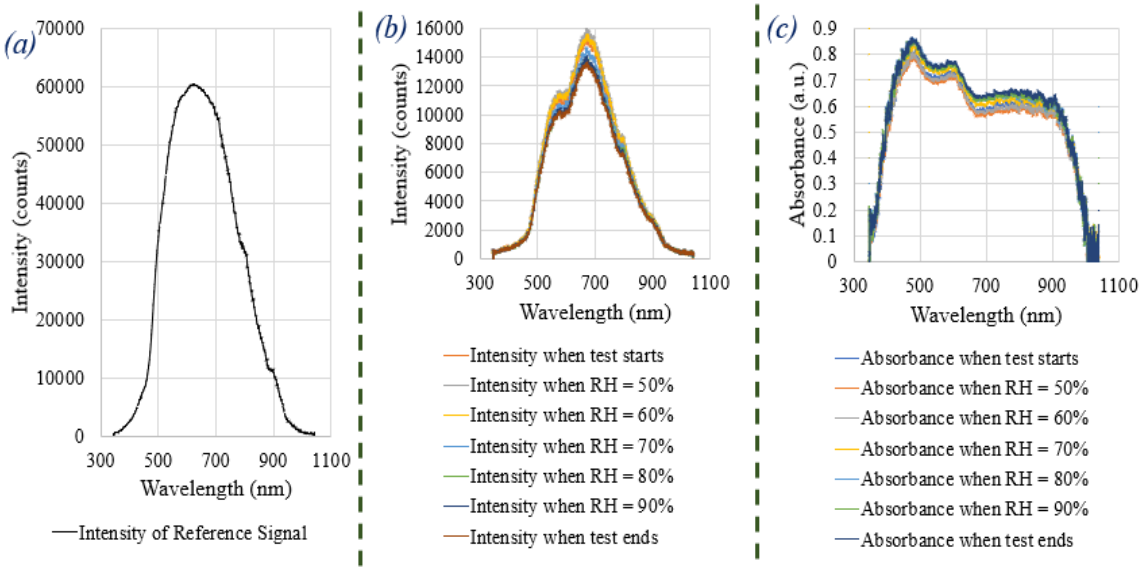


Figure 3.24: *(a) Reflection spectrum of bare fibre (b) Reflection spectra (c) Absorption spectra of OFCS to different RH values*

Figure 3.24 (a) shows the reference signal, which is reflected from the BF's tip, and this reference signal was used to calculate the absorbance using Eq. (3.10) in Figures 3.25 (b) and 3.27 (b). The intensity of the BF is 59328 counts at a wavelength of 600 nm. The reflection spectrum of the BF was recorded with an integration time of 1 second using SpectraSuite Software. Figures 3.24 (b) and (c) illustrates the reflection and absorption

spectra of the OFCS for the maximum (90% RH) and minimum (50% RH) limit of RH level, respectively, using the set-up, as shown in Figure 3.23. The reflection intensity decreases, and absorbance increases due to the increment of RH values.

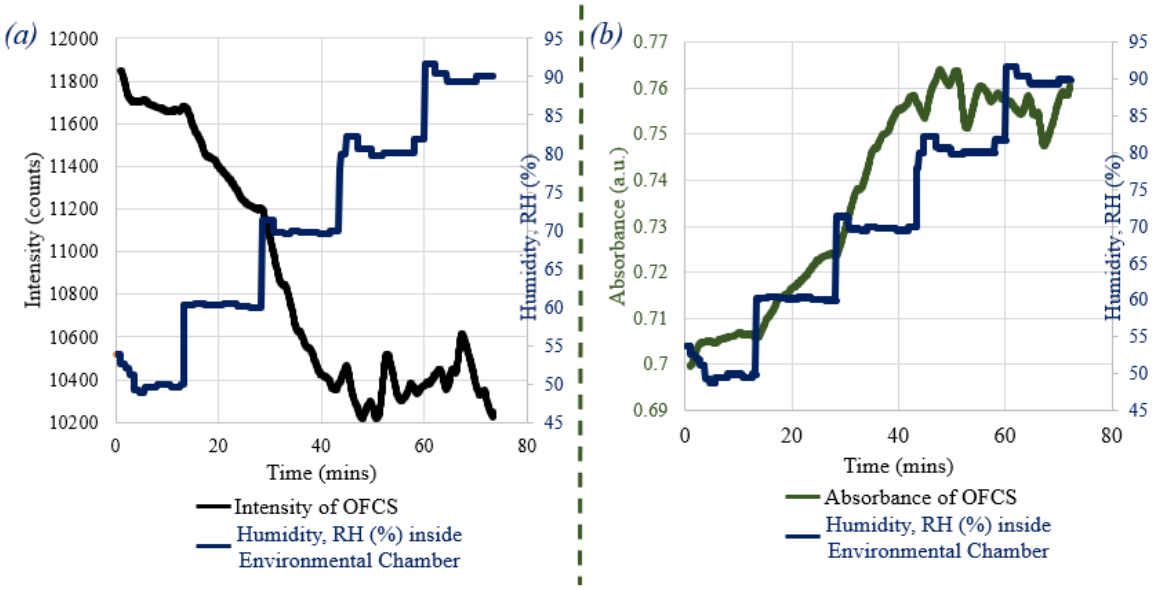


Figure 3.25: *(a) Reflection intensity (b) Absorbance of OFCS to different RH values at wavelength 600 nm*

In Figures 3.25 (a) and (b), the reflection intensity and absorbance of the OFCS at a wavelength of around 600 nm decline and rise with increasing RH levels from 50% RH to 90% RH, respectively. The reflection intensity and absorbance decrease and increases sharply from 50% RH to 70% RH, respectively. The reflection intensity and absorbance fluctuate from 70% RH to 90% RH. There is a 13.65 % reflection intensity decrease, and a 9.16 % absorbance increase for RH levels between 50% RH and 90% RH. The reflection signal changes as CO_2 penetrates through the Ormosil film and interacts with the dye-ion pair. CO_2 permeability to the Ormosil film determines the OFCS's sensitivity. The Ormosil coating has a greater permeability to water molecules due to selective absorption by the silanol group (Si-OH), causing a blocking effect on the pore gas channel, which may restrict CO_2 permeability. Many factors affect the blocking effect such as gas pressure, film's drying conditions, and pore size [103].

3.4.3 Nullifying humidity effects on OFCS

A PTFE cast film (FLONFILM™ 100, Polyflon, UK) is a single layer, multi-laminar film which acts as a semi-permeable membrane [119], allows gas flow and prevents water condensation. To investigate whether this film can be used as a barrier to prevent RH cross-sensitivity (Section 3.4.2), the PTFE film (thickness = 5 μm, tensile strength = 29.65 MPa or 4300 psi [119]) was placed as a sandwiched layer within a small GCC. The GCC (Figure 3.26 (a)) is custom made of biocompatible soft room temperature vulcanizing (RTV) silicone rubber (Polycraft ZA 22, MB Fibreglass, UK). The combination of GCC with the PTFE film can be used to nullify the humidity cross-sensitivity. The GCC's external diameter (D_1) is 48 mm, and the internal diameter (D_2) is 24 mm. A plastic tube was appropriately fixed through a hole of the GCC, which is called a channel, to allow the OFCS to be inserted into the environmental chamber. The OFCS tip was protected by a black polyolefin tube, reducing the chances of breakage, and avoiding background light affecting the measurement. The humidity calibration was performed inside the environment chamber by placing the OFCS tip into the GCC according to Figure 3.26 (b).

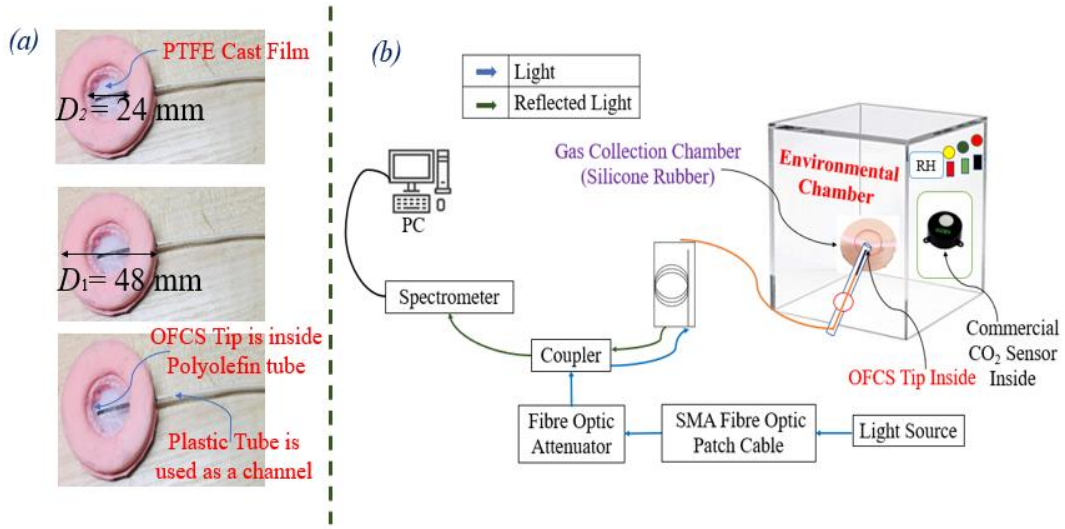


Figure 3.26: *(a) Dimension of GCC (b) Experimental set-up for RH calibration of OFCS inside GCC with PTFE film*

In Figure 3.26 (b), the same experimental set-up is used with the same equipment, as detailed in Section 3.3.1. The OFCS tip was connected to the GCC through the channel. The GCC contained the PTFE film layer to prevent humidity from reaching the OFCS tip.

The GCC with OFCS was placed inside the environmental chamber for RH calibration at a level (up to 70% RH). The environmental chamber can be controlled manually for the step-by-step variation from 50% RH to 70% RH. The commercial CO_2 sensor measured the CO_2 concentrations inside the environmental chamber during the experiment. The reflection spectrum of the OFCS was recorded with an integration time of 1 second using SpectraSuite Software. The RH values were noted down manually every 1 minute from the environmental chamber during the experiment. The CO_2 concentrations (from the commercial CO_2 Sensor) were recorded every 20 seconds using Gaslab Software. The temperature inside the environmental chamber was controlled at 35 °C (similar to normal human body temperature).

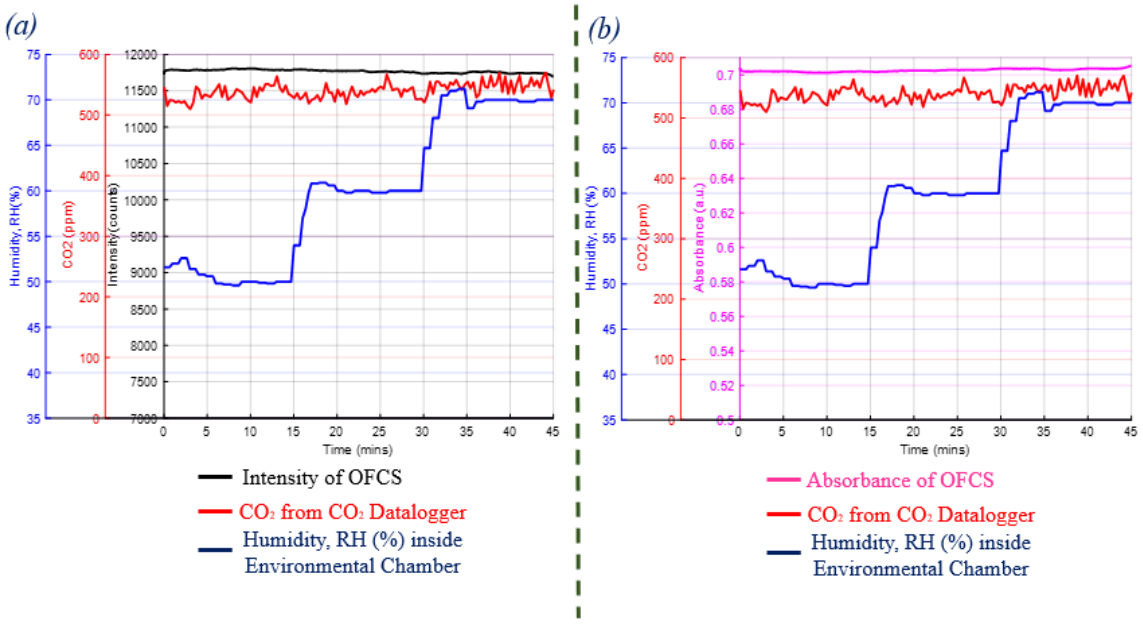


Figure 3.27: *(a) Reflection intensity (b) Absorbance of OFCS inside GCC sandwiched with PTFE film and commercial CO_2 sensor to different RH values at wavelength 600 nm*

In Figures 3.27 (a) and (b), the reflection intensity and absorbance of the OFCS at a wavelength of around 600 nm are almost stable, respectively, and the CO_2 concentrations (from the commercial CO_2 Sensor) vary (510-570 ppm) with increasing RH levels from 50% RH to 70% RH. Compared to Figure 3.25 (a) and (b), the variation in reflection intensity and absorbance of the OFCS at 600 nm inside the environmental chamber is minor. The PTFE film successfully prevents the humidity effects from the response of the

OFCS at 600 nm. The humidity effects can be nullified using the PTFE film inside the GCC.

3.5 Reducing film cracking

The film cracking can be removed by adding a chemical (Triton X-100) to provide a smooth film surface on the optical fibre tip.

3.5.1 Cracking demonstrated on GS

The preparation process (Section 3.2.5) of the sol-gel solutions inside the glass vial was used for this experiment. The GS was cleaned according to the process mentioned in Section 3.2.6. The GS was dip-coated 3 times employing the commercial dip-coating unit (see Figure 3.7 (b)) having a withdrawal speed of 3 mm/s. The drying interval was 2 minutes between each coating layer in ambient air.

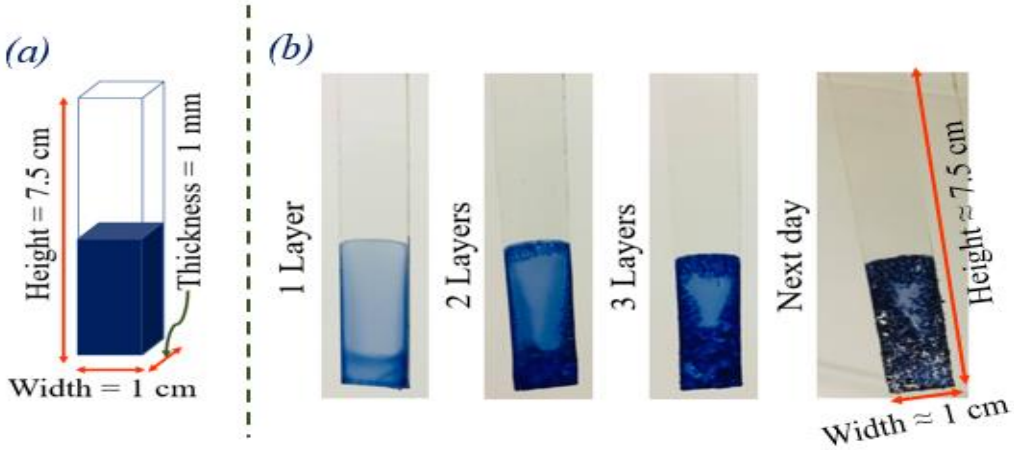


Figure 3.28: *(a) Dimension of GS (b) Observation of coated GS with 1, 2, and 3 layers and dried GS with 3 layers after 24 hours*

Figure 3.28 shows the effect after each coating cycle on the GS during the coating process on the day the process is carried out. Also shown is the 3-layer GS following the drying process in ambient air for around 24 hours after coating, where cracking appeared on the GS. The sol-gel matrix's volume shrinks significantly during the gelation and drying stages due to evaporation of organic solvent and water from the GS. The pore size relies on the amount of evaporation. The smaller pores remain wetted by the solvent when the bigger pores are emptied, after that the cracks are formed in monoliths due to the large internal pressure gradients [116].

3.5.2 Fibre sensor with and without Triton X-100

The preparation process (Section 3.2.5) of the sol-gel solutions inside the glass vial was followed according to Table 3.3. The optical fibre tip was cleaned and cleaved following the same process mentioned in Section 3.2.5 and then dip-coated 3 times using the commercial dip coating machine with a withdrawal speed of 3 mm/s, as shown in Figure 3.7 (b). The drying interval was 2 minutes between each coating layer in ambient air. Before use, the coated fibres were placed inside the pure N_2 (CO_2 and humidity free) environment for around 24 hours [103].

Table 3.3: *Preparation protocol of sol-gel solutions (Solution 1 and Solution 2) inside glass vial [103]*

Solution 1	*Solution 2*
TEOS (0.2 ml) + MTEOS (1.8 ml)	TEOS (0.2 ml) + MTEOS (1.8 ml)
Stirring for 10 mins	Stirring for 10 mins
Ethanol (6 ml)	Ethanol (5 ml)
Stirring for 10 mins	Stirring for 10 mins
Thymol Blue (22 mg)	Thymol Blue (22 mg)
Stirring for 15 mins	Stirring for 15 mins
TMAH (0.5 ml)	Triton X-100 (0.1 ml) + DI H_2O (0.9 ml)
Stirring for 1 hour	Stirring for 15 mins
	TMAH (0.5 ml)
	Stirring for 1 hour

The non-ionic surfactant Triton X-100 was used in Solution 2. The surfactants belong to the poly(ethylene glycol) family which is a useful ingredient for microporous silica preparation. The inclusion of the surfactant resulted in a smooth surface texture, transmittance of coating as well as improved homogeneity, uniformity, and porosity. Triton X-100 prevented the previously mentioned cracking by raising molecular mass, lowering interfacial energy and capillary stresses when it is added to the pore liquid [116] [120-121]. Reference [117] shows the images of platinum octaethylporphyrin (PtOEP)-doped silica gel glass without and with Triton X-100. The images were obtained by Nomarski differential-interference contrast microscopy. PtOEP-doped glass aggregates and the

cracking became visible in Figure 3.29 (a). Figure 3.29 (b) demonstrates PtOEP was homogeneously dispersed and immobilised in the silica matrix after adding Triton X-100 [117].

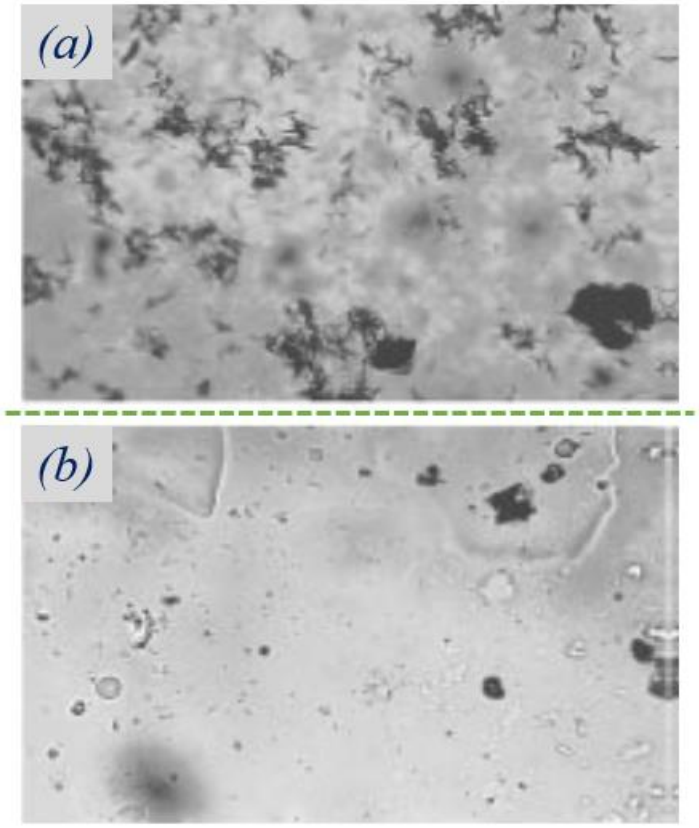


Figure 3.29: *Images of PtOEP immobilised in silica matrices (a) without (b) with Triton X-100 [117]*

3.5.3 OFCS spectra with and without Triton X-100

OFCS 1 and OFCS 2 consist of Solution 1 (without Triton X-100), and Solution 2 (with Triton X-100) coated onto the tip of the optical fibre 1 and optical fibre 2, respectively. Figures 3.30 (a) and (b) demonstrate the reflection and absorption spectra of OFCS 1 and OFCS 2 respectively with 3 layers of coating on the day they are created. Figures 3.30 (c) and (d) illustrate the reflection and absorption spectra of OFCS 1 and OFCS 2 respectively with 3 layers of coating after drying in pure N_2 (CO_2 and humidity free) environment for around 24 hours. The noticeable change of reflection intensity and absorbance at a wavelength of around 600 nm is observed.

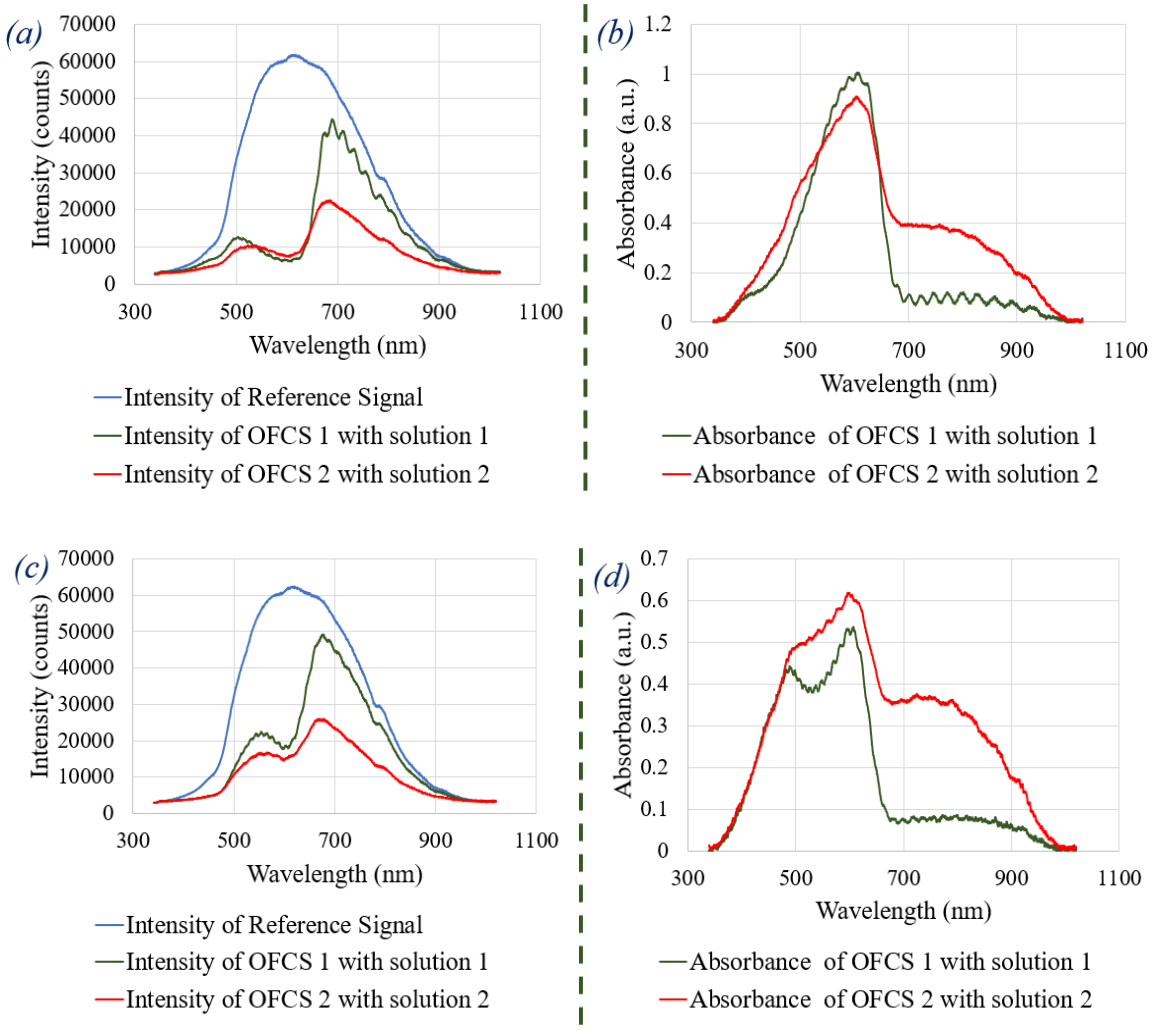


Figure 3.30: *(a) Reflection spectra (b) Absorption spectra of OFCSs with 3 layers after coating on that day (c) Reflection spectra (d) Absorption spectra of OFCSs with 3 layers coating after drying for 24 hours on next day*

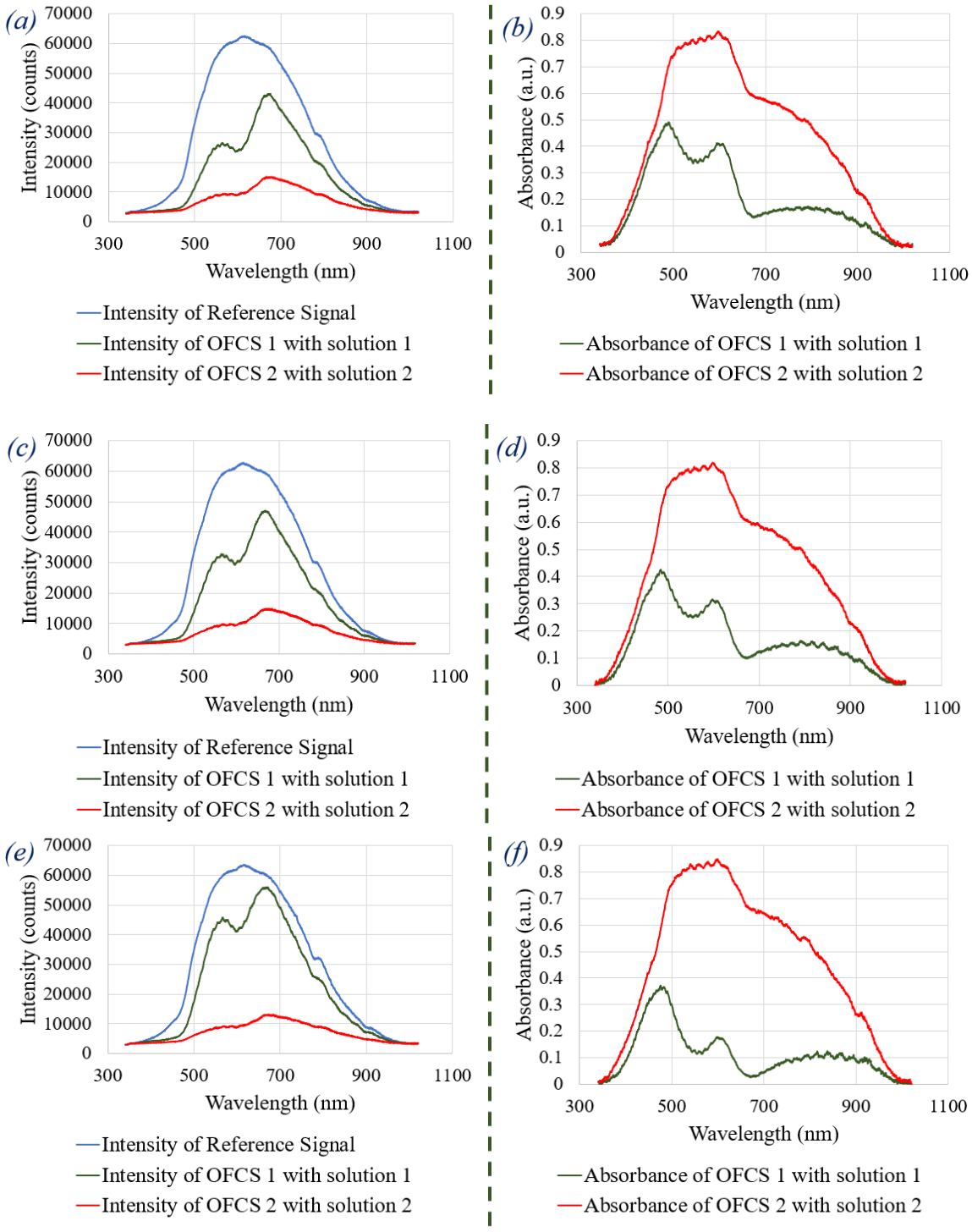


Figure 3.31: *(a) Reflection spectra (b) Absorption spectra of OFCSs with 3 layers coating after storing for 9 days (c) Reflection spectra (d) Absorption spectra of OFCSs with 3 layers coating after storing for 16 days (e) Reflection spectra (f) Absorption spectra of OFCSs with 3 layers coating after storing for 35 days*

Changes are visible between the reflection and absorption spectra of OFCS 1 and OFCS 2 when the OFCSs are stored inside vacuum sealed bags inside a wooden drawer for around 35 days. Figures 3.31 (a)-(f) show a comparison between the 3 pairs.

Firstly, Figures 3.31 (a) and (b) present the reflection and absorption spectra of OFCS 1 and OFCS 2 with 3 layers of the coating after storing for 9 days. Secondly, Figures 3.31 (c) and (d) illustrate the reflection and absorption spectra of OFCS 1 and OFCS 2 with 3 layers of the coating after storing for 16 days. Finally, Figures 3.31 (e) and (f) demonstrate the reflection and absorption spectra of OFCS 1 and OFCS 2 with 3 layers of the coating after storing for 35 days. Table 3.4 illustrates the reflection intensity and absorbance of OFCS 1 and OFCS 2 and the reflection spectrum of the BF at a wavelength of around 600 nm according to the number of OFCSs' storing days.

Table 3.4: *Reflection intensity and absorbance of OFCS 1 and OFCS 2 and reflection intensity of bare fibre at wavelength 600 nm based on number of* OFCSs' *storing days*

Number of OFCSs' storing days	OFCS 1 without Triton X-100		OFCS 2 with Triton X-100		BF
	Intensity (counts)	Absorbance (a.u.)	Intensity (counts)	Absorbance (a.u.)	Intensity (counts)
9	24115 ± 79.413	0.405 ± 0.00112	9204 ± 50.518	0.823 ± 0.00207	61271 ± 45.065
16	29924 ± 47.976	0.312 ± 0.00029	9425 ± 20.539	0.813 ± 0.00063	61302 ± 58.829
35	41333 ± 72.896	0.177 ± 0.00016	8927 ± 18.176	0.843 ± 0.00026	62147 ± 91.518

The reflection intensity of the BF is needed to calculate the absorbance of OFCS 1 and OFCS 2 using Eq. (3.10). The reflection intensity (24115-41333 counts) and the absorbance (0.405-0.177) of OFCS 1 at 600 nm increase and decrease from Figures 3.31 (a)-(f). On the other hand, the reflection intensity (8927-9425 counts) and the absorbance (0.813-0.843) of OFCS 2 at 600 nm varies from Figures 3.31 (a)-(f). The absorbance

variation of OFCS 2 is small compared to the absorbance variation of OFCS 1 after several storing days.

The improvement of the stability of OFCS 2 with Solution 2 was achieved because of the effect of Triton X-100. The OFCS 2 demonstrated a relatively prolonged shelf life (> 35 days) with minor absorbance variation. This experiment was performed with only the optical fibres. So, the same glass substrate wasn't stored for many days to perform the stability test, but it may be performed in the future.

3.6 Film thickness measurement of an OFCS from SEM images

The film thickness was measured from the dried film on the coated fibre tip using the scanning electron microscope (SEM) images. This film thickness was utilised for calculating dye concentration from the dried film and simulating the normalised intensity and absorbance of an FPI sensor.

The OFCSs (OFCS 1-3) were fabricated and dried using the same set-up with the same equipment, as detailed in Sections 3.2.5 and 3.5.2 (OFCS preparation scheme using Solution 2). After coating and drying, the reflection spectra of the OFCSs (OFCS 1-3) were measured using the same equipment, as detailed in Sections 3.2.5 and 3.3.1, such as the light source, coupler, spectrometer, and PC.

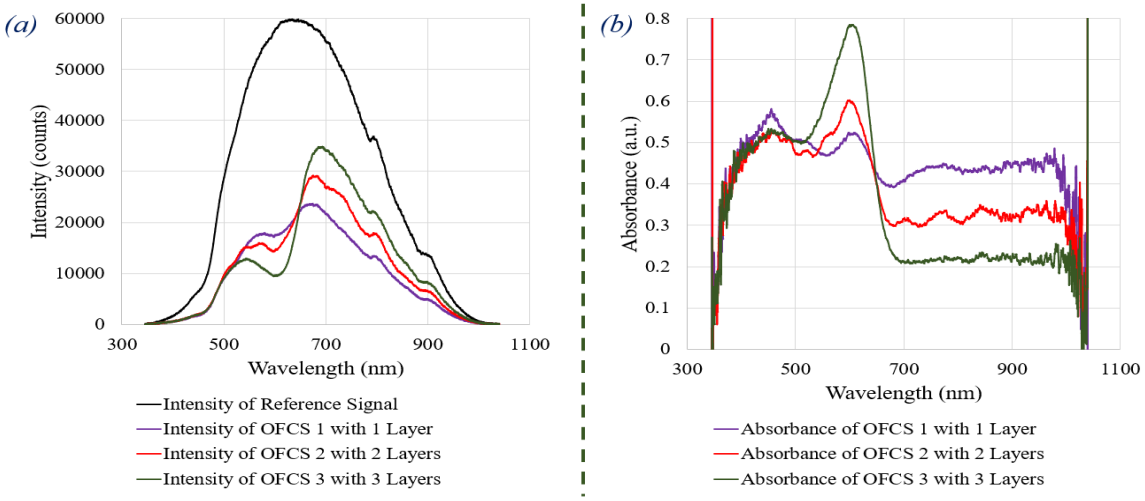


Figure 3.32: *(a) Reflection spectra (b) Absorption spectra of OFCSs after drying for 24 hours*

Figures 3.32 (a) and (b) demonstrate the reflection and absorption spectra of the OFCSs (OFCS 1-3) with 1, 2, and 3 layers of the coating after drying in a pure N_2 (CO_2 and humidity free) environment for around 24 hours.

The fibre tip was detached from the whole fibre using the fibre optic stripper for the SEM measurements. The BF was used for 0 layers of coating. The tip of an OFCS 1, 2, and 3 was coated with 1, 2, and 3 layers, respectively. The fibre tips (0, 1, 2, and 3 layers) were placed on a specimen holder for the SEM measurements, as shown in Figure 3.33. The SEM images were taken by one of the research technicians at the Nanoscale and Microscale Research Centre (nmRC), University of Nottingham (UoN).

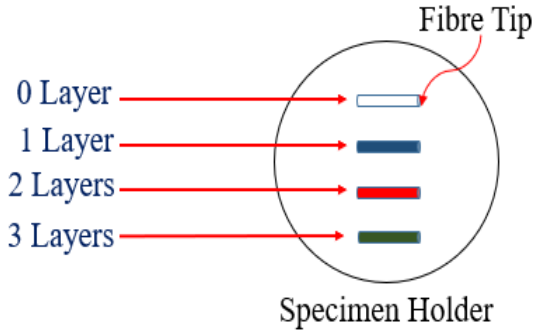


Figure 3.33: *Schematic diagram of fibre tips on specimen holder*

Figure 3.34 illustrates the SEM images of the BF's tip, including the residue left on the fibre tip.

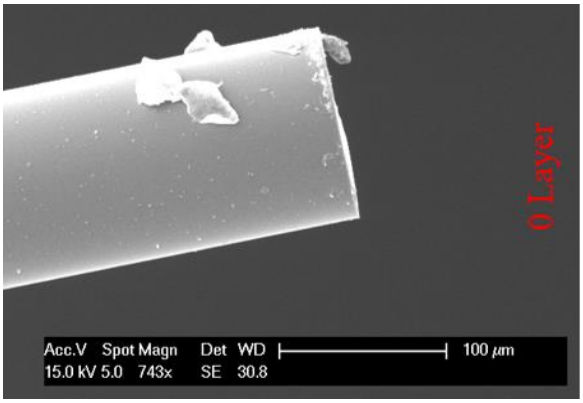


Figure 3.34: *SEM images of bare fibre's tip*

Figures 3.35 (a), 3.36 (a), and 3.37 (a) show the SEM images of coated fibres with 1, 2, and 3 layers, respectively. Figures 3.35 (b), 3.36 (b), and 3.37 (b) demonstrate the SEM images, including the film thickness at different parts of the coated fibre tips.

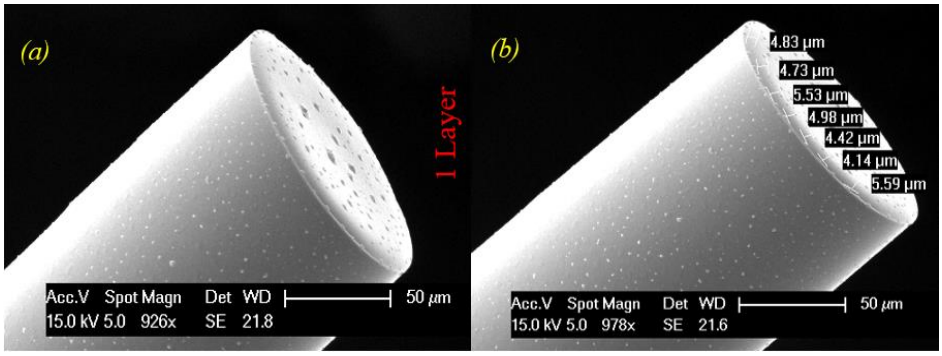


Figure 3.35: *SEM images of OFCS 1's tip with (a) 1 layer (b) film thickness measurement*

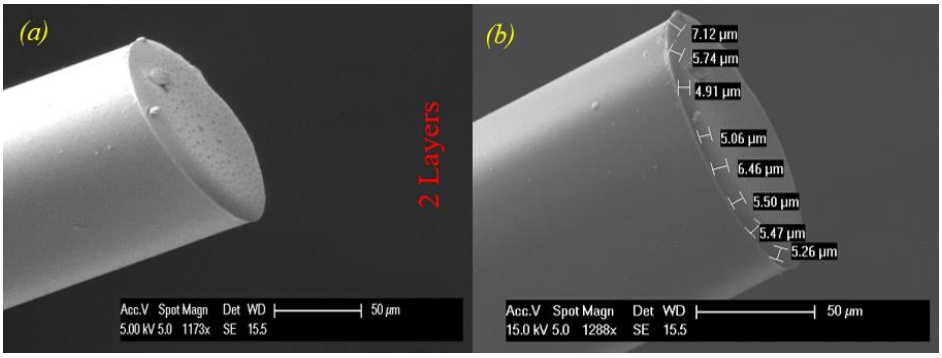


Figure 3.36: *SEM images of OFCS 2's tip with (a) 2 layers (b) film thickness measurement*

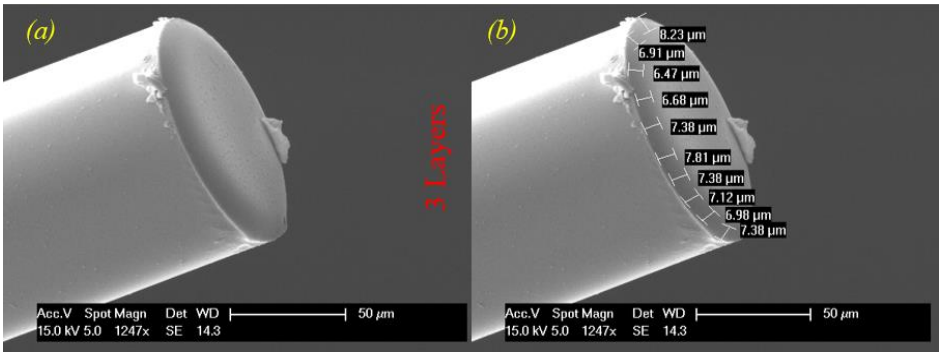


Figure 3.37: *SEM images of OFCS 3's tip with (a) 3 layers (b) film thickness measurement*

The molar weight of dye, TB is 466.59 g/mol [96] or 466590 mg/ml. The TB concentration inside Solution 2 (Section 3.5.2) is:

TB concentration inside solution = TB amounts inside solution / Total volume of solution

= (22.03 mg / 8.5 ml) = 2.592 mg/ml

= (2.592 mg/ml) / (466590 mg/ml)

= 0.000005555 mol/ml = 0.0055 mol/L = 0.0055 M

The TB concentration from the dried film was calculated using the average film thickness (cm) from Table 3.5, the MAC (35144 $M^{-1}cm^{-1}$ at nearly 606 nm for TB (blue)) from Figure 3.6 (c) and the absorbance at around 600 nm from Figure 3.32 (b).

An example of calculating the TB concentration from the dried film (1 layer, OFCS 1) using Eq. (3.8) is as follows:

TB concentration from dried film = Absorbance at 600 nm / (MAC x film thickness)

= 0.5192 / (35144 $M^{-1}cm^{-1}$ x 0.0004888 cm) = 0.0302 M

TB concentration from the dried film is higher than the TB concentration inside the solution. The volume of the coated tip shrinks after drying the film. When the volume decreases, the concentration increases, according to Eq. (3.13) [122].

$$c = \frac{n}{V} \qquad (3.13)$$

where c is the concentration (mol/Litre, mol/L, or M), n is number of moles (mol), and V is the volume (Litre, L) [122].

Table 3.5: *Average film thickness and TB concentration measurement from SEM images of OFCSs*

OFCS number and layer number	Film thickness (μm) at different parts	Mean of film thickness (μm)	Mean of film thickness (cm)	Standard deviation of film thickness (μm)	Absorbance at 600 nm (a.u.)	Dye concentration (M)
OFCS 1 1 layer	4.8, 4.73 5.53, 4.98 4.42, 4.14 5.59	4.8886	0.0004888	0.5354	0.5192	0.0302
OFCS 2 2 layers	7.12, 5.74 4.91, 5.06 6.46, 5.5 5.47, 5.26	5.69	0.000569	0.7479	0.6007	0.0300
OFCS 3 3 layers	8.23, 6.91 6.47, 6.68 7.38, 7.81 7.38, 7.12 6.98, 7.38	7.234	0.0007234	0.5229	0.7835	0.0308

3.7 Fibre-to-fibre variability

10 OFCSs (OFCS 1-10) were fabricated and calibrated for the skin CO_2 measurement. The calibration results of these 10 coated fibres are useful to understand how much the measurement varies from one fibre to another. In Figure 3.38, the same experimental set-up is used with the same equipment, as detailed in Section 3.3.1. The PLA based holder containing the OFCS tip and commercial CO_2 sensor was put inside a gas chamber. N_2 gas was flushed inside the gas chamber for the first 5 minutes for the OFCS calibration. A line regulator (GCE druva, UK) and a blowgun were used to control the step-by-step variation of lower CO_2 concentrations inside the gas chamber via the gas route. A minimum of around 10 minutes was needed for the CO_2 concentrations inside the gas chamber to stabilise. The reflection spectrum of the OFCS was recorded with an integration time of 1 second using SpectraSuite Software. The CO_2 concentrations (from the commercial CO_2 sensor) were recorded every 20 seconds using Gaslab Software.

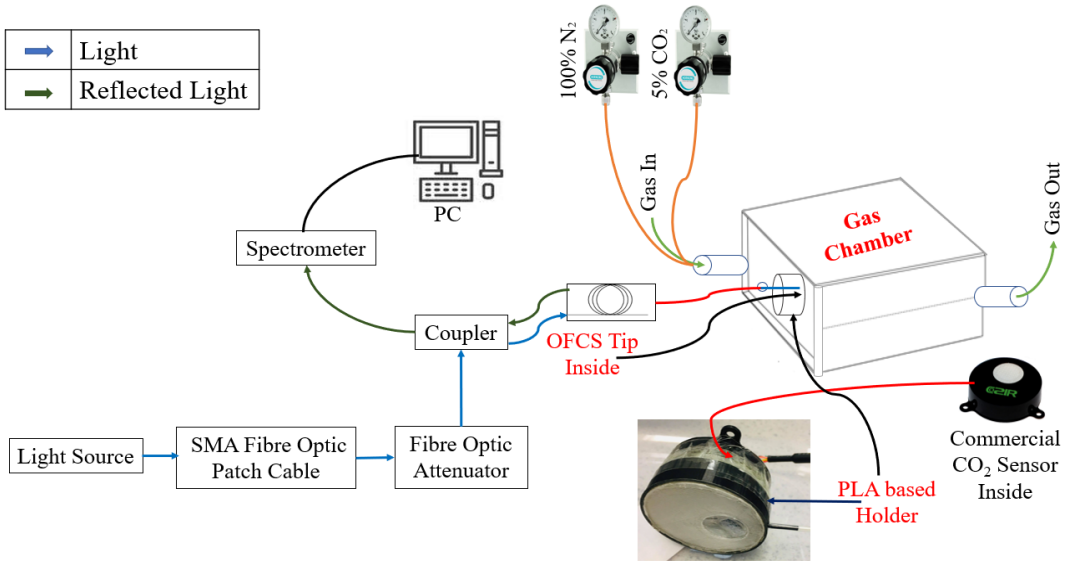


Figure 3.38: *Experimental set-up for CO_2 calibration of OFCS for skin CO_2 measurement*

Figure 3.39 shows the reference signal, which is reflected from the BF's tip, and this reference signal was used to calculate the absorbance using Eq. (3.10) in Figures 3.40 (b) and odd numbers of Figures A.1 (b)-A.17 (b) [Appendix A]. The intensity of the BF is 52601 counts at a wavelength of 600 nm. This response of the BF is achieved using the

same experimental set-up as detailed in Section 3.3.1. The reflection spectrum of the BF was recorded with an integration time of 1 second using SpectraSuite Software.

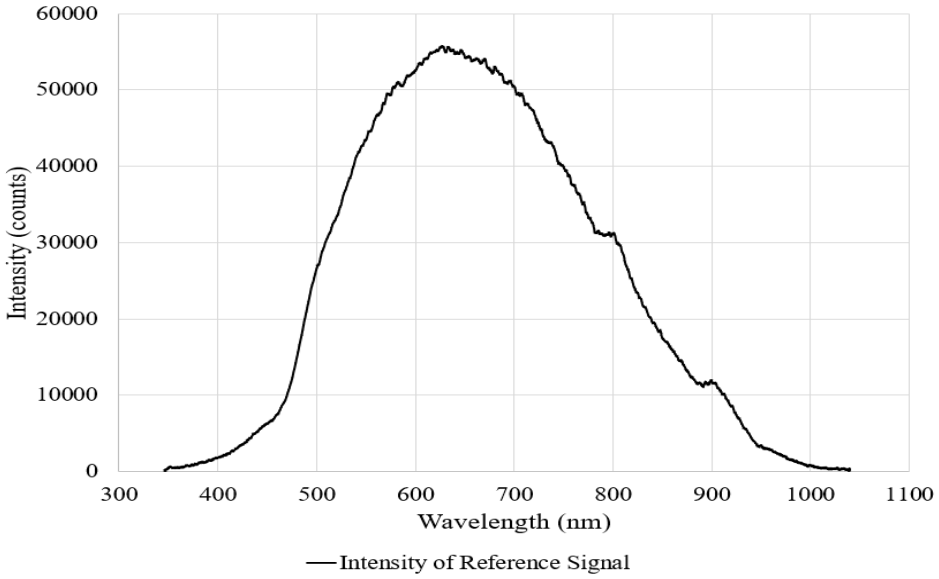


Figure 3.39: *Reflection spectrum of bare fibre for fibre to fibre variability*

Figure 3.40 and odd numbers of Figures A.1-A.17 [Appendix A] show the step-up response of the OFCS 1-10 to the CO_2 concentrations (from the commercial CO_2 sensor) using the set-up shown in Figure 3.38. The intensity (counts) of the OFCS 1-10 and CO_2 (ppm) from the commercial CO_2 sensor are not stable because of lower CO_2 concentrations. Table 3.6 and Tables A.1-A.9 [Appendix A] illustrate the CO_2 (ppm), intensity (counts), and absorbance (a.u.) variation for every step of the OFCS 1-10 (blue dot in the intensity response curves such as Figure 3.40 (a) and green dot in the absorbance response curves such as Figure 3.40 (b)).

In Figures 3.40 (a) and (b), the blue and green dots represent the start of each step for intensity (counts) and absorbance (a.u.) changes respectively due to the CO_2 (ppm). The CO_2 gas was inserted into the gas chamber in amounts of 378-469 ppm, 469-671 ppm, and 671-961 ppm within the intervals 6-17, 17-19, and 29-45 minutes, respectively. The reflection intensity and absorbance of OFCS 1 at a wavelength of 600 nm increases and decreases, respectively, with rising CO_2 concentration.

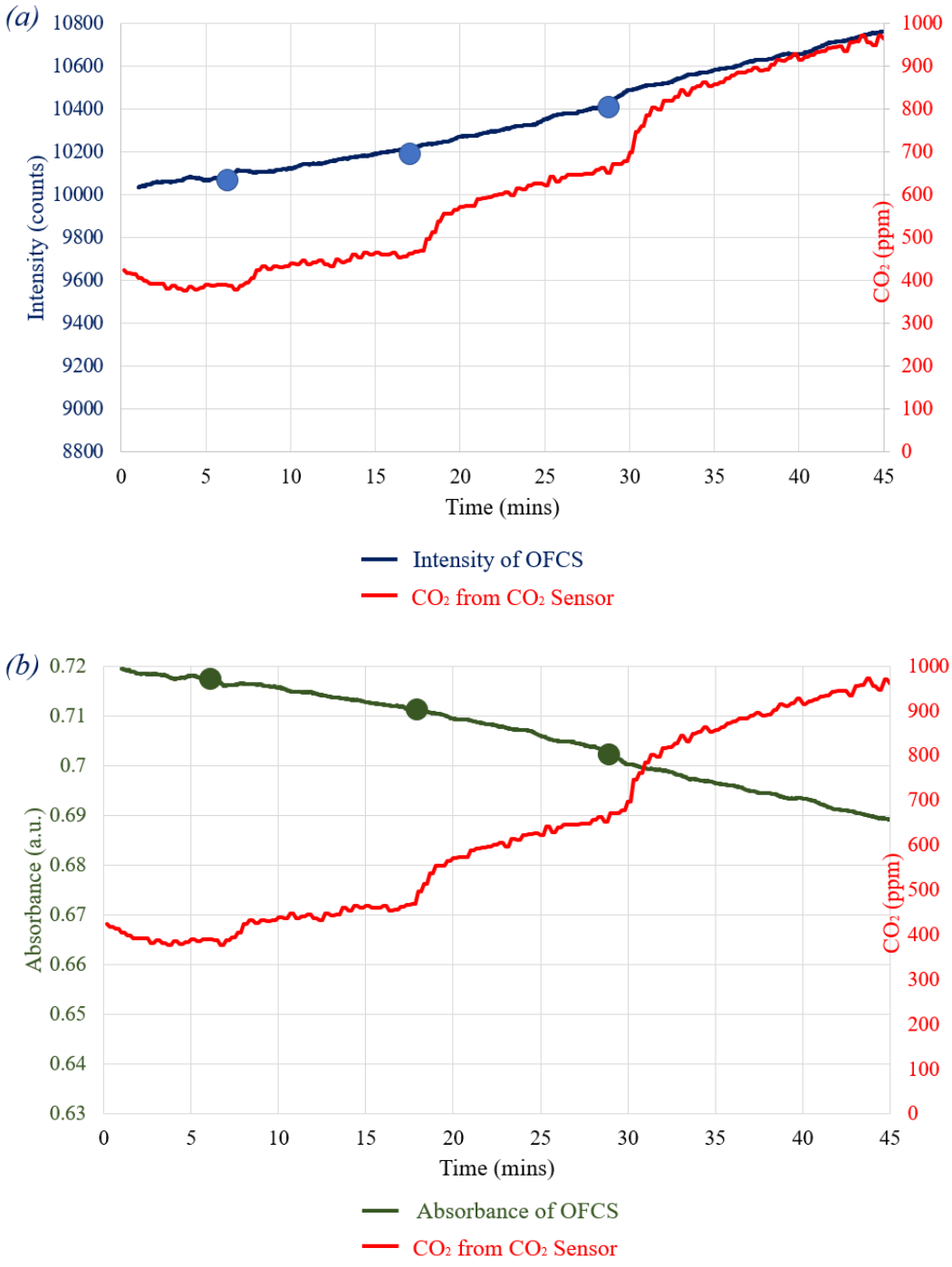


Figure 3.40: *Response (a) Reflection Intensity (b) Absorbance of OFCS 1 for different CO_2 concentrations at wavelength 600 nm*

Table 3.6 shows the values of CO_2 (ppm), intensity (counts), and absorbance (a.u.) at each of the beginning of the steps, such as 6, 17, 29, and 45 minutes (last step). The first 5 minutes were not considered a step response because the N_2 gas was flushed inside the gas chamber during that period. The change in CO_2 (ppm), intensity (counts), and absorbance (a.u.) was calculated between each of the steps from Figures 3.40 (a) and (b), such as between 6-17, 17-19, and 19-45 minutes. The change in intensity (counts) and absorbance (a.u.) were plotted with respect to the change in CO_2 (ppm) in Figure 3.41. Two linear correlations were found from this figure, one is between intensity (counts) and CO_2 (ppm), and another is between absorbance (a.u.) and CO_2 (ppm). Those linear equations represent the sensitivity of OFCS 1, such as 1.20239 counts/ppm for intensity and 0.00004 a.u./ppm for absorbance. The linear equations are used to calculate the variation in OFCS's response (intensity and absorbance) and commercial CO_2 datalogger during the skin CO_2 measurement.

Table 3.6: *Variation of CO_2 concentration and response (reflection intensity and absorbance) of OFCS 1 at wavelength 600 nm for different time periods*

Time (mins)	CO_2 (ppm)	Intensity (counts)	Absorbance (a.u.)	Time duration (mins) for measuring the change in CO_2, Intensity, and Absorbance	Change in CO_2 (ppm)	Change in Intensity (counts)	Change in Absorbance (a.u.)
6	378	10126	0.715				
17	469	10201	0.712	6-17	91	75	0.003
29	671	10499	0.699	17-29	202	298	0.013
45	961	10769	0.688	29-45	290	270	0.011

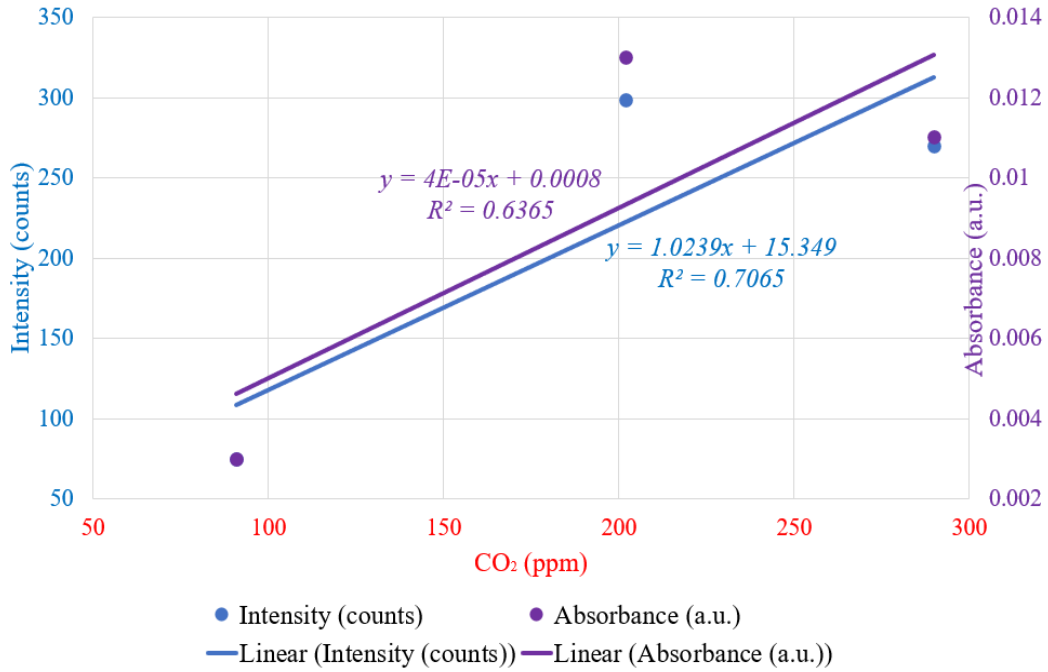


Figure 3.41: *Linear fitting of variation in response (reflection intensity and absorbance) of OFCS 1 to different CO_2 concentrations at wavelength 600 nm*

Odd numbers of Figures A.1-A.17 [Appendix A] represents the response (intensity (counts) and absorbance (a.u.)) of the OFCS 2-10, respectively. Those graphs follow the same trend as Figure 3.40.

Tables A.1-A.9 [Appendix A] also represent the change in intensity (counts) and absorbance (a.u.) according to the change in CO_2 concentrations for the OFCS 2-9, respectively. Even numbers of Figures A.2-A.18 [Appendix A] illustrate the linear correlations (from Tables A.1-A.9) between intensity (counts) and CO_2 (ppm) and between absorbance (a.u.) and CO_2 (ppm) for the OFCS 2-10. Those linear correlations show the sensitivity of the OFCS 2-10.

The fibre-to-fibre variability is transparent due to the obtained sensitivity of the 10 OFCSs (OFCS 1-10) from those linear correlations (Figure 3.41 and even numbers of Figures A.2-A.18 [Appendix A] between the OFCSs' (OFCS 1-10) responses (intensity and absorbance) and CO_2 (ppm).

Table 3.7: *OFCS's sensitivity w.r.t. intensity and absorbance*

OFCS number	OFCS's Sensitivity w.r.t. Intensity (counts/ppm)	OFCS's Sensitivity w.r.t. Absorbance (a.u./ppm)
1	1.0239	0.00004
2	1.2182	0.00007
3	1.2366	0.00003
4	1.8839	0.00005
5	2.7503	0.00007
6	0.5448	0.00002
7	0.3962	0.000008
8	0.3742	0.00001
9	0.4189	0.00001
10	0.4668	0.00003
Mean	1.0314	0.00003
Standard deviation	0.7835	0.00002

Table 3.7 shows the variation in fibre to fibre according to the sensitivity of the 10 OFCSs (OFCS 1-10). The sensitivity w.r.t. intensity varies from 0.3742 counts/ppm to 2.7503 counts/ppm. The sensitivity w.r.t. absorbance also varies from 0.000008 a.u./ppm to 0.00007 a.u./ppm. This variability was obtained due to the changes in film properties (such as dye concentration rising due to the sol-gel matrix's shrinks) after drying. Each sensor is made manually and requires individual calibration, however, in future these variations can be reduced by introducing automation into the manufacturing process.

3.8 Summary

The fabrication and characterisation of an OFCS utilising a MM optical fibre tip coated with Ormosil films containing TB as a colorimetric pH indicator dye has been described. The spectrum of TB changes due to the various pH values and CO_2 flow. The highest absorption peak was achieved at a wavelength of 549, 452, and 606 nm for TB (red), TB (yellow), and TB (blue), respectively.

The spectra characteristics of the OFCS were studied, and the highest absorption peak was found at a wavelength of approximately 600 nm. The response of the highest absorption peak was tested between 0 ppm (0% CO_2) and 50000 ppm (5% CO_2). Measurements of CO_2 from the OFCS were compared to the commercial CO_2 datalogger and t_C Sensor 92 probe. The response time of the commercial CO_2 datalogger is approximately 20 seconds [47]. The 90 % response time of T_CPCO_2 electrode is almost 78 seconds [4] which is higher than that of the OFCS of 60 seconds.

The OFCS was characterised by cross-sensitivity effects. There was a negligible temperature effect on the OFCS at a stable temperature, as found in the previous literature review [108]. Humidity degrades the OFCS's performance, but the PTFE film can be used to prevent the humidity effects on the OFCS. A sol-gel coating with Triton X-100 was used in the fabrication process of the OFCS to remove cracking from the optical fibre tip and improve the shelf life and stability.

The TB concentration was calculated using the film thickness from the dried film on the OFCS tip with the aid of the SEM images. The 10 different OFCSs (OFCS 1-10) were calibrated at a range of CO_2 concentrations from 276 ppm to 1383 ppm according to the mentioned process in Section 3.7. The response time of the OFCS 1-10 couldn't be measured during the calibration process because the response of the OFCS 1-10 and commercial CO_2 sensor was unstable due to lower CO_2 concentration inside the gas chamber. The sensitivity varied in intensity from 0.3742 counts/ppm to 2.7503 counts/ppm, and the sensitivity also varied in absorbance from 0.000008 a.u./ppm to 0.00007 a.u./ppm for the 10 OFCSs (OFCS 1-10).

The measurement range varies according to the different loading amounts on the skin, such as the PCO_2 value of 36-44 mmHg (for 40 mmHg or 5.3 kPa loading) [8]. The OFCS detects changes in CO_2 of around 46000 ppm and 53000 ppm, equivalent to the PCO_2 value of 31.5 mmHg and 44 mmHg during the calibration (step up and down responses), respectively. Therefore, the OFCS can detect the first pressure mode, Mode 1 [8], from our collaborators at the University of Southampton, mentioned in Sections 1.3 and 2.3.1.

The achieved results from the developed OFCS {small with tubular geometry, lightweight, doesn't require heating, contact gel, and temperature calibration (mentioned in Section 3.4.1) compared to the commercial T_CPCO_2 electrode} demonstrate the potential for monitoring T_CPCO_2 from human skin using optical fibre, and this will be explored further in Chapter 5.

4. Chapter 4

Shape Analysis of Dye's Spectrum & Modelling of Fabry-Perot Interferometer

4.1 Introduction

To fully explore the effect of different parameters on the sensor response, a numerical model is very useful. To develop the model, it is important to understand the dye's transmission and absorption spectra at different concentrations and typical film thickness values. Dye concentration can then be combined with film thickness and used to model the tip of the optical fibre CO_2 sensor as a Fabry-Perot interferometer. Section 4.2 describes the shape of the dye's transmission and absorption spectra with and without CO_2 flow. Section 4.3 describes the model based on Fabry-Perot interferometry and its relevant equations. Section 4.4 illustrates the simulated reflection and absorption spectrum of an FPI and the calculation of fringe visibility by varying film thickness, and finally, Section 4.5 concludes with a summary of this chapter.

4.2 Analysis of Thymol Blue spectrum shape

Tracking the changes in the TB peaks absorbance spectrum, it is worthwhile investigating whether any other properties of the absorption spectrum can be used to achieve more robust measurements of pH. Two unitless shape measurements were investigated: skewness and kurtosis [123]. These are potentially useful as they depend on the full shape of the spectrum and not on absolute intensity measurements.

4.2.1 Relevant theory of skewness and kurtosis

Skewness includes information on the magnitude and direction of skew, and kurtosis provides information about the centre peak's height and sharpness relative to a typical bell curve. Excess kurtosis is simply **kurtosis−3**. Microsoft Excel's skewness and kurtosis function calculate skewness and excess kurtosis, respectively [123].

Skewness and kurtosis are calculated as follows [124]:

$$Skewness = \frac{n\sum_{i=1}^{n}(x_i - \bar{x})^3}{(n-1)(n-2)s^3} \quad (4.1)$$

$$Kurtosis = \frac{n(n+1)\sum_{i=1}^{n}(x_i - \bar{x})^4}{(n-1)(n-2)(n-3)s^4} - \frac{3(n-1)^2}{(n-2)(n-3)} \quad (4.2)$$

where n is the sample size, x_i is the value of i^{th} value of datasheet, $\bar{x}$ is the mean of sample, and s is the standard deviation of the sample [124].

Tables 4.1 and 4.2 show the interpretation of skewness and kurtosis values. The values mention the curve's distribution, tails, and centre peaks movement.

Table 4.1: *Interpretation of skewness values [123]*

Skewness	Data	Meaning
Positive	Positively skewed or skewed right	The right tail is longer than the left tail
Negative	Negatively skewed or skewed left	The left tail is longer than the right tail

Skewness	Distribution
0	Perfectly symmetric
Less than -1 or greater than +1	Highly skewed
Between -1 and -0.5 or between +0.5 and +1	Moderately skewed
Between -0.5 and +0.5	Approximately symmetric

Table 4.2: *Interpretation of kurtosis values [123]*

Kurtosis	Excess kurtosis	Name	Distribution		
3	0	Mesokurtic	Normal		
Less than 3	Less than 0	Platykurtic	Compared to Normal Distribution	Tails are shorter and thinner	Central peak is lower and broader
Greater than 3	Greater than 0	Leptokurtic	Compared to Normal Distribution	Tails are longer and fatter	Central peak is higher and sharper

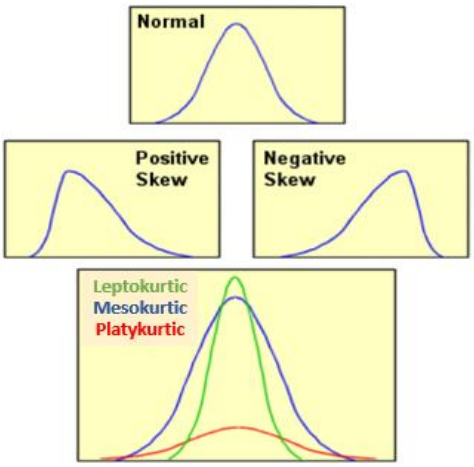


Figure 4.1: *Illustration of skewness and kurtosis (adapted from [125])*

Figure 4.1 demonstrates different curves such as the standard bell curve with normal distribution, positive skewed, negative skewed, leptokurtic, mesokurtic, and platykurtic curves. Leptokurtic, mesokurtic, and platykurtic curves can use a full width at half maximum (FWHM) to define width.

4.2.2 CO_2 and pH relationship

Eq. (2.1) shows how CO_2 reacts with water (H_2O) to develop carbonic acid (H_2CO_3), a weak acid breaks into bicarbonate ions (HCO_3^-) and hydrogen ions (H^+) [26].

A test was performed by adding CO_2 to DI water as shown in Figure 4.2. The pH of DI water was observed before and after adding CO_2 using pH colour strips (pH 0-14, resolution 1.0 pH unit, Sigma-Aldrich, UK [126]). Although a pH meter could be used, it needs to be calibrated in buffer solution before every measurement and so pH strips were preferred for convenience. The pH test strips with colour coding are presented in Figure 4.3. The pH value of DI water is 6 before adding CO_2 and the pH value of DI water became 5 after adding CO_2. So, H_2CO_3 reduced the pH value of DI water.

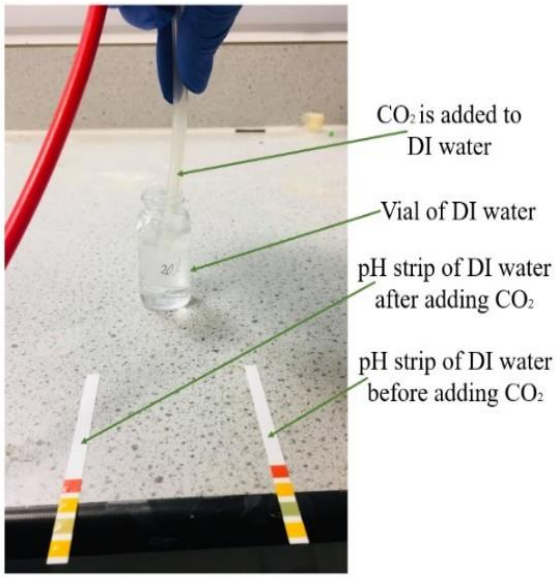


Figure 4.2: *A process of adding CO_2 with DI water*



Figure 4.3: *pH test strips (P4786, Sigma-Aldrich, UK) [126]*

4.2.3 Experimental set-up for adding CO_2 inside Thymol Blue solution

In Figure 4.4, the same experimental set-up is used with the same equipment, as detailed in Section 3.2.4.2. The CO_2 concentration was controlled inside the solution using the PTFE flowmeter. The flowmeter with a valve was used to control the flow rate. The flow rate was set to 7.30 ml/min or 0.1216 ml/sec on the flowmeter for 10 seconds. Any changes in pH, colour, and shape of the spectrum were monitored during the process.

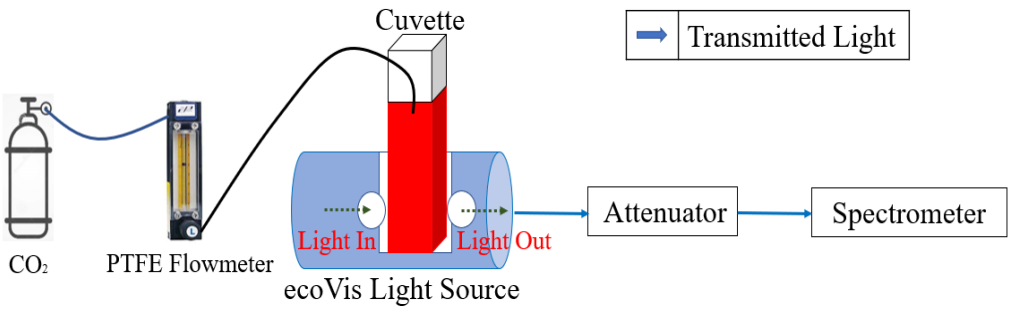


Figure 4.4: *Experimental set-up for monitoring pH variation of TB with CO_2*

Figure 4.5 illustrates ethanol and different colours of TB inside the cuvette before and after adding CO_2 into the solution. There was no change in pH value and colour in ethanol, TB (red), and TB (yellow) after adding CO_2 into the solution. The pH value of ethanol and TB (red) is 6, and the pH value of TB (yellow) is 5 with and without CO_2, measured by the pH strips. However, the colour of TB (blue) turned into TB (yellow), and the pH value dropped from 11 to 8 after adding CO_2 into the TB (blue) solution.

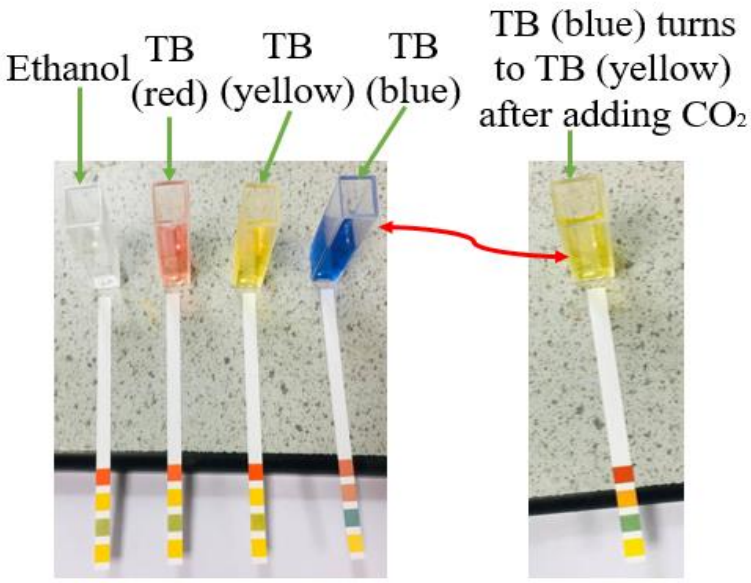


Figure 4.5: *Monitoring pH variation of TB with CO_2 using pH strip*

4.2.4 Spectrum of Thymol Blue according to pH variation with and without CO_2

The transmission spectra of ethanol, TB (red), TB (yellow), and TB (blue) were recorded for 10 seconds with an interval of 1 second. So, there are 10 sets of data (Serial 1, S1-Serial 10, S10) for calculating the average of skewness, kurtosis, intensity, absorbance, and MAC

curve with and without CO_2 inside the solutions. The transmission spectra of ethanol with and without CO_2 is used as a reference signal with an integration time of 56 ms using the set-up as shown in Figure 4.4. All the spectra without CO_2 flow are illustrated in Figures 4.6-4.9.

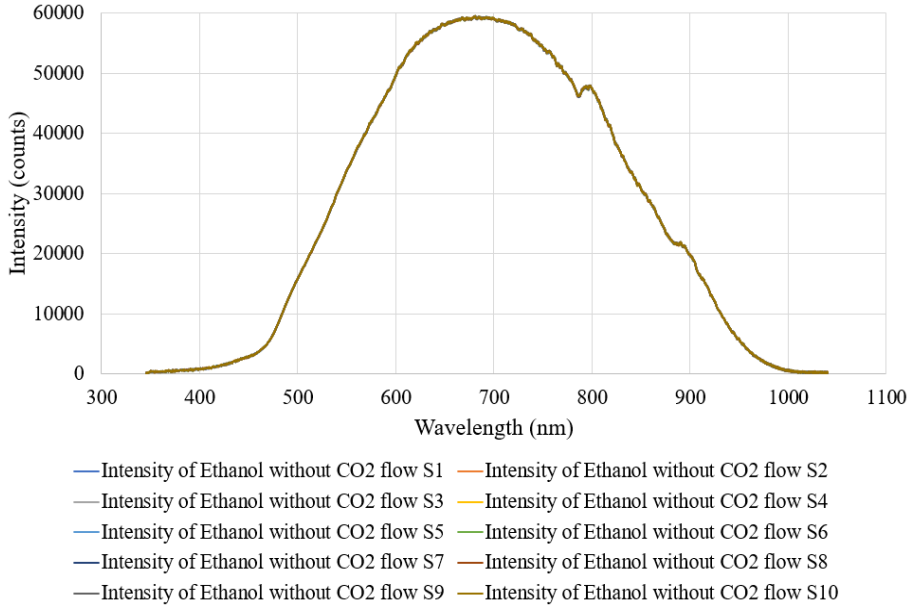


Figure 4.6: *Transmission spectra of Ethanol without CO_2 flow*

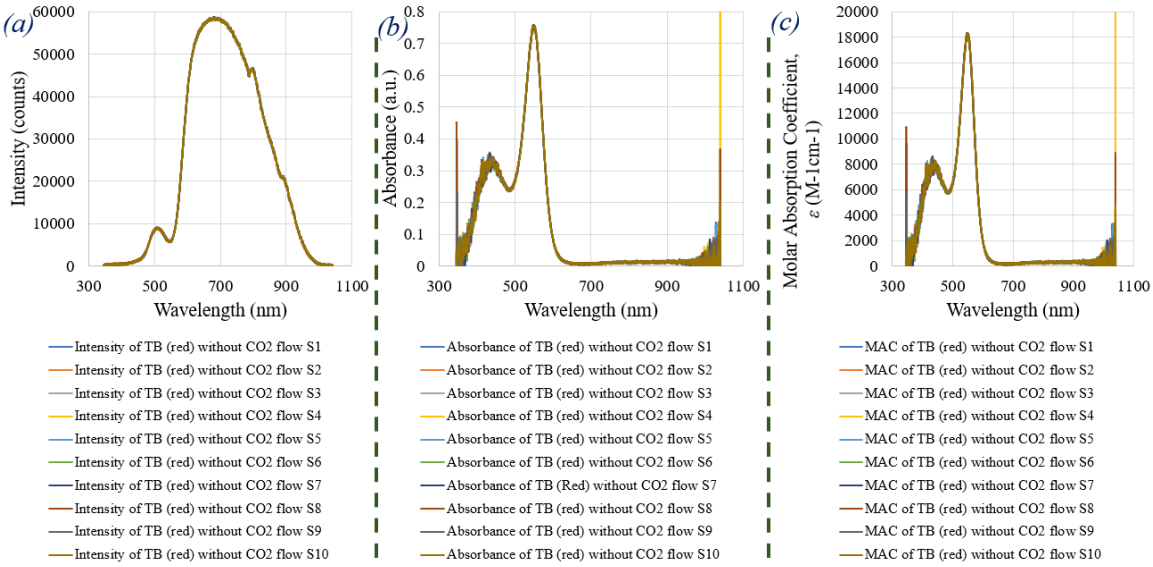


Figure 4.7: *(a) Transmission spectra (b) Absorption spectra (c) MAC curve of TB (red) without CO_2 flow*

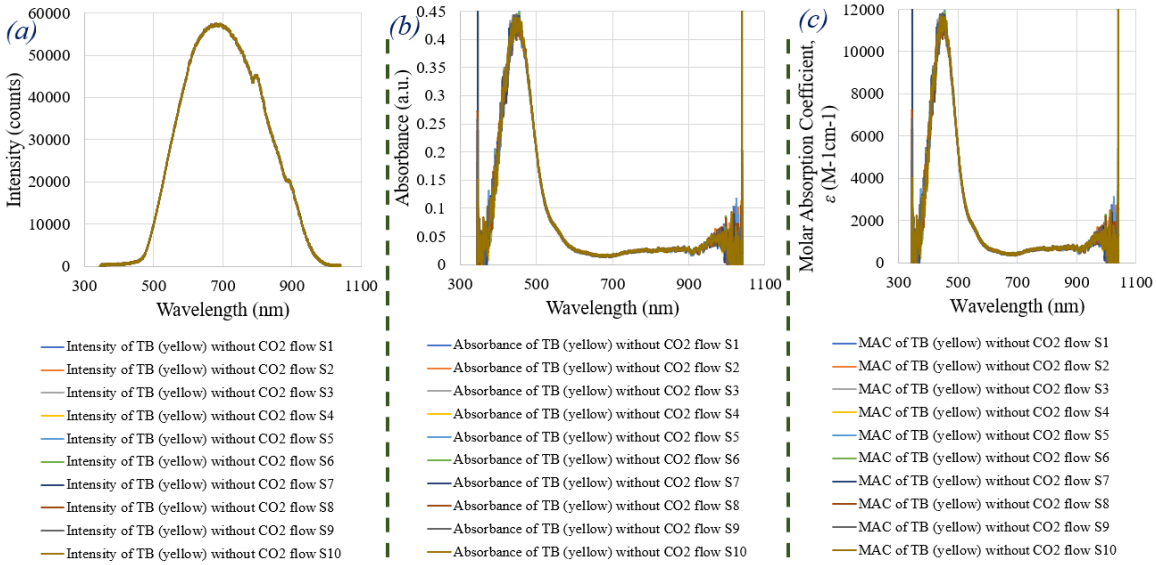


Figure 4.8: *(a) Transmission spectra (b) Absorption spectra (c) MAC curve of TB (yellow) without CO_2 flow*

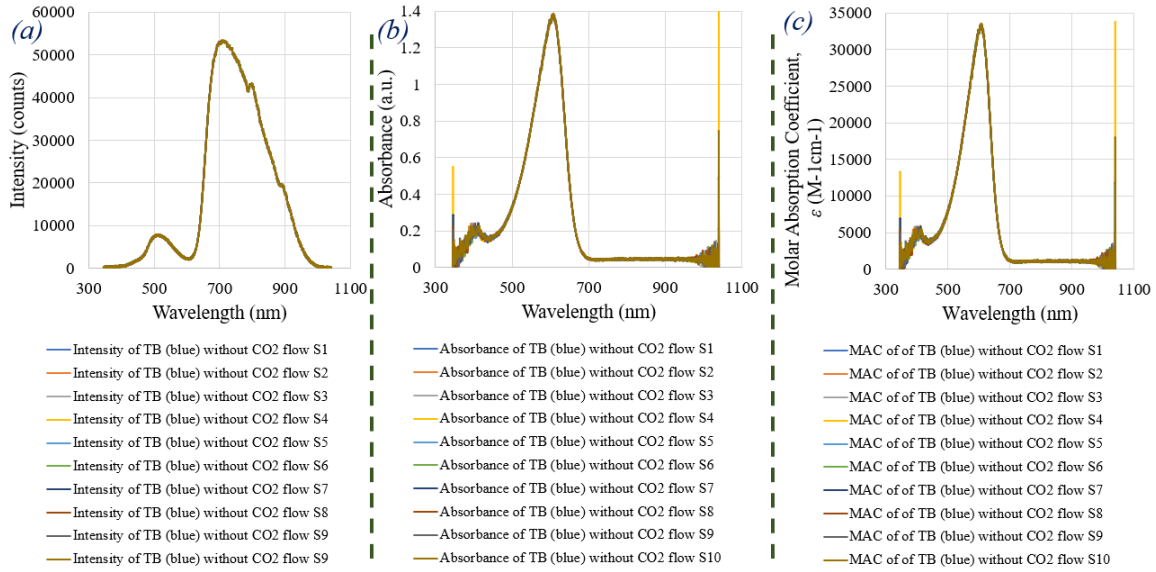


Figure 4.9: *(a) Transmission spectra (b) Absorption spectra (c) MAC curve of TB (blue) without CO_2 flow*

All the spectra with CO_2 flow are illustrated in Figures 4.10-4.13. In Figures 4.10, 4.11 (a), and 4.12 (a), the transmission spectrum is unstable because of bubbling CO_2 inside the solution, and the pH doesn't change due to bubbling CO_2 inside ethanol, TB (red), and TB (yellow). In Figure 4.13 (a), the transmission spectrum of TB (blue) becomes similar to the

transmission spectrum of TB (yellow), and the absorption at around 600 nm is lost due to changing pH because of bubbling CO_2 inside TB (blue) solution.

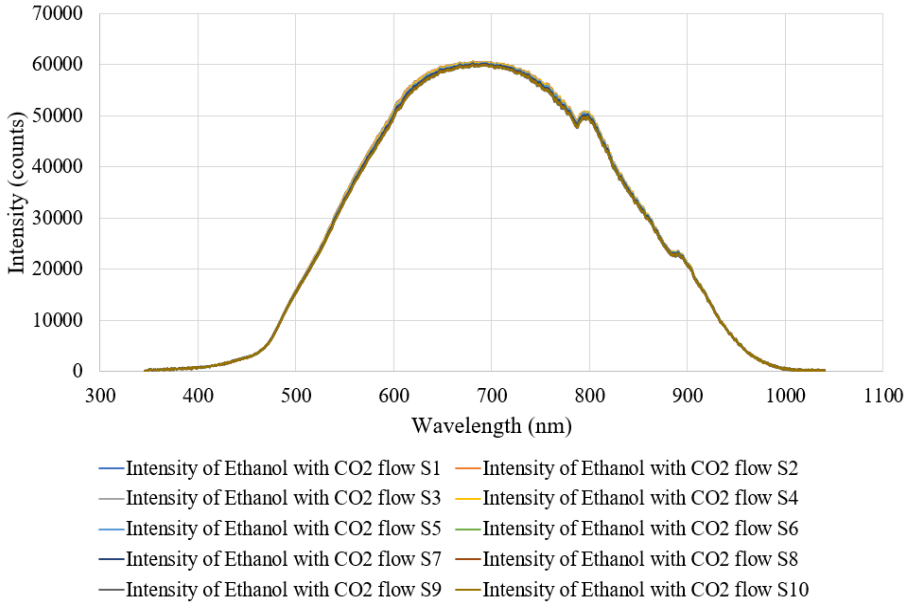


Figure 4.10: *Transmission spectra of Ethanol with CO_2 flow*

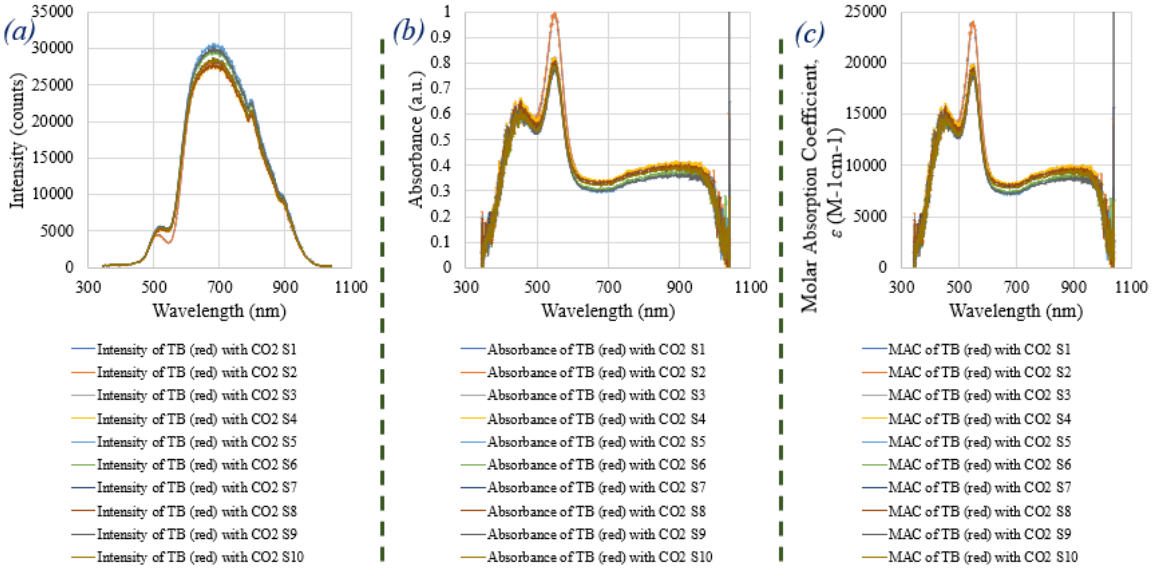


Figure 4.11: *(a) Transmission spectra (b) Absorption spectra (c) MAC curve of TB (red) with CO_2 flow*

All the graphs represent TB characteristics without CO_2 in Figure 4.7; on the other hand, all the graphs represent TB characteristics with CO_2 in Figure 4.11. The baseline between a wavelength of 700-900 nm is high because TB has the highest intensity at 700-900 nm,

and the intensity difference at this wavelength range was observed due to bubbling CO_2 inside TB solutions (creates non-regularity of the solution and the intensity was not steady state).

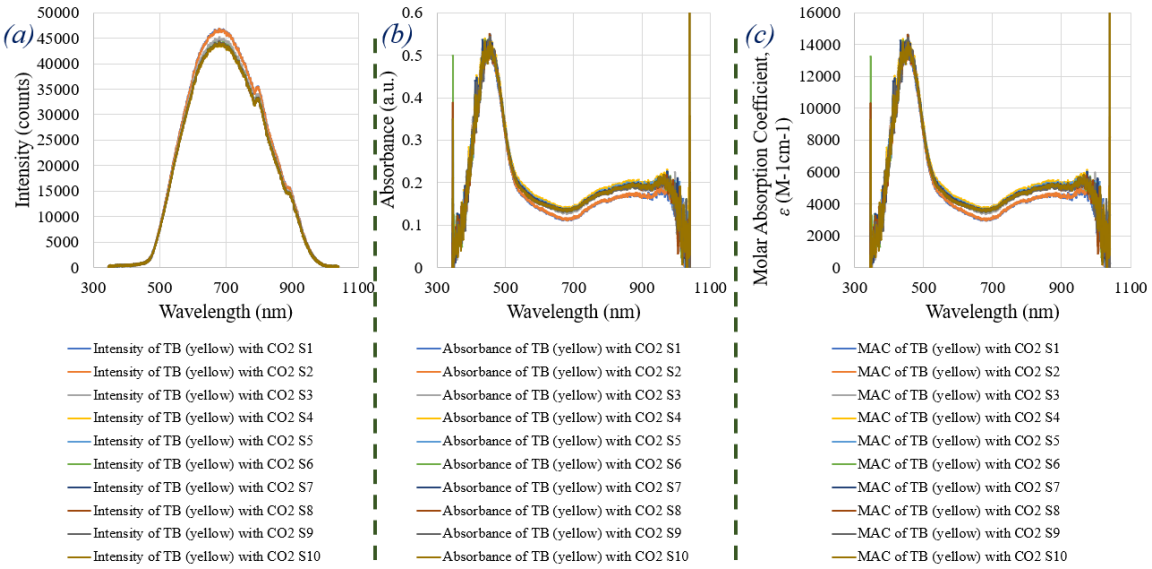


Figure 4.12: *(a) Transmission spectra (b) Absorption spectra (c) MAC curve of TB (yellow) with CO_2 flow*

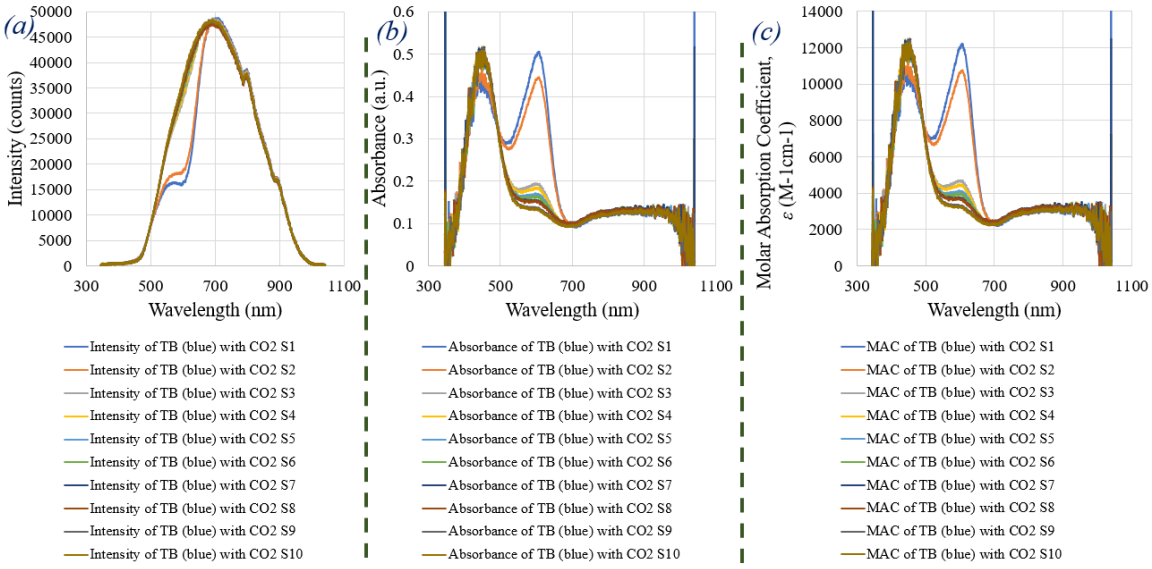


Figure 4.13: *(a) Transmission spectra (b) Absorption spectra (c) MAC curve of TB (blue) with CO_2 flow*

Comments about the shape of the response of TB (red), TB (yellow), and TB (blue) are presented in Table 4.3 according to the skewness and kurtosis values.

Table 4.3: *Interpretation of all spectra of TB for different pH values*

Thymol Blue	Average value of skewness for transmission spectra and comments	Average value of kurtosis for transmission spectra and comments	Average value of skewness for absorption Spectra and MAC curve and comments	Average value of kurtosis for absorption spectra and MAC curve and comments
Red without CO_2	0.43 Approximately Symmetric	-1.47 Platykurtic	1.89 Highly, Positively Skewed	3.06 Leptokurtic
Red with CO_2	0.45 Approximately Symmetric	-1.39 Platykurtic	0.57 Moderately, Positively Skewed	1.08 Leptokurtic
Yellow without CO_2	0.22 Approximately Symmetric	-1.55 Platykurtic	2.06 Highly, Positively Skewed	3.32 Leptokurtic
Yellow with CO_2	0.26 Approximately Symmetric	-1.51 Platykurtic	1.66 Highly, Positively Skewed	2.74 Leptokurtic
Blue without CO_2	0.83 Moderately, Positively Skewed	-0.89 Platykurtic	1.89 Highly, Positively Skewed	2.37 Leptokurtic
Blue with CO_2	0.29 Approximately Symmetric	-1.42 Platykurtic	1.62 Highly, Positively Skewed	2.21 Leptokurtic

Figure 4.14 shows the mean intensity, absorbance, and MAC at different wavelengths. Those wavelengths are based on the highest absorption peak of TB (red), TB (yellow), and TB (blue). The pH value of TB (red) and TB (yellow) is 6 and 5, respectively, with and without CO_2, but the pH value drops from 11 to 8 after bubbling CO_2 inside the TB (blue)

solution, and TB (blue) turns into TB (yellow). In Figure 4.14 (a), the mean intensity of TB (red) and TB (yellow) without CO_2 flow is slightly higher than with CO_2 at 549 nm and 452 nm, respectively. The mean intensity of TB (blue) without CO_2 flow is much lower than with CO_2 flow at 606 nm. The mean absorbance and MAC have the opposite trend of mean intensity. In Figures 4.14 (b) and (c), the mean absorbance and MAC of TB (red) and TB (yellow) without CO_2 flow are slightly lower than with CO_2 at 549 nm and 452 nm, respectively. The mean absorbance and MAC of TB (blue) without CO_2 flow are much higher than with CO_2 flow at 606 nm.

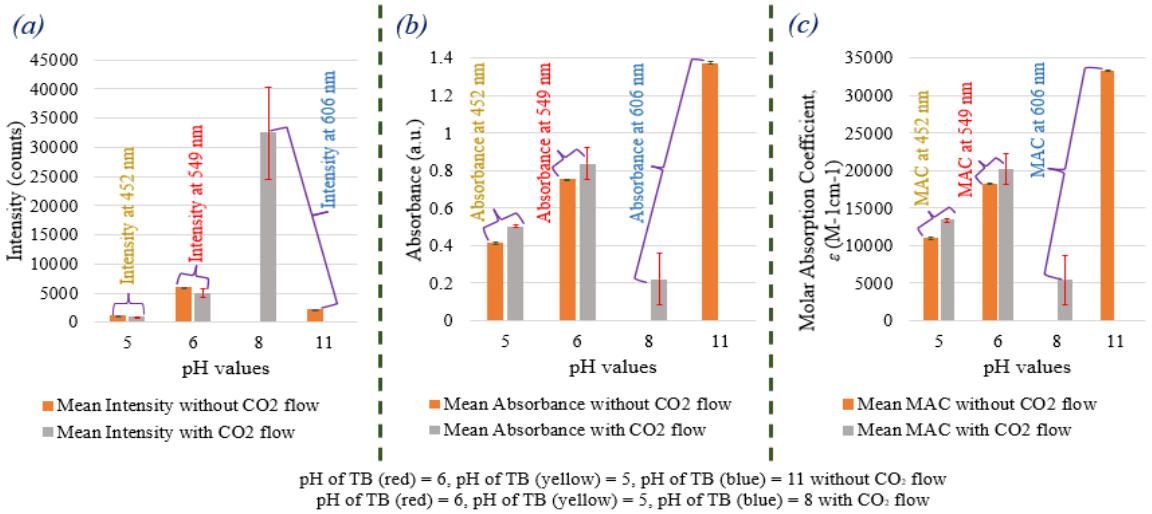


Figure 4.14: *(a) Mean Intensity (b) Mean Absorbance (c) Mean MAC of TB with and without CO_2 flow*

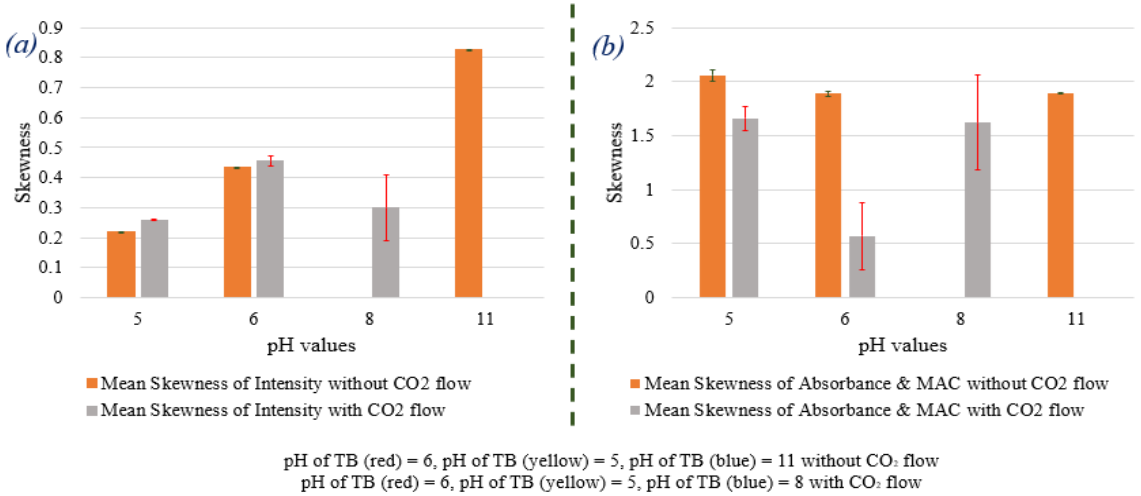


Figure 4.15: *Mean Skewness of (a) Intensity (b) Absorbance and MAC of TB with and without CO_2 flow*

In Figure 4.15 (a), the mean skewness of TB (blue) is higher than TB (red) and TB (yellow) without CO_2 flow. The mean skewness of TB (red) is higher than TB (blue) and TB (yellow) with CO_2 flow. In Figure 4.15 (b), the mean skewness of absorbance and MAC of TB (yellow) is higher than TB (red) and TB (blue) without CO_2 flow. The mean skewness of absorbance and MAC of TB (red) and TB (blue) are almost same without CO_2 flow. The mean skewness of absorbance and MAC of TB (red) is lower than TB (yellow) and TB (blue) with CO_2 flow. The mean skewness of absorbance and MAC of TB (yellow) and TB (red) are almost same with CO_2 flow.

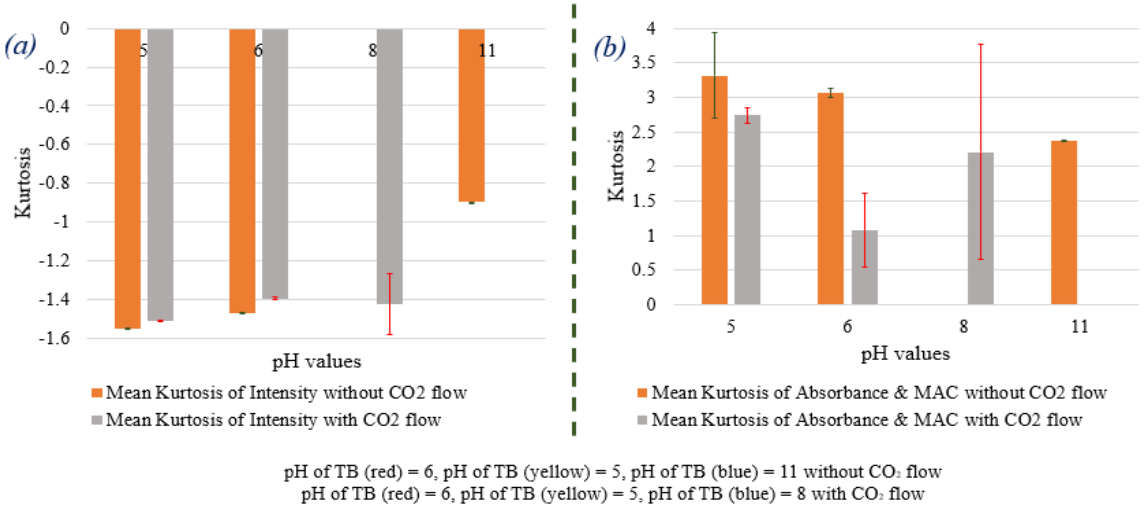


Figure 4.16: *Mean Kurtosis of (a) Intensity (b) Absorbance and MAC of TB with and without CO_2 flow*

In Figure 4.16 (a), the mean kurtosis of TB (blue) is higher than TB (red) and TB (yellow) without CO_2 flow. The mean kurtosis of TB (red) is higher than TB (blue) and TB (yellow) with CO_2 flow. In Figure 4.16 (b), the mean kurtosis of absorbance and MAC of TB (blue) is lower than TB (red) and TB (yellow) without CO_2 flow. The mean kurtosis of absorbance and MAC of TB (red) is lower than TB (yellow) and TB (blue) with CO_2 flow.

Skewness and kurtosis are parameters that might be useful in observing how the shape of the spectrum of TB varies according to pH and CO_2 variation. As shape is independent of the absolute intensity value it is potentially more reliable than measurements of attenuation. The skewness and kurtosis weren't used in the skin CO_2 measurements. The skewness and kurtosis can be used in future measurements according to Section 6.3.2.

4.3 Fabry-Perot interferometer

A Fabry-Perot arrangement is an optical cavity device that acts as an interferometer and is known as a Fabry-Perot interferometer. French physicists Charles Fabry and Alfred Perot invented the FPI in 1899 [127].

4.3.1 Principle of operation

An FPI consists of 2 optical reflectors M_1 and M_2, with reflectance R_1 and R_2 on either side of an optically transparent medium with length L, as shown in Figure 4.17. Two planar mirrors allow propagation of the light between the mirrors [127]. Current advancements have permitted FPIs to be developed also at an optical fibre tip. A fibre-tip FPI sensor merges the exclusive features of both optical fibre and FPI sensors. The thickness of the FPI is controlled with a multiple cycle dip-coating process for visualising the interference fringes. In Figure 4.17, film materials such as silica, polymer, pyrex, and graphene can be coated on the fibre tip for the optical fibre FPI sensor. The optical fibre FPI sensor provides immunity to EMI, the ability to respond to a large variety of factors, high sensitivity, high resolution, high accuracy, easy fabrication, small size, and low cost [128]. For example, pressure can be measured using an optical fibre FP pressure sensor. The incident light on the FP cavity changes when pressure is applied to the diaphragm. The reflected light is wavelength modulated by variations in this FP cavity's width [58].

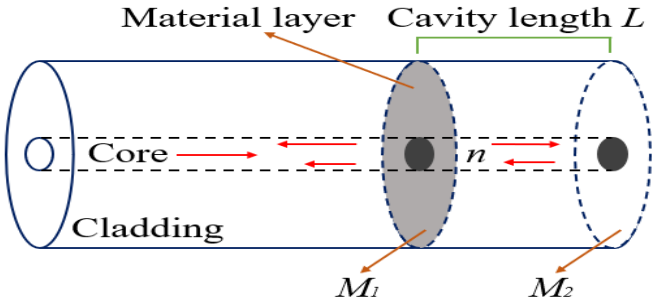


Figure 4.17: *Schematic diagram of fibre-tip FPI sensor (adapted from [127])*

The interference between the multiple reflections of light between 2 interfaces affects the transmitted beams of an FPI. Constructive interference occurs when the transmitted beams are in phase resulting in maximum transmission. Figure 4.18 (a) shows that constructive interference retains the frequency and doubles the amplitude when 2 identical waves (in

phase) of the same period and amplitude arrive at the detector simultaneously. On the other hand, destructive interference occurs when the transmitted beams are out-of-phase, resulting in minimum transmission. Figure 4.18 (b) illustrates that destructive interference occurs when 2 identical waves (out-of-phase) arrive simultaneously, and the amplitude becomes zero. Depending on the optical path difference, the reflected beams will be in-phase or out-of-phase. The optical path difference between 2 neighbouring rays depends on the RI of the medium in the cavity, the FPI cavity's thickness, and the incidence angle. The progression of constructive and destructive interference leads to the bright and dark fringes that form an interference pattern [129-131].

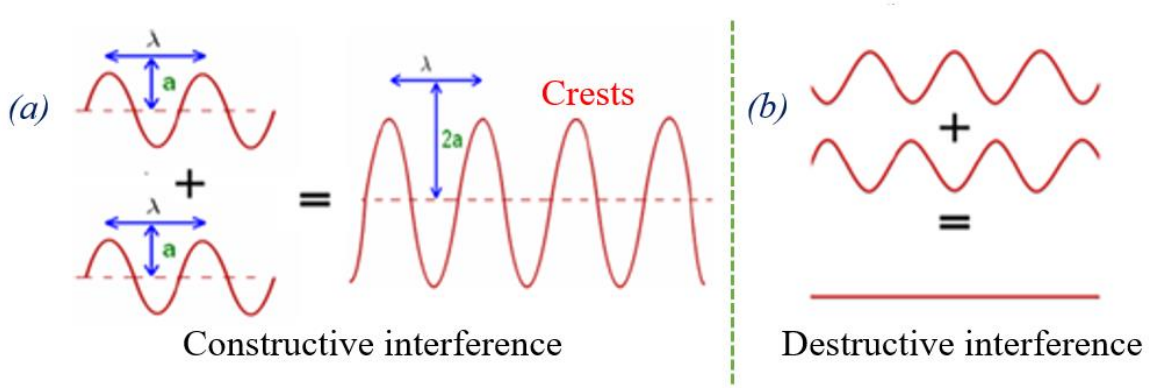


Figure 4.18: *(a) Constructive (b) Destructive interference occurs when 2 waves meet [130]*

In this thesis, the OFCS was coated onto the fibre tip with Ormosil films consisting of TB and TMAH during the sol-gel process to detect CO_2. The sensitive coated tip layer of the optical fibre forms the FPI cavity with a length of a few micrometres depending upon the layer thickness. The light transmits from the fibre into the film and from this film into the air; reflectance happens at every interface (presenting a differential RI medium) on its route, and as a result FPI fringes are observed [109].

4.3.2 Relevant formulas

The relationship between reflectance, R_i and transmittance, T_i of the FPI in a lossless cavity is given by [127]:

$$R_i + T_i = 1 \qquad (4.3)$$

where i is the number of optical reflections [127].

The reflectance, *R* and transmittance, *T* are calculated using the following equations [127]:

$$R = \frac{R_1 + R_2 + 2\sqrt{R_1 R_2}cos\,\varphi}{1 + R_1 + R_2 + 2\sqrt{R_1 R_2}cos\,\varphi} \quad (4.4)$$

$$T = \frac{T_1 T_2}{1 + R_1 + R_2 + 2\sqrt{R_1 R_2}\cos\varphi} \quad (4.5)$$

where *R* is the ratio of the reflected intensity I_r to the incident intensity I_i, *T* is the ratio of the transmitted intensity I_t to the incident intensity I_i, and φ is the propagation phase shift in the FPI, which is calculated as follows [127]:

$$\varphi = \frac{2\pi}{\lambda}\Delta \quad (4.6)$$

where Δ is the optical path difference (OPD), that mainly depends on the characteristics of the cavity and λ is the free-space optical wavelength [127].

The optical difference is given by [129]:

$$\Delta = 2nLcos\theta \quad (4.7)$$

where *n* the RI of the medium in cavity, *L* is the thickness of the FPI cavity, and θ is the angle of incidence [129].

The Fresnel reflection describes how the incident light is reflected at both surfaces, here Fresnel coefficient, R_1 and R_2 are given by [132]:

$$R_1 = \left(\frac{n_1 - n_f}{n_1 + n_f}\right)^2 \quad (4.8)$$

$$R_2 = \left(\frac{n_f - n_{air}}{n_f + n_{air}}\right)^2 \quad (4.9)$$

where n_1, n_f, and n_{air} are the refractive indices of the fibre, thin film, and air, respectively. R_1 and R_2 are the power reflection coefficients at surfaces 1 and 2, respectively [132].

Reference [131] has extended the FPI model by incorporating a lossy cavity. The normalised reflection spectrum, $I_{FP}(\lambda)$ for the thin film FPI case is described by [132]:

$$I_{FP}(\lambda) = R_1 + (1 - T_L)^2 (1 - R_1)^2 (1 - \alpha)^2 R_2 - 2\sqrt{R_1 R_2}\,(1 - T_L)(1 - R_1)(1 - \alpha)\cos\left(\frac{4\pi n_f L}{\lambda}\right) \quad (4.10)$$

The absorption spectrum, $A(\lambda)$ is possible to measure using the normalised reflection spectrum as follows [109]:

$$A(\lambda) = log_{10}\left(\frac{1}{I_{FP}(\lambda)}\right) \quad (4.11)$$

The equivalent total loss factor, K of the coated fibre tip is measured using the following formula [133]:

$$K = (1 - T_L)(1 - \alpha) \quad (4.12)$$

where α is the cavity loss (it depends on the amount of absorbed light within the cavity length), T_L is the transmission loss (it occurs due to the transmission at each interface), L is the physical thickness of the coating, n_f is the effective RI of the film, and λ is the wavelength [68].

The fringe visibility (FV) is calculated by identifying the maximum intensity, $I_{max,}$ and minimum intensity, I_{min} of the fringes [134]:

$$FV = \frac{I_{max} - I_{min}}{I_{max} + I_{min}} \quad (4.13)$$

Eq. (4.10) describes the interference pattern of the light reflected from the coated fibre tip with the FP cavity [132]. The film thickness affects the period of the interference pattern, fringe visibility, and cavity loss factor. The cavity's loss factor and beam divergence will rise as the film thickness does. The parameters K, FV, and interference period will all decrease with increasing film thickness. As the film thickness increases, the device's performance will suffer [133].

Fringe visibility doesn't have any significance for CO_2 detection using the OFCS. Fringe visibility was calculated from the simulated reflection spectrum to observe the film thickness and fringe visibility relationship.

4.4 Optimise film thickness according to fringe visibility

The simulated normalised intensity and absorbance of the FPI can be found using Eq. (4.10) and (4.11), respectively, using MATLAB. The MAC value is taken from Figure 3.6 (c) and presented separately in Figure 4.19 for simulation.

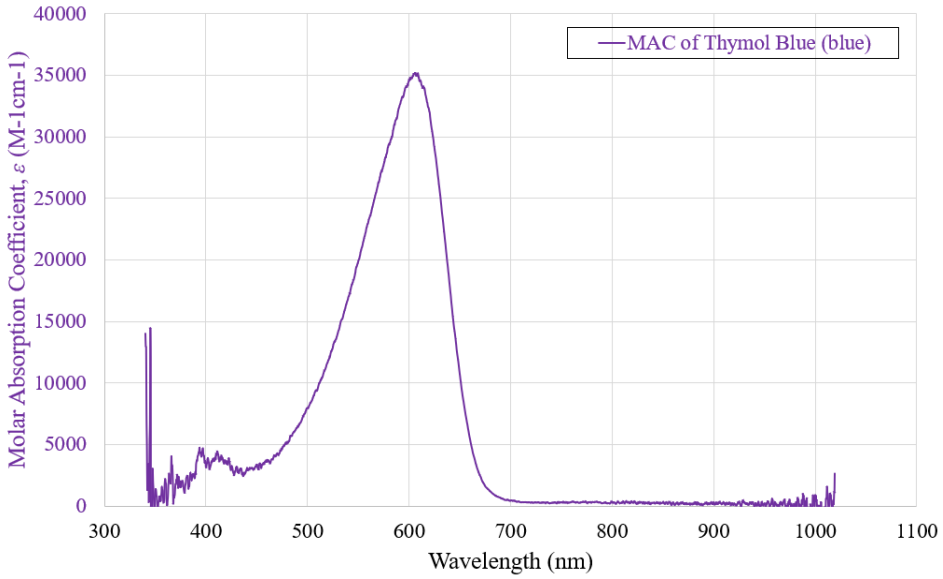


Figure 4.19: *MAC curve of TB (blue)*

The value of the parameters which is used in Eq. (4.10) and (4.11) is provided in Table 4.4. The abbreviation of the parameters is mentioned in Section 4.3.2.

Table 4.4: *The necessary parameters' values for simulation of FPI*

Parameter's symbol	Value
R_1 & R_2 is calculated using Eq. (4.8) & (4.9)	
n_1	1.475 [114]
n_f	1.501 [109]
n_{air}	1.003 [135]
T_L	0.4 [135]
α is calculated using Eq. (3.8)	
$\varepsilon\ (\lambda)$	Figure 4.19
c	0.030 M from dried film
L	4.888 / 5.690 / 7.234 µm from SEM images
λ	340-1019 nm

Figures 4.20 (a), 4.21 (a), and 4.22 (a) illustrate the simulated reflection spectrum of the FPI for the film thickness of 4.888, 5.690, and 7.234 µm, respectively. There is a trough, and the intensity value is low at around 600 nm. Figures 4.20 (b), 4.21 (b), and 4.22 (b) demonstrate the simulated absorption spectrum of the FPI for the film thickness of 4.888, 5.690, and 7.234 µm, respectively. There is a peak, and the absorbance value is high at around 600 nm. The normalised intensity and fringe visibility at about 600 nm decrease, absorbance at nearly 600 nm and the number of fringes increase due to rising film thickness.

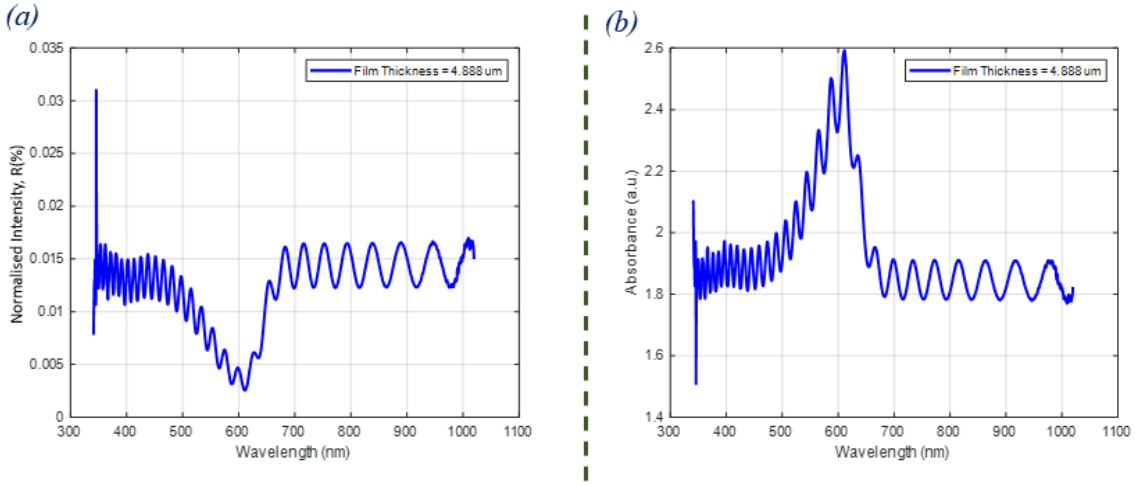


Figure 4.20: *Simulated (a) Reflection spectrum (b) Absorption spectrum of FPI for film thickness 4.888 µm*

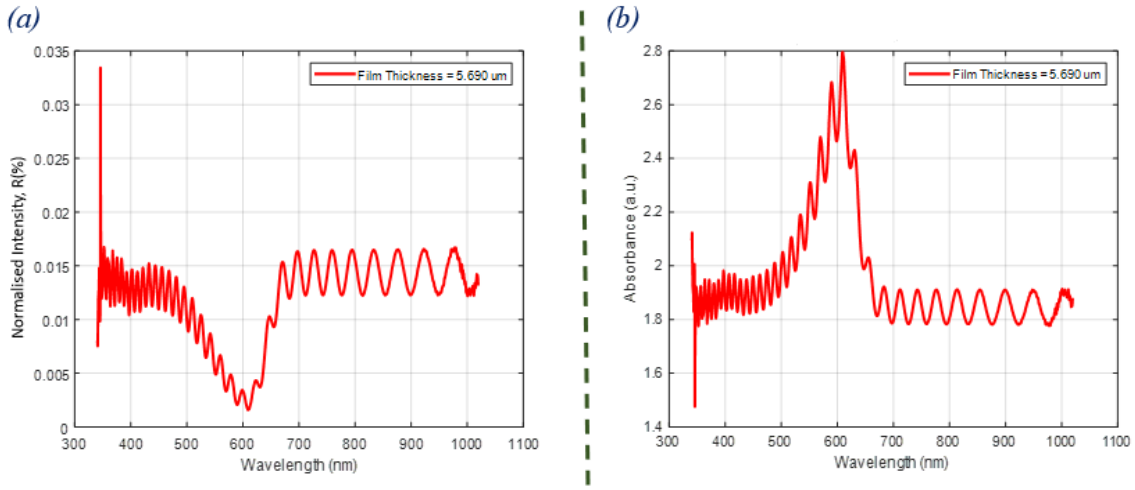


Figure 4.21: *Simulated (a) Reflection spectrum (b) Absorption spectrum of FPI for film thickness 5.690 µm*

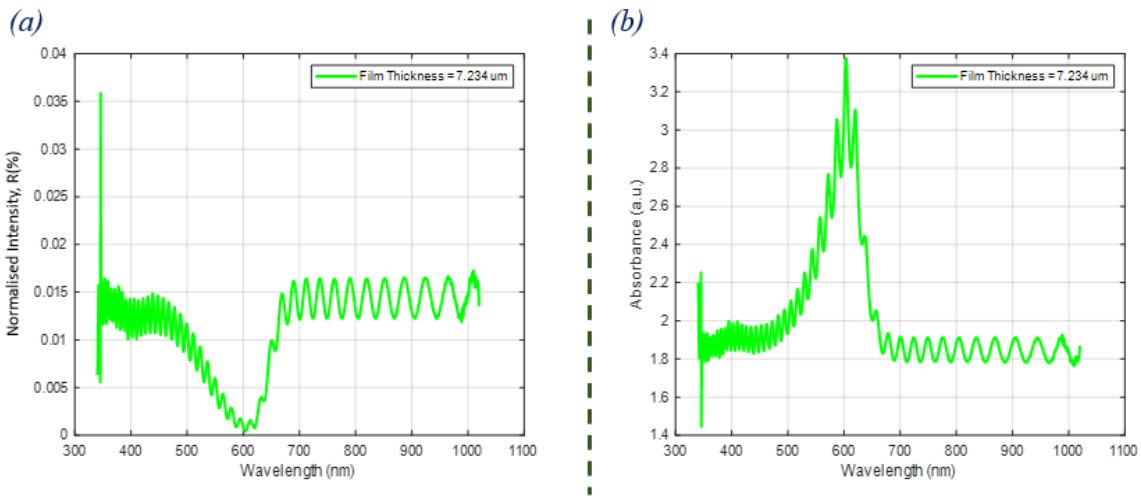


Figure 4.22: *Simulated (a) Reflection spectrum (b) Absorption spectrum of FPI for film thickness 7.234 µm*

The FV of the FPI is calculated using Eq. (4.13) for the film thickness (L) of 4.888, 5.690, and 7.234 µm, respectively. The maximum and minimum intensities at a wavelength range of 586-598 nm area are found in Figures 4.23-4.25. The wavelength gap between maximum and minimum intensities is 12, 8, and 6 nm for the film thickness of 4.888, 5.690, and 7.234 µm, respectively.

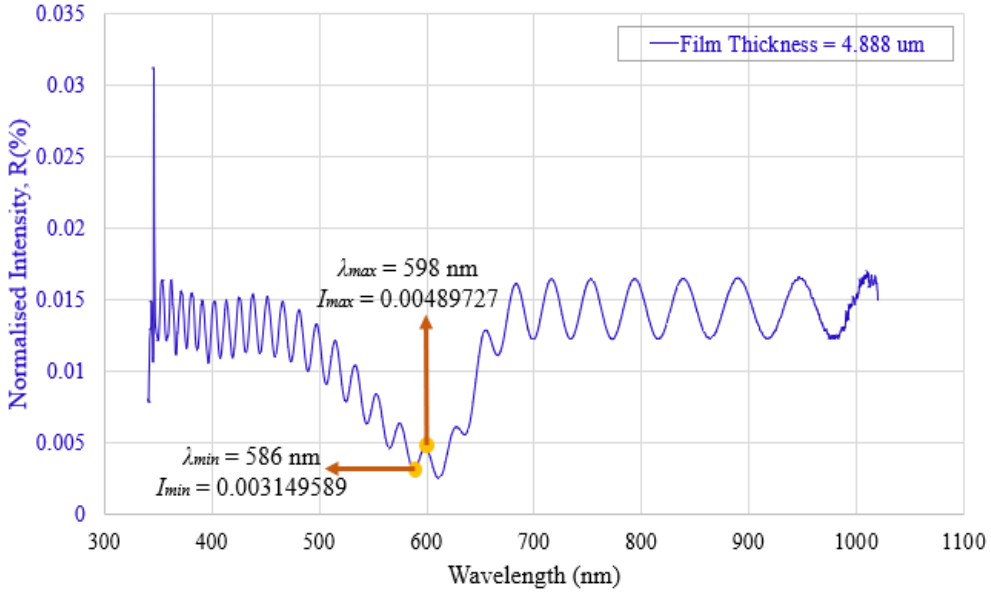


Figure 4.23: *The maximum and minimum intensity detection from simulated reflection spectrum of FPI for film thickness 4.888 µm at wavelengths 586-598 nm*

$FV_{(L=4.888\ \mu m)} = [(0.004489727 - 0.003149589) / (0.004489727 + 0.003149589)] = 0.2172$

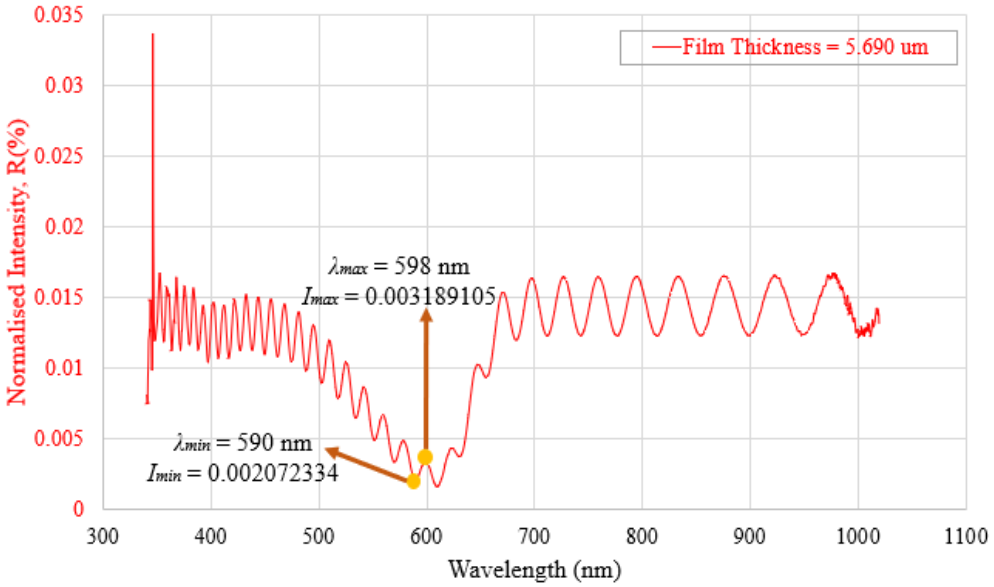


Figure 4.24: *The maximum and minimum intensity detection from simulated reflection spectrum of FPI for film thickness 5.690 µm at wavelengths 586-598 nm*

$FV_{(L=5.690\ \mu m)} = [(0.003189105 - 0.002072334) / (0.003189105 + 0.002072334)] = 0.2122$

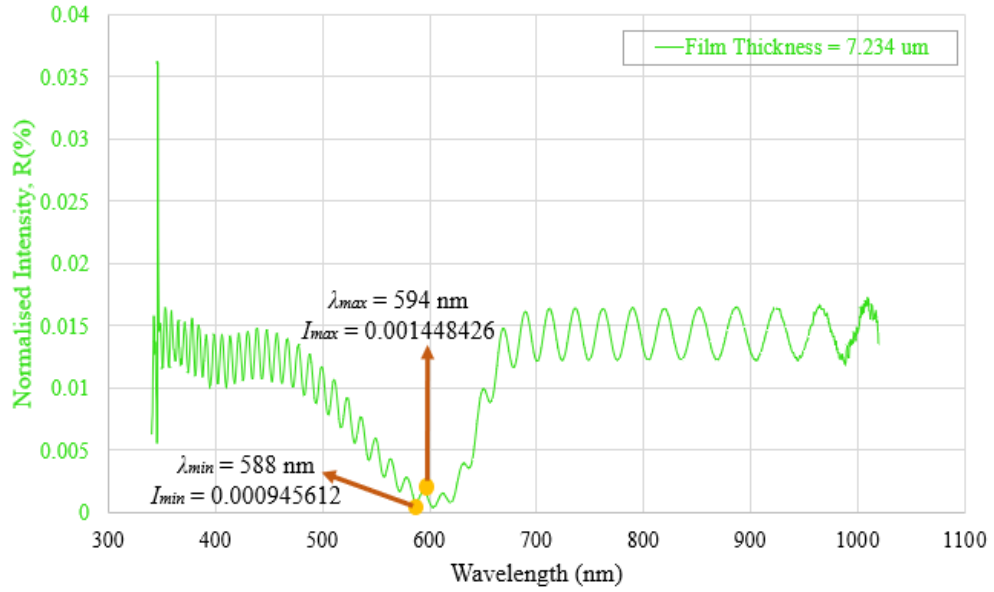


Figure 4.25: *The maximum and minimum intensity detection from simulated reflection spectrum of FPI for film thickness 7.234 µm at wavelengths 586-598 nm*

$FV_{(L=7.234\ \mu m)} = [(0.001448426 - 0.000945612) / (0.001448426 + 0.000945612)] = 0.2100$

Figure 4.26 shows the relationship between the film thickness and fringe visibility. The film thickness is inversely proportional to the fringe visibility at a wavelength range of 586-598 nm.

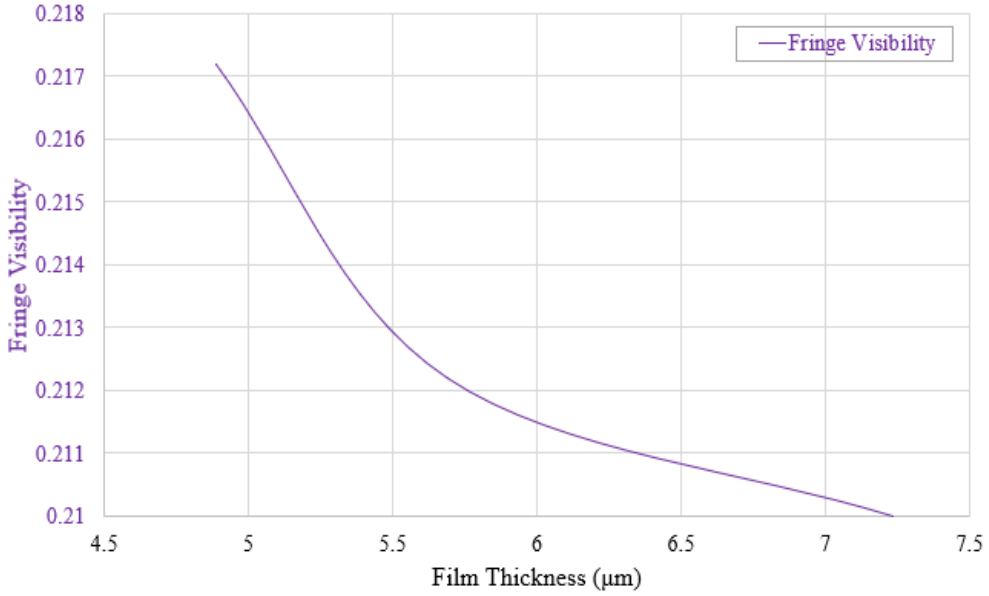


Figure 4.26: *Fringe visibility of FPI by varying film thickness at wavelengths 586-598 nm*

The fringe became less visible for 3 layers of coating for simulation at a wavelength range of 586-598 nm, (inside the absorption window) and it is also observed from the fabricated OFCSs, as mentioned in Section 3.3.2. The wavelength window (585-615 nm) is sensitive to CO_2. However, the fringe visibility improves at a wavelength window (700-900 nm) due to rising film thickness. The wavelength window (700-900 nm) is not sensitive to CO_2. If the film thickness is increased, the cavity loss will also increase, as discussed in Section 4.3.2. So, 7.234 μm can be selected as an optimum film thickness for the simulation of the FPI.

Figure 3.12 is presented separately in Figure 4.27 for calculating the fringe visibility of the OFCS. The FV of the FPI is calculated using Eq. (4.13) for the film thickness (L) of 3.835 μm (1 layer) and 6.259 μm (2 layers). This film thickness is obtained from Table 3.2. The maximum and minimum intensities at a wavelength range of 525-567 nm are found in Figure 4.27. The wavelength separation between maximum and minimum intensities is 16 nm and 13 nm for the film thickness of 3.835 μm and 6.259 μm, respectively.

$FV_{(L=3.835\ \mu m)}$ = [(15739 – 12113) / (15739 + 12113)] = 0.1302

$FV_{(L=6.259\ \mu m)}$ = [(27207 – 24153) / (27207 + 24153)] = 0.0595

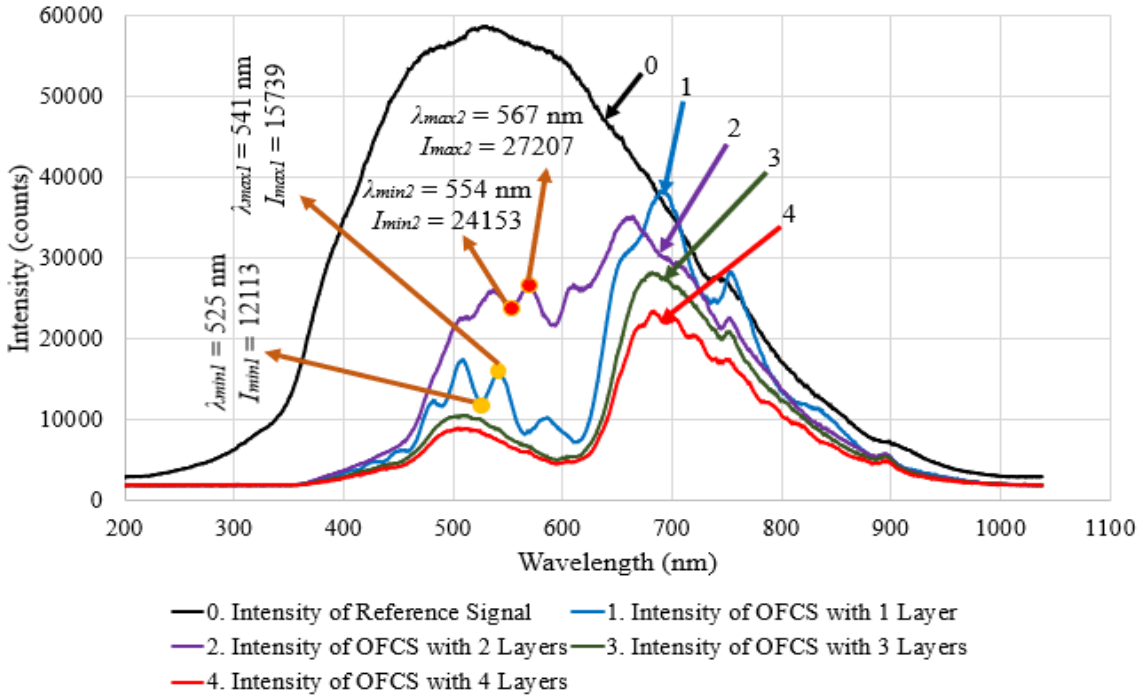


Figure 4.27: *The maximum and minimum intensity detection from reflection spectrum of OFCS for film thickness 3.835 µm and 6.259 µm at wavelengths 525-567 nm*

The minimum FV is calculated as 0.0595 for 2nd layer, which is shown in Figure 4.27. The fringes are no longer visible for thicker layers. The film thickness used in the FPI simulation was obtained from SEM images of other OFCSs (Section 3.6). The film thickness for the OFCS 3 with 3 layers is 7.234 µm in Figure 3.37. The fringes are no longer visible after the 2nd layer, according to Figure 4.27. The fringe visibility differs between the experiment (0.0595 for 2nd layer) and simulations (0.2122 for 2nd layer) because of the different values of reflection intensities obtained from experimental and simulated reflection spectra. This is due to not considering the experimental film roughness and thickness (practically controlled by the withdrawal speed) during FPI simulation. Therefore 7.234 µm is considered as an optimum film thickness. More discussion about choosing the optimum film thickness can be found in Section 3.3.3.

4.5 Summary

This chapter has demonstrated the different shapes of the spectrum of TB according to CO_2 flow and pH variation using skewness and kurtosis. TB (blue) turned to TB (yellow) after mixing the CO_2, and the spectrum's shape was also changed.

The basic principle of the FPI was described by using the relevant equations. The fringe visibility within the absorption band (wavelength window 585-615 nm) became lower due to the rise of film thickness. The optimum film thickness was obtained as 7.234 μm by considering the relationship between the fringe visibility and film thickness.

Qualitatively, the experimental and simulated reflection and absorption spectra of the OFCS had similar features in Figure 3.13 (b), Section 3.3.2 and Figures 4.20 (b), 4.21 (b), and 4.22 (b), respectively. Each spectrum had clearly visible fringes and the highest absorption peak at around 600 nm. However, quantitatively, the experimental and simulated reflection, absorption spectra, and fringe visibility of the OFCS were not the same because the experimental film roughness and thickness were not considered during the FPI simulation because, practically, the film thickness of the FPI was controlled by the withdrawal speed according to Section 3.2.6. Improvements to the FPI model will be discussed in Chapter 6.

5. Chapter 5

Monitoring CO_2 Emitted from Human Skin

5.1 Introduction

To understand the behaviour of an optical fibre CO_2 sensor, a commercial CO_2 sensor, and a t_C Sensor 92 probe, it is important to test the devices on the skin and monitor their responses. Section 5.2 describes the set-up for monitoring CO_2 emitted from the skin using the t_C Sensor 92 probe and presents the achieved results. Section 5.3 discusses the set-up for monitoring CO_2 emitted from the skin during loading using the OFCS and commercial CO_2 sensor and illustrates the achieved results from both set-ups. Finally, Section 5.4 provides the summary of this chapter.

5.2 Monitoring CO_2 emitted from human skin using a t_C Sensor 92 probe

This section contains the experimental procedure and the results of PCO_2 measurements from volunteers' forearms at 2 different temperatures. This test is essential to understand the effect of temperature on the possibility of detecting PCO_2 values and the consistency of measurements for different volunteers. The ethical approval and risk assessment are provided by the Faculty of Engineering Ethics Committee and Health and Safety Advisor of the University of Nottingham (UoN), respectively [Appendix D].

5.2.1 Experimental set-up for monitoring CO_2 emitted from human skin using a t_C Sensor 92 probe

In Figure 5.1, a fixation ring is attached to the volunteer's hand alongside the t_C Sensor 92 probe. The t_C Sensor 92 probe is connected to the monitoring unit, TCM TOSCA monitor, which is used to observe the data and record the results. The working principle of the t_C Sensor 92 probe during PCO_2 measurement from human skin is described in Section 2.5.

Before the experiment, the participants were asked to clean the skin under test using alcohol wipe tissue (70 % alcohol) provided by the experimenter and allow their skin to adjust to the environment. At the beginning, all participants were required to sit quietly for 5 minutes

before the experiment commences. The surface of the t_C Sensor 92 was also cleaned by alcohol wipe tissue (70 % alcohol). The sensor was calibrated at the temperature at which experiments were conducted (37 °C and 42 °C). Figure 5.2 shows the sensor is placed in the calibration chamber of the TCM TOSCA monitor and the ready screen appears after completing the calibration. A study that took 40 patients aged between 66 and 97 years old has shown that a sensor temperature of 43 °C was well tolerated by the patients for around 8 hours of continuous monitoring at the same measuring site [4].

Following manufacturer's instructions, the following procedure is followed:

a) Volunteers were asked to place a fixation ring (as shown in Figure 5.1) just on top of the skin (forearm).

b) A small drop of the contact gel (as shown in Figure 5.1) was applied to the skin area in the centre of the fixation ring and there was a 2-minute delay.

c) The sensor was attached to the adhesive layer in the centre of the fixation ring and was pressed gently against the skin to spread the contact gel.

d) The experiments were run at sensor temperatures of 37 °C or 42 °C, and the duration of the experiment was 30 minutes.

e) Each participant was tested 5 times. The sensor requires around 10-15 minutes to stabilise and so the average PCO_2 value was calculated for the last 15 minutes for all volunteers. The measurements were conducted with at least 2 hours break to avoid prolonged exposure of the skin using the attached sensor to the skin.

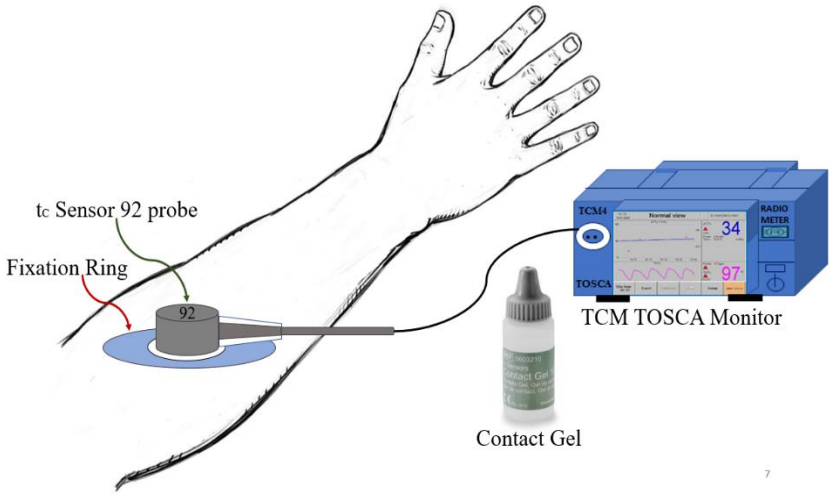


Figure 5.1: *Experimental set-up for monitoring PCO_2 from human skin using t_C Sensor 92 probe*

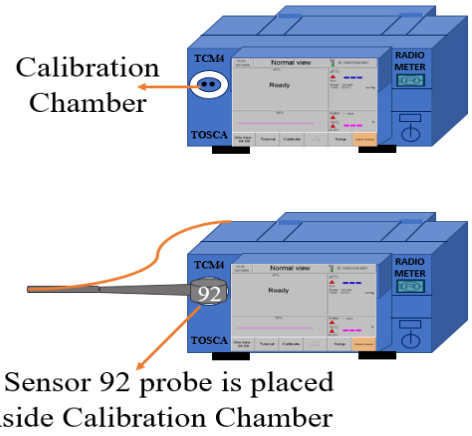


Figure 5.2: *Calibration process of t_C Sensor 92 probe using TCM TOSCA monitor*

According to the manufacturer (personal communication), the contact gel (CE marked) has been routinely used in cosmetics and healthcare, and there are no reported allergic reactions. The amount of sensitising substance present in the gel is very small, it contains 36.7 % propylene glycol and 0.125 % cis-1-(3-Chloroallyl)-3, 5, 7-triaza-1-azoniaadamantane chloride (Quaternium-15). Propylene glycol does not contain any hazardous substance or mixture and this ingredient's level of hazard is low. However, there is a tiny quantity of Quaternium-15, which may provoke an allergic reaction among individuals with sensitive skin [5]. Before the experiment, the volunteer was asked via a questionnaire if they had any allergies that are caused by exposing the skin to certain chemicals. If the volunteer had sensitive skin, they were excluded from this experiment.

After 2 minutes of observation, it was easier to detect if a participant with an unknown sensitivity does react to the chemicals used. If any rash arose after 2 minutes of observation, the volunteer was excluded from this experiment. It has been noted by the manufacturer (personal communication) that in more than 20 years of routine usage of the TCM probes in clinical practice, no allergic reaction was observed.

The PCO_2 values from a volunteer's forearm were recorded every 10 seconds using the TCM TOSCA monitor during the experiment. This experiment took around 30 minutes to complete steps a)-e) for each participant.

5.2.2 Calibration of PCO_2 and Temperature corrected PCO_2 values

The TCM TOSCA monitor has a reference gas chamber with 75000 ppm (7.5% CO_2) for calibration. The following calibrated PCO_2 values are calculated using the 7.5% CO_2 (at a barometric pressure, *B*, of 760 mmHg) [55]:

$$PCO_2(CAL) = B \times \left(\frac{\%\, CO_2}{100}\right) \qquad (5.1)$$

$$PCO_2(CAL) = 760\ mmHg \times \left(\frac{7.5}{100}\right) = 57\ mmHg$$

The PCO_2 value can also be found from the step up and step down response curve in Figure 3.16, Section 3.3.2. During this independent calibration, the t_C Sensor 92 probe was tested inside an alternative gas chamber during the calibration of the OFCS in Figure 3.11, Section 3.3.1. Table 5.1 shows the comparison between the PCO_2 values obtained from theoretical results [using Eq. (5.1)] and experimental results (using calibration data) for increasing and decreasing trends, respectively. The percentage error for 10000 ppm (1% CO_2) to 50000 ppm (5% CO_2) range is calculated in Table 5.1. The error range is 0.44 % to 12.01 % for 30000 ppm (3% CO_2) to 50000 ppm (5% CO_2) range. On the other hand, the error is around 24 % and 50 % for 20000 ppm (2% CO_2) and below 20000 ppm (2% CO_2), respectively.

Table 5.1: *PCO_2 value measurement for different CO_2 concentrations [obtained from Figures 3.16 (a) and (c), increasing trend (1.7% CO_2 to 4.6% CO_2) and Figures 3.16 (b) and (d), decreasing trend (5.3% CO_2 to 1.0% CO_2) respectively]*

CO_2 Concentration ppm (%)	10870 (1.0)	17400 (1.7)	19250 (1.9)	24030 (2.4)	29070 (2.9)	31240 (3.1)	38880 (3.8)	41290 (4.1)	46050 (4.6)	53500 (5.3)
Theoretical PCO_2, *ThP* (mmHg)	8.26	13.22	14.63	18.26	22.09	23.74	29.55	31.86	34.99	40.66
Experimental PCO_2, *ExP* (mmHg)	4	7	11	14	20	23	26	32	32	44
% Error = *(|ExP-ThP|/ThP) x 100*	51.57	47.05	24.81	23.33	9.46	3.12	12.01	0.44	3.13	8.21

Table 5.2: *Temperature correction factor for $T_C PCO_2$ measurement at different temperatures [55]*

Sensor temp, *T* (°C)	37	38	39	40	41	42	43	44	45
Temperature corr. factor	1.00	1.04	1.09	1.14	1.19	1.24	1.30	1.36	1.42
Temperature corr. PCO_2 value (mmHg)	57	55	52	50	48	46	44	42	40

The Severinghaus temperature correction factor is used in most clinical settings for measuring T_CPCO_2. Patients of all ages show a strong association between T_CPCO_2 and P_aCO_2. T_CPCO_2 is higher than P_aCO_2 due to the sensor's elevated temperature. The temperature correction factor is applied on the t_C Sensor 92 probe to achieve the T_CPCO_2 value, which will provide a closer estimation to the P_aCO_2 value [39] [55].

Two key reasons are responsible for the increase in the T_CPCO_2 levels. Firstly, the elevated temperature of the sensor causes the local blood and tissue PCO_2 measurement to increase by approximately 4.5 %/°C (anaerobic factor). Secondly, CO_2 is released from the living epidermal cells and capillary CO_2 level receives a continuous inflow of this CO_2 (metabolic constant). Skin thickness, age, and other physiological properties significantly affect the metabolic contribution. T_CPCO_2 increases by about 6-7 mmHg due to the skin metabolism increment [39] [55]. The T_CPCO_2 values are corrected to 37 °C (normal body temperature) using Eq. (5.3) [55]:

$$Temperature\ correction\ value = 10^{\alpha(T-37°C)} \qquad (5.2)$$

$$Temperature\ corrected\ value, T_CPCO_2\ (T) = \frac{PCO_2\ (CAL)}{10^{\alpha(T-37°C)}} \qquad (5.3)$$

where the anaerobic temperature coefficient of CO_2 in blood, α is 0.019 /ºC, T is the set sensor temperature, $PCO_2\ (CAL)$ value is 57 mmHg. The temperature correction factors calculated using these equations are shown in Table 5.2.

5.2.3 Results from monitoring CO_2 emitted from human skin using a t_C Sensor 92 probe

Figure 5.3 shows the changes of PCO_2 from the human forearm of one of the volunteers using the set-up, as shown in Figure 5.1.

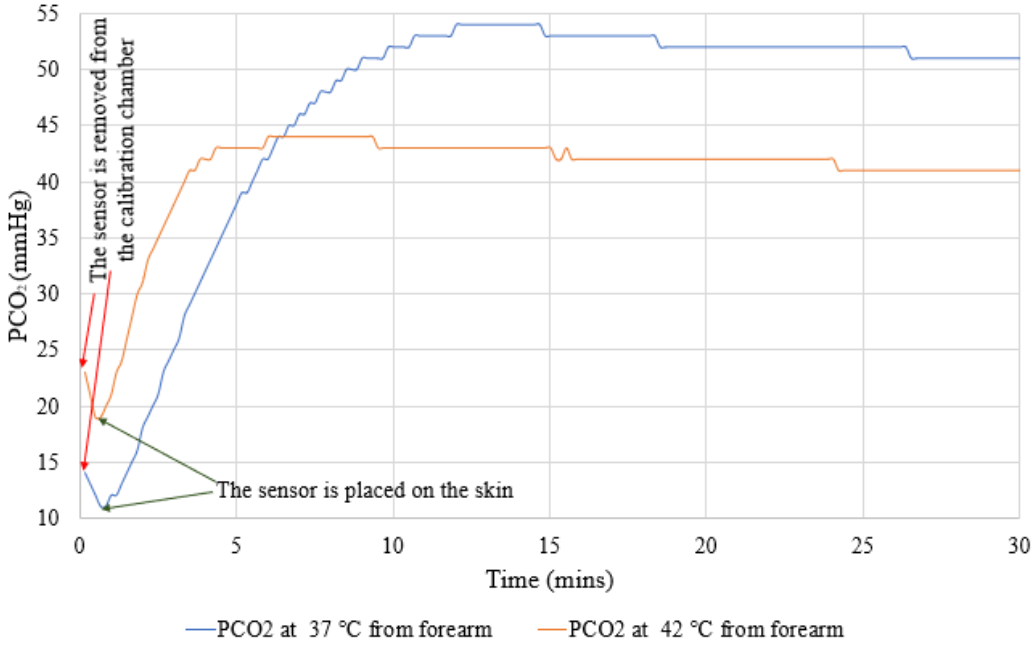


Figure 5.3: *PCO_2 measurement using t_C Sensor 92 probe for different temperatures when temperature correction factor is turned on*

When the sensor was placed on the skin, it took about 10-15 minutes for vasodilation to take place: only then were the transcutaneous readings meaningful. The temperature correction factor was turned on during this test. In Figure 5.3, a rapid rise is noticed for the first 5 minutes because the sensor is removed from the calibration chamber when t = 0 mins and placed on the skin at t = 45 seconds. In Table 5.2, the normal PCO_2 value is 57 mmHg and 46 mmHg at sensor temperatures of 37 °C and 42 °C, respectively. In Figure 5.3, the PCO_2 value rises with increasing time and reaches 52 mmHg and 42 mmHg (close to the normal range of PCO_2) when the contact gel is applied to the skin at temperatures of 37 °C and 42 °C, respectively. The obtained results from one of the volunteers in Figure 5.3 has same trend compared to the results mentioned in Table 5.2 but there are some differences.

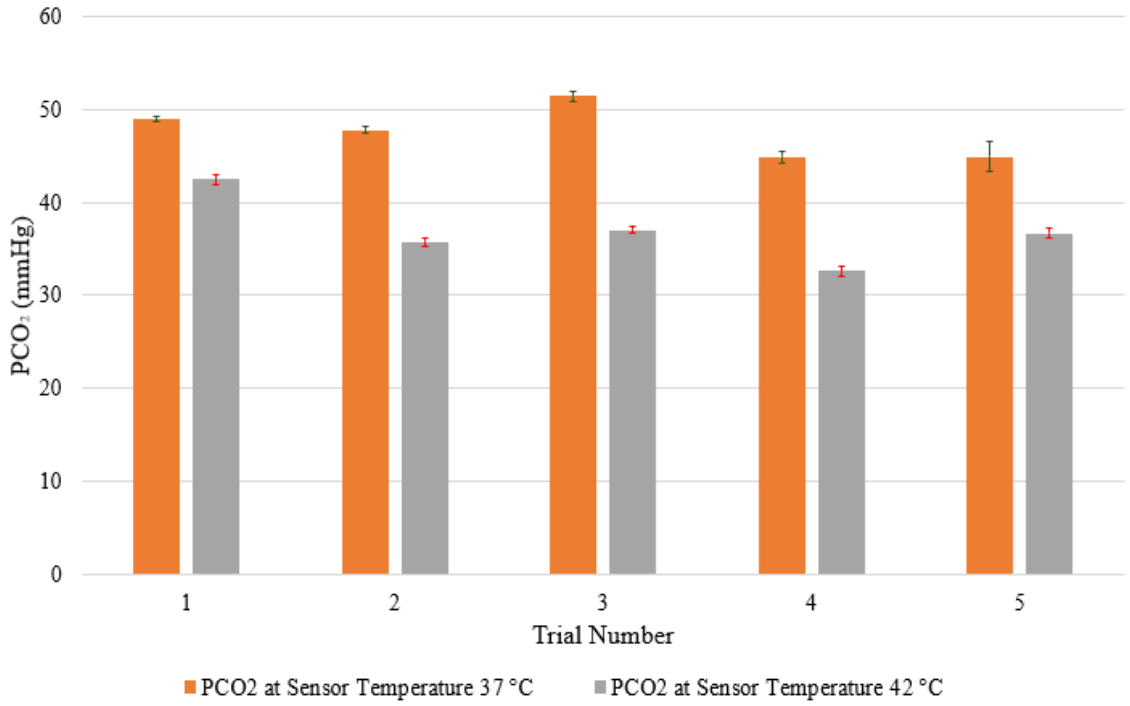


Figure 5.4: *Average PCO_2 measurement using t_C Sensor 92 probe from Volunteer 1's forearm (5 trials)*

Figure 5.4 and Figures B.1-B.9 [Appendix B] show the average PCO_2 measurement (last 15 minutes of data) using the t_C Sensor 92 probe from 10 volunteers' (Volunteer 1-10) forearms for 5 trials. The achieved PCO_2 values for 10 volunteers' (Volunteer 1-10) forearms are provided in Table 5.3.

Table 5.3: *Average PCO_2 values of 10 volunteers' at different sensor temperatures for 5 trials*

Volunteer number	Range of average PCO_2 values (mmHg) at 37 °C	Range of average PCO_2 values (mmHg) at 42 °C
1	44-51	32-42
2	43-47	33-39
3	50-55	39-44
4	45-48	35-36
5	48-51	37-48
6	47-55	39-42

Volunteer number	Range of average PCO_2 values (mmHg) at 37 °C	Range of average PCO_2 values (mmHg) at 42 °C
7	44-54	34-39
8	41-49	36-40
9	45-59	37-45
10	46-55	38-44

The achieved PCO_2 value at 37 °C is always higher than the obtained PCO_2 value at 42 °C. It happened due to applying the Severinghaus temperature correction factor during this experiment. The normal range of P_aCO_2 is 36-44 mmHg, as mentioned in Section 2.3.1. Table 5.2 shows the temperature corrected PCO_2 values for 37-45 °C (the t_C Sensor 92 probe's operating temperature). T_CPCO_2 increases as the sensor's temperature increases. However, the Severinghaus temperature correction factor is applied to balance the T_CPCO_2 and P_aCO_2 values. Therefore, the T_CPCO_2 value is calculated as 40 mmHg (matched to the P_aCO_2 value) for sensor temperature 45 °C, as opposed to the actual value. The P_aCO_2 values are not always close to the obtained PCO_2 values from the 10 volunteers (Volunteer 1-10). Also, the PCO_2 values from the 10 volunteers (Volunteer 1-10) differ. Variations in results could be attributed to 2 factors. Firstly, the sensor position is not the same for all the volunteers' (Volunteer 1-10) forearms at each trial. Secondly, the volunteer's physiological properties (such as age, skin thickness, and other variables) are different.

5.3 Monitoring CO_2 emitted from human skin during loading using an OFCS and a commercial CO_2 sensor

The skin under pressure reacts to loading, which cuts off the gas exchange and helps to accumulate CO_2 in the tissue, as mentioned in Section 2.2.4. The GCC (RTV silicone rubber) is replaced by a holder (polylactic acid, PLA, MP002267, Multicomp Pro, Farnell, UK) for a skin loading experiment. It was found that the RTV silicone is too soft (tensile strength = 5.8 MPa or 841 psi [136]), takes a long time to cure inside the mould and the bottom part of the GCC bends too easily when applying the load. The PLA based holder is easy to build with a 3D printing machine, and it's strong (tensile strength = 50 MPa or 7250

psi [137]) enough to withstand loading. It's also easy to make a hole as a further requirement.

5.3.1 Introduction to a loading machine

A loading machine has been implemented which consists of a weight holder and a steel rod with a ball bearing and a PLA based circular plate (Figure 5.5 (a)). The circular plate and PLA based holder have the same dimension. The circular plate attached to the ball bearing via a threaded nut provides a uniform load on the PLA based holder. In Figures 5.5 (b) and (c), the weight of the empty holder with the steel rod is around 0.5 kg. In Figure 5.5 (d), an additional slotted mass (100 g) is placed inside the weight holder to increase the load.

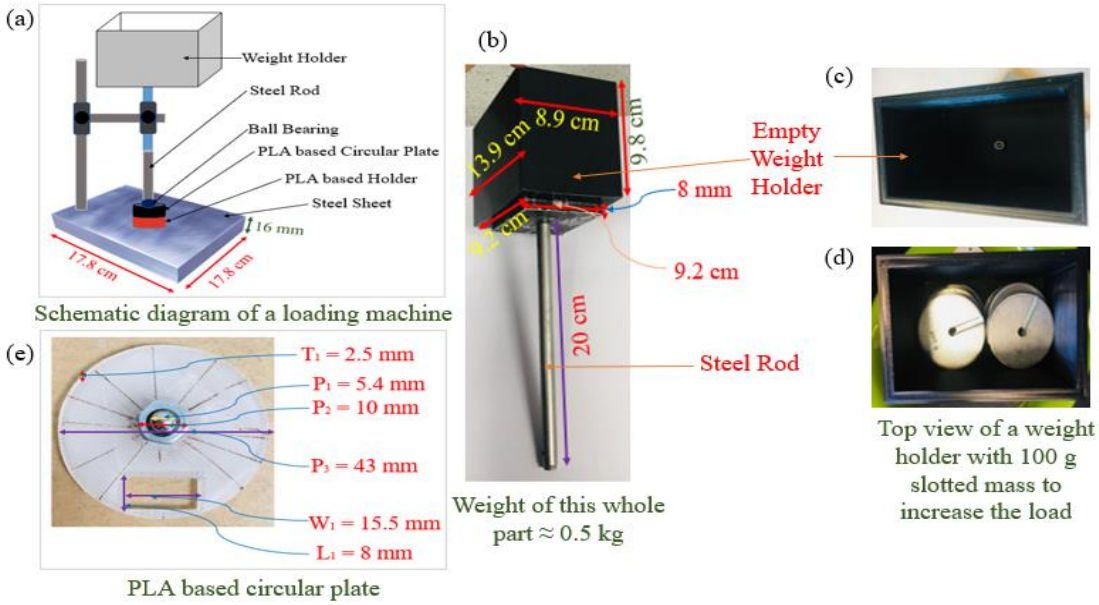


Figure 5.5: *(a) Schematic diagram of loading machine (b) Dimension of empty weight holder with steel rod (c) Top view of empty weight holder (d) Top view of weight holder with 100 g slotted mass (e) Dimension of PLA based circular plate*

In Figure 5.5 (e), the diameter of the ball bearing (P_1), the outer diameter of the threaded nut (P_2), and the diameter of the circular plate (P_3) are 5.4, 10, and 43 mm, respectively. The thickness of the circular plate (T_1) is 2.5 mm. There is a rectangular hole (length, L_1 = 8 mm and width, W_1 = 15.5 mm) to pass all pins of the commercial CO_2 sensor to perform the skin loading experiment. Different weights are added to the weight holder and the emission of CO_2 can be measured.

5.3.2 Experimental set-up for monitoring CO_2 emitted from human skin during loading using an OFCS and a commercial CO_2 sensor

In Figure 5.6, the same experimental set-up is used with the same equipment, as detailed in Section 3.3.1. A biocompatible PLA based holder containing the commercial CO_2 sensor and an OFCS tip was placed on a volunteer's forearm. The OFCS tip was connected to the holder through the channel. The OFCS was not directly in contact with the skin. The holder contained the PTFE film layer to prevent humidity from reaching the OFCS tip. The PTFE film acted as a membrane barrier.

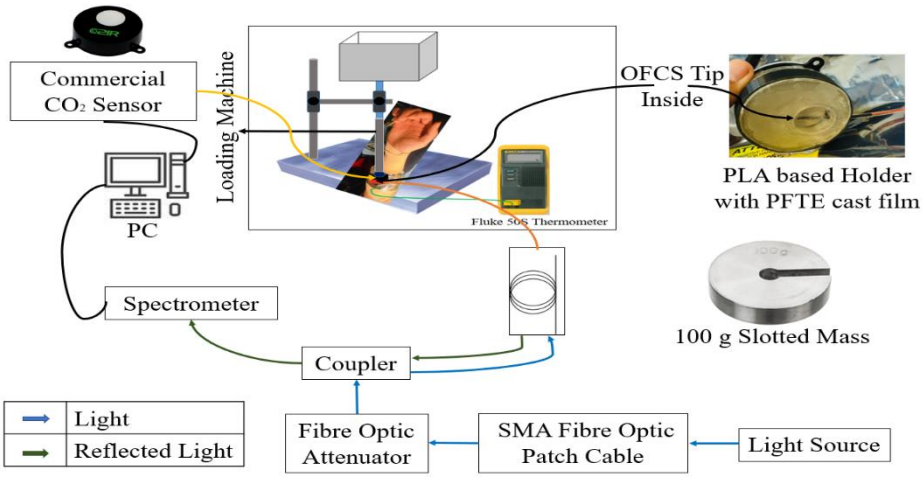


Figure 5.6: *Experimental set-up for monitoring CO_2 emitted from wrapped human skin during loading using OFCS and commercial CO_2 sensor*

Figure 5.7 shows the dimension of the holder. The external diameter (D_1) is 43 mm, and this external space was used for placing the commercial CO_2 sensor. The internal diameter (D_2) is 18 mm, and this internal space was used to collect gas from the skin. A plastic tube was appropriately fixed through the holder and used as the channel. The presence of the PTFE film beneath the holder shielded the OFCS tip from the skin.

Figure 5.8 illustrates the dimension of a hot & cold therapy disc (3D hot & cold therapy disc, Neo G, UK) that was used to change skin temperature. The diameter of the whole disc is 141 mm. The diameter of the disc's hole is 24 mm, which was used to place the holder. The disc was cleaned by a sanitiser (70 % alcohol) after the experiment was completed. A foil blanket (QZ9200, JaxFirstAid, UK) was used to cover the hot & cold therapy disc on the human forearm and keep the skin warm during the skin loading experiment. The

temperature effects on the skin and PCO_2 measurement from human skin using the tc Sensor 92 probe at 37 °C or 42 °C, as discussed in Sections 1.5.2.2 and 5.2, respectively. So, the obtained results from the experimental set-up (Figure 5.6) can be compared to the achieved results from the experimental set-up (Figure 5.1).

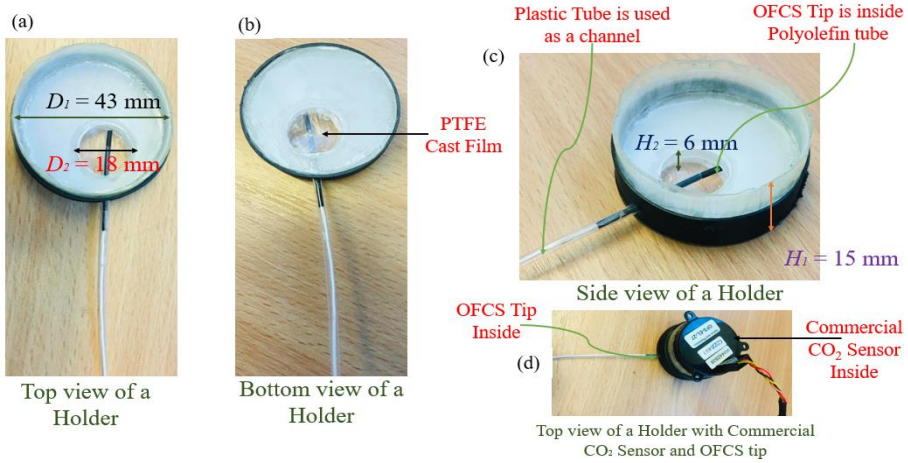


Figure 5.7: *Different views of holder for simultaneous CO_2 measurement using OFCS and commercial CO_2 sensor*

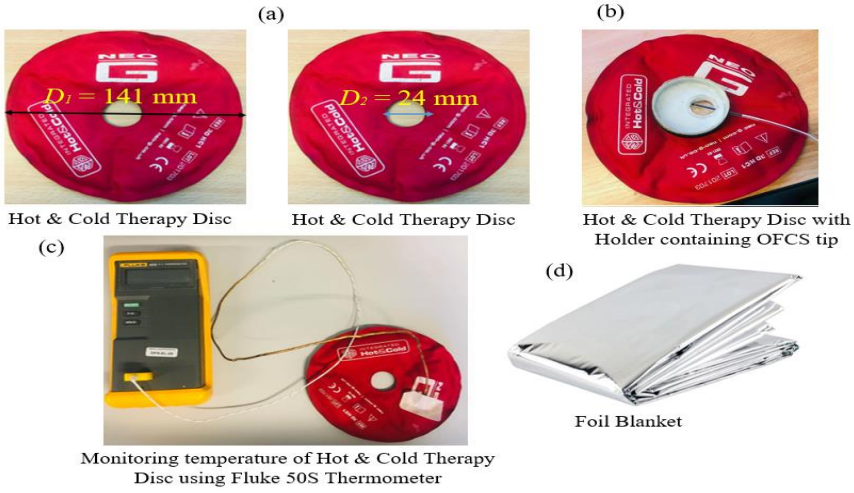


Figure 5.8: *Hot & cold therapy disc and Foil blanket*

The procedure for measuring CO_2 by varying skin temperature is described below:

Before the experiment, the participants were asked to clean their forearms using alcohol gel (70 % alcohol) provided by the experimenter and allow their skin to adjust to the environment. At the beginning, all participants were required to sit quietly for 5 minutes before the experiment commences. The participants wore 2 surgical masks during the

experiment because the commercial CO_2 sensor was highly sensitive and could detect exhaled breath CO_2 quickly.

A maximum pressure of 16 kPa (120 mmHg) was applied to the holder, and the loading effects on the skin tissues were observed. This has been shown to be a safe level in other studies previously conducted by our collaborators at the University of Southampton [8]. The contact area between the skin and holder is 1286 mm^2. 16 kPa is equivalent to a 2.1 kg load which was provided by the loading machine. If the participant feels any pain or discomfort during the experiment, the participant should indicate this, and the experiment will be stopped immediately.

The hot & cold therapy disc was heated by hot water. The process is described below:

i) Water was boiled in a kettle; ii) Hot water was poured into a heat resistant container, and a thermocouple probe was inserted into the hot water to measure the temperature; iii) The disc was dropped into the hot water for a few minutes; iv) The disc was then removed from hot water using tongs; v) Paper tissue was used to soak the excess water from the disc; vi) The thermocouple probe was placed on the disc to monitor the temperature; vii) The disc with a thermocouple probe was placed on the skin when the disc's temperature was approximately 42 °C; viii) The disc was cleaned with the sanitiser (70 % alcohol) after the experiment is completed.

The human volunteer experiment is then conducted as follows:

a) Volunteers were asked to place the heated disc with the thermocouple probe on the skin. The foil blanket was wrapped over the disc, avoiding the hole in the middle of the disc. A compression bandage was also wrapped around the outer parts of the foil blanket to hold it in place.

b) The holder was placed through the disc's hole with the PTFE film face down on the volunteer's skin (Figure 5.8 (b)) for correct sensor placement.

c) The experiments were run between 32 °C and 43.4 °C, depending on the heat retention provided by the foil blanket and disc.

d) The holder with the OFCS tip and commercial CO_2 sensor was placed on the forearm with a minimum load (0.5 kg) for 5 mins to provide a baseline measurement. The 0.5 kg load ensured the sensors remain in place and there was a gas seal between the skin and sensors.

e) A 2.1 kg load was applied for the next 10 mins.

f) Load was reduced to 0.5 kg for the next 5 mins.

g) The holder was removed from the forearm.

The reflection spectrum of the OFCS was recorded with an integration time of 1 second using SpectraSuite Software. The CO_2 concentrations (from the commercial CO_2 sensor) were recorded every 20 seconds using Gaslab Software. This experiment took approximately 20 minutes to complete steps b)-g) for each participant. Each participant was tested 3 times per day and the measurements were conducted with at least 30 minutes of break between each test to relax and rest the forearm.

The ethical approval and risk assessment were provided by the Faculty of Engineering Ethics Committee and Health and Safety Advisor of the University of Nottingham (UoN), respectively [Appendix D].

5.3.3 Calibration of OFCSs (used for skin CO_2 measurement)

The calibration process of the 10 OFCSs (OFCS 1-10) used for the skin CO_2 measurement is mentioned in Section 3.7. The OFCS 1-6 were used for the skin CO_2 measurement on Volunteer 1-6, respectively. First, the OFCS 1-6 were calibrated the day after fabrication. Next, the OFCS 1-6 were placed on the volunteers' (Volunteer 1-6) forearms respectively, the day after calibration.

The system stopped performing well after preparing 6 successful OFCSs. Reasons for this are that the film of the OFCS might have started cracking, or the base catalyst, TMAH (volatile compound), might have evaporated from the film (which is coated with silica matrix). Different strategies were tried to solve this problem, such as new OFCSs being fabricated, as mentioned in Section 3.5.2 (OFCS preparation scheme using Solution 2), and new PLA based holders were prepared using the 3D printing machine. The new and old

OFCSs were tried on different volunteers using the new and old holders. Unfortunately, this problem couldn't be resolved due to the time limitation.

The calibration and skin CO_2 measurement protocols are similar for the OFCS 1-6 and OFCS 7-10. But the sequence of performing the calibration and skin CO_2 measurement for the OFCS 7-10 is the reverse sequence of performing the calibration and skin CO_2 measurement for the OFCS 1-6.

OFCS 7-10 were used for the skin CO_2 measurement on Volunteer 7-10, respectively and were placed on the volunteers' (Volunteer 7-10) forearms the day after fabrication. OFCS 7-10 were calibrated after completing the skin CO_2 measurement on the volunteers' (Volunteer 7-10) forearms on the same day.

5.3.4 Results from monitoring CO_2 emitted from human skin during loading using an OFCS and a commercial CO_2 sensor

This reference signal from Figure 3.39 was used to calculate the absorbance using Eq. (3.10) during the skin CO_2 measurement.

Figures 5.9 (a)-(f) show the reflection and absorption spectra of OFCS 1 for Trials 1-3 of Volunteer 1, respectively. The response of OFCS 1 is achieved using the same method, as detailed in Section 5.3.2. The reflection spectra of OFCS 1 contains a trough at a wavelength of 600 nm, and the trough becomes flat in Trials 2 and 3. During Trials 1-3 of OFCS 1, the start reflection intensity (10534-11467 counts) increases and the absorbance (0.698-0.662) decreases. The reflection spectra increase, and absorption spectra decrease when the OFCS 1 is moved from air to skin. The new baseline is created for OFCS 1 on the skin during loading. The reflection spectra rise, and absorption spectra fall due to loading (0.5 kg and 2.1 kg) on the skin. The reflection spectra decrease, and absorption spectra increase when OFCS 1 is moved from skin to air for Trials 1-3. Results for 3 trials for Volunteer 1 are shown in this section. To avoid repetition of similar results from other volunteers, the trends of results for all other volunteers are summarised in a Table following each set of Volunteer 1 results. The full sets of results for all other volunteers are provided in Appendix C.

The purpose of the 3 trials is to observe the variation in response of OFCSs (OFCS 1-10) and commercial CO_2 sensor between each trial. The percentage error helps to show the variability of the response of different OFCSs (OFCS 1-10) and commercial CO_2 sensor.

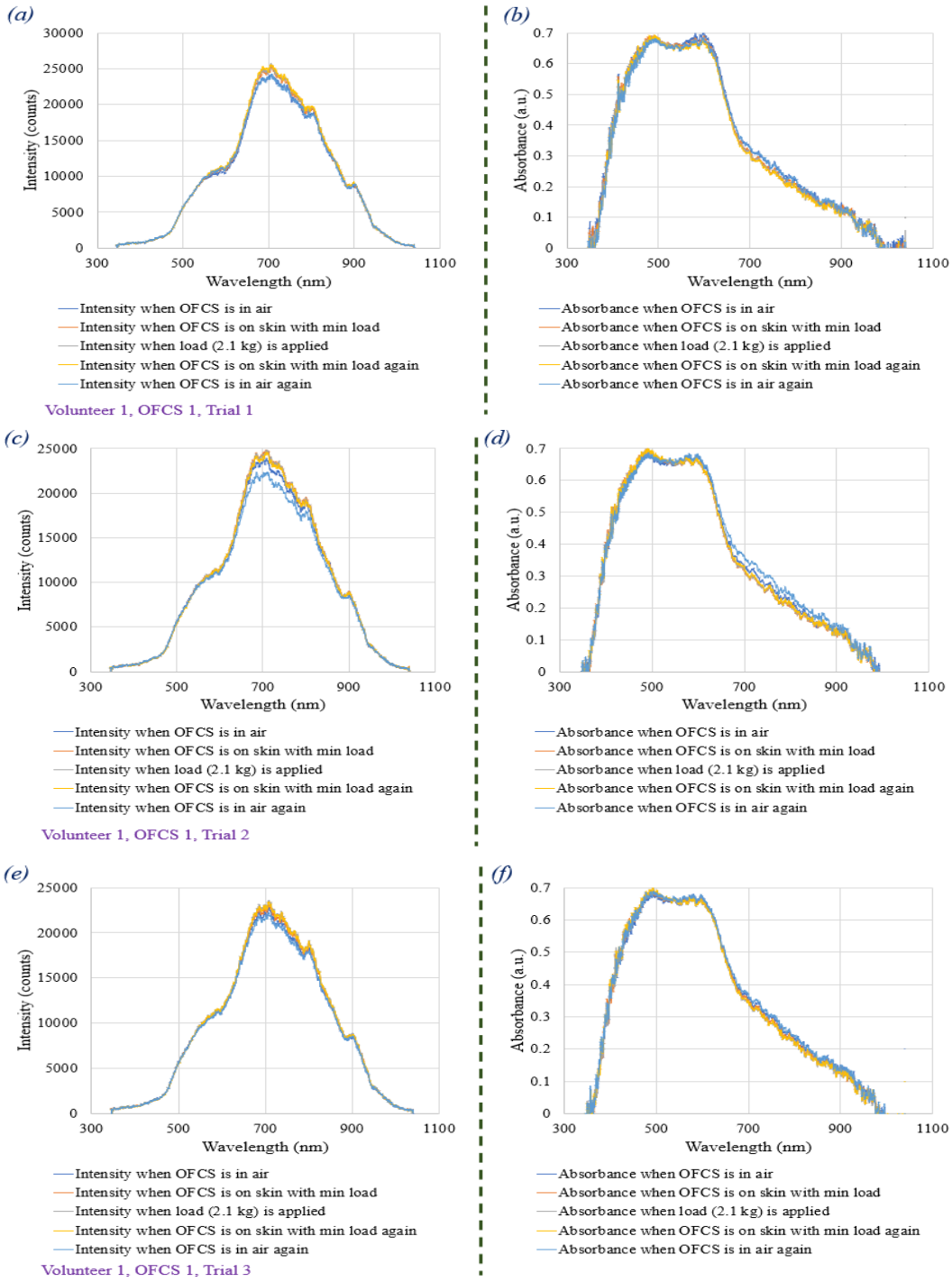


Figure 5.9: *(a) (c) (e) Reflection spectra and (b) (d) (f) Absorption spectra of OFCS 1. Each row represents a different Trial 1-3 for Volunteer 1*

The nature of the reflection and absorption spectra of the 10 OFCSs (OFCS 1-10) is mentioned in Table 5.4 according to similar or different trends of other OFCSs. The first

column refers to an OFCS (corresponding to a different Volunteer), the number of the Trial (1 of 3), and where the relevant experimental results can be found in the Appendix C. The second column confirms where a Volunteer 1 result that has the same trend can be found in the thesis. As noted in Section 5.3.3, OFCS 1-6 demonstrated consistent trends, but OFCS 7-10 were inconsistent.

Table 5.4: *Nature of reflection and absorption spectra of OFCSs (OFCS 1-10)*

Reflection and absorption spectra of OFCS number {Trial (T) number, Figure (F) number}	Following the similar trend of reflection and absorption spectra of OFCS number {Trial (T) number, Figure (F) number} or different trend
OFCS 2, T 1-3, F C.1 (a)-(f)	OFCS 1, T 1-3, F 5.9 (a)-(f)
OFCS 3, T 1-3, F C.2 (a)-(f)	OFCS 1, T 1-3, F 5.9 (a)-(f)
OFCS 4, T 1-3, F C.3 (a)-(f)	OFCS 1, T 1-3, F 5.9 (a)-(f)
OFCS 5, T 1-3, F C.4 (a)-(f)	OFCS 1, T 1-3, F 5.9 (a)-(f)
OFCS 6, T 1-3, F C.5 (a)-(f)	OFCS 1, T 1-3, F 5.9 (a)-(f)
OFCS 7, T 1-3, F C.6 (a)-(f)	Different trend: The reflection spectra increase, and absorption spectra decrease at a wavelength window (500-700 nm). On the other hand, the reflection spectra decrease, and absorption spectra increase at a wavelength window (700-900 nm). This trend continues during the entire experiments for Trials 1-3.
OFCS 8, T 1, F C.7 (a) (b)	OFCS 1, T 1-3, F 5.9 (a)-(f)
OFCS 8, T 2&3, F C.7 (c)-(f)	Different trend: The overall reflection spectra decrease, and absorption spectra increase when OFCS 8 is moved from air to skin. The new baseline is created for OFCS 8 on the skin during loading. The reflection spectra climb, and absorption spectra drop due to loading (2.1 kg and 0.5 kg) on the skin. The reflection spectra decrease, and absorption spectra increase when OFCS 8 is shifted from skin to air for Trials 2 and 3.
OFCS 9, T 1&2, F C.8 (a)-(d)	OFCS 7, T 1-3, F C.6 (a)-(f)
OFCS 9, T 3, F C.8 (e) (f)	OFCS 1, T 1-3, F 5.9 (a)-(f)
OFCS 10, T 1&2, F C.9 (a)-(d)	Different trend: The overall reflection spectra drop, and absorption spectra rise drastically during the entire experiments for Trials 1 and 2.
OFCS 10, T 3, F C.9 (e) (f)	OFCS 7, T 1-3, F C.6 (a)-(f)

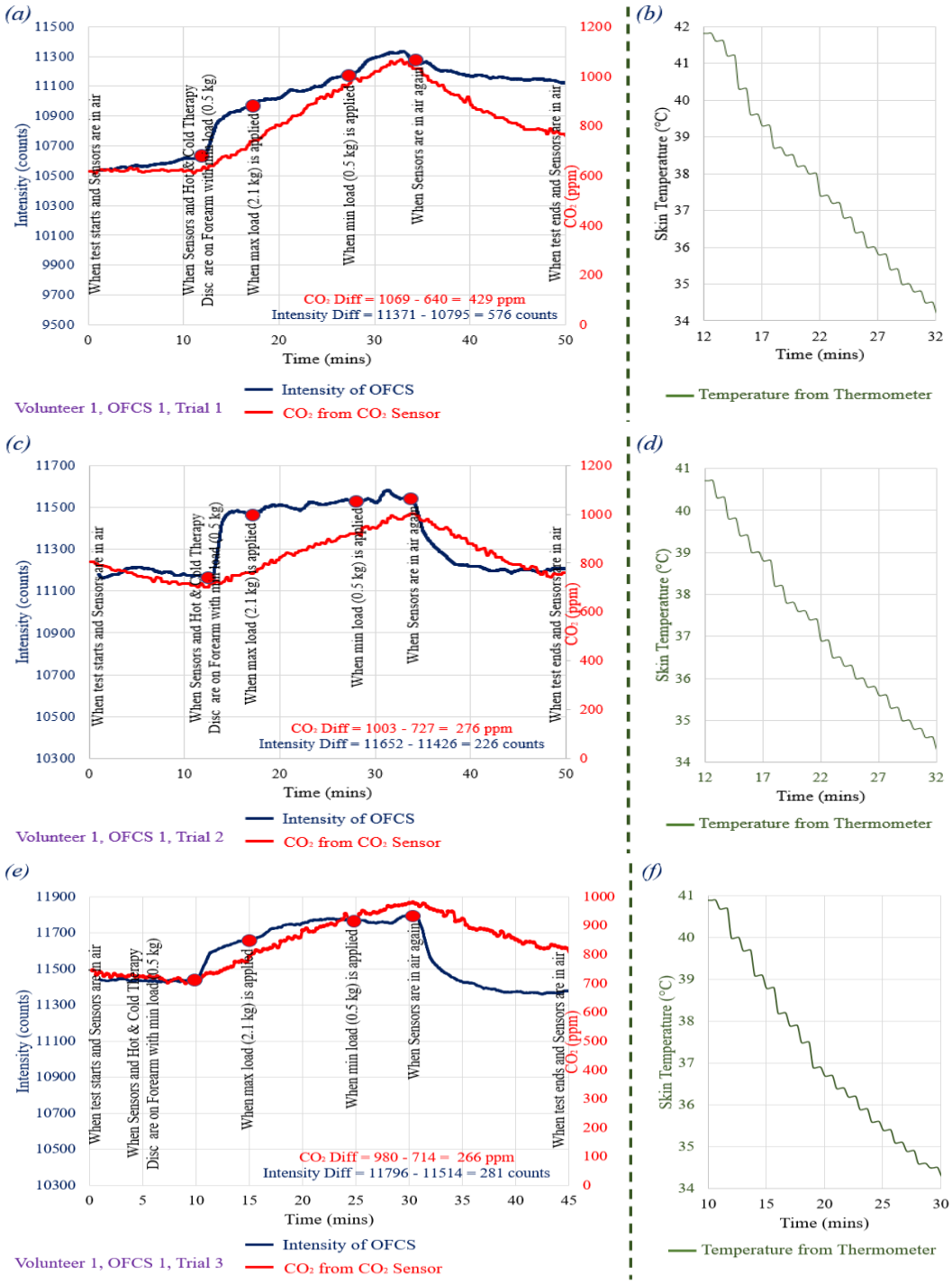


Figure 5.10: *(a) (c) (e) Response (Reflection Intensity) of OFCS 1 at wavelength 600 nm and commercial CO_2 sensor on Volunteer 1's forearm (b) (d) (f) Volunteer 1's skin temperature while heated disc is on forearm for Trials 1-3, respectively*

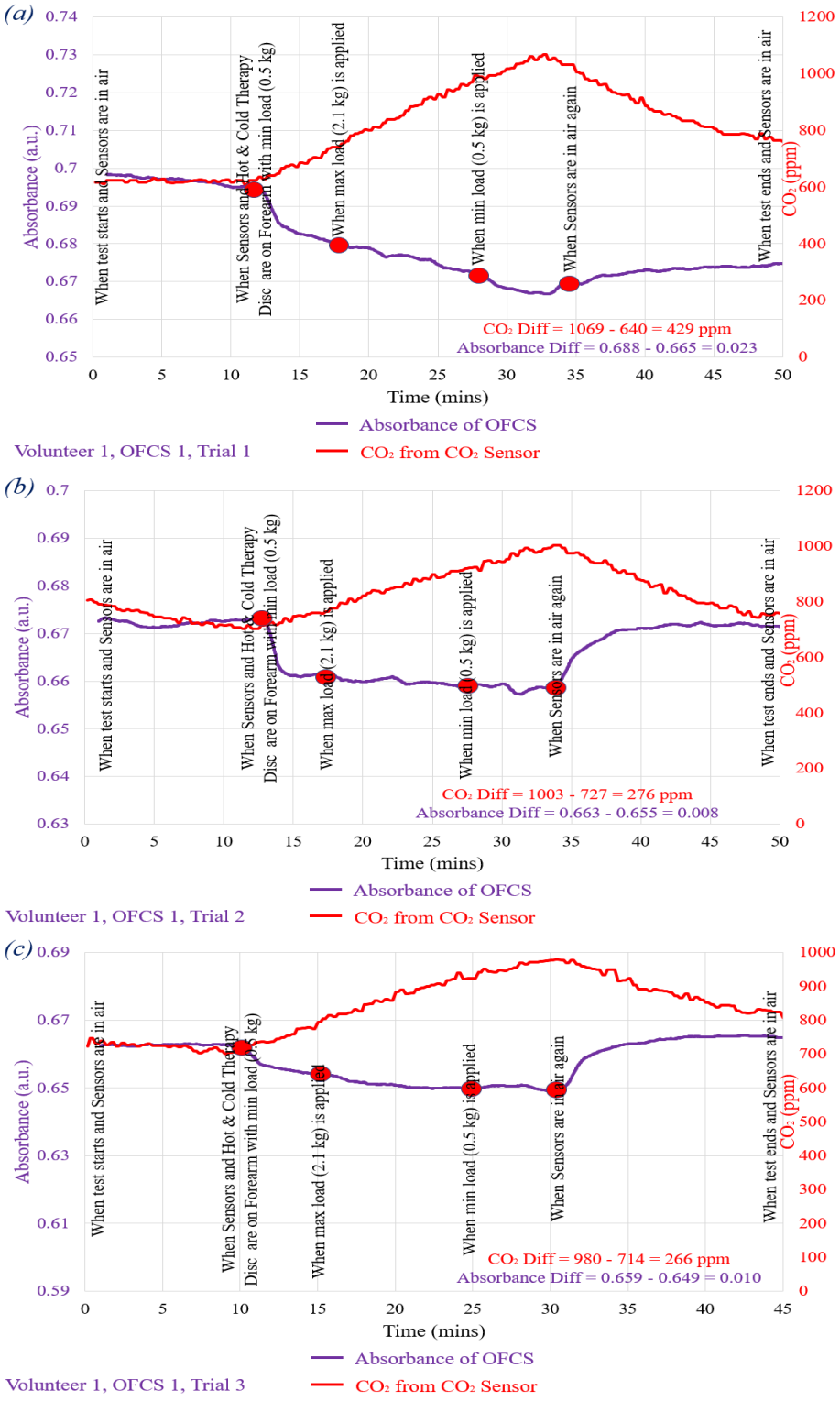


Figure 5.11: *(a)-(c) Response (Absorbance) of OFCS 1 at wavelength 600 nm and commercial CO_2 sensor on Volunteer 1's forearm for Trials 1-3, respectively*

Figures 5.10 (a), (c), and (e) show the changes in reflection intensity at a wavelength of 600 nm and the CO_2 concentration (from the commercial CO_2 sensor) during loading on Volunteer 1's forearm for Trials 1-3. Figures 5.11 (a)-(c) illustrate the variation in absorbance at a wavelength of 600 nm during the loading on Volunteer 1's forearm for Trials 1-3. The reflection intensity, absorbance, and CO_2 concentration are relatively stable for the first 12 minutes when OFCS 1 is in the air. The reflection intensity and CO_2 concentration increase, whilst the absorbance decreases when OFCS 1 and the hot & cold therapy disc are placed on the forearm with the load (0.5 kg) for 5 minutes. Again, the reflection intensity and CO_2 concentration increase, and absorbance decreases when the load (2.1 kg and 0.5 kg) is applied for the next 10 and 5 minutes, respectively. Finally, the reflection intensity and CO_2 concentration decrease, and absorbance increases when OFCS 1 is shifted from the skin to the air for 18 minutes.

The nature of the reflection intensity and absorbance of the 10 OFCSs (OFCS 1-10) during the skin CO_2 measurement is mentioned in Table 5.5 according to similar or different trends of other OFCSs. Similar to Table 5.4, the first column states where the relevant data for different Volunteers can be found in the thesis (OFCS 2-10). The second column states whether the trend is similar to the same experiment for Volunteer 1 and cross-references the data. As noted previously, results for OFCS 1-6 are consistent, but OFCS 7-10 are not.

Table 5.5: *Nature of reflection intensity and absorbance of OFCSs (OFCS 1-10)*

Reflection intensity and absorbance of OFCS number {Trial (T) number, Figure (F) number}	Following the similar trend of reflection intensity and absorbance of OFCS number {Trial (T) number, Figure (F) number} or different trend
OFCS 2, T 1-3, F C.10 (a) (c) (e) & C.11 (a)-(c)	OFCS 1, T 1-3, F 5.10 (a) (c) (e) & 5.11 (a)-(c)
OFCS 3, T 1-3, F C.13 (a) (c) (e) & C.14 (a)-(c)	OFCS 1, T 1-3, F 5.10 (a) (c) (e) & 5.11 (a)-(c)
OFCS 4, T 1-3, F C.16 (a) (c) (e) & C.17 (a)-(c)	OFCS 1, T 1-3, F 5.10 (a) (c) (e) & 5.11 (a)-(c)
OFCS 5, T 1-3, F C.19 (a) (c) (e) & C.20 (a)-(c)	OFCS 1, T 1-3, F 5.10 (a) (c) (e) & 5.11 (a)-(c)
OFCS 6, T 1-3, F C.22 (a) (c) (e) & C.23 (a)-(c)	OFCS 1, T 1-3, F 5.10 (a) (c) (e) & 5.11 (a)-(c)
OFCS 7, T 1-3, F C.25 (a) (c) (e) & C.26 (a)-(c)	Different trend: The reflection intensity at 600 nm increases, and absorbance at 600 nm decreases during the entire experiments for Trials 1-3.
OFCS 8, T 1, F C.28 (a) & C.29 (a)	OFCS 1, T 1-3, F 5.10 (a) (c) (e) & 5.11 (a)-(c)

Reflection intensity and absorbance of OFCS number {Trial (T) number, Figure (F) number}	Following the similar trend of reflection intensity and absorbance of OFCS number {Trial (T) number, Figure (F) number} or different trend
OFCS 8, T 2&3, F C.28 (c) (e) & C.29 (b) (c)	Different trend: The reflection intensity at 600 nm decreases, and absorbance at 600 nm increases when OFCS 8 is in the air. The new baseline is created for OFCS 8 on the skin during loading (0.5 kg). The reflection intensity climbs, and absorption drops due to loading (2.1 kg and 0.5 kg) on the skin. The reflection intensity decreases, and absorption increases when OFCS 8 is shifted from skin to air for Trials 2 and 3.
OFCS 9, T 1, F C.31 (a) & C.32 (a)	OFCS 7, T 1-3, F C.25 (a) (c) (e) & C.26 (a)-(c)
OFCS 9, T 2, F C.31 (c) & C.32 (b)	Different trend: The reflection intensity at 600 nm increases, and absorbance at 600 nm decreases when OFCS 9 is in the air. The new baseline is created for OFCS 9 on the skin during loading (0.5 kg). The reflection intensity drops, and absorption climbs due to loading (2.1 kg and 0.5 kg) on the skin. The reflection intensity increases, and absorption decreases when OFCS 9 is shifted from skin to air for Trial 2.
OFCS 9, T 3, F C.31 (e) & C.32 (c)	OFCS 1, T 1-3, F 5.10 (a) (c) (e) & 5.11 (a)-(c) except the reflection intensity at 600 nm increases, and absorbance at 600 nm decreases for the first 10 minutes when OFCS 9 is in the air for Trial 3.
OFCS 10, T 1&2, F C.34 (a) (c) & C.35 (a) (b)	Different trend: The reflection intensity drops, and absorbance rises drastically during the entire experiments for Trials 1 and 2.
OFCS 10, T 3, F C.34 (e) & C.35 (c)	OFCS 7, F C.25 (a) (c) (e) & C.26 (a)-(c) except the reflection intensity and absorbance at 600 nm are relatively stable for the first 10 minutes when the OFCS 10 is in the air.

Volunteer 1's skin temperature is illustrated in Figures 5.10 (b), (d), and (f) for Trials 1-3, respectively. The temperature decreases gradually for Trials 1-3. Figures {C.10, C.13, C.16, C.19, C.22, C.25, C.28, C.31, and C.34} (b) (d) (f) [Appendix C] represent the skin

temperature of Volunteer 2-10 for Trials 1-3, respectively. These graphs follow the same trend as Figure 5.10 (b) (d) (f).

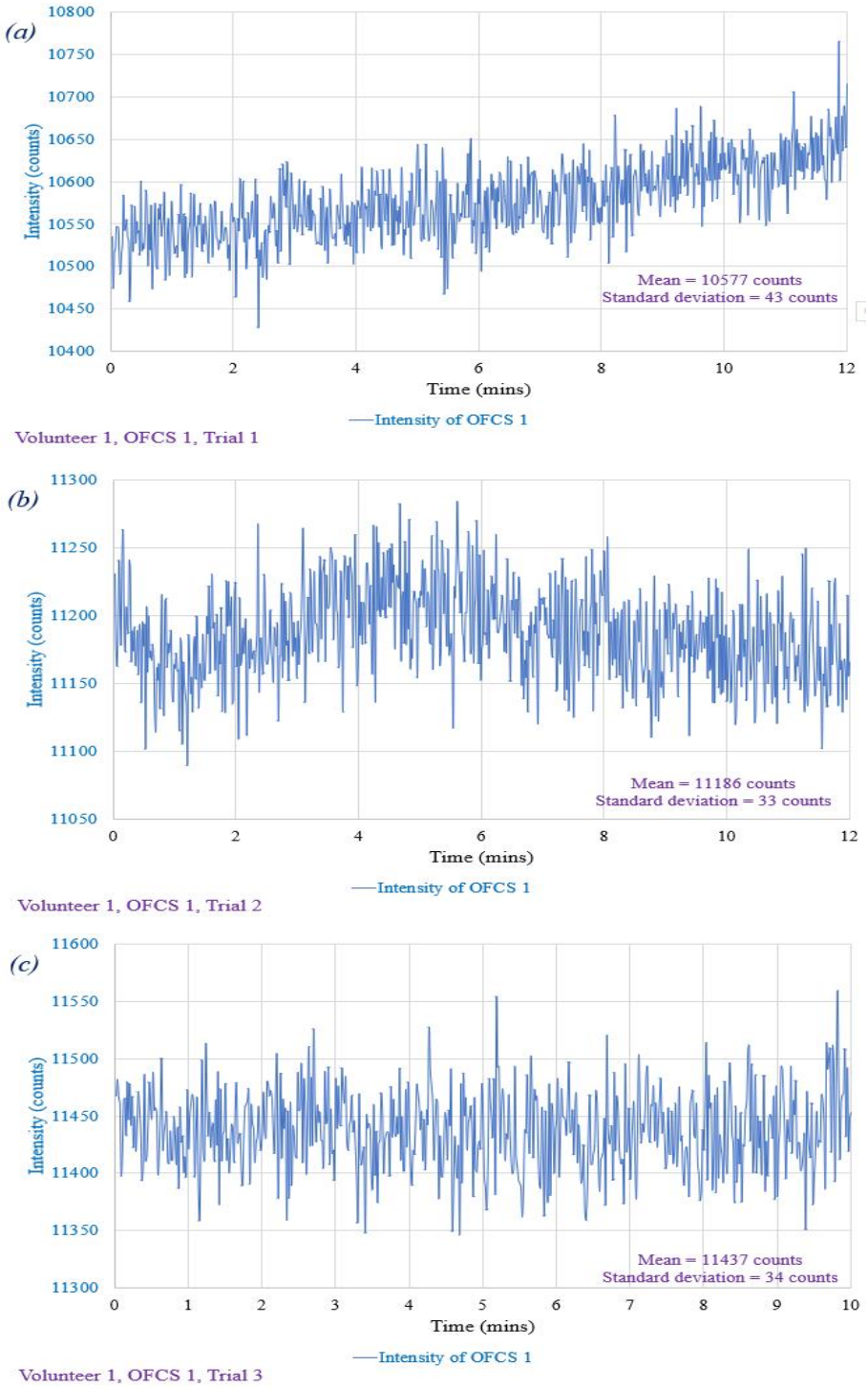


Figure 5.12: *(a)-(c) Response (Raw Reflection Intensity) of OFCS 1 at wavelength 600 nm in the air for Trials 1-3, respectively*

5.3.4.1 Signal to Noise Ratio

The OFCSs' (OFCS 1-10) responses (reflection intensities and absorbances) are presented in this section by applying a moving average filter with a width of 60, which provides a smooth response. The reflection intensity of OFCS 1 in Figure 5.10 (a) has 3 parts: The 1st (0-12 mins), 2nd (12-32 mins), and 3rd (32-50 mins) part of the response (reflection intensity) which were taken in the air, on volunteer 1's forearm, and then in the air again.

Figures 5.12 (a)-(c) demonstrate the 1st {(0-12 mins for Trials 1 and 2) and (0-10 mins for Trial 3)} part of the response (raw signal or reflection intensity) when the OFCS 1 was in the air. The mean and standard deviation is calculated from the 1st part of the OFCS 1.

The noise level can be calculated from the signal's variation (standard deviation). The standard deviation of the 1st part of the OFCS 1's response (reflection intensity) is considered to provide an estimated of the fluctuation of the measurement due to noise because the OFCS 1 was in the air, and the reflection intensity was varied only according to the room CO_2 concentrations. On the other hand, the 2nd part of the reflection intensity was varied by the skin CO_2 concentrations and temperature, and the 3rd part of the reflection intensity was changed by the skin CO_2 concentrations (which escaped from the GCC) and the room CO_2 concentrations.

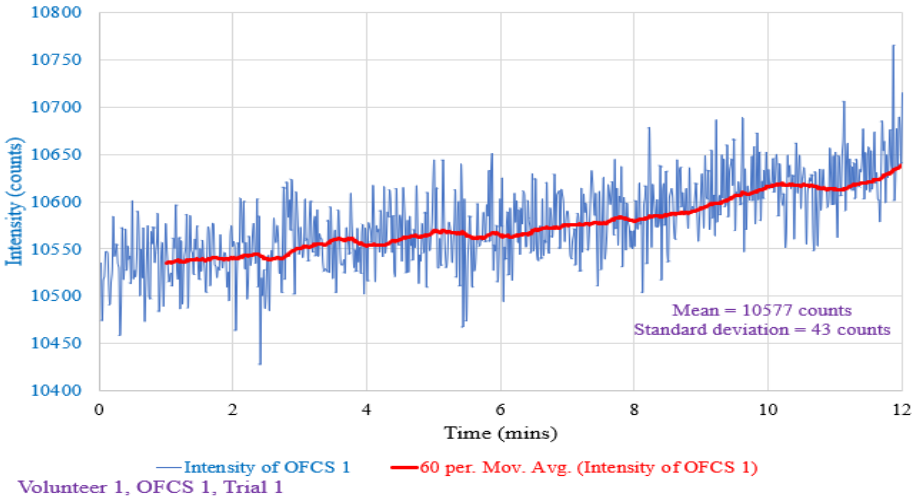


Figure 5.13: *Response (Raw and Smooth Reflection Intensity) of OFCS 1 at wavelength 600 nm in the air for Trial 1*

The raw signal or reflection intensity and the smooth signal are shown in Figure 5.13 for OFCS 1 in the air for Trial 1.

The signal-to-noise ratio (SNR) is a useful parameter for characterising skin CO_2 measurements and is calculated using the following formula:

$$SNR = \frac{Intensity\ changes\ in\ volunteer's\ forearm}{Noise\ (Standard\ deviation\ of\ the\ OFCS\ in\ the\ air)} \qquad (5.4)$$

An example of calculating the noise as a standard variation of the 1st part of the response (Volunteer 1 Trial 1 OFCS 1) when OFCS 1 is in the air from Figure 5.13:

Noise = 43 counts

An example of calculating the SNR using Eq. (5.4) (Volunteer 1 Trial 1 OFCS 1) as follows:

Intensity changes in Volunteer 1's forearm = 576 counts

SNR = 576 counts / 43 counts = 13.4

Figures {C.12, C.15, C.18, C.21, C.24, C.27, C.30, C.33, and C.36} (a)-(c) [Appendix C] represent the raw signal or reflection intensity of the OFCS 2-10 for Trials 1-3, respectively.

5.3.4.2 Percentage error

The percentage error between the OFCSs (OFCS 1-10) and commercial CO_2 sensor can be calculated from the conversion of intensity (counts) and absorbance (a.u.) to CO_2 (ppm) for the OFCSs (OFCS 1-10) and CO_2 (ppm) obtained from the volunteers' (Volunteer 1-10) skin.

An example of calculating the theoretical CO_2 from Figure 3.41 using the linear relationship equations of intensity vs CO_2 and absorbance vs CO_2 (Volunteer 1 Trial 1 OFCS 1) as follows:

Formula for intensity vs CO_2: $y = 1.0239x + 15.349$, where x is change in CO_2 concentration (ppm), and y is change in intensity (counts).

In Figure 5.10 (a), Intensity changes in Volunteer 1's forearm = 576 counts

Change in CO_2 concentration, C_I = (ΔIntensity – 15.349) / 1.0239 = (576 – 15.349) / 1.0239 = 547.6 ppm

Formula for absorbance vs CO_2: $y = 0.00004x + 0.0008$, where x is change in CO_2 concentration (ppm), and y is change in absorbance (a.u.).

In Figure 5.11 (a), Absorbance changes in Volunteer 1's forearm = 0.023 a.u.

Change in CO_2 concentration, C_A = (ΔAbsorbance – 0.0008) / 0.00004 = (0.023 – 0.0008) / 0.00004 = 555 ppm

In Figures 5.10 (a) and 5.11 (a), change in CO_2 concentration from Volunteer 1's forearm measured by the commercial CO_2 sensor, C_S = 429 ppm

% Error w.r.t. intensity, $E_I = (|C_S - C_I| / C_I) \times 100 = (|429 - 547.6| / 547.6) \times 100 = 21.7$

% Error w.r.t. absorbance, $E_A = (|C_S - C_A| / C_A) \times 100 = (|429 - 555| / 555) \times 100 = 22.7$

Table 5.6 summarises the achieved results (error and SNR) of Volunteer 1-10 and the commercial CO_2 sensor for Trials 1-3. The first column refers to the number of volunteers and OFCS. The second column refers to the Trial number (1 of 3). The third column shows the change in CO_2 (ppm) obtained from the commercial CO_2 sensor. The fourth column presents the conversion of change in intensity (counts) and change in absorbance (a.u.) to change in CO_2 (ppm) for the OFCSs (OFCS 1-10) using the linear relationship in Figure 3.41 and even numbers of Figures A.2-A.18 [Appendix A], respectively. The fifth column shows the percentage error based on the comparison between the data obtained from the third and fourth columns. The sixth column represents the SNR value for the OFCSs (OFCS 1-10).

Table 5.6: *Error and SNR calculation of 10 volunteers' for 3 trials*

Volunteer (V) number, OFCS number	Trial (T) number	ΔCO_2 (ppm) from Commercial sensor, C_S	CO_2 (ppm) from OFCS's response		% Error w.r.t.		SNR
			ΔIntensity, C_I	ΔAbsorbance, C_A	Intensity, E_I	Absorbance, E_A	
V 1, OFCS 1	T 1	429	547.6	555	21.7	22.7	13.4
	T 2	276	205.7	180	34.2	53.3	6.8
	T 3	266	259.5	230	2.5	15.7	8.3
V 2, OFCS 2	T 1	271	213.4	338.6	27.0	20.0	7.7
	T 2	165	166.6	252.9	1.0	34.8	7.0
	T 3	197	148.6	210	32.6	6.2	5.9
V 3, OFCS 3	T 1	261	268.3	583.3	2.7	55.3	8.2
	T 2	266	261.8	516.7	1.6	48.5	11.8
	T 3	279	240.8	483.3	15.9	42.3	10.7
V 4, OFCS 4	T 1	149	167.7	276	11.2	46.0	5.7
	T 2	193	191	276	1.0	30.1	9.2
	T 3	180	179.3	256	0.4	29.7	8.5
V 5, OFCS 5	T 1	215	183.2	164.3	17.4	30.9	7.7
	T 2	267	198.8	164.3	34.3	62.5	11.3
	T 3	253	182.1	135.7	38.9	86.4	11.3
V 6, OFCS 6	T 1	199	181.2	325	9.8	38.8	6.7
	T 2	236	240	425	1.7	44.5	7.7
	T 3	197	168.4	325	17.0	39.4	6.5
V 7, OFCS 7	T 1	184	698	1200	73.6	84.7	3.3
	T 2	278	316.8	450	12.2	38.2	3.7
	T 3	196	251.2	200	22.0	2.0	2.6
V 8, OFCS 8	T 1	251	224.7	400	11.7	37.3	1.6
	T 2	240	222	300	8.1	20.0	2.5
	T 3	230	208.6	400	10.3	42.5	0.5
V 9, OFCS 9	T 1	380	386.4	1800	1.7	78.9	9.4
	T 2	388	52.9	94.6	86.4	75.6	3.3
	T 3	401	395.9	1000	1.3	59.9	2.6
V 10, OFCS 10	T 1	287	283.8	216.7	1.1	32.4	1.7
	T 2	330	324.5	283.3	1.7	16.5	4.4
	T 3	300	253.8	283.3	18.2	5.9	5.4

The SNR range is 0.5-13.4. The poor SNR (0.5) is achieved due to obtaining the highest standard deviation (217 counts) for Volunteer 8, OFCS 8, Trial 3 because OFCS 8 wasn't stable when it was in the air. The error range is 0.4-86.4 % for intensity and 2-86.4 % for absorbance. The error values obtained from intensity conversion differ from those obtained from absorbance conversion because the absorbance changes in small fractions (which makes a big difference during conversion and provides higher error values than intensity conversion).

5.3.5 Discussion of obtained results from volunteer's skin CO_2 measurement

To the author's knowledge, these are the first results with the gas CO_2 measurement on human skin during loading using either an OFCS or a commercial CO_2 sensor. Both sensors (the OFCS 1-6 and commercial CO_2 sensor) can measure the CO_2 changes on the volunteers' (Volunteer 1-6) skin and in the air. Both sensors have a similar trend, such as the response of both sensors going up when the sensors are put on the volunteers' (Volunteer 1-6) skin and going down when the sensors are placed in the air. Still, the commercial CO_2 sensor can measure the CO_2 changes on the volunteers' (Volunteer 7-10) skin and in the air. Unfortunately, the OFCS 7-10 doesn't follow the same trend as the commercial CO_2 sensor on the volunteers' (Volunteer 7-10) skin and in the air. The different OFCSs weren't tried on the same volunteers' skin.

The results vary from trial to trial, depending on the physiological properties of volunteers (each volunteer is different and there is a gap between individual experiments on the same volunteer) and the OFCS losing its dye properties. The OFCS 1-10 lose their dye properties in 3 different ways during the skin CO_2 measurement. Firstly, the overall reflection spectra of the OFCSs drop continuously. Secondly, the trough at a wavelength of 600 nm becomes flat. Finally, the reflection intensity of OFCSs increases at a wavelength window (500-700 nm) and decreases at a wavelength window (700-900 nm). The response of the OFCS has variability due to light exposure to the sensor (photobleaching) which changes the dye properties over time. The initial intensities of the OFCS 1-10 are not the same due to the photobleaching during Trials 1-3 hence the response is not always the same as the calibration results.

The start CO_2 concentrations are different because the room CO_2 varies during Trials 1-3. When the loading amount is 0.5 kg for the last 5 minutes on the skin, the CO_2 concentrations (from the commercial CO_2 sensor) don't decrease because the stored gas can't escape from the PLA based holder as it is a closed gas chamber. The CO_2 variation is different because of changes in physiological properties, and skin temperatures are not the same and stable during Trials 1-3. The CO_2 concentrations (from the commercial CO_2 sensor) do not always return to the baseline because CO_2 dissipates slowly through the PTFE film on the PLA based holder.

Bending losses are another source of error in which there is an unwanted change in intensity. Figure 5.14 (a) shows the PLA based holder which contains the OFCS tip and commercial CO_2 sensor. Figures 5.14 (b) and (c) demonstrate the OFCS placement in the air without and with bending, respectively. It is not easy to put the fibre in its original position and location at the end of the experiment.

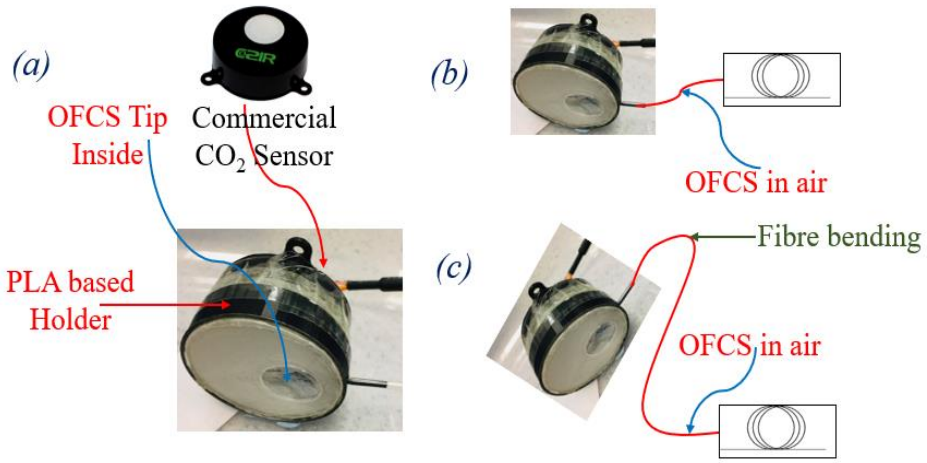


Figure 5.14: *(a) PLA based holder containing OFCS tip and commercial CO_2 sensor (b) OFCS is placed in air without bending (c) OFCS is placed in air with bending*

In Table 5.7, the observation, and possible reasons for achieved results of 10 OFCSs (OFCS 1-10) on volunteers' (Volunteer 1-10) forearms during Trials 1-3 are described.

Table 5.7: *Observation and possible reasons for variation in obtained results during skin CO_2 measurement*

Volunteer (V) number, OFCS number, Trial (T) number	Figure number	Observation and possible reasons
V 1, OFCS 1, T 1 V 2, OFCS 2, T 1-3 V 3, OFCS 3, T 1-3 V 4, OFCS 4, T 1 V 5, OFCS 5, T 1-3 V 6, OFCS 6, T 1	5.10 (a) C.10 (a) (c) (e) C.13 (a) (c) (e) C.16 (a) C.19 (a) (c) (e) C.22 (a)	The reflection intensity of OFCS 1-6 at 600 nm doesn't return to the baseline after placing it in the air for the last 10-15 minutes. It may happen due to photobleaching when the OFCS 1-6 is placed in the air again according to the fibre position, which is shown in Figure 5.14 (b).
V 8, OFCS 8, T 3	C.28 (e)	The reflection intensity of OFCS 8 at 600 nm is decreased because the reflection spectra of OFCS 8 drops continuously when it is in the air for the first 14 minutes. The OFCS 8 loses its dye properties. It may happen due to photobleaching when OFCS is placed in the air again according to the fibre position, which is shown in Figure 5.14 (b).
V 9, OFCS 9, T 3	C.31 (e)	The reflection intensity of OFCS 9 at 600 nm is increased because the reflection spectra of OFCS 9 rises rapidly when it is in the air for the first 10 minutes. The reflection intensity of OFCS 9 at 600 nm doesn't return to the baseline after placing it in the air for the last 10 minutes. It may happen due to photobleaching when the OFCS 9 is placed in the air again according to the fibre position, which is shown in Figure 5.14 (b).
V 1, OFCS 1, T 2&3 V 4, OFCS 4, T 2&3 V 8, OFCS 8, T 1	5.10 (c) (e) C.16 (c) (e) C.28 (a)	The reflection intensity of OFCS 1, 4, and 8 at 600 nm returns to the baseline after placing it in the air for the last 10-15 minutes.

Volunteer (V) number, OFCS number, Trial (T) number	Figure number	Observation and possible reasons
V 6, OFCS 6, T 2&3	C.22 (c) (e)	The reflection intensity of OFCS 6 at 600 nm goes beyond the baseline after placing it in the air for the last 10-15 minutes.
		It may happen due to the fibre bending when the OFCS 1, 4, 6, and 8 is placed in the air again according to the fibre position, which is shown in Figure 5.14 (c).
V 7, OFCS 7, T 1-3 V 9, OFCS 9, T 1&2 V 10, OFCS 10, T 3	C.25 (a) (c) (e) C.31 (a) (c) C.34 (e)	The reflection intensity of OFCS 7, 9, and 10 at 600 nm doesn't return to the baseline after placing it in the air for the last 10-15 minutes. The OFCS 7, 9, and 10 loses its dye properties because of reflection intensity's increment at a wavelength window (500-700 nm) and reflection intensity's decrement at a wavelength window (700-900 nm).
V 8, OFCS 8, T 2	C.28 (c)	The reflection intensity of OFCS 8 at 600 nm drops due to the fibre bending when the OFSC 8 is placed on the skin from the air. The intensity at 600 nm doesn't return to the baseline after putting it in the air for the last 10-15 minutes because the OFSC 8 isn't placed in its initial position when the experiment starts.
V 10, OFCS 10, T 1&2	C.34 (a) (c)	The reflection intensity of OFCS 10 at 600 nm is decreased because the reflection spectra of OFCS 10 drops drastically. The reflection intensity of OFCS 10 at 600 nm doesn't return to the baseline after placing it in the air for the last 10-15 minutes because the OFCS 10 loses its dye properties.

5.4 Summary

The skin CO_2 measurement from the human forearm using the t_C Sensor 92 probe, commercial CO_2 sensor and OFCS has been demonstrated. To the author's knowledge this is the first time either a commercial CO_2 sensor or an OFCS has been used to investigate CO_2 emitted from the skin during loading. Both could be viable alternatives to measuring

T_CPCO_2. The PCO_2 values from the t_C Sensor 92 probe inside the gas chamber were compared to the theoretical calculation of PCO_2 values. The theoretical PCO_2 values were compared to the experimental PCO_2 values from the t_C sensor 92 probe's calibration inside the gas chamber with the help of percentage error for 10000 ppm (1% CO_2) to 50000 ppm (5% CO_2) range.

The PCO_2 values were monitored from 10 volunteers' (Volunteer 1-10) forearms using the t_C Sensor 92 probe at 37 °C and 42 °C for Trials 1-5. The maximum obtained average PCO_2 value is 55 mmHg and 48 mmHg at 37 °C and 42 °C, respectively, over 5 trials. The minimum obtained average PCO_2 value is 41 mmHg and 32 mmHg at 37 °C and 42 °C, respectively, over 5 trials. Due to applying the Severinghaus temperature correction factor, the obtained PCO_2 value at 42 °C is always lower than the achieved PCO_2 value at 37 °C.

The loading machine was built to provide a load on the volunteer's forearm. The reflection intensity of the OFCS and the CO_2 concentrations (from the commercial CO_2 sensor) were monitored from 10 volunteers' (Volunteer 1-10) forearms during loading using the 10 OFCSs (OFCS 1-10) and commercial CO_2 sensor at a range of 32 °C and 43.4 °C at the surface of the skin (3 experiments/volunteer).

The 10 calibrated OFCSs (OFCS 1-10) were used for the skin CO_2 measurement on 10 volunteers' (Volunteer 1-10) forearms during loading for Trials 1-3 in Section 5.3.2. The maximum obtained skin CO_2 concentration is 429 ppm, and the minimum achieved skin CO_2 concentration is 149 ppm. The SNR of OFCSs (OFCS 1-10) varied from 0.5 to 13.4. The error range w.r.t. intensity was 0.4 % to 86.4 %, and the error range w.r.t. absorbance was 2 % to 86.4 % for the OFCSs (OFCS 1-10) and commercial CO_2 sensor. In Section 5.3.4, the obtained results vary from one OFCS to another, one trial to another and one volunteer to another. Although the OFCS suffered from photobleaching and bending, the OFCS and commercial CO_2 sensor perform relatively well in measuring the CO_2 from the skin during loading.

In Figure 5.10 (c), the best result was achieved from Volunteer 1's forearm using the OFCS 1 and commercial CO_2 sensor for Trial 2 because the start and end values of both intensities and CO_2 concentrations were almost the same for Trial 2. The observation and possible

reasons were discussed for variation in obtained results during the skin CO_2 measurement. The response of the OFCS and commercial CO_2 sensor were not always close to each other because the OFCS lost its dye properties over time. Also, the physiological properties and skin temperature were not the same for each of the trials. The possible steps for minimising the photobleaching and bending effects of the OFCS will be discussed in future directions, Chapter 6.

6. Chapter 6

Summary, Conclusions & Future Work

6.1 Introduction

This chapter provides the conclusions from this research and a discussion about future work. Section 6.2 summarises the achieved results and concludes those results. Section 6.3 proposes the fabrication process for a batch of optical fibre CO_2 sensors at a same time, the storage process of an OFCS, steps to refine an FPI model, experimental protocol, and design of a prototype and portable clinical unit for the skin CO_2 measurement using an OFCS. This chapter also reflects on the accomplishment of the goals set out at the beginning of this PhD (Section 1.2).

6.2 Summary and Conclusions

The application of fibre optic technology in healthcare was explored by developing an OFS to monitor the skin CO_2. To the author's knowledge, this is the first application of either an OFCS or a commercial CO_2 sensor to measure the skin CO_2 during loading, which has applications in the early detection of PUs.

The fabrication of an OFCS was described in Section 3.2.5. The optical fibre tip was coated with a sol-gel film which included a pH indicator dye, thymol blue. The OFCS has cross-sensitivity with temperature and humidity, as mentioned in Section 3.4. However, a negligible temperature effect on the OFCS at a fixed temperature was found in the previous literature review [108]. The PTFE film was used to prevent the humidity effects on the OFCS. The PTFE film was placed beneath the sensors' (the OFCS and commercial CO_2 sensor) holder to prevent humidity from reaching the OFCS tip, as mentioned in Section 3.4.3.

In Section 3.2.4.3, the transmission and absorption spectra of TB were observed for different pH values. The highest absorption peak was found at a wavelength of 549, 452, and 606 nm for TB (red), TB (yellow), and TB (blue), respectively. In Section 3.6, the SEM images were used to calculate the TB concentration using the film thickness from the dried film on the OFCS tip. The preparation scheme (Solution 2, Section 3.5.2) was

optimised by adding Triton X-100 to improve the quality of the sol-gel film by removing cracking from the optical fibre tip, referred to in Section 3.5.3. Improved performance and an extended lifetime were achieved using this modified preparation scheme.

In Section 3.7, the 10 OFCSs (OFCS 1-10) were calibrated inside a gas chamber alongside the commercial CO_2 sensor for lower CO_2 concentrations (276-1383 ppm). The fibre-to-fibre variability was found from the sensitivity of the 10 calibrated OFCSs (OFCS 1-10). The sensitivity range w.r.t. intensity was 0.3742-2.7503 counts/ppm. The sensitivity range w.r.t. absorbance was 0.000008-0.00007 a.u./ppm. The changes in film properties after drying caused this variation in OFCSs' (OFCS 1-10) sensitivity.

The highest absorption peak was achieved at a wavelength of approximately 600 nm. The response time of the commercial CO_2 datalogger is around 20 seconds [48]. The response time of the OFCS is 60 seconds, whereas the response time of the t_C Sensor 92 probe is almost 78 seconds [4]. Although these slow response times would mean the sensors are not appropriate for some applications, such as breath to breath, skin damage is comparatively slow, and it is likely that these times will be acceptable to clinicians and require no further improvement.

The calibration of an OFCS inside a gas chamber alongside a commercial CO_2 datalogger (K33 ICB 10% CO_2 Sensor, CO2Meter.com, USA) and a t_C Sensor 92 probe (Radiometer, UK) for 0 ppm (0% CO_2) to 50000 ppm (5% CO_2) range was illustrated in Section 3.3.1. The error range between the theoretical and experimental PCO_2 values was calculated in Section 5.2.2. The error was from 0.44 % to 12.01 % for 30000 ppm (3% CO_2) to 50000 ppm (5% CO_2) range, respectively. The error was around 24 % for 20000 ppm (2% CO_2), but the error was almost 50 % for below 20000 ppm (2% CO_2). The larger error value was achieved for the below 20000 ppm (2% CO_2) due to the limitation of the t_C Sensor 92 probe. The measuring range for the t_C Sensor 92 probe is 5-200 mmHg [52]. In Table 5.1, the maximum error (51.57 % and 47. 05 %) was achieved with the experimental PCO_2 values 4 mmHg (below the limit of detection) and 7 mmHg (close to the minimum limit of detection) for the 1% CO_2 and 1.7% CO_2, respectively. So, the probe does not respond well in the low CO_2 concentration range. The typical PCO_2 range is 36-44 mmHg, as mentioned in Section 2.3.1, and this range was covered from 40000 ppm (4% CO_2) to 50000 ppm (5%

CO_2) range with the error range of 0.44-8.21 %, respectively. Therefore, the t_C Sensor 92 probe is useful for measuring PCO_2 from the skin due to its lower error between the theoretical and experimental PCO_2 values.

The model based on Fabry-Perot interferometry on the OFCS tip was developed to observe and understand the effects of various parameters on the sensor performance. In order to populate the model, it was necessary to obtain the dye absorption properties and film thickness at the fibre tip. Skewness and kurtosis helped to describe the different shapes of the spectrum of TB according to CO_2 flow and pH variation. More robust in presence of baseline drifting compared to absorption measurement TB (blue) transformed to TB (yellow) after mixing CO_2, and the spectrum's shape was also changed.

In Section 4.3.2, relevant equations were used to express the fundamental principle of an FPI. In Section 4.4, the reflection and absorption spectrum of the FPI was simulated with varying film thickness. The lower fringe visibility was found within the absorption band (wavelength window 585-615 nm) due to the rise of film thickness. The optimum film thickness was achieved as 7.234 μm by reviewing the correlation between the fringe visibility and film thickness.

Qualitatively, the reflection and absorption spectra of the OFCS had similar features between simulations and experiments. The clearly visible fringes with a fringe visibility of 0.21 were achieved in the simulated reflection spectrum, and the highest absorption peak was found at around 600 nm. However, the reflection, absorption spectra, and fringe visibility of the OFCS were quantitively not the same between simulations and experiments because the FPI simulation didn't take the experimental film roughness and thickness into account. Experimentally, the film thickness of the FPI depended on the withdrawal speed, as mentioned in Section 3.2.6.

In Section 5.2.1, the experimental set-up was designed to measure the PCO_2 values on 10 volunteers' (Volunteer 1-10) forearms using the t_C Sensor 92 probe at 37 °C and 42 °C for 30 minutes. In Section 5.2.3, the maximum obtained average PCO_2 value was 55 mmHg and 48 mmHg at 37 °C and 42 °C, respectively, over 5 trials. The minimum obtained average PCO_2 value was 41 mmHg and 32 mmHg at 37 °C and 42 °C, respectively, over

5 trials. The obtained PCO_2 value at 42 °C is always lower than the achieved PCO_2 value at 37 °C due to applying the Severinghaus temperature correction factor.

In Section 5.3.2, the experimental set-up was designed to measure the skin CO_2 during loading on 10 volunteers' (Volunteer 1-10) forearms using a commercial CO_2 sensor (CozIR-A 10,000 ppm CO_2 Sensor, CO2Meter.com, USA) and 10 OFCSs (OFCS 1-10) at a range of 32 °C and 43.4 °C for 20 minutes. The response time of the commercial CO_2 sensor is 30 seconds. In Section 5.3.4, the maximum and minimum obtained skin CO_2 concentration was 429 ppm and 149 ppm, respectively, over 3 trials. The SNR of OFCSs (OFCS 1-10) range was 0.5-13.4. The error range w.r.t. intensity was 0.4-86.4 %, and the error range w.r.t. absorbance was 2-86.4 % for the OFCSs (OFCS 1-10) and commercial CO_2 sensor. This error range varied due to the sensitivity obtained from the OFCSs (OFCS 1-10) in Section 3.7.

The OFCS 1-6 and commercial CO_2 sensor measured the CO_2 changes on the volunteers' (Volunteer 1-6) skin and in the air. The response of both sensors climbed when both sensors were put on the volunteers' (Volunteer 1-6) skin. Similarly, the response of both sensors declined when both sensors were placed in the air. The commercial CO_2 sensor also measured the CO_2 changes on the volunteers' (Volunteer 7-10) skin and in the air. Unfortunately, the OFCS 7-10 couldn't measure the CO_2 changes on the volunteers' (Volunteer 7-10) skin and in the air. The variation in response between the OFCS and commercial CO_2 sensor was found because the OFCS lost its dye properties over time. Also, the physiological properties and skin temperature varied for each trial. The performance of the OFCS suffered photobleaching and bending during the skin CO_2 measurement.

In Section 5.3.5, the bending is a problem, which can be reduced using the experimental set-up, as mentioned in Figures 6.5 (a) and 6.7 (a), by placing the optical fibre as straight as possible inside a PLA based GCC on the fixation ring.

In conclusion, the potential of the OFCS for healthcare applications has been initially demonstrated, but there is still future work to be carried out to obtain a better performance of the OFCS as described in the next section.

6.3 Future work

The OFCS showed promising results for the skin CO_2 measurement for healthcare applications. For example, the best result was shown in Figure 5.10 (c), where the OFCS 1 and commercial CO_2 sensor followed the same trend to measure the CO_2 changes on the Volunteer 1's skin and in the air successfully. On the other hand, the OFCS 7 was not working properly according to Figure C.25 (a) [Appendix C]; the OFCS 7 and commercial CO_2 sensor didn't follow the same trend to measure the CO_2 changes on the Volunteer 7's skin and in the air. Overall, the first 6 OFCSs (OFCS 1-6) measured the CO_2 changes on the volunteers' (Volunteer 1-6) skin and in the air successfully, as shown in Figures 5.10 (a) (c) (e) and {C.10, C.13, C.16, C.19, and C.22} (a) (c) (e) [Appendix C]. Unfortunately, the other 4 OFCSs (OFCS 7-10) couldn't measure the CO_2 changes on the volunteers' (Volunteer 7-10) skin and in the air, as shown in Figures {C.25, C.28, C.31, and C.34} (a) (c) (e) [Appendix C]. The success rate could be increased by performing the suggested future work.

Future work is suggested around:

i) Guidelines to fabricate, store, and perform the experiment with an OFCS have been provided below.
ii) A few steps to refine the model of an FPI are proposed to make it more accurate.
iii) In addition, the design of a prototype and portable clinical unit for the skin CO_2 measurement using an OFCS is proposed.

These are discussed below.

6.3.1 Guidelines to fabricate, store, and perform experiment with OFCSs

The fabrication process of a batch of OFCSs to be manufactured all at the same time is mentioned below. It is hypothesised that this would provide more reproducible response across a single batch of OFCSs. The suggested procedure is as follows:

A PLA based fibre holder and microcentrifuge tube (MT) holder are proposed to fabricate a batch of OFCSs (typically 10 OFCSs) simultaneously following the film preparation

method, as mentioned in Section 3.2.5. The number of slots of the fibre holder and MT holder can be modified according to the user's requirements. In Figure 6.1 (a), the optical fibres and MTs are placed in the fibre holders' slots and MT holders' slots, respectively. The sol-gel solutions are kept inside the MTs, and the optical fibre tips are dipped inside the solution.

The cap of the MTs needs to be closed properly during the drying interval of the OFCSs between each coating layer (such as 2 minutes) in the air, as shown in Figure 6.1 (b). Otherwise, the sol-gel will evaporate quickly and become gel because ethanol is contained inside this solution.

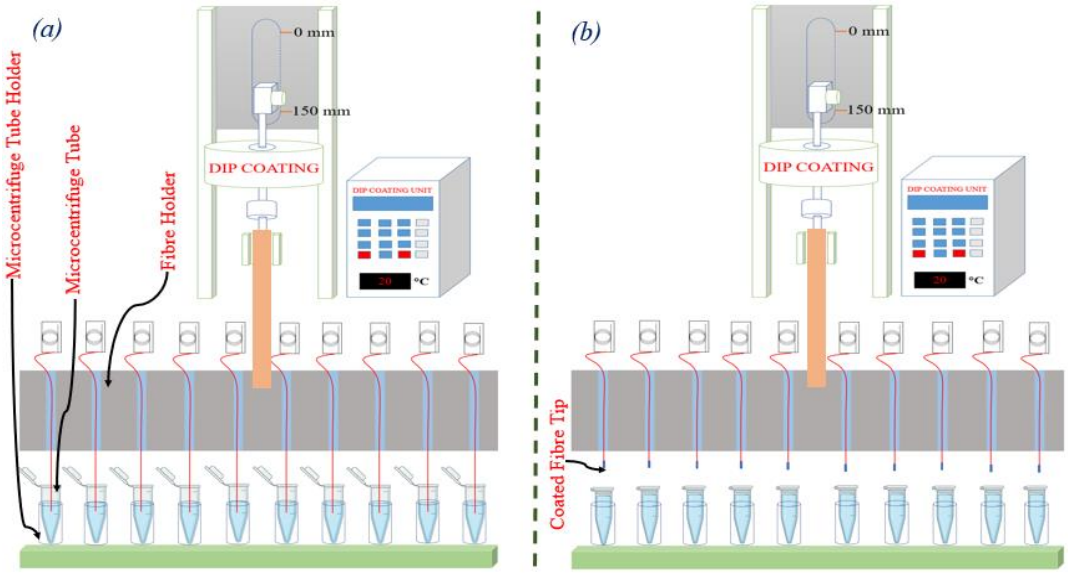


***Figure 6.1**: Experimental set-up for a simultaneous coating process onto multiple optical fibre tips during (a) coating (b) drying intervals using commercial dip coating unit*

An immersed length plays a vital role in fabricating the OFCS. The immersed length of the optical fibre needs to be minimised to avoid cracking the film. The drying process and cracking formation are mentioned in Sections 3.3.2 and 3.5.1, respectively. In Figure 6.2 (a), it's better to choose the immersed length, L as around or less than 3 mm; this value is observed during the coating process. The small drop of solvent is applied to the optical fibre tip, reducing the chances of cracking formation after drying due to choosing a minimum immersed length.

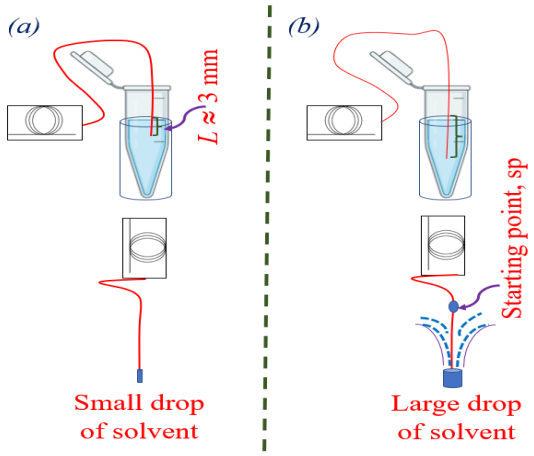


Figure 6.2: *Coating of optical fibre tip for (a) lower (b) higher immersed length*

Figure 6.2 (b) shows the drying steps for choosing a higher immersed length. The liquid drips from a starting point (marked as sp) to the fibre tip, and the liquid adheres and creates a large drop of solvent at the fibre tip. Finally, it starts cracking due to the evaporation of the solvent and higher capillary force.

The guidelines about storing and performing the experiment with the OFCS are provided below:

The OFCS needs to be fabricated using the preparation scheme, Solution 2, as mentioned in Section 3.5.2. The extended lifetime was achieved using Triton X-100 in the preparation scheme, according to Section 3.5.3. The OFCS must be stored inside a vacuum sealer bag after finishing the experiment. The air toxicity affects the performance of the OFCS because of putting the OFCS in the air for a long time. All the vacuum sealer bags having the OFCS can be placed in a dark container to avoid photobleaching of the dye (TB).

The OFCS suffers from photobleaching, affecting the lifetime and performance of the OFCS. So, the calibration of the OFCS needs to be performed at a reduced light intensity not to exceed a threshold of photobleaching of the dye (TB). Also, for the proof-of-concept experiments, the skin CO_2 needs to be measured for a short period. The response of the OFCS on the skin can be correlated to the calibration results of the OFCS. A light source with a shutter is preferable to calibrate the OFCS and skin CO_2 measurement using the OFCS for an extended period.

Photobleaching is a potential barrier to widespread use and needs to be better characterised in future work. Photobleaching can be observed and characterised using Ultraviolet-Visible (UV-Vis) or absorption spectroscopy. UV-Vis spectroscopy is an analytical technique that measures how much a chemical substance absorbs light. The absorbance w.r.t. time can be observed for different intensity levels, indicating photobleaching (such as how much the absorbance changes according to intensity levels).

6.3.2 Steps to refine an FPI model

Generally, a simulation is helpful because it allows the investigation of different parameters such as mean, variance, skewness, kurtosis, and SNR more easily and rapidly than performing this experimentally. The opportunities to improve the FPI model are given below:

I) To date, only discrete wavelengths have been investigated using the FPI model; however, the shape of the entire spectrum can be measured. Mainly, the absorption spectrum of the FPI model changes due to the baseline and room light variation, making measurements of absolute intensity challenging. A better and more reliable sensor performance can be achieved by investigating the shape of the entire spectrum (such as getting the stable baseline at a single wavelength). The measurement of the moments (such as mean, variance, skewness, and kurtosis) of the FPI model is more reliable because this relies on the shape of the spectral distribution rather than the absolute intensity. The spectral shape of the FPI model can be refined by detecting the moments of the FPI model. For example, the skew and kurtosis values can be simulated, and it is possible to observe whether these are more robust than absorbance values in obtaining the CO_2 concentrations.

II) Practically, the spikes (a form of noise) are found due to the room light effect on the absorption spectrum of the FPI model. The noise effects on the FPI model can be observed via the FPI simulation (such as calculating a theoretical SNR). A noise generator can be added to introduce white noise or systematic noise (such as baseline drifts) to investigate the noise effects on the FPI model. The SNR can be investigated by simulating the noise using the FPI model.

Finally, the simulated results should be compared further to the experimental results.

6.3.3 Design of a GCC on a fixation ring

Figures 6.3 (a) and (b) demonstrate the front and back sides of a commercial fixation ring (Radiometer, UK), respectively. The fixation ring's external diameter (D_1) is 32 mm, and the internal diameter (D_2) is 16 mm. Another space with a diameter (D_3) is 10 mm, which is used for T_CPCO_2 measurement from the skin. This fixation ring can be adapted for the OFCS applications.

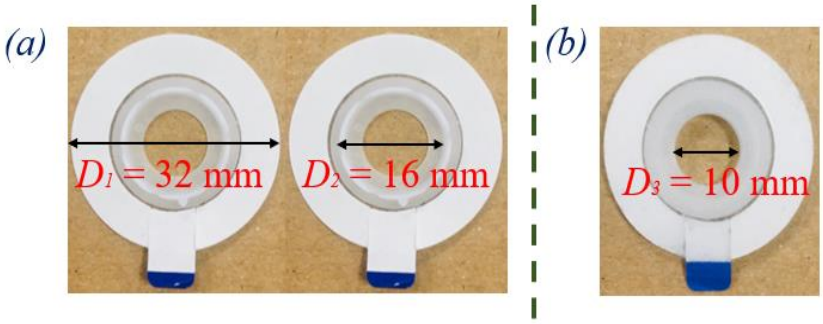


Figure 6.3: *(a) Front (b) Back view of fixation ring*

The fixation ring will be capped with a PLA based circular GCC. The PLA based GCC will prevent leaking the skin CO_2 during this experiment. The fixation ring with the PTFE film will nullify the humidity effect of the OFCS. The approximate dimension of the PLA based GCC is mentioned in Figure 6.4 based on the fixation ring's size, and this dimension is chosen by considering the size of the t_C Sensor 92 probe demonstrated in Figure 2.13 (a). The diameter (D_4), height (H_1), and thickness (T_1) of the PLA based GCC will be around 16, 10, and 1 mm, respectively. The adhesive fixation ring is attached to the skin very easily.

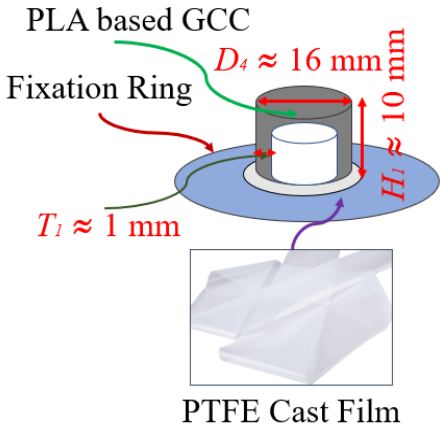


Figure 6.4: *Dimension of PLA based GCC on fixation ring*

6.3.4 Design of a prototype for skin CO_2 measurement

The motivation for designing a prototype for measuring the skin CO_2 comes from the previously carried out research by our collaborators at the University of Southampton. The OFCS will be integrated and used in a similar test our collaborators performed at the University of Southampton. The experiment protocol is mentioned in Section 2.3.1. T_CPCO_2 was measured from 14 healthy participants' skins from the back side of a human body (such as the sacrum, according to Figure 2.5) when the participants laid on the hospital bed in a prone position for 20 minutes and different ranges of pressure were applied on the sacrum during this test [8].

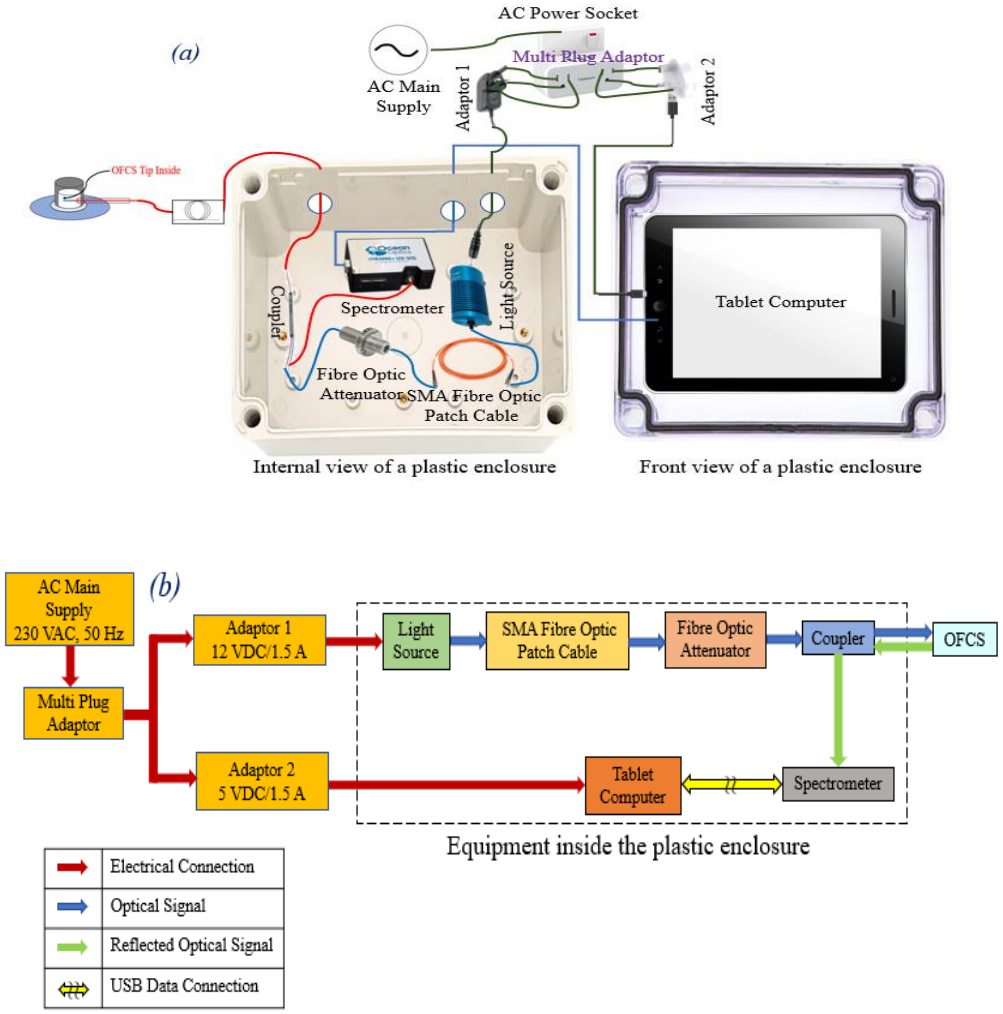


Figure 6.5: *(a) Internal structure (b) Block diagram of prototype for skin CO_2 measurement using OFCS*

Figure 6.5 (a) shows the internal structure of the prototype for measuring the skin CO_2 using an OFCS. In Figure 6.5 (a), the same experimental set-up will be used (from Figure 4.6) with the same equipment, as detailed in Section 3.3.1. A tablet computer is inserted at the front side of a plastic enclosure (around 160 mm (L) x 220 mm (W) x 60 mm (H)). The tablet computer functions as a screen. A light source, a patch cable, an attenuator, a coupler, and a spectrometer are placed inside the plastic enclosure. The coupler's connecting port is placed outside the plastic enclosure to connect to the OFCS. The OFCS tip is connected to the PLA based GCC through the channel for designing the prototype and a portable clinical unit for measuring the skin CO_2. The OFCS is not directly in contact with the skin. The commercial CO_2 sensor is not included in this proposed experimental protocol for designing the prototype and portable clinical unit for measuring the skin CO_2.

Figure 6.5 (b) shows the block diagram of the prototype for measuring the skin CO_2 using the OFCS. The different colours of arrows are used as a representation of different connections. Such as red, blue, green, and yellow arrows represent an electrical connection, an optical signal, a reflected optical signal, and a USB data connection, respectively. The light source is connected to the fibre optic attenuator via the SMA fibre optic patch cable. The light travels to the OFCS tip through the coupler, and the reflected light is captured using the spectrometer (through the coupler again), which is connected to the tablet computer to record the OFCS's response.

In Figures 6.5 (a) and (b), Adaptors 1 and 2 are needed to turn on the light source and tablet computer, respectively. Adaptors 1 and 2 are connected to an AC main supply via a multi plug adaptor and an AC power socket.

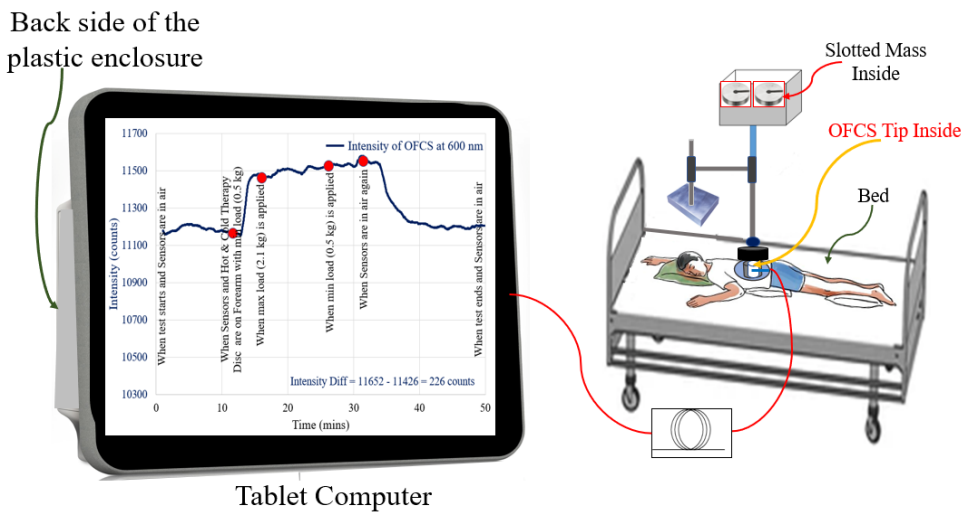


Figure 6.6: *Experimental set-up for monitoring CO_2 emitted from human skin during loading using OFCS and prototype*

In Figure 6.6, a volunteer lay on the bed in a prone position. The fixation ring with the PLA based GCC is placed on the back of the volunteer (such as the sacrum) and is pressed by the loading machine (from Figure 5.5 (a), Section 5.3.1); it will provide loading to the skin through the fixation ring. The additional slotted mass is placed inside the weight holder to increase the load. This prototype is straightforward to carry out for an experimenter. The OFCS placement inside the PLA based GCC on the fixation ring will reduce the bending problem observed during the skin CO_2 measurement, and how the bending occurred is described in Section 5.3.5.

6.3.5 Design of a portable clinical unit for skin CO_2 measurement

The motivation for designing the portable clinical unit for measuring the skin CO_2 comes from the previously done research by our collaborators at the University of Southampton. The OFCS will be integrated and used in a similar test that our collaborators performed at the University of Southampton. The experiment protocol is mentioned in Section 2.3.1. T_CPCO_2 was measured from 12 healthy participants' skins when the participants laid on the APAM in a supine position for 40 minutes [2].

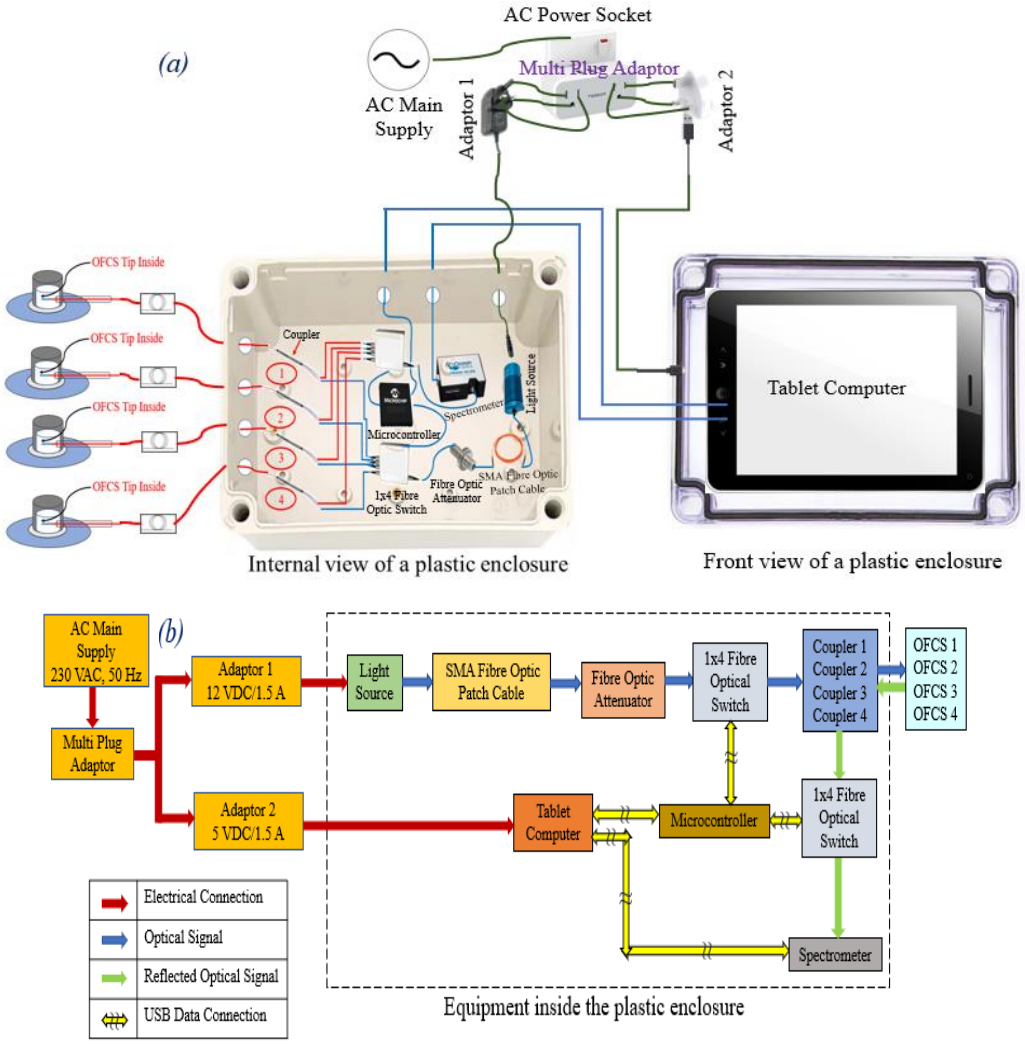


Figure 6.7: *(a) Internal structure (b) Block diagram of portable clinical unit for skin CO_2 measurement using 4 OFCSs*

Figure 6.7 (a) shows the internal structure of the portable clinical unit for measuring the skin CO_2 using 4 OFCSs (OFCS 1-4). In Figure 6.7 (a), the same experimental set-up will be used (from Figure 4.6) with the same equipment, as detailed in Section 3.3.1, except for 2 fibre optical switches and a microcontroller. A tablet computer is inserted at the front side of a plastic enclosure (around 180 mm (L) x 240 mm (W) x 60 mm (H)). The tablet computer functions as a screen. A light source, a patch cable, an attenuator, 2 fibre optical switches, a microcontroller, 4 couplers, and a spectrometer are placed inside the plastic enclosure. The 1x4 fibre optical switch is used to connect the 4 OFCSs (OFCS 1-4) to the

4 couplers (Coupler 1-4), and the reflected light is captured by the spectrometer via another 1x4 fibre optical switch. The 1x4 fibre optical switches will select each channel at a specific interval (such as every 20 seconds) to collect the reflected light from each OFCS one at a time. The microcontroller will control the sampling frequency of the 1x4 fibre optical switch. This way, all 4 OFCSs (OFCS 1-4) are placed on the 4 different places on the patient's skin and the response of the 4 OFCSs (OFCS 1-4) can be monitored sequentially. The 4 couplers' (Coupler 1-4) connecting ports are placed outside the plastic enclosure to connect the 4 OFCSs (OFCS 1-4).

Figure 6.7 (b) shows the block diagram of a portable clinical unit for measuring the skin CO_2 using the 4 OFCSs (OFCS 1-4). The different colours of arrows are used as a representation of different connections. Such as red, blue, green, and yellow arrows represent an electrical connection, an optical signal, a reflected optical signal, and a USB data connection, respectively. The light source is connected to the fibre optic attenuator via the SMA fibre optic patch cable. The light travels to the 4 OFCSs' (OFCS 1-4) tips through the 1x4 fibre optical switch and couplers (Coupler 1-4), and the reflected light is captured using the spectrometer (through the 1x4 fibre optical switch and couplers (Coupler 1-4) again). The microcontroller is connected to both 1x4 fibre optical switches to maintain the specific interval for switching from one channel to another. The spectrometer is connected to the tablet computer to record the 4 OFCSs' (OFCS 1-4) responses with the help of the microcontroller.

In Figures 6.7 (a) and (b), Adaptors 1 and 2 are needed to turn on the light source and tablet computer, respectively. Adaptors 1 and 2 are connected to the AC main supply via the multi plug adaptor and AC power socket. The microcontroller is also turned on the USB data connection of the tablet computer.

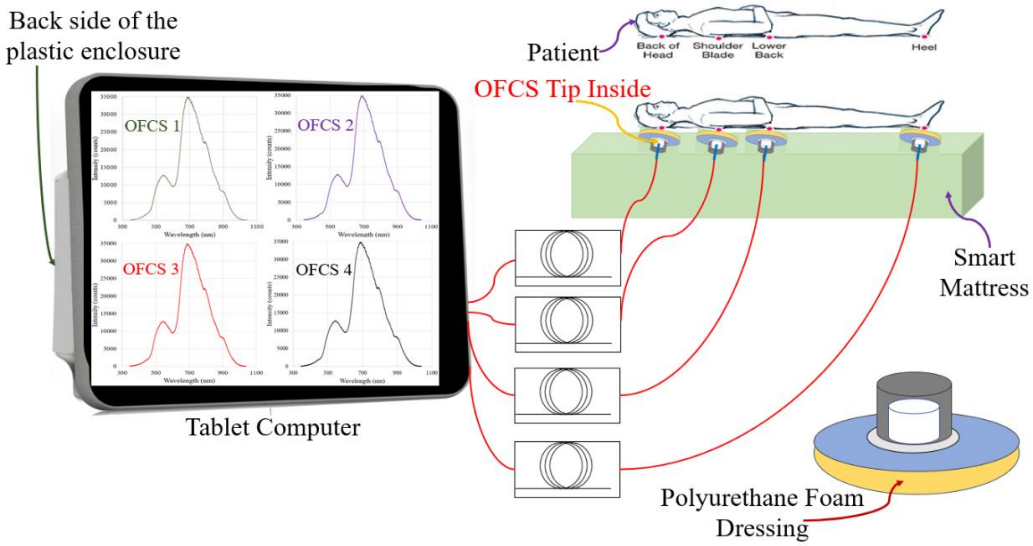


Figure 6.8: *Experimental set-up for monitoring CO_2 emitted from human skin during loading using 4 OFCSs and portable clinical unit*

This experiment will be performed on the patients susceptible to PUs who will lie in bed for a long period. The affected area is shown in Figure 6.8; it's located in different areas such as the back of the head, shoulder blade, heel, and lower back [32]. A patient lies on a smart mattress (such as a mattress, Tactile Pressure Experts, Sensors Products Inc., USA). This mattress has built-in pressure and temperature sensors which can sense the pressure and temperature distribution between the patient's body and mattress surface. The pressure sensor is a matrix-based surface sensor that operates by the principles of piezo-resistance, and the thermistors sense temperature. The detectable pressure and temperature range is 0-103.4 mmHg and 20-70 °C, respectively [138-140].

In Figure 6.8, the adhesive polyurethane foam dressing (Biatain, Coloplast GmbH, Germany [141]) is placed on different body parts of the patient. The fixation ring with PLA based GCC is placed on the polyurethane foam dressing. The PLA based GCC will be covered by adhesive flexible fabric to avoid the rough surfaces of this GCC which may hurt the patients. The adhesive polyurethane dressing and flexible fabric make the PLA based GCC comfortable for the patients. The PLA based GCC with OFCS is pressed by the mattress; it will provide loading to the skin through the fixation ring.

By addressing the above future work, it is hoped that the new OFCSs will have a much higher success rate moving this research device closer to the clinic.

References

[1] Radiometer, “Solutions for transcutaneous monitoring,” pp. 2, 7, 2014 [Online]. https://usermanual.wiki/m/0eb48eff7ffc875e1adca939e9129161cab5dcbde075f6df4fbbb82fc6eb4706.pdf [Accessed: 28 June 2023]

[2] P. Mirtaheri, T. Gjovaag, P.R. Worsley, D.L. Bader, “A Review of the Role of the Partial Pressure of Carbon Dioxide in Mechanically Loaded Tissues: The Canary in the Cage Singing in Tune with the Pressure Ulcer Mantra,” *Annals of Biomedical Engineering*, vol. 43, no. 2, pp. 336-347, 2015, DOI: 10.1007/s10439-014-1233-z.

[3] W.van Weteringen, T.G. Goos, T.van Essen, C. Ellenberger, J. Hayoz, R.C.J. de Jonge, I.K.M. Reiss, P.M. Schumacher, “Novel transcutaneous sensor combining optical t_CPO_2 and electrochemical t_CPCO_2 monitoring with reflectance pulse oximetry,” *Medical & Biological Engineering & Computing*, vol. 58, no. 2, pp. 239-247, 2020, DOI: 10.1007/s11517-019-02067-x.

[4] Radiometer, “The $tcpCO_2$ Handbook,” pp. 7-31, 2011 [Online]. http://mss.co.th/media/trancutaneous/TC100_Understanding_transcutaneous%20pO2_and_pCO2/tcpco2handbook.pdf [Accessed: 28 June 2023]

[5] Radiometer, “Safety Data Sheet of Chemicals for Radiometer Equipment,” pp. 1-10, 2013 [Online]. https://punchout.medline.com/media/catalog/Docs/MSDS/MSD_SDSD80360.pdf [Accessed: 28 June 2023]

[6] N. Sabri, S.A. Aljunid, M.S. Salim, S. Fouad, “Fibre Optic Sensors: Short Review and Applications,” *Recent Trends in Physics of Material Science and Technology, Springer Series in Materials Science*, vol. 204, pp. 299-311, 2015, DOI: 10.1007/978-981-287-128-2_19.

[7] NHS inform, “Pressure ulcers, Causes of pressure ulcers” 2023 [Online]. https://www.nhsinform.scot/illnesses-and-conditions/skin-hair-and-nails/pressure-ulcers#causes-of-pressure-ulcers [Accessed: 28 June 2023]

[8] S.L. Knight, R.P. Taylor, A.A. Polliack, D.L. Bader, “Establishing predictive indicators for the status of loaded tissues,” *Journal of Applied Physiology*, vol. 90, no. 6, pp. 2231-2237, 2001, DOI: 10.1152/jappl.2001.90.6.2231.

[9] S. Ghetia, R. Gajjar, P. Trivedi, "Classification of Fibre Optical Sensors," *International Journal of Electronics Communication and Computer Technology (IJECCT)*, vol. 3, issue 4, pp. 442-445, 2013, ISSN:2249-7838.

[10] V.L. Kalyani, V. Sharma, "Optical Sensors and Their Use in Medical Field," *Journal of Management Engineering and Information Technology (JMEIT)*, vol 3, issue 5, pp. 1-4, 2016, ISSN: 2394-8124.

[11] CLU-IN, ORG., "Fibre Optic Chemical Sensors," 2023 [Online]. https://clu-in.org/characterization/technologies/focs.cfm [Accessed: 28 June 2023]

[12] Intelligent Optical Systems, Inc., "Distributed Intrinsic Fiber Optic Chemical Sensors," slide no. 4-7, 2023 [Online]. https://www.netl.doe.gov/sites/default/files/2017-12/FE0012706-Alonso.pdf [Accessed: 28 June 2023]

[13] PreSens Precision Sensing, "In Process Monitoring of Dissolved Carbon Dioxide," CO_2 Dipping Probe DP-CD1," 2023 [Online]. https://www.presens.de/products/detail/co2-dipping-probe-dp-cd1 [Accessed: 28 June 2023]

[14] A.G.A. Al-kaf, A.M. Othman, "A review on Needle Free Injection," *Universal Journal of Pharmaceutical Research (UJPR)*, vol. 2, issue 2, pp. 1-5, 2017, DOI: 10.22270/ujpr.v2i2.RW1.

[15] C. Miller, "Human Biology, 10.2 Introduction to the Integumentary System," *Thompson River University*, 2023 [Online]. https://humanbiology.pressbooks.tru.ca/chapter/12-2-introduction-to-the-integumentary-system/ [Accessed: 28 June 2023]

[16] S.-H. Kuo, C.-J. Shen, C.-F. Shen, C.-M. Cheng, "Role of pH Value in Clinically Relevant Diagnosis," *Diagnostics*, vol. 10, issue 2, pp. 1-17, 2020, DOI: 10.3390/diagnostics10020107.

[17] T. Newman, "Skin: How it works," *Medical News Today*, 2021 [Online]. https://www.medicalnewstoday.com/articles/320435 [Accessed: 28 June 2023]

[18] Pediatric & Young Adult Medicine, "Skin Trauma," 2023 [Online]. https://www.pyam.com/services/health-issues-and-illnesses/skin-trauma/ [Accessed: 28 June 2023]

[19] Beth Israel Lahey Health Winchester Hospital, "Health Library, Skin Wound," 2023 [Online]. https://www.winchesterhospital.org/health-library/article?id=744867 [Accessed: 28 June 2023]

[20] B.S. Hulka, T.C. Wilcosky, J.D. Griffith, "Overview of biological markers, Biological Markers in Epidemiology," *Oxford University Press, New York*, pp. 3-15, 1990, ISBN: 0-505984-0.

[21] R. Mayeux, "Biomarkers: Potential Uses and Limitations," *NeuroRx*, vol. 1, issue 2, pp. 182-188, 2004, DOI: 10.1602/neurorx.1.2.182.

[22] I. Bromley, "Transcutaneous monitoring – understanding the principles," *Infant*, vol. 4, issue 3, pp. 95-98, 2008.

[23] P. Christensen, J. Hjarbæk, B. Jensen, J. Grønlund, "Measurement of transcutaneous PO_2, PCO_2 and skin blood flow at different probe temperatures using mass spectrometry," *Acta Anaesthesiologica Scandinavica*, vol. 35, issue 7, pp. 631-634, 1991, DOI: 10.1111/j.1399-6576.1991.tb03362.x.

[24] D. L. Thomas, M. F. Lythgoe, G. S. Pell, F. Calamante and R. J. Ordidge, "The measurement of diffusion and perfusion in biological systems using magnetic resonance imaging," *Physics in Medicine & Biology*, vol. 45, no. 8, p. R97, 2000, DOI: 10.1088/0031-9155/45/8/201.

[25] A.-M. Kelly, S. Klim, "Agreement between arterial and transcutaneous PCO_2 in patients undergoing non-invasive ventilation," *Respiratory Medicine*, vol. 105, issue 2, pp. 226-229, 2011, DOI: 10.1016/j.rmed.2010.11.010.

[26] Course Hero, "Gas Exchange," *Boundless Anatomy and Physiology*, 2023 [Online]. https://www.coursehero.com/study-guides/boundless-ap/gas-exchange/ [Accessed: 28 June 2023]

[27] G.J. Tortora, B.H. Derrickson, "Principles of anatomy and physiology," *John Wiley & Sons*, 14th Edition, pp. 863-866, 2014, ISBN: 978-1-118-34500-9.

[28] A. R. Cupp, J. A. Tix, J. R. Smerud, R. A. Erickson, K. T. Fredricks, J. J. Amberg, C. D. Suski, R. Wakeman, "Using dissolved carbon dioxide to alter the behaviour of invasive round goby," *Management of Biological Invasions*, vol. 8, issue 4, pp. 567-574, 2017, DOI: 10.3391/mbi.2017.8.4.12.

[29] C. Sissons, “What is the average percentage of water in the human body?,” *Medical News Today,* 2020 [Online]. https://www.medicalnewstoday.com/articles/what-percentage-of-the-human-body-is-water [Accessed: 28 June 2023]

[30] P.von. Dadelszen, “ABG (Arterial Blood Gas),” *The Global Library of Women’s Medicine (GLOWM),* 2001 [Online]. https://www.glowm.com/lab-text/item/3# [Accessed: 28 June 2023]

[31] Q. Zhang, Z. Sun, J. Yue, “Massage therapy for preventing pressure ulcers,” *Cochrane Database of Systematic Reviews, The Cochrane Collaboration, John Wiley & Sons,* issue 6, art no. CD010518, p. 2, 2015, DOI: 10.1002/14651858.CD010518.pub2.

[32] J.L. Zeller, C. Lynm, R.M. Glass, “Pressure Ulcers,” *The Journal of American Medical Association*, vol. 296, no. 8, p. 1020, 2006, DOI: 10.1001/jama.296.8.1020.

[33] M. Stephens, C.A. Bartley, “Understanding the association between pressure ulcers and sitting in adults what does it mean for me and my carers? Seating guidelines for people, carers, and health & social care professionals,” *Journal of Tissue Viability*, vol. 27, issue 1, pp. 59-73, 2018, DOI: 10.1016/j.jtv.2017.09.004.

[34] Y. Brazier, “Bed sores or pressure ulcers: What you need to know,” *Medical News Today,* 2020 [Online]. https://www.medicalnewstoday.com/articles/173972 [Accessed: 28 June 2023]

[35] G. Bennet, C. Dealey, J. Posnett, “The cost of pressure ulcers in the UK,” *Age and Ageing*, vol. 33, no. 3, pp. 230-235, 2004, DOI: 10.1093/ageing/afh086.

[36] M. Xue, D. Wang, Z. Zhang, Z. Cao, Z. Luo, Y. Zheng, J. Lu, Q. Zhao, X. D. Zhang, “Demonstrating the Potential of Using Transcutaneous Oxygen and Carbon Dioxide Tensions to Assess the Risk of Pressure Injuries*,” International Journal of Biological Sciences*, vol. 14, no. 11, pp. 1466-1471, 2018, DOI: 10.7150/ijbs.26987.

[37] S. Warner, “Pressure Ulcer Risk Assessment the Braden Scale,” *Oxford Health NHS Foundation Trust*, slide no. 4-6, 2014 [Online].

https://www.oxfordhealth.nhs.uk/wp-content/uploads/2015/08/Braden-teaching.pdf [Accessed: 28 June 2023]

[38] D. Salzmann, P. Eberhard, C. Depeursinge, "Optical Transcutaneous Blood Gas Measurement," *Chimia*, vol. 59, no. 5, pp. 261-262, 2005, ISSN 0009-4293.

[39] P. Eberhard, "The Design, Use, and Results of Transcutaneous Carbon Dioxide Analysis: Current and Future Directions," *International Anesthesia Research Society*, vol. 105, no. 6, pp. S48-S52, 2007, DOI: 10.1213/01.ane.0000278642.16117.f8.

[40] J. J. Davenport, M. Hickey, J. P. Phillips, P. A. Kyriacou, "Dual pO2/pCO2 fibre optic sensing film," *Analyst*, vol. 142, issue 10, pp. 1711-1719, 2017, DOI: 10.1039/c7an00173h.

[41] J. Hromadka, B. Tokay, R. Correia, S. Morgan, S. Korposh, "Carbon dioxide measurements using long period grating optical fibre sensor coated with metal organic framework HKUST-1," *Sensors and Actuators B: Chemical*, vol. 255, pp. 2483-2494, 2018, DOI: 10.1016/j.snb.2017.09.041.

[42] W. Ma, J. Xing, R. Wang, Q. Rong, W. Zhang, Y. Li, J. Zang, X. Qiao, "Optical Fibre Fabry-Perot Interferometric CO_2 Gas Sensor Using Guanidine Derivative Polymer Functionalized Layer," *IEEE Sensors Journal*, vol. 18, no. 5, pp. 1924-1929, 2018, DOI: 10.1109/JSEN.2018.2790973.

[43] W. Ma, R. Wang, Q. Rong, Z. Shao, W. Zhang, T. Guo, J. Wang, X. Qiao, "CO_2 Gas Sensing Using Optical Fibre Fabry-Perot Interferometer Based on Polyethyleneimine/Poly(Vinyl Alcohol) Coating," *IEEE Photonics Journal*, vol. 9, no. 3, pp. 1-8, 2017, DOI: 10.1109/JPHOT.2017.2700053.

[44] C.-S. Chu, M.-W. Hsieh, "Optical fibre carbon dioxide sensor based on colorimetric change of α-naphtholphthalein and CIS/ZnS quantum dots incorporated with a polymer matrix," *Optical Materials Express*, vol. 9, issue 7, pp. 2937-2945, 2019, DOI: 10.1364/OME.9.002937.

[45] S.-K. Yao, C.K. Asawa, "Fiber Optical Intensity Sensors," *IEEE Journal on Selected Areas in Communications*, vol. 1, issue 3, pp. 562-575, 1983, DOI: 10.1109/JSAC.1983.1145942.

[46] D.C. Harris, "Charles David Keeling and the story of atmospheric CO_2 measurements," *Analytical Chemistry*, vol. 82, no. 19, pp. 7865-7870, 2010, DOI: 10.1021/ac1001492.

[47] CO2Meter.com, "How does an NDIR CO_2 Sensor Work?," 2023 [Online]. https://www.co2meter.com/blogs/news/6010192-how-does-an-ndir-co2-sensor-work [Accessed: 28 June 2023]

[48] CO2Meter.com, "K33 ICB 10% CO_2 Sensor," 2023 [Online]. https://www.co2meter.com/collections/10-co2/products/k-33-icb-10-co2-sensor [Accessed: 28 June 2023]

[49] CO2Meter.com, "CozIR-A 10,000 ppm CO_2 Sensor," 2023 [Online]. https://www.co2meter.com/products/cozir-ambient-10000-ppm-co2-sensor?variant=840094613524 [Accessed: 28 June 2023]

[50] L.B. Mendes, N.W.M. Ogink, N. Edouard, H.J.C.van Dooren, I.de F.F. Tinôco, J. Mosquera, "NDIR Gas Sensor for Spatial Monitoring of Carbon Dioxide Concentrations in Naturally Ventilated Livestock Buildings," *Sensors*, vol. 15, issue 5, pp. 11239-11257, 2015, DOI: 10.3390/s150511239.

[51] Sentec.com, "Specification Sheet of SenTec Digital Monitor with V-Sign™ Sensor," pp. 1-2, 2023 [Online]. https://www.sentec.com/fileadmin/documents/Labeling/Spec_Sheets/RF-005856-m-SDM-VS_SpecSheet.pdf [Accessed: 28 June 2023]

[52] Radiometer, "TCM4 and TCM40 Specifications," pp. 2-3, 2008 [Online]. http://www.pulmodata.si/veleprodaja/pdf/TCM4.pdf [Accessed: 28 June 2023]

[53] J.J. Bray, P.A. Cragg, A.D.C. Macknight, R.G. Mills, D.W. Taylor, "Lecture Notes on Human Physiology," *Blackwell Science Ltd.*, 4th edition, p. 556, 1999, ISBN: 0865427755.

[54] R. Sunheimer, L. Graves, "Chapter 4, Instrumentation Laboratory Automation and Informatics," *Clinical Laboratory Chemistry, Pearson*, 2nd Edition, p. 102, 2018, ISBN-10: 0134413326, ISBN-13: 9780134413327.

[55] Radiometer, "TCM TOSCA/CombiM, Operator's manual," 1st Edition, pp. 4-8, 5-1, 6-12, 8-13, 9-3, 9-7, 9-8, 2018.

[56] K. Fidanboylu, H. S. Efendioglu, "Fiber optic sensors and their applications," *5th International Advanced Technologies Symposium (IATS), Karabuk, Turkey*, pp. 1-6, May 13-15, 2009.

[57] L. Schennato, "Fiber-Optic Sensors for Geo-Hydrological Applications: basic concepts and applications," *Rendiconti Online della Società Geologica Italiana*, vol. 30, pp. 51-54, 2014, DOI: 10.3301/RO.2014.11.

[58] M. L. Tuma, "Fundamentals Concepts of Integrated and Fibre Optic Sensors," *NASA Technical Memorandum 106920*, pp. 2-26, 1995.

[59] C. He, S. Korposh, F.U. Hernandez, L. Liu, R. Correia, B.R. Hayes-Gill, S.P. Morgan, "Real-Time Humidity Measurement during Sports Activity using Optical Fibre Sensing," *Sensors*, vol. 20, issue 7, pp. 1-4, 2020, DOI: 10.3390/s20071904.

[60] P. Khandelwal, "Optical Fiber Sensors: Classification & Applications," *International Journal of Latest Technology in Engineering, Management & Applied Science*, vol. 2, issue 7, p. 23, 2013, ISSN 2278-2540.

[61] M. Hernaez, C.R. Zamarreño, S. M.-Espina, L.R. Bird, A.G. Mayes, F.J. Arregui, "Optical Fibre Sensors Using Graphene-Based Materials: A Review," *Sensors*, vol.17, issue 1, pp. 1-24, 2017, DOI: 10.3390/s17010155.

[62] Y. Zhao, X.-G. Li, X. Zhou, Y.-N. Zhang, "Review on the graphene based optical fibre chemical and biological sensors," Sensors and Actuators B: Chemical, vol. 231, pp. 324-340, 2016, DOI: 10.1016/j.snb.2016.03.026.

[63] X. Sun, Q. Sun, W. Jia, Z. Xu, J. Wo, D. Liu, and L. Zhang, "Graphene Coated Microfiber for Temperature Sensor," *International Photonics and OptoElectronics Meetings, Optica Publishing Group*, paper FF4B.3, 2014, DOI: 10.1364/FBTA.2014.FF4B.3.

[64] J. Zhang, G. Liao, S. Jin, D. Cao, Q. Wei, H. Lu, J. Yu, X. Cai, S. Tan, Y. Xiao, J. Tang, Y. Luo, Z. Chen, "All-fibre-optic temperature sensor based on reduced graphene oxide," *Laser Physics Letters*, vol. 11, no. 3, pp. 1-6, 2014, DOI: 10.1088/1612-2011/11/3/035901.

[65] P. Lesiak, P. Sobotka, M. Bieda, A. Duzynska, A. Wroblewska, M. Chychlowski, T.R. Wolinski, "Innovative UV sensor based on highly birefringent fibre covered

by graphene oxide," Photonics Letters of Poland, vol. 7, no. 4, pp. 124-126, 2015, DOI: 10.4302/plp.2015.4.13.

[66] Z. Tian, H. Lu, B.Yang, Y. Wang, W. Qiu, J. Yu, J. Tang, Y. Luo, X. Cai, S. Tan, Z. Chen, J. Zhang, "Microfiber With Methyl Blue-Functionalized Reduced Graphene Oxide and Violet Light Sensing," *IEEE Photonics Technology Letters*, vol. 27, no. 7, pp. 798-801, 2015, DOI: 10.1109/LPT.2015.2392795.

[67] Y. Xiao, J. Zhang, X. Cai, S. Tan, J. Yu, H. Lu, Y. Luo, G. Liao, S. Li, J. Tang, Z. Chen, "Reduced graphene oxide for fibre-optic humidity sensing," *Optics Express*, vol. 22, issue 25, pp. 31555-31567, 2014, DOI: 10.1364/OE.22.031555.

[68] R. Correia, S. James, S.-W. Lee, S. P. Morgan, S. Korposh, "Biomedical application of optical fibre sensors," *Journal of Optics*, vol. 20, no. 7, pp. 1-25, 2018, DOI: 10.1088/2040-8986/aac68d.

[69] C.E. Campanella, A. Cuccovillo, C. Campanella, A. Yurt, V.M.N. Passaro, "Fibre Bragg Grating Based Strain Sensors: Review of Technology and Applications," *Sensors*, vol. 18, issue 9, pp. 2, 6, 2018, DOI: 10.3390/s18093115.

[70] M.-fu Liang, X.-qiu Fang, G. Wu, G.-zhe Xue, H.-wei Li, "A fiber bragg grating pressure sensor with temperature compensation based on diaphragm-cantilever structure," *Optik*, vol 145, pp. 503-512, 2017, DOI: 10.1016/j.ijleo.2017.08.014.

[71] L. Liu, S. P. Morgan, R. Correia, S. -W. Lee, S. Korposh, "Multi-Parameter Optical Fiber Sensing of Gaseous Ammonia and Carbon Dioxide," *Journal of Lightwave Technology*, vol. 38, issue 7, pp. 2037-2045, 2020, DOI: 10.1109/JLT.2019.2953271.

[72] G. Long, L. Wan, B. Xia, C. Zhao, K. Niu, J. Hou, D. Lyu, L. Li, F. Zhu, N. Wang, "Rapid-Response and Wide-Range pH Sensors Enabled by Self-Assembled Functional PAni/PAA Layer on No-Core Fibre," *Materials (Basel)*, vol. 15, no. 21, pp. 1-12, 2022, DOI: 10.3390/ma15217449.

[73] J. Werner, M. Belz, K.-F. Klein, T. Sun, and K. T. V. Grattan, "Characterization of a fast response fibre-optic pH sensor and illustration in a biological application," *Analyst*, vol. 146, issue 15, pp. 4811-4821, 2021, DOI: 10.1039/D1AN00631B.

[74] X. Cheng, J. Bonefacino, B. O. Guan, H. Y. Tam, "All-polymer fibre-optic pH sensor," *Optics Express*, vol. 26, no. 11, pp. 14610-14616, 2018, DOI: 10.1364/OE.26.014610.

[75] V. Bhardwaj, A. K. Pathak, V. K. Singh, "No-core fibre-based highly sensitive optical fibre pH sensor," *Journal of Biomedical Optics*, vol. 22, issue 5, pp. 057001–1-057001–9, 2017, DOI: 10.1117/1.JBO.22.5.057001.

[76] J.J. Richardson, M. Björnmalm, F. Caruso, "Technology-driven layer-by-layer assembly of nanofilms," *Science*, vol. 348, issue 6233, pp. aaa2491-1 – aaa2491-11, 2015, DOI: 10.1126/science.aaa2491.

[77] I.I. Yusoff, R. Rohani, A.W. Mohammad, "Pressure Driven Conducting Polymer Membranes Derived from Layer by Layer Formation and Characterization: A Review," *Journal of Engineering Science and Technology*, vol. 11, no. 8, pp. 1183-1206, 2016, ISSN: 1823-4690.

[78] L.C. Klein, E.J.A. Pope, S. Sakka, J.L. Woolfrey, "Sol-Gel Processing of Advanced Materials," *Ceramic Transactions, Westervill, Ohio: American Ceramics Society*, vol. 81, pp-4-5, 1998, ISBN: 1574980424.

[79] R.B. Figueira, I.R. Fontinha, C.J. R. Silva and E.V. Pereira, "Hybrid Sol-Gel Coatings: Smart and Green Materials for Corrosion Mitigation," *Coatings*, vol. 6, no. 1, pp. 1-19, 2016, DOI: 10.3390/coatings6010012.

[80] D. Wencel, T. Abel, C. McDonagh, "Optical Chemical pH Sensors,", *Analytical Chemistry*, vol. 86, no. 1, pp. 15-29, 2014, DOI: 10.1021/ac4035168.

[81] P.C.A. Jerónimo, A.N. Araújo, M.C.B.S.M. Montenegro, "Optical sensors and biosensors based on sol-gel films," *Talanta*, vol. 72, issue 1, pp. 13-27, 2007, DOI: 10.1016/j.talanta.2006.09.029.

[82] K. Wysokinski, M. Napierala, T. Stanczyk, S. Lipinski, T. Nasilowski, "Study on the Sensing Coating of the Optical Fibre CO_2 Sensor," *Sensors*, vol. 15, no. 12, pp. 31888-31903, 2015, DOI: 10.3390/s151229890.

[83] P.J. Rivero, J. Goicoechea, F.J. Arregui, "Optical Fiber Sensors Based on Polymetric Sensitive Coatings," *Polymers*, vol. 10, no. 3, pp. 1-26, 2018, DOI: 10.3390/polym10030280.

[84] J. J. Davenport, M. Hickey, J. P. Phillips, P. A. Kyriacou, “Dual pO2/pCO2 fibre optic sensing film,” *Analyst*, vol. 142, issue 10, pp. 1711-1719, 2017, DOI: 10.1039/c7an00173h.

[85] C. J. Gouveia, A. Markovics, J. M. Baptista, B. Kovács, P. A. S. Jorge, “Colorimetric and refractometric measurements of carbon dioxide,” *International Conference on Applications of Optics and Photonics, Proc. of SPIE,* vol. 8001, pp. 80013C–1-80013C–4, 2011, DOI: 10.1117/12.892091.

[86] C. Malins, B.D. MacCraith, “Dye-doped organically modified silica glass for fluorescence based carbon dioxide gas detection,” *Analyst*, vol. 123, issue 11, pp. 2373-2376, 1998, DOI: 10.1039/A805803B.

[87] D.A. Nivens, M.V. Schiza, S. Michael Angel, “Multilayer sol–gel membranes for optical sensing applications: single layer pH and dual layer CO_2 and NH_3 sensors,” *Talanta*, vol. 58, issue 3, pp. 543-550, 2002, DOI:10.1016/S0039-9140(02)00323-5.

[88] C. von Bültzingslöwen, A.K. McEvoy, C. McDonagh, B.D. MacCraith, I. Klimant, C. Krause, O.S. Wolfbeis, “Sol-gel based optical carbon dioxide sensor employing dual luminophore referencing for application in food packaging technology,” *Analyst*, vol. 127, issue 11, pp. 1478-1483, 2002, DOI: 10.1039/B207438A.

[89] H. Segawa, E. Ohnishi, Y. Arai, K. Yoshida, “Sensitivity of fiber-optic carbon dioxide sensors utilizing indicator dye,” *Sensors and Actuators B: Chemical*, vol. 94, issue 3, pp. 276-283, 2003, DOI:10.1016/S0925-4005(03)00372-1.

[90] J. Hromadka, B. Tokay, R. Correia, S. Morgan, S. Korposh, “Carbon dioxide measurements using long period grating optical fibre sensor coated with metal organic framework HKUST-1,” *Sensors and Actuators B: Chemical,* vol. 255, pp. 2483-2494, 2018, DOI: 10.1016/j.snb.2017.09.041.

[91] D. Jones, “Module 24–Introduction to Fiber Optics,” *Navy Electricity and Electronics Training Series, Naval Education and Training Professional Development and Technology Center,* pp. 2-10, 2-11, 3-2, 1998.

[92] G. Held, “Deploying Optical Networking Components,” *McGraw-Hill Telecom,* pp. 51-69, 2001, ISBN10: 0071375058, ISBN13: 9780071375054.

[93] Siyavula, "5.7 Critical angles and total internal reflection, Geometrical optics, Physics Sciences Grade 11," 2023 [Online]. https://ng.siyavula.com/read/science/grade-11/geometrical-optics/05-geometrical-optics-07 [Accessed: 28 June 2023]

[94] K. Azil, K. Ferria, S. Bouzid, "Cladless optical fiber sensor based on evanescent wave absorption for monitoring methylene blue induced water pollution," Journal of the Optical Society of America B, vol. 37, issue 11, pp. A253-A258, 2020, DOI: 10.1364/JOSAB.396646.

[95] Y. Zhao, "Chapter 3, Electromagnetic Waves & Maxwell's Equations," *Lecture notes of PHYS3330, University of Georgia*, slide no. 5, 15, 17, 2023 [Online]. https://www.physast.uga.edu/classes/phys3330/zhao/downloads/download/1175 [Accessed: 28 June 2023]

[96] G. Verhoeven, "The reflection of two fields – Electromagnetic radiation and its role in (aerial) imaging," *Aerial Archaeology Research Group (AARG) news*, issue 55, p. 14, 2017, DOI: 10.5281/zenodo.3534245.

[97] V. Giurgiutiu, "Chapter 7, Fiber-Optic Sensors," *Structural Health Monitoring of Aerospace Composites, Academic Press*, p. 254, 2016, ISBN: 9780124096059, DOI: 10.1016/B978-0-12-409605-9.00007-6.

[98] R. Paschotto, "Modes," *RP Photonics Encyclopedia*, 2023 [Online]. https://www.rp-photonics.com/modes.html [Accessed: 28 June 2023]

[99] Gp Capt. K. S. Mathur (Retd.), "Fiber Optics Fundamentals and Advances in Optical Communications," *Blue Rose Publishers*, p. 87, 2021, ISBN: 978-93-5427-327-8.

[100] H. Saad, M.K. A. Rahman, I. Yassin, A. M. Muad, "Characterization of ethanol concentrations at ultraviolet wavelength region," *Journal of Fundamental and Applied Sciences*, vol. 9, no. 4S, pp. 384-400, 2017, DOI: 10.4314/jfas.v9i4S.22.

[101] A.A. Amanu, "Macro Bending Losses in Single Mode Step Index Fiber," *Advances in Applied Sciences*, vol. 1, issue 1, pp. 1-6, 2016, DOI: 10.11648/j.aas.20160101.11.

[102] Polymer Properties Database, "Orthosilicates," 2023 [Online]. https://polymerdatabase.com/Polymer%20Brands/Orthosilicates.html [Accessed: 28 June 2023]

[103] L.L. Liu, F.H. Hao, S.P. Morgan, R. Correia, A. Norris, S. Korposh, "A reflection-mode fibre-optic sensor for breath carbon dioxide measurement in healthcare," *Sensing and Bio-Sensing Research*, vol. 22, pp. 1-8, 2019, DOI: 10.1016/j.sbsr.2018.100254.

[104] A. Jircitano, "Lab Manual of A Beer's Law Experiment," *The Pennsylvania State University*, pp. 6-7, 2023 [Online]. https://pdf4pro.com/cdn/a-beer-s-law-experiment-introduction-5140d8.pdf [Accessed: 28 June 2023]

[105] P.K. Harimech, R. Hartmann, J. Rejman, P. del Pino, P.R. Gil, W.J. Parak, "Supporting Information of Encapsulated enzymes with integrated fluorescence-control of enzymatic activity," *Journal of Materials Chemistry B*, vol. 3, issue 14, pp. 2-3, 2015, DOI: 10.1039/C4TB02077D.

[106] Sigma-Aldrich, "Product Specification: Thymol Blue - ACS reagent," p. 1, 2023 [Online]. https://www.sigmaaldrich.com/specification-sheets/313/074/114545-BULK_____SIAL_____.pdf [Accessed: 28 June 2023]

[107] S. Wildman, C. Branch, J. Durodie, A. Lea, "At a Glance/Pharmacy calculation," *University of Kent, Student Learning Advisory Service*, p. 1, 2023 [Online]. https://www.mathcentre.ac.uk/resources/uploaded/c1v1c2v2.pdf [Accessed: 28 June 2023]

[108] C. J. Brinker, "Chapter 10, Dip Coating, Chemical Solution Deposition of Functional Oxide Thin Films," *Springer*, pp. 237-238, 2013, ISBN: 978-3-211-99310-1.

[109] L.L. Liu, S.P. Morgan, R. Correia, S. Korposh, "A single-film fiber optical sensor for simultaneous measurement of carbon dioxide and relative humidity," *Optics & Laser Technology*, vol. 147, issue 107696, pp. 1-9, 2022, DOI: 10.1016/j.optlastec.2021.107696.

[110] P. Ewart, "Optics: the science of light," *Lecture notes of 2nd year Physics FHS A2, University of Oxford*, p. 36, 2014 [Online]. https://www2.physics.ox.ac.uk/sites/default/files/2011-10-19/optics_lectures_2014rev_6mar14_pdf_13254.pdf [Accessed: 28 June 2023]

[111] P. Norby, "Sol-Gel Methods," *Teaching material, KJM 5100, University of Oslo*, p. 27, Autumn 2006 [Online]. https://www.uio.no/studier/emner/matnat/kjemi/KJM5100/h08/undervisningsmateriale/10KJM5100_2008_sol_gel_a.pdf [Accessed: 28 June 2023]

[112] K. Wysokiński, M. Napierała, T. Stańczyk, S. Lipiński, T. Nasiłowski, "Study on the sensing Coating of the Optical Fibre CO_2 Sensor," *Sensors*, vol. 15, issue 12, pp. 31888-31903, 2015, DOI: 10.3390/s151229890.

[113] A.R. Hind, L. Chomette, "The determination of thin film thickness using reflectance spectroscopy," *Agilent Technologies, Inc*., pp. 1-4, 2011, Publication Number: SI-A-1205.

[114] Crystran, "Silica Glass (SiO_2) Data Sheet," p. 2, 2023 [Online]. https://www.crystran.co.uk/optical-materials/silica-glass-sio2 [Accessed: 28 June 2023]

[115] R. Ramaswami, K.N. Sivarajan, G. H. Sasaki, "chapter 2 - Propagation of Signals in Optical Fiber," *Optical Networks*, 3rd Edition, pp. 47-112, 2010, ISBN: 9780123740922, DOI: 10.1016/B978-0-12-374092-2.50010-2.

[116] S.-K. Lee, I. Okura, "Porphyrin-doped sol-gel glass as a probe for oxygen sensing," *Analytica Chimica Acta*, vol. 342, issues 2-3, pp. 181-188, 1997, DOI: 10.1016/S0003-2670(96)00562-4.

[117] S.-K. Lee, I. Okura, "Optical Sensor for Oxygen Using a Porphyrin-doped Sol-Gel Glass," *Analyst*, vol. 122, issue 1, pp. 81-84, 1997, DOI: 10.1039/A604885D.

[118] Preserve Skincare, "Complete Humidity Guide Fore Healthy Hydrated Skin," 2019 [Online].

https://www.preservskincare.com/blog/snnsay76gtd6rujzssxyysoztvmebx [Accessed: 28 June 2023]

[119] Polyflon Technology Limited, "PTFE Cast Film," 2023 [Online]. https://www.polyflon.co.uk/products/cast-ptfe-film/ptfe-cast-film/ [Accessed: 28 June 2023]

[120] S. Ahangarani, N. Lari, A. Shanaghi, "Influence of TEOS concentration and Triton additive on the nanostructure silica sol-gel anti-reflective coatings," *International Journal of Materials and Product Technology*, vol. 55, no. 4, pp. 319-330, 2017, DOI:10.1504/IJMPT.2017.087027.

[121] K. Ertekin, C. Karapire, S. Alp, B. Yenigul, S. Icli, "Photophysical and photochemical characteristics of an azlactone dye in sol-gel matrix; a new fluorescent pH indicator," *Dyes and Pigments*, vol. 56, issue 2, pp. 125-133, 2003, DOI :10.1016/S0143-7208(02)00125-0.

[122] Oxford Cambridge and RSA (OCR), "AS and A Level Chemistry," version 1.1, p. 24, 2019 [Online]. https://www.ocr.org.uk/Images/295468-chemistry-mathematical-skills-handbook.pdf [Accessed: 28 June 2023]

[123] S. Brown, "Measure of Shape: Skewness and Kurtosis," *Statistics, BrownMath.com*, pp. 1-8, 2023 [Online]. https://brownmath.com/stat/shape.htm [Accessed: 28 June 2023]

[124] C. Zaiontz, "Symmetry, Skewness and Kurtosis," *Real Statistics using Excel*, 2023 [Online]. https://www.real-statistics.com/descriptive-statistics/symmetry-skewness-kurtosis/ [Accessed: 28 June 2023]

[125] P. Cisar, S. M. Cisar, "Skewness and Kurtosis in Function of Selection of Network Traffic Distribution," *Acta Polytechnica Hungarica*, vol. 7, no. 2, p. 96, 2010, ISSN: 1785-8860.

[126] Merck, "pH test strips," 2023 [Online]. https://www.sigmaaldrich.com/GB/en/product/sigma/p4786 [Accessed: 28 June 2023]

[127] Y.-J. Rao, Z.-L. Ran, Y. Gong, "Fibre-Optic Fabry-Perot Sensors an Introduction," 1st Edition, *CRC Press, Taylor & Francis Group*, pp. 1, 2, 28, 2017, ISBN: 9781498736930.

[128] F. Guo, "Fibre-Tip Fabry-Perot Interferometric Sensor based on a Thin Silver Film," *M.Sc. Thesis, Department of Electrical & Computer Engineering, University of Nebraska–Lincoln*, pp. 2-3, 2012 [Online]. https://digitalcommons.unl.edu/cgi/viewcontent.cgi?article=1050&context=elecengtheses [Accessed: 28 June 2023]

[129] S.G. Lipson, H. Lipson, D.S. Tannhauser, "Optical Physics," *Cambridge University Press*, 3rd Edition, p. 248, 1995, ISBN: 0-521-06926-2.

[130] B. Keeley, A. Keeley, P. Houlahan, "Ridge number in bat ears is related to both guild membership and ear length," *Plos One*, vol. 13, no. 7, p. 4, 2018, DOI: 10.1371/journal.pone.0200255.

[131] B.H. Walker, "Forming Interference Fringes," *Optics and Photonics News*, vol. 7, issue 5, pp. 34-37, 1996, DOI: 10.1364/OPN.7.5.000034.

[132] J.-H. Chen, X.-G. Huang, Z.-J. Huang, "Simple thin-film fiber optic temperature sensor based on Fabry-Perot interference," *Optical Engineering*, vol. 49, issue 4, pp. 044402-1 – 044402-4, 2010, DOI: 10.1117/1.3407460.

[133] J.-R. Zhao, X.-G. Huang, W.-X. He, J.-H. Chen, "High-Resolution and Temperature-Insensitive Fiber Optic Refractive Index Sensor Based on Fresnel Reflection Modulated by Fabry-Perot Interference," in *Journal of Lightwave Technology*, vol. 28, no. 19, pp. 2799-2803, 2010, DOI: 10.1109/JLT.2010.2065215.

[134] C. Ma, B. Dong, J. Gong, and A. Wang, "Decoding the spectra of low-finesse extrinsic optical fiber Fabry-Perot interferometers," *Optics Express*, vol. 19, no. 24, pp. 23727-23742, 2011, DOI:10.1364/OE.19.023727.

[135] Z. L. Ran, Y. J. Rao, W. J. Liu, X. Liao, K. S. Chiang, "Laser-micromachined Fabry-Perot optical fiber tip sensor for high-resolution temperature-independent

measurement of refractive index," *Optics Express*, vol. 16, no. 3, pp. 2252-2263, 2008, DOI: 10.1364/OE.16.002252.

[136] Shin-Etsu Chemical Co., Ltd., "RTV Silicone Rubber," p. 7, 2023 [Online]. https://chilternconnections.co.uk/sites/default/files/downloadables/brochures/rtv_silicone_rubber_electronic_applications_2.pdf [Accessed: 28 June 2023]

[137] L. Langnau, "How tensile strength relates to 3D printing," *Make Parts Fast*, 2019 [Online]. https://www.makepartsfast.com/how-tensile-strength-relates-to-3d-printing/ [Accessed: 28 June 2023]

[138] Sensor Products Inc., "Body Mapping Mattress," 2023 [Online]. https://www.sensorprod.com/dynamic/mattress.php [Accessed: 28 June 2023]

[139] Sensor Products Inc., "Real-Time Tactile Temperature Analysis," 2023 [Online]. https://www.sensorprod.com/pdf/mattress-tem_brochure.pdf [Accessed: 28 June 2023]

[140] Sensor Products Inc., "Mattress Sensor," 2023 [Online]. https://www.sensorprod.com/glossary/mattress-sensor/mattress-sensor.php [Accessed: 28 June 2023]

[141] Coloplast, "Biatain Adhesive," 2023 [Online]. https://products.coloplast.co.uk/coloplast/wound-care/biatain/biatain-adhesive/ [Accessed: 28 June 2023]

A. Appendix A

Results from calibration of OFCSs (used for skin CO_2 measurement)

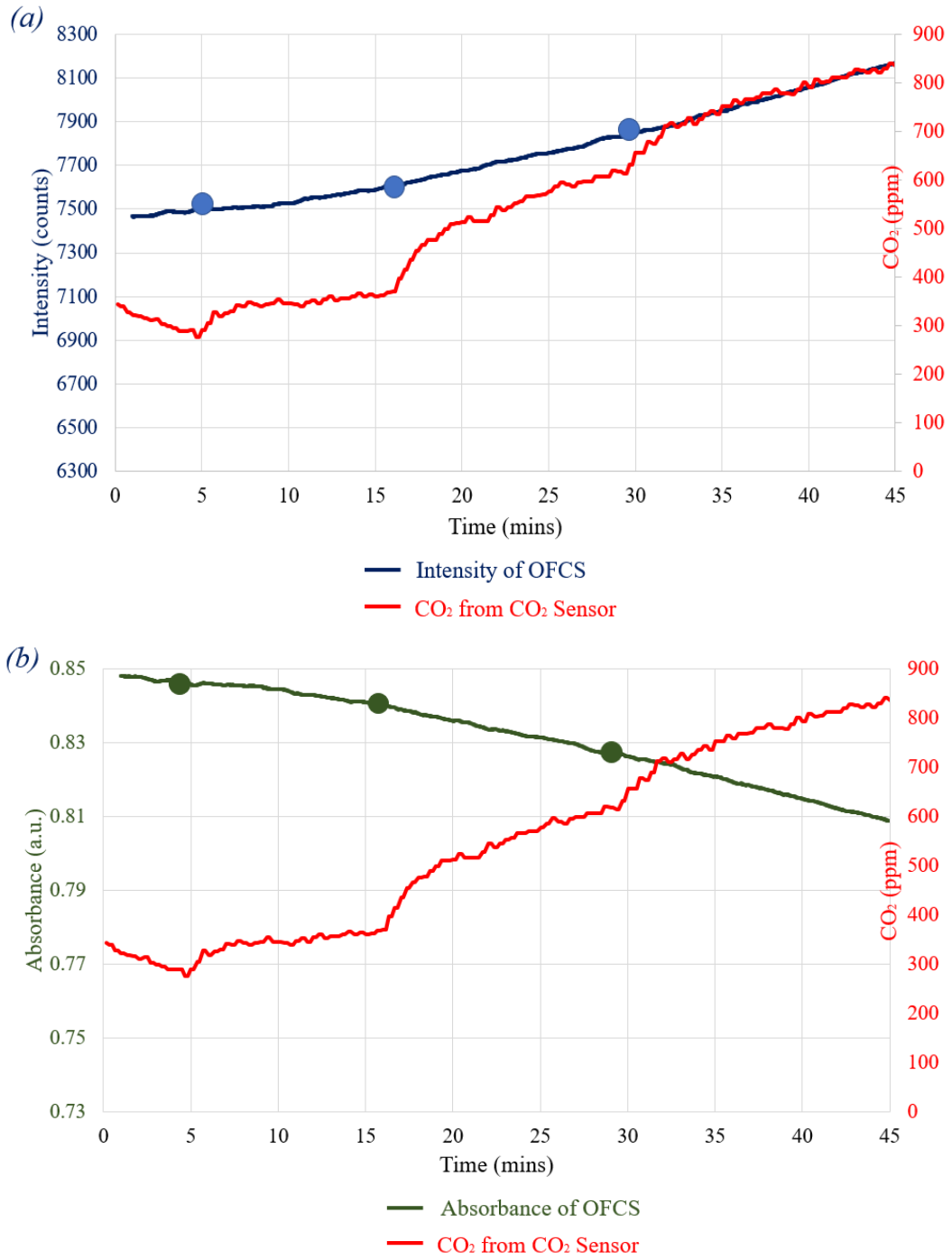


Figure A.1: *Response (a) Reflection Intensity (b) Absorbance of OFCS 2 for different CO_2 concentrations at wavelength 600 nm*

Table A.1: *Variation of CO_2 concentration and response (reflection intensity and absorbance) of OFCS 2 at wavelength 600 nm for different time periods*

Time (mins)	CO_2 (ppm)	Intensity (counts)	Absorbance (a.u.)	Time duration (mins) for measuring the change in CO_2, Intensity, and Absorbance	Change in CO_2 (ppm)	Change in Intensity (counts)	Change in Absorbance (a.u.)
4	276	7533	0.844				
16	371	7611	0.839	4-16	95	78	0.005
29	614	7828	0.827	16-29	243	217	0.012
45	835	8127	0.811	29-45	221	299	0.016

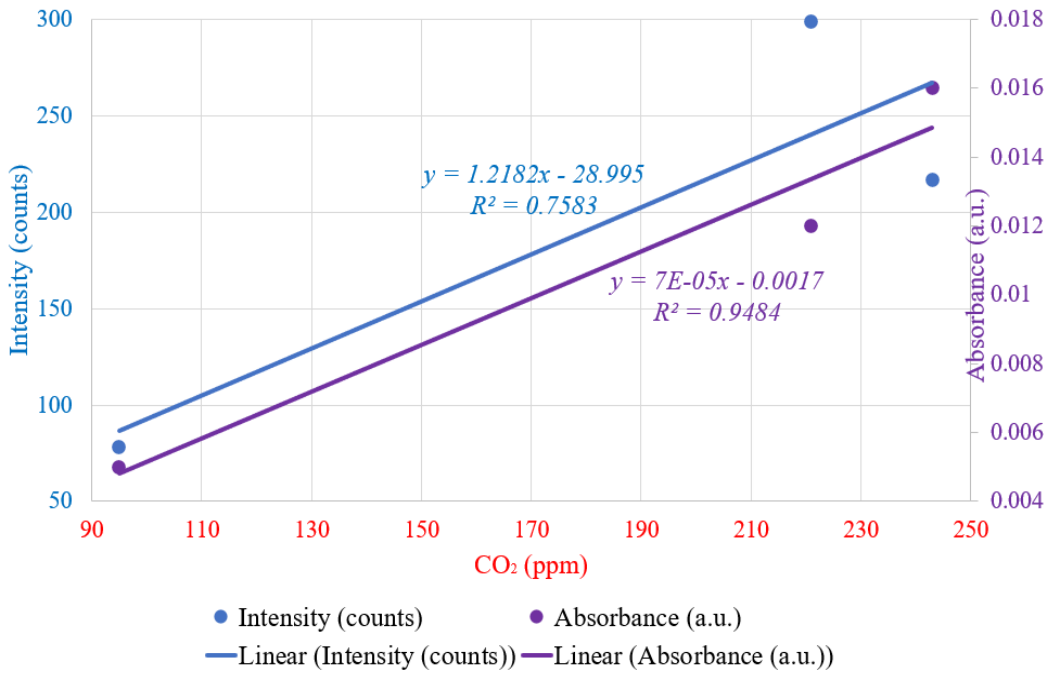


Figure A.2: *Linear fitting of variation in response (reflection intensity and absorbance) of OFCS 2 to different CO_2 concentrations at wavelength 600 nm*

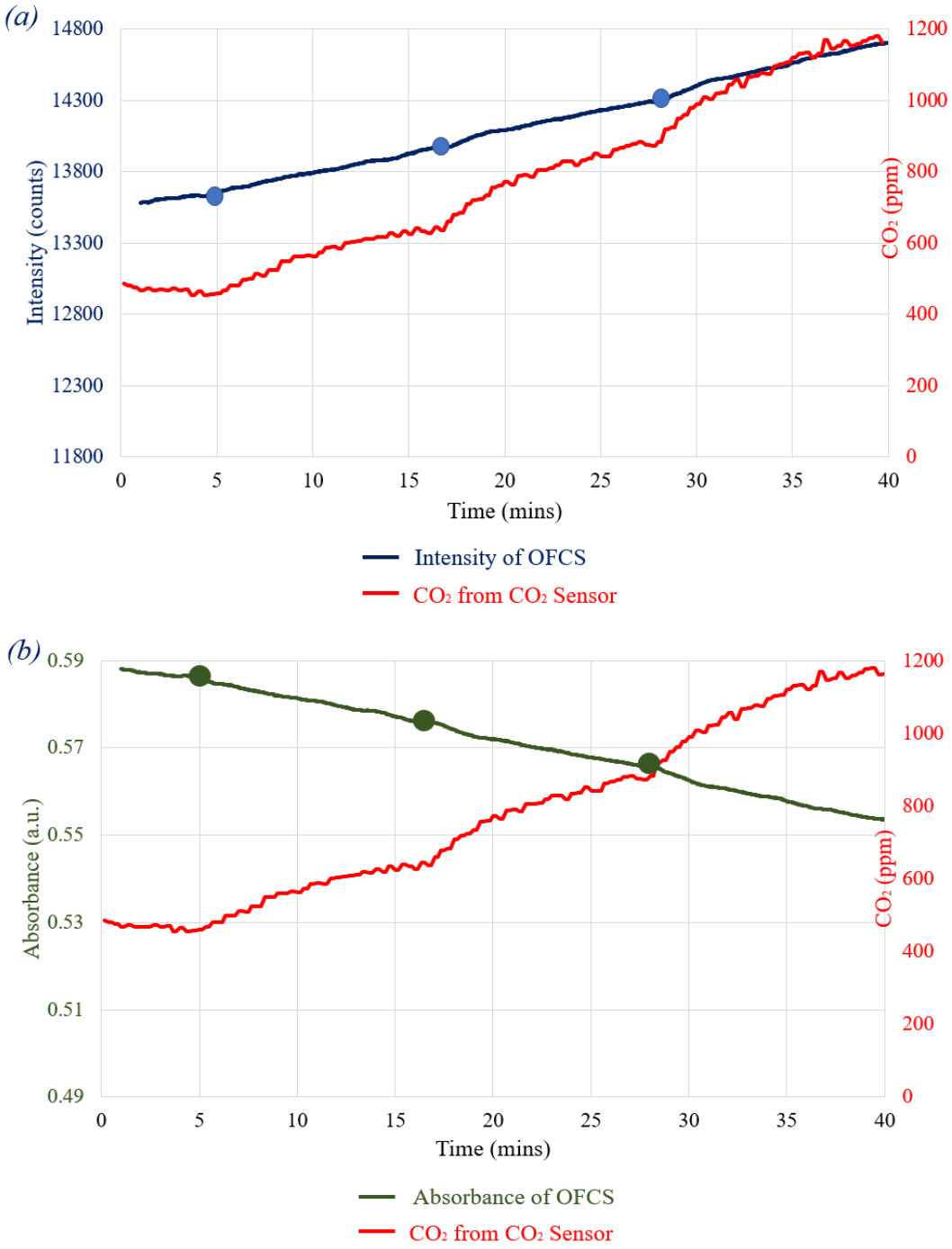


Figure A.3: *Response (a) Reflection Intensity (b) Absorbance of OFCS 3 for different CO_2 concentrations at wavelength 600 nm*

Table A.2: *Variation of CO_2 concentration and response (reflection intensity and absorbance) of OFCS 3 at wavelength 600 nm for different time periods*

Time (mins)	CO_2 (ppm)	Intensity (counts)	Absorbance (a.u.)	Time duration (mins) for measuring the change in CO_2, Intensity, and Absorbance	Change in CO_2 (ppm)	Change in Intensity (counts)	Change in Absorbance (a.u.)
5	468	13719	0.584				
16	637	13977	0.576	5-16	169	258	0.008
27	873	14335	0.565	16-27	236	358	0.011
39	1162	14740	0.553	27-39	289	405	0.012

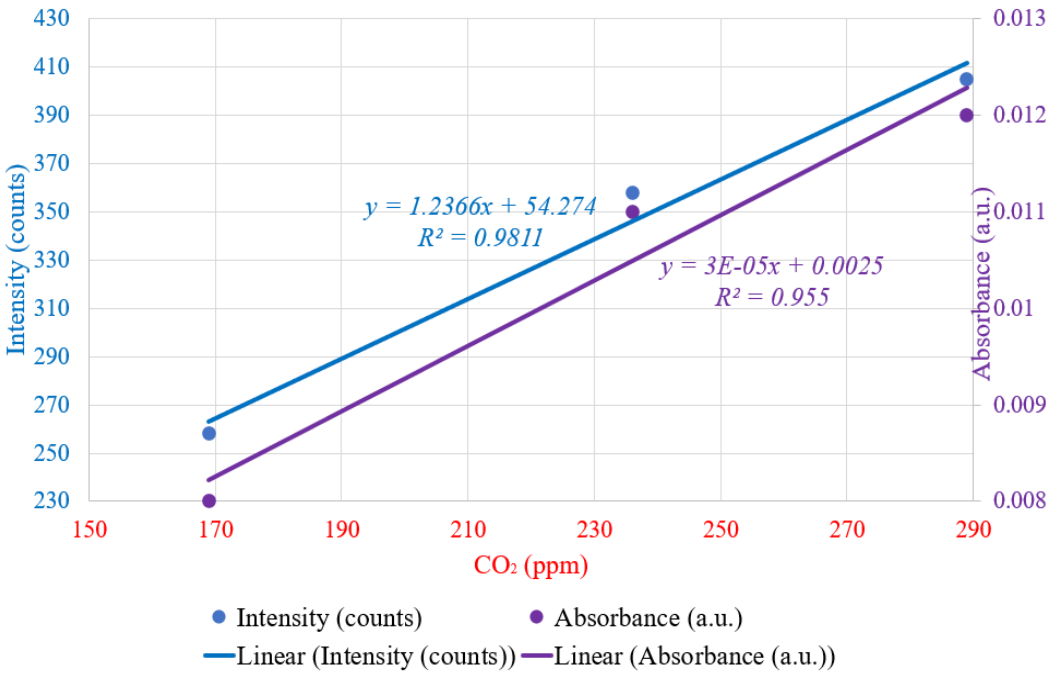


Figure A.4: *Linear fitting of variation in response (reflection intensity and absorbance) of OFCS 3 to different CO_2 concentrations at wavelength 600 nm*

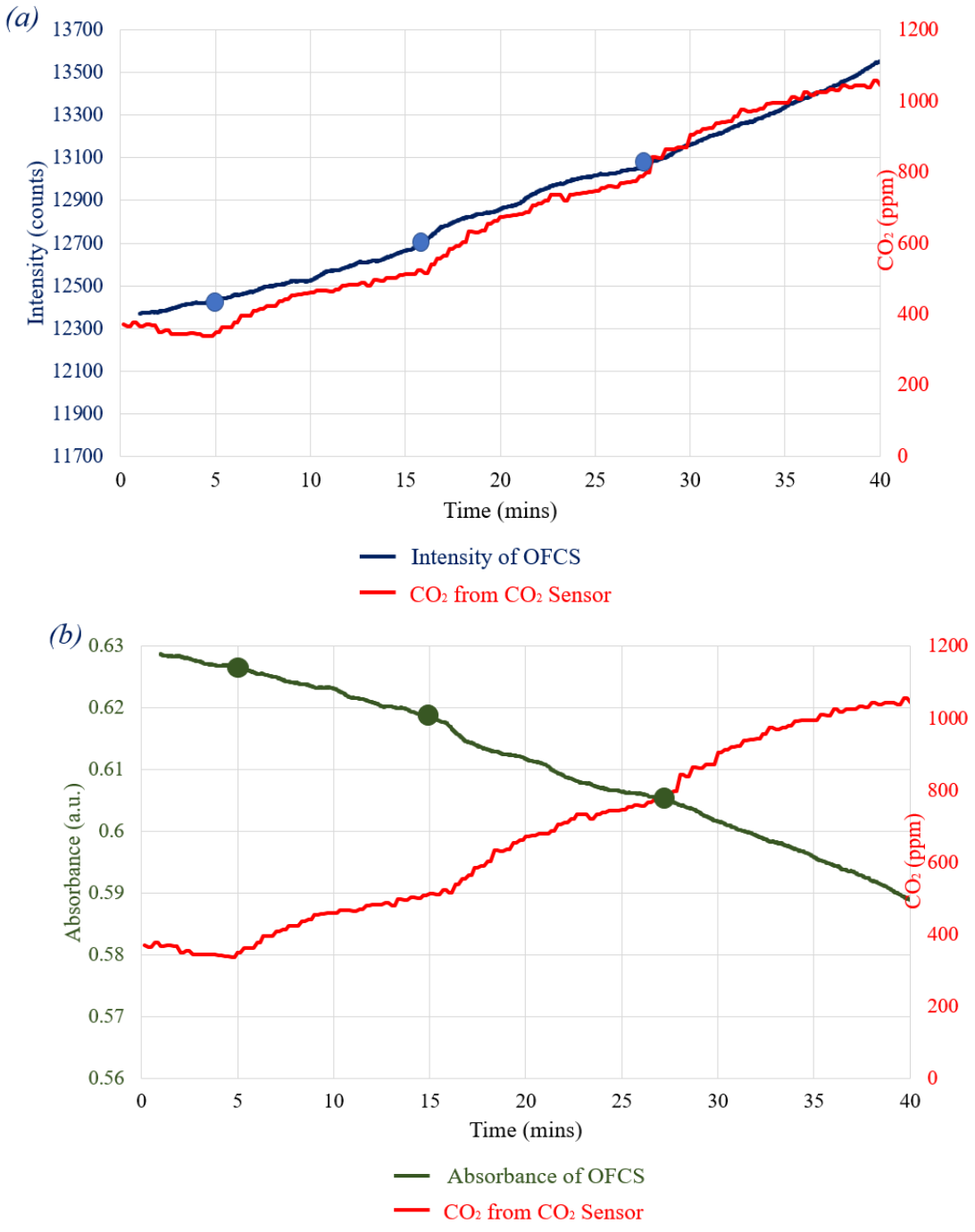


Figure A.5: *Response (a) Reflection Intensity (b) Absorbance of OFCS 4 for different CO_2 concentrations at wavelength 600 nm*

Table A.3: *Variation of CO_2 concentration and response (reflection intensity and absorbance) of OFCS 4 at wavelength 600 nm for different time periods*

Time (mins)	CO_2 (ppm)	Intensity (counts)	Absorbance (a.u.)	Time duration (mins) for measuring the change in CO_2, Intensity, and Absorbance	Change in CO_2 (ppm)	Change in Intensity (counts)	Change in Absorbance (a.u.)
5	351	12463	0.625				
15	523	12692	0.617	5-15	172	229	0.008
27	799	13113	0.603	15-27	276	421	0.014
39	1043	13491	0.590	27-39	244	378	0.013

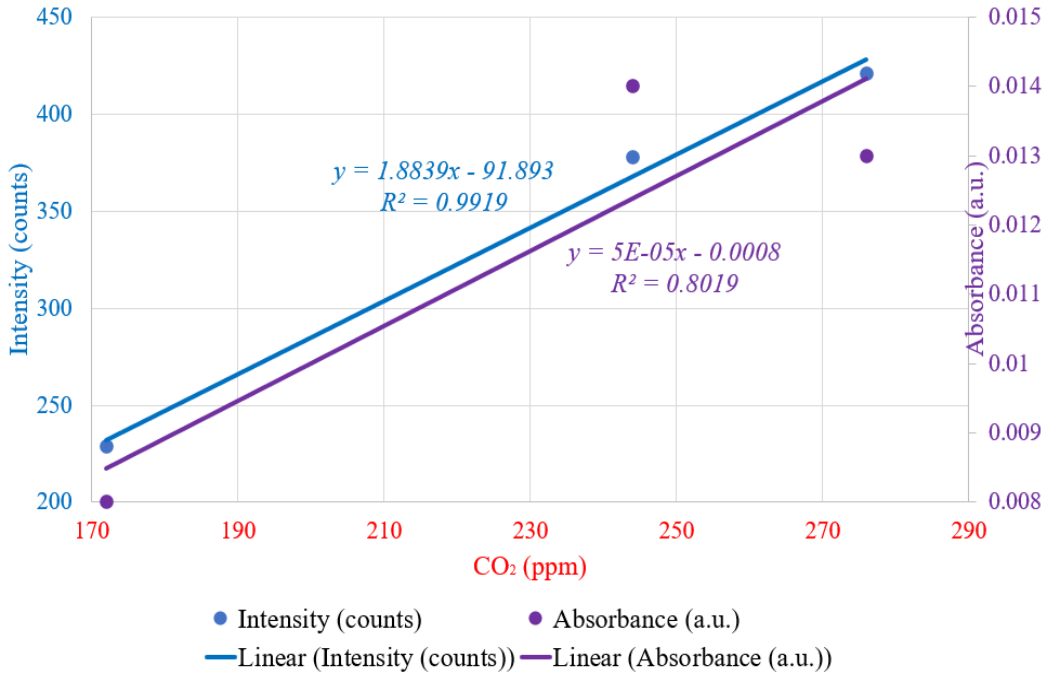


Figure A.6: *Linear fitting of variation in response (reflection intensity and absorbance) of OFCS 4 to different CO_2 concentrations at wavelength 600 nm*

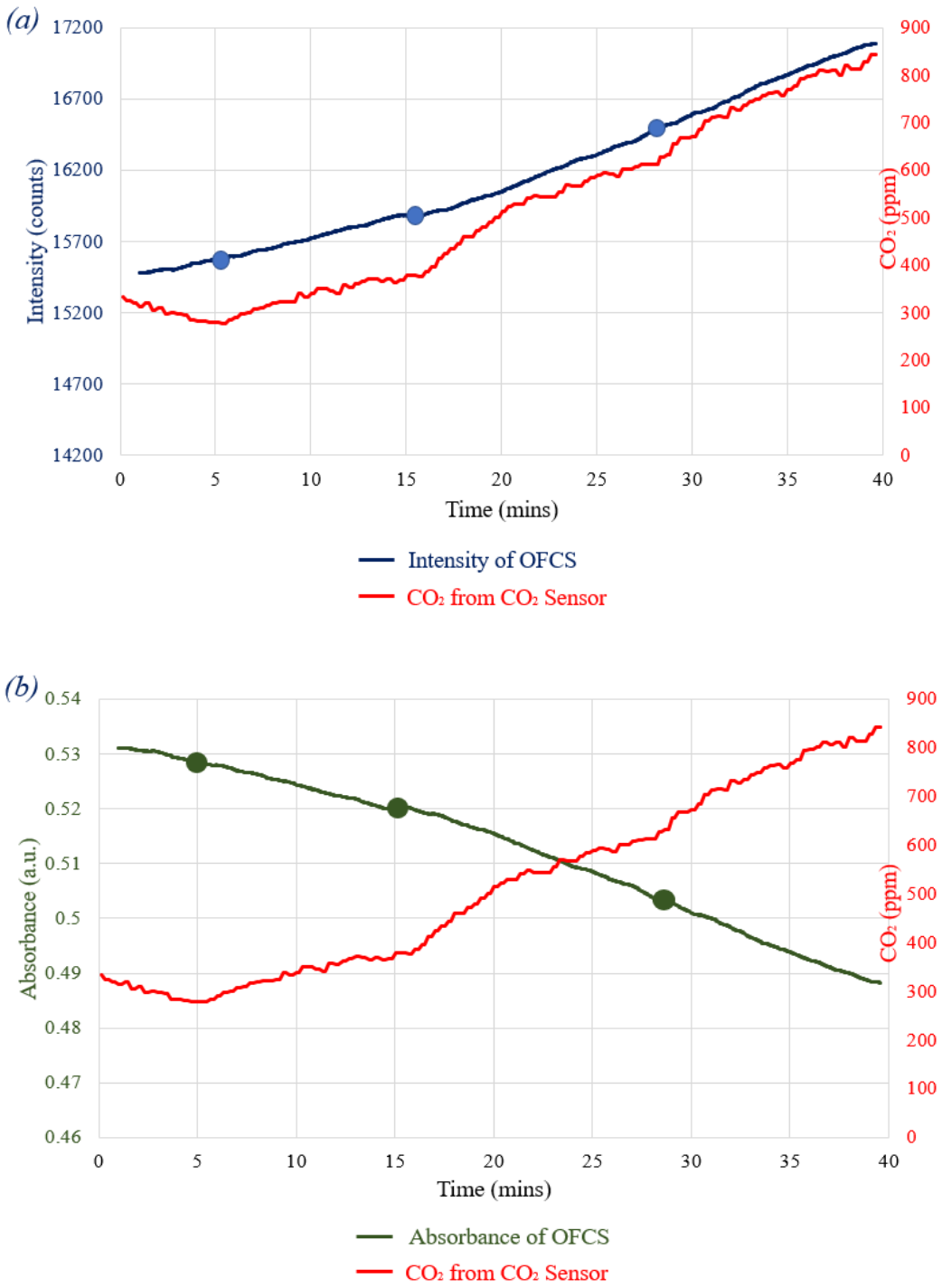


Figure A.7: *Response (a) Reflection Intensity (b) Absorbance of OFCS 5 for different CO_2 concentrations at wavelength 600 nm*

Table A.4: *Variation of CO_2 concentration and response (reflection intensity and absorbance) of OFCS 5 at wavelength 600 nm for different time periods*

Time (mins)	CO_2 (ppm)	Intensity (counts)	Absorbance (a.u.)	Time duration (mins) for measuring the change in CO_2, Intensity, and Absorbance	Change in CO_2 (ppm)	Change in Intensity (counts)	Change in Absorbance (a.u.)
5	279	15627	0.527				
15	376	15854	0.520	5-15	97	227	0.007
28	614	16427	0.505	15-28	238	573	0.015
39	843	17068	0.488	28-39	229	641	0.017

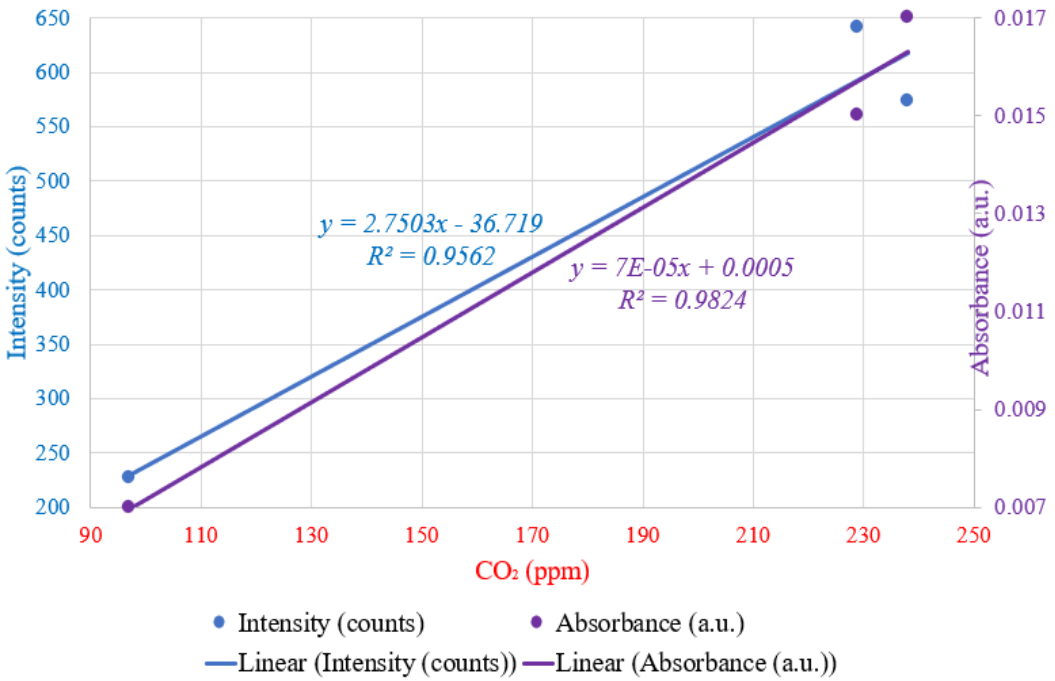


Figure A.8: *Linear fitting of variation in response (reflection intensity and absorbance) of OFCS 5 to different CO_2 concentrations at wavelength 600 nm*

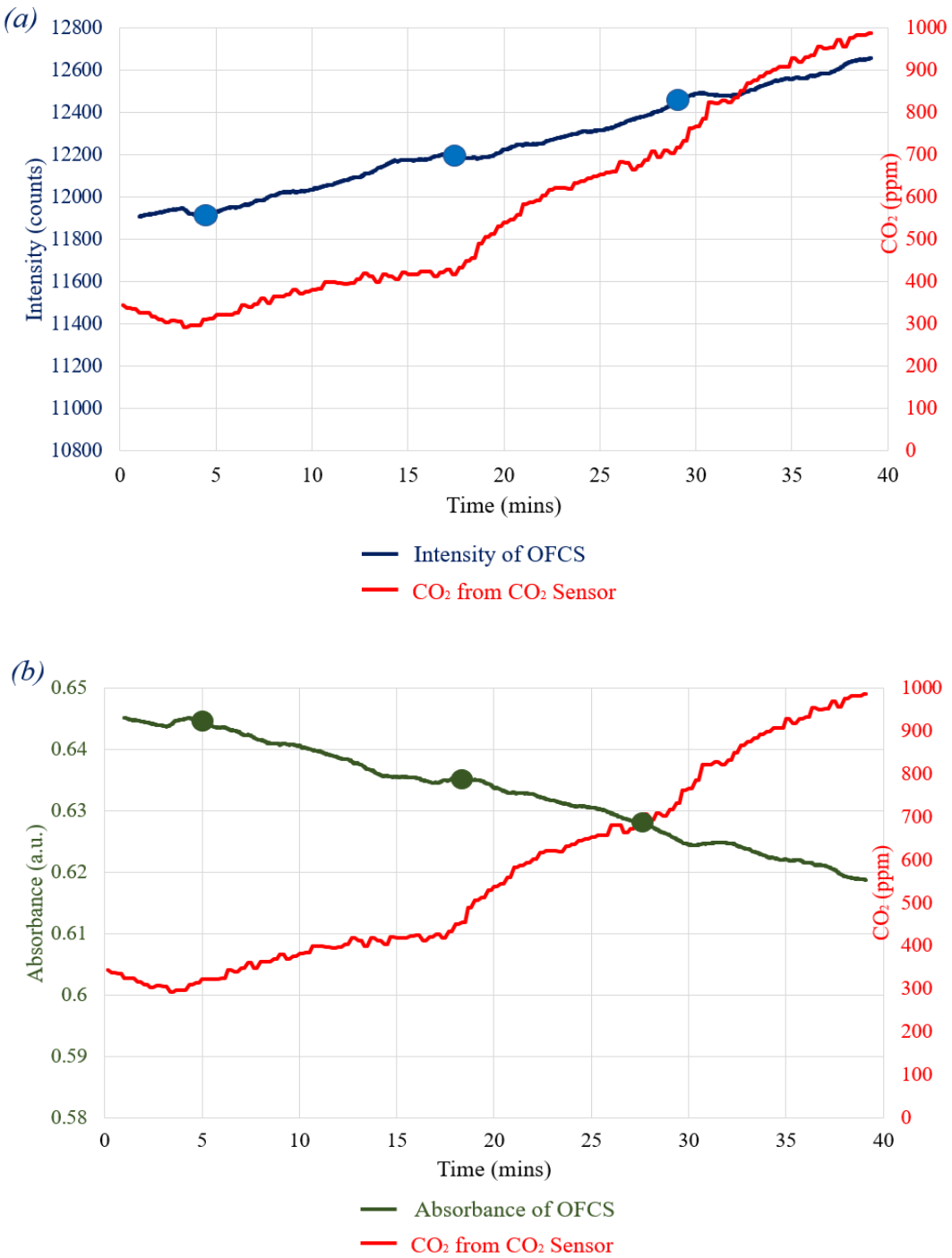


Figure A.9: *Response (a) Reflection Intensity (b) Absorbance of OFCS 6 for different CO_2 concentrations at wavelength 600 nm*

Table A.5: *Variation of CO_2 concentration and response (reflection intensity and absorbance) of OFCS 6 at wavelength 600 nm for different time periods*

Time (mins)	CO_2 (ppm)	Intensity (counts)	Absorbance (a.u.)	Time duration (mins) for measuring the change in CO_2, Intensity, and Absorbance	Change in CO_2 (ppm)	Change in Intensity (counts)	Change in Absorbance (a.u.)
5	323	11989	0.642				
17	418	12150	0.636	5-17	95	161	0.006
28	703	12413	0.627	17-28	285	263	0.009
39	986	12678	0.618	28-39	283	265	0.009

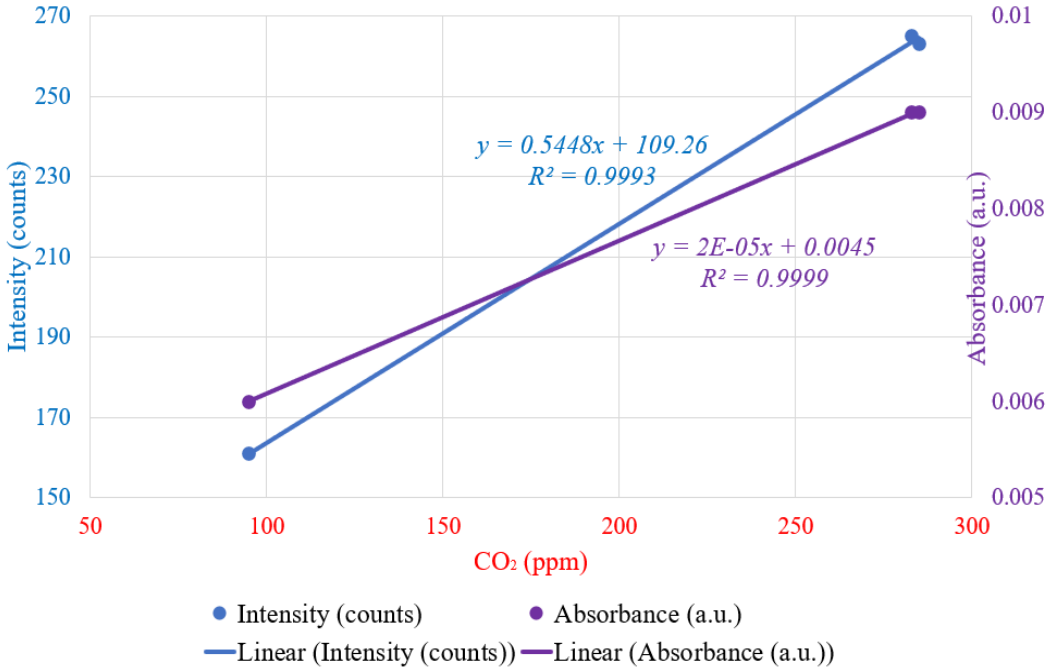


Figure A.10: *Linear fitting of variation in response (reflection intensity and absorbance) of OFCS 6 to different CO_2 concentrations at wavelength 600 nm*



Figure A.11: *Response (a) Reflection Intensity (b) Absorbance of OFCS 7 for different CO_2 concentrations at wavelength 600 nm*

Table A.6: *Variation of CO_2 concentration and response (reflection intensity and absorbance) of OFCS 7 at wavelength 600 nm for different time periods*

Time (mins)	CO_2 (ppm)	Intensity (counts)	Absorbance (a.u.)	Time duration (mins) for measuring the change in CO_2, Intensity, and Absorbance	Change in CO_2 (ppm)	Change in Intensity (counts)	Change in Absorbance (a.u.)
5	392	18454	0.455				
15	520	18618	0.451	5-15	128	164	0.004
28	1038	18939	0.444	15-28	518	321	0.007
40	1383	19207	0.437	28-40	345	218	0.007

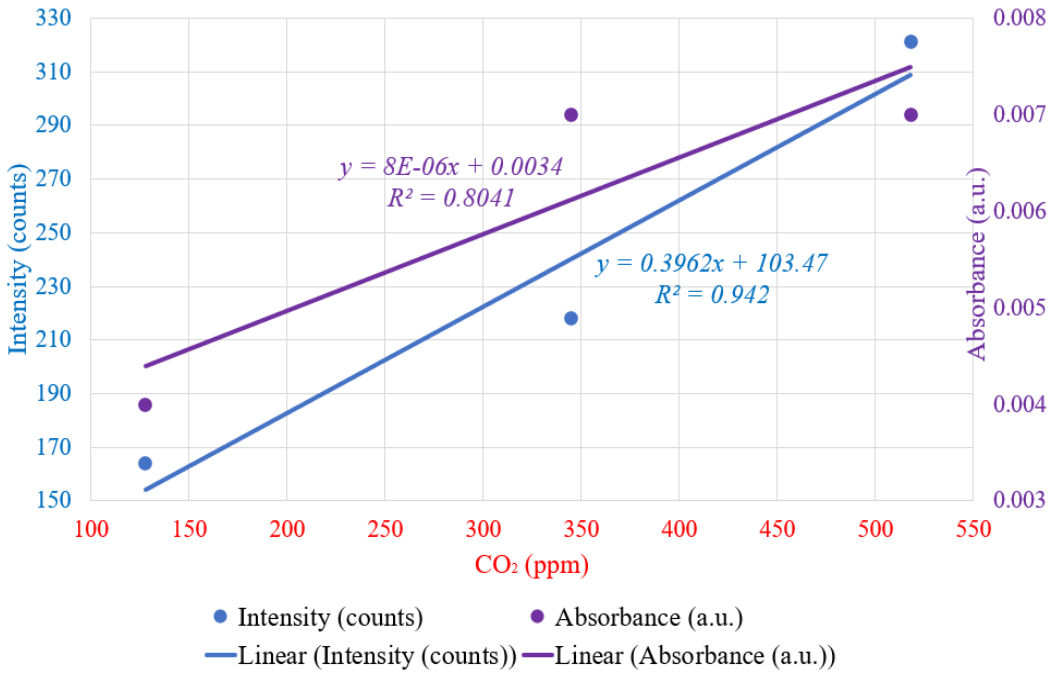


Figure A.12: *Linear fitting of variation in response (reflection intensity and absorbance) of OFCS 7 to different CO_2 concentrations at wavelength 600 nm*

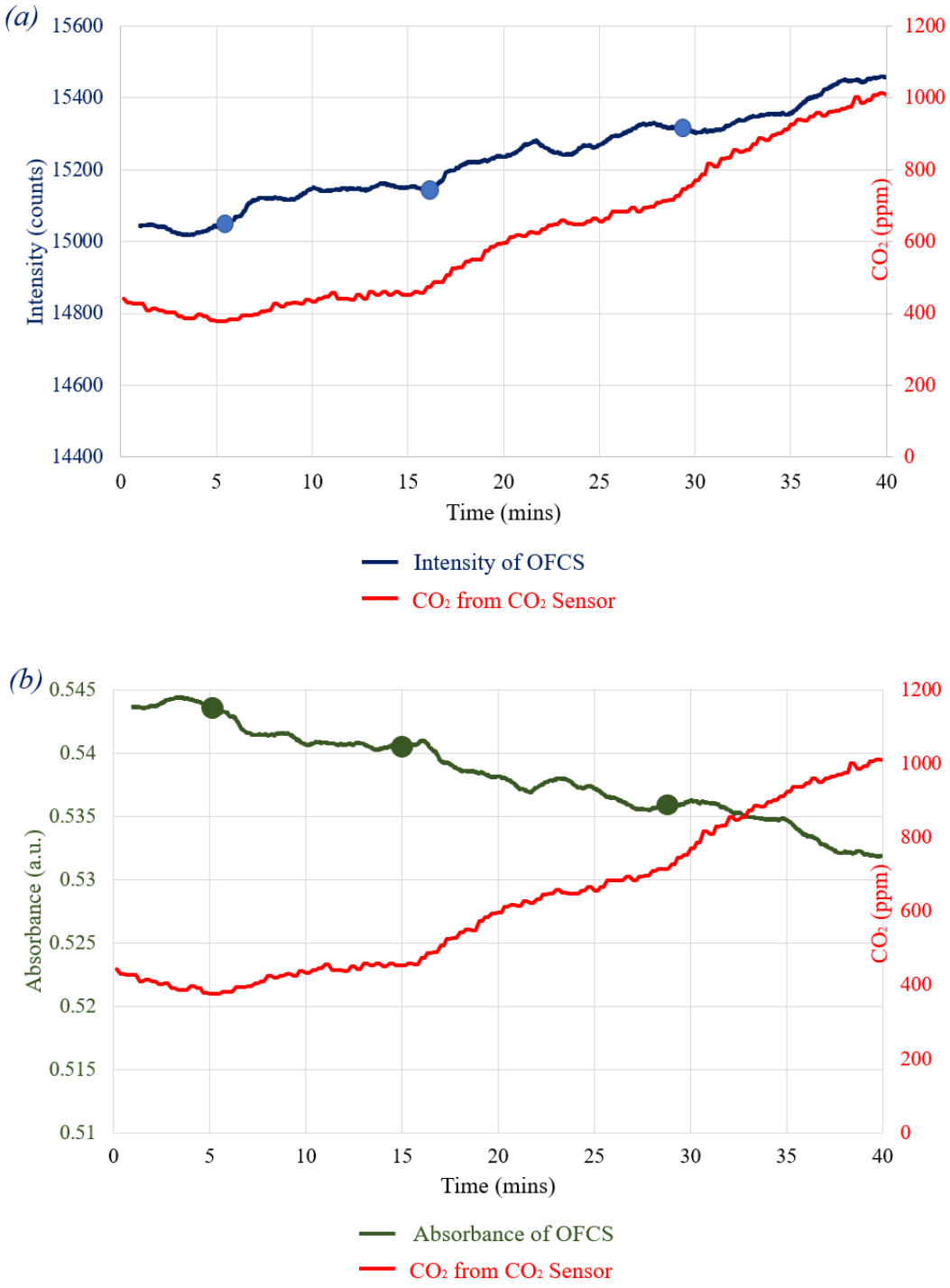


Figure A.13: *Response (a) Reflection Intensity (b) Absorbance of OFCS 8 for different CO_2 concentrations at wavelength 600 nm*

Table A.7: *Variation of CO_2 concentration and response (reflection intensity and absorbance) of OFCS 8 at wavelength 600 nm for different time periods*

Time (mins)	CO_2 (ppm)	Intensity (counts)	Absorbance (a.u.)	Time duration (mins) for measuring the change in CO_2, Intensity, and Absorbance	Change in CO_2 (ppm)	Change in Intensity (counts)	Change in Absorbance (a.u.)
5	378	15111	0.542				
15	457	15204	0.539	5-15	79	93	0.003
28	715	15354	0.535	15-28	258	150	0.004
40	1012	15534	0.529	28-40	297	180	0.006

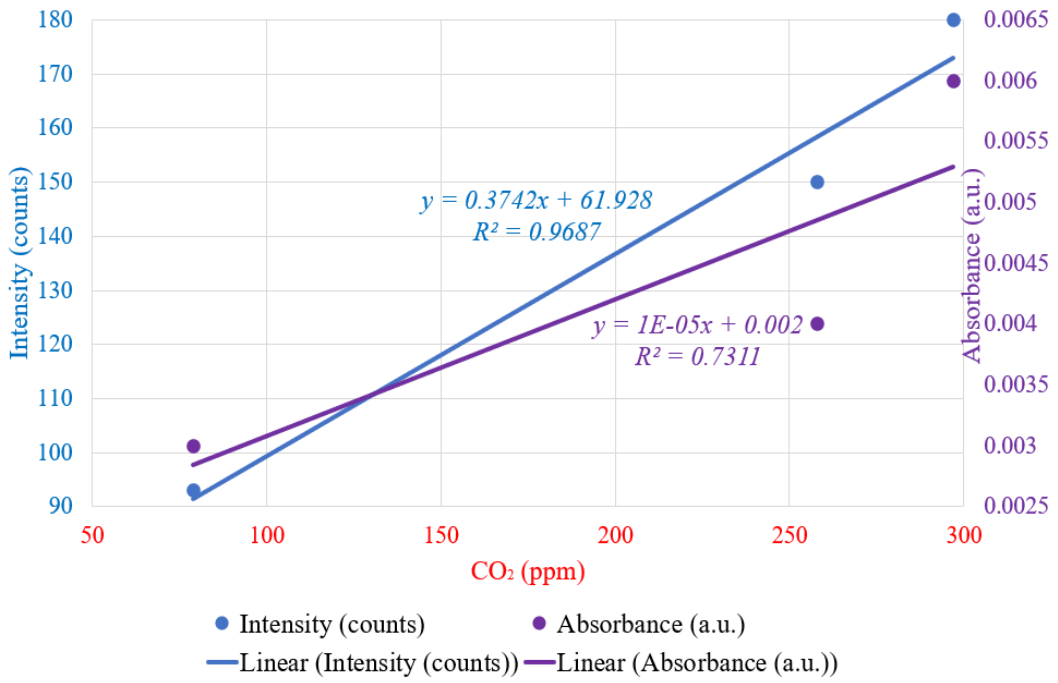


Figure A.14: *Linear fitting of variation in response (reflection intensity and absorbance) of OFCS 8 to different CO_2 concentrations at wavelength 600 nm*

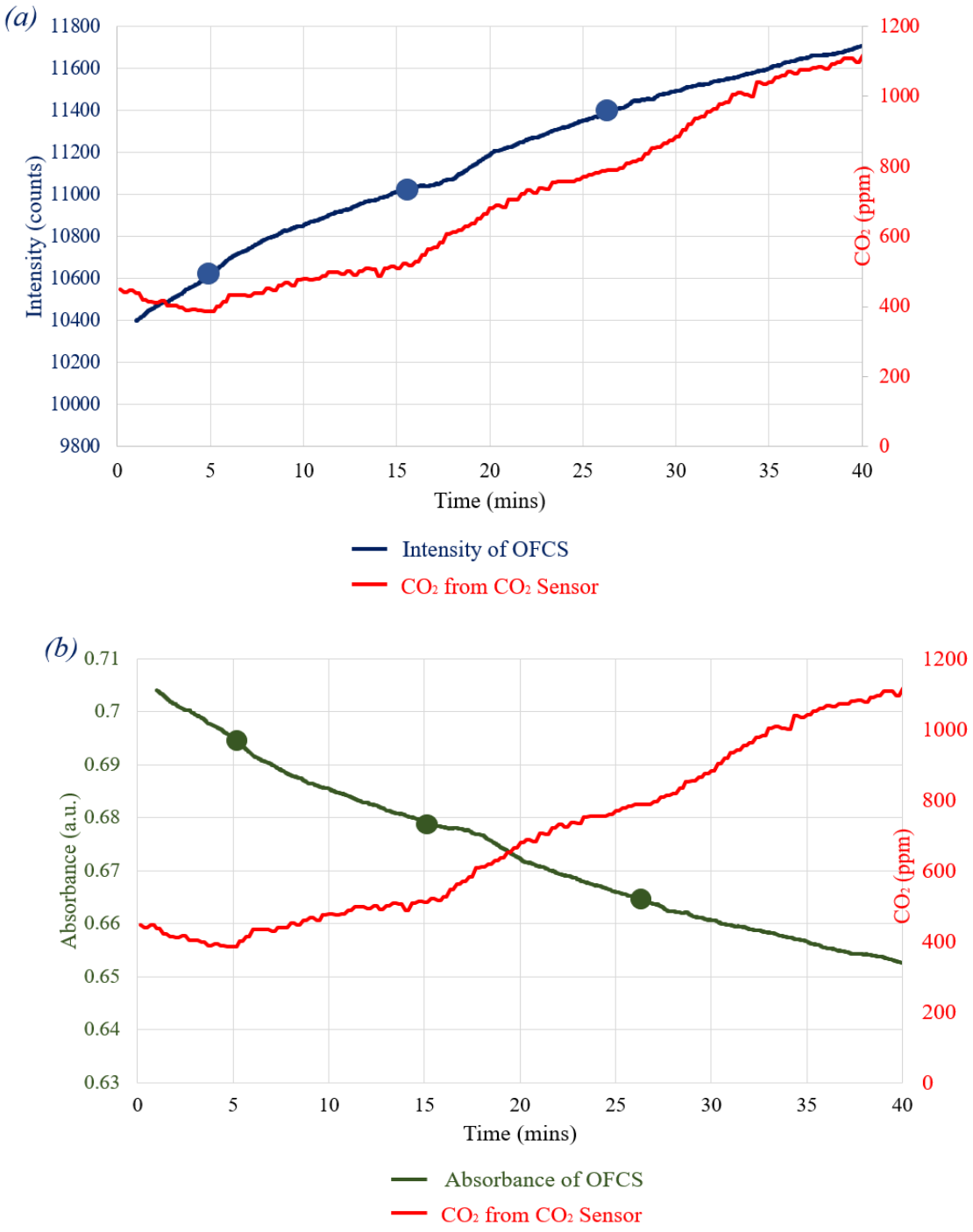


Figure A.15: *Response (a) Reflection Intensity (b) Absorbance of OFCS 9 for different CO_2 concentrations at wavelength 600 nm*

Table A.8: *Variation of CO_2 concentration and response (reflection intensity and absorbance) of OFCS 9 at wavelength 600 nm for different time periods*

Time (mins)	CO_2 (ppm)	Intensity (counts)	Absorbance (a.u.)	Time duration (mins) for measuring the change in CO_2, Intensity, and Absorbance	Change in CO_2 (ppm)	Change in Intensity (counts)	Change in Absorbance (a.u.)
5	386	10761	0.689				
15	516	11041	0.678	5-15	130	280	0.011
26	789	11363	0.666	15-26	273	322	0.012
40	1106	11729	0.652	26-40	317	366	0.014

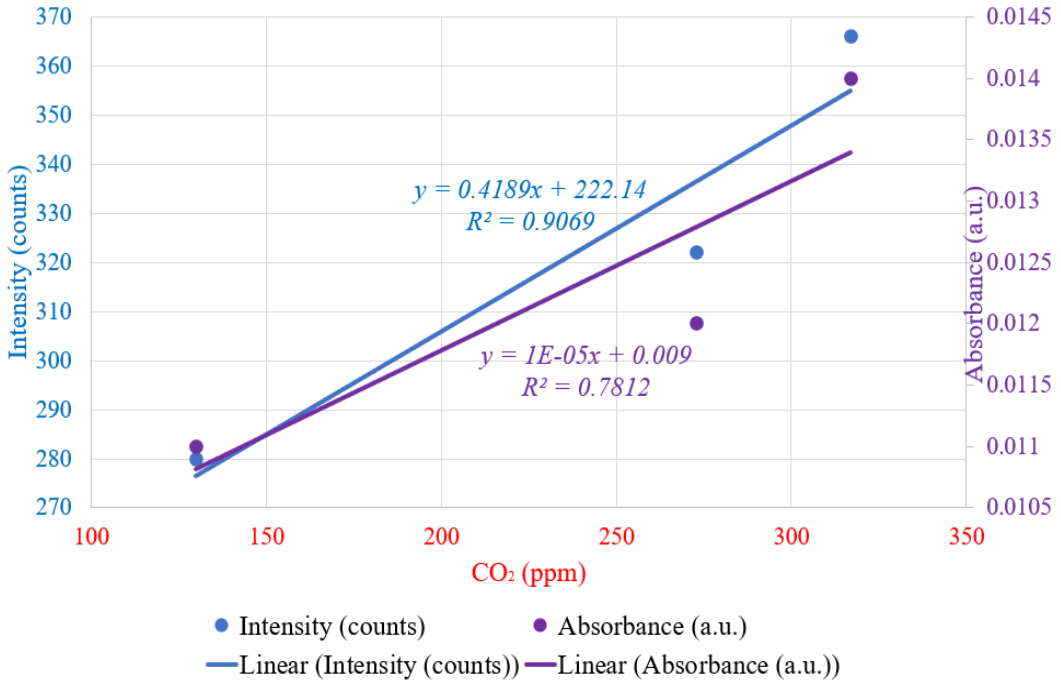


Figure A.16: *Linear fitting of variation in response (reflection intensity and absorbance) of OFCS 9 to different CO_2 concentrations at wavelength 600 nm*

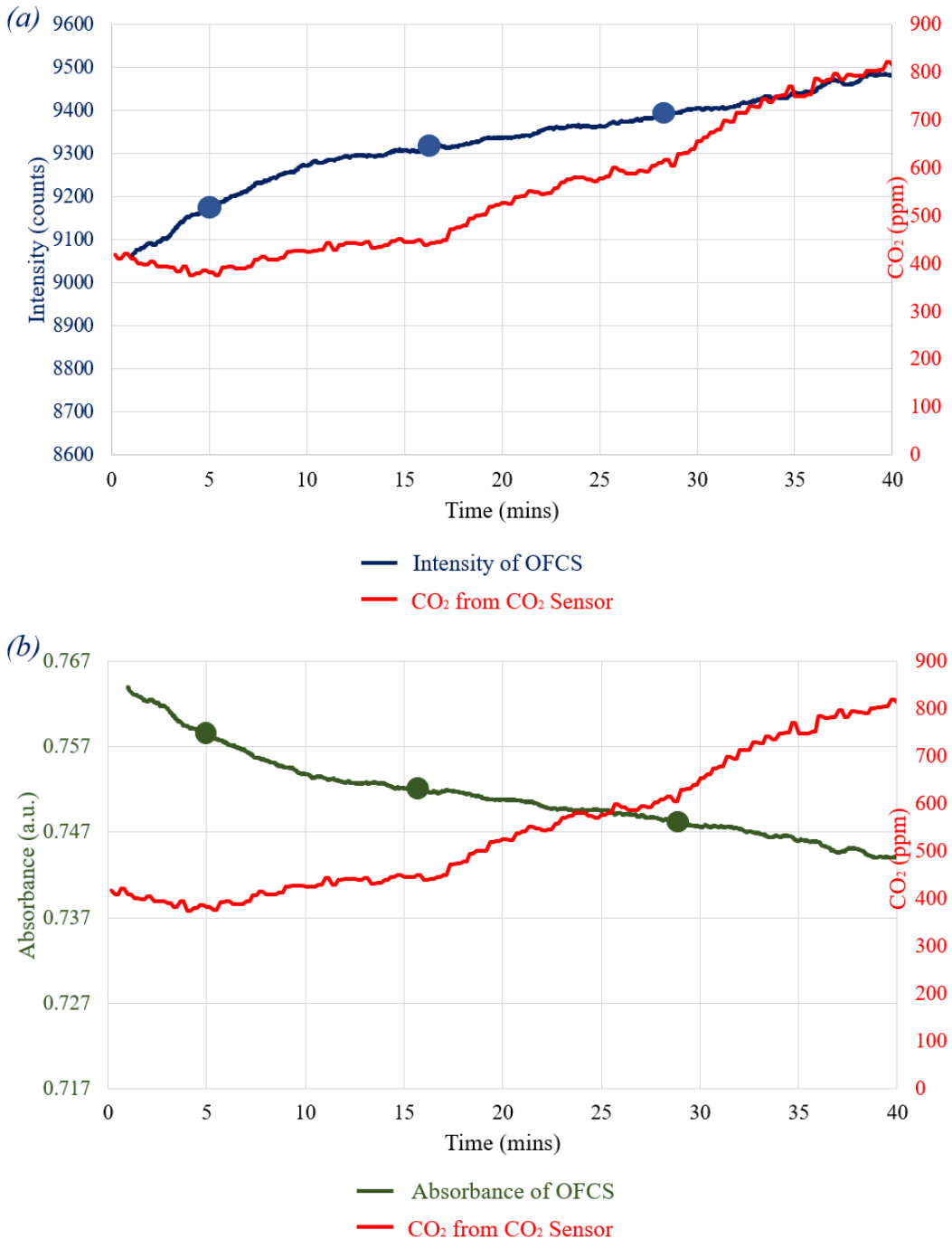


Figure A.17: *Response (a) Reflection Intensity (b) Absorbance of OFCS 10 for different CO_2 concentrations at wavelength 600 nm*

Table A.9: *Variation of CO_2 concentration and response (reflection intensity and absorbance) of OFCS 10 at wavelength 600 nm for different time periods*

Time (mins)	CO_2 (ppm)	Intensity (counts)	Absorbance (a.u.)	Time duration (mins) for measuring the change in CO_2, Intensity, and Absorbance	Change in CO_2 (ppm)	Change in Intensity (counts)	Change in Absorbance (a.u.)
5	376	9222	0.756				
16	439	9296	0.753	5-16	63	74	0.003
28	605	9414	0.747	16-28	166	118	0.006
40	829	9564	0.740	28-40	224	150	0.007

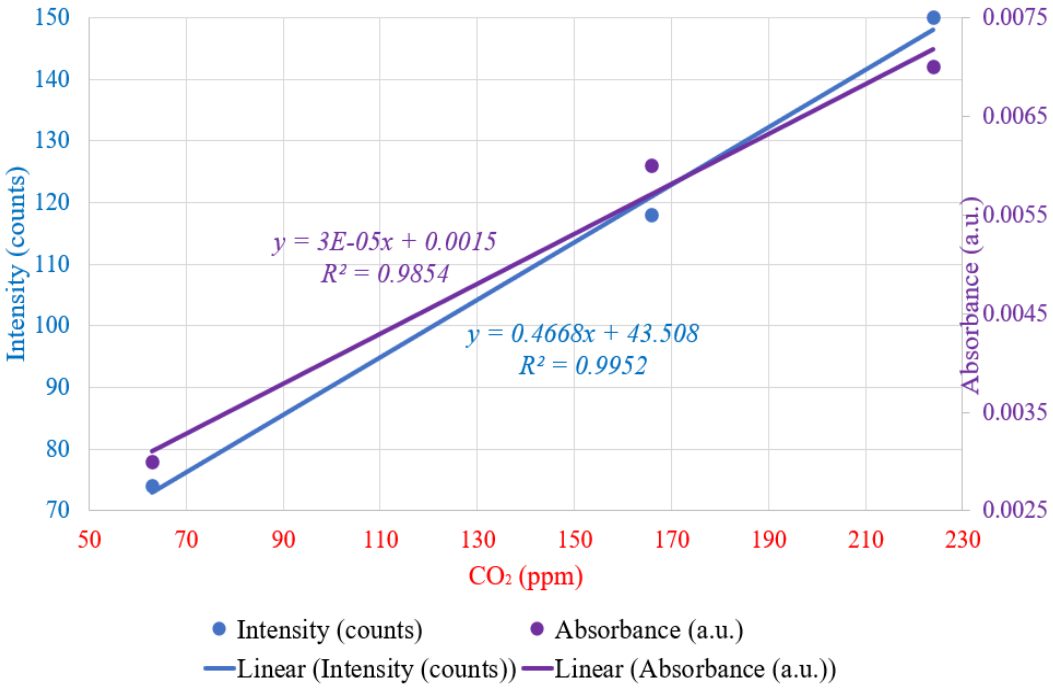


Figure A.18: *Linear fitting of variation in response (reflection intensity and absorbance) of OFCS 10 to different CO_2 concentrations at wavelength 600 nm*

B. Appendix B

Results from monitoring CO_2 emitted from human skin using a t_C Sensor 92 probe

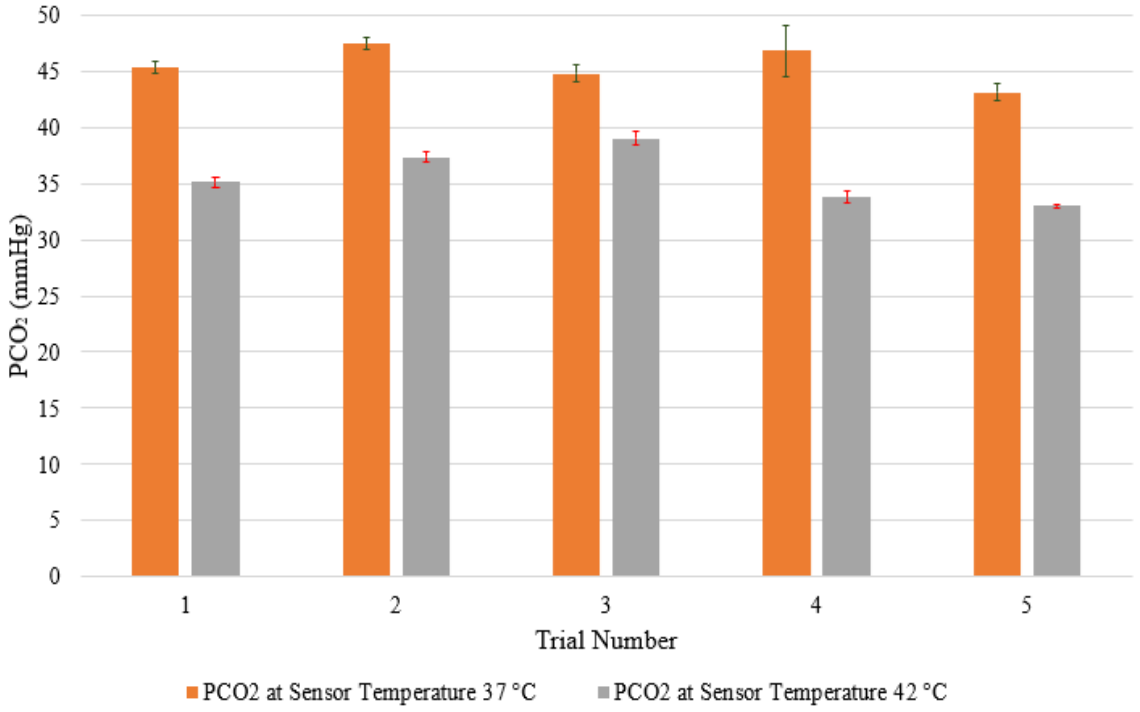


***Figure B.1**: Average PCO_2 measurement using t_C Sensor 92 probe from Volunteer 2's forearm*

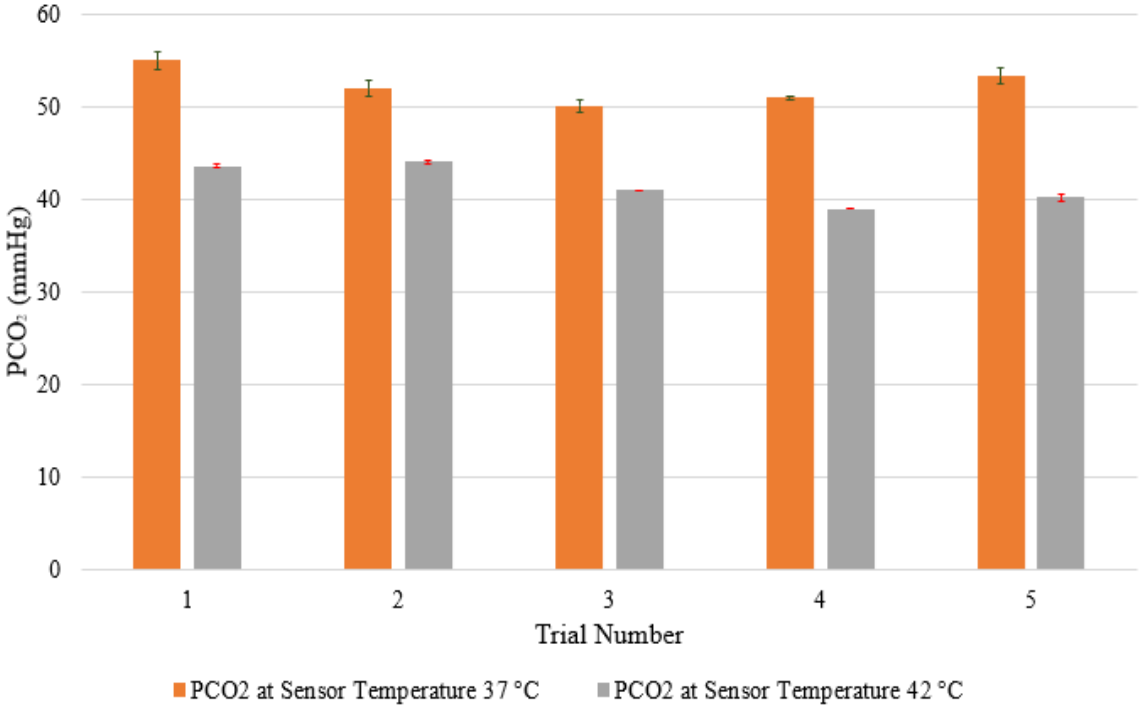


***Figure B.2**: Average PCO_2 measurement using t_C Sensor 92 probe from Volunteer 3's forearm*

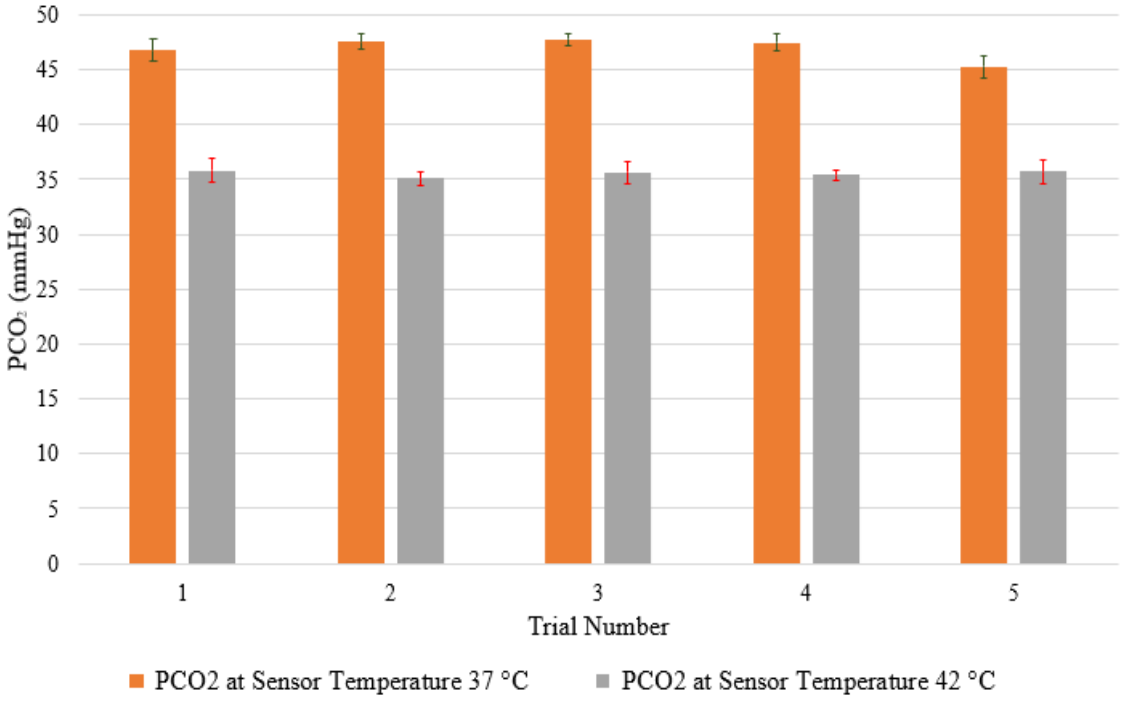


***Figure B.3**: Average PCO_2 measurement using t_C Sensor 92 probe from Volunteer 4's forearm*

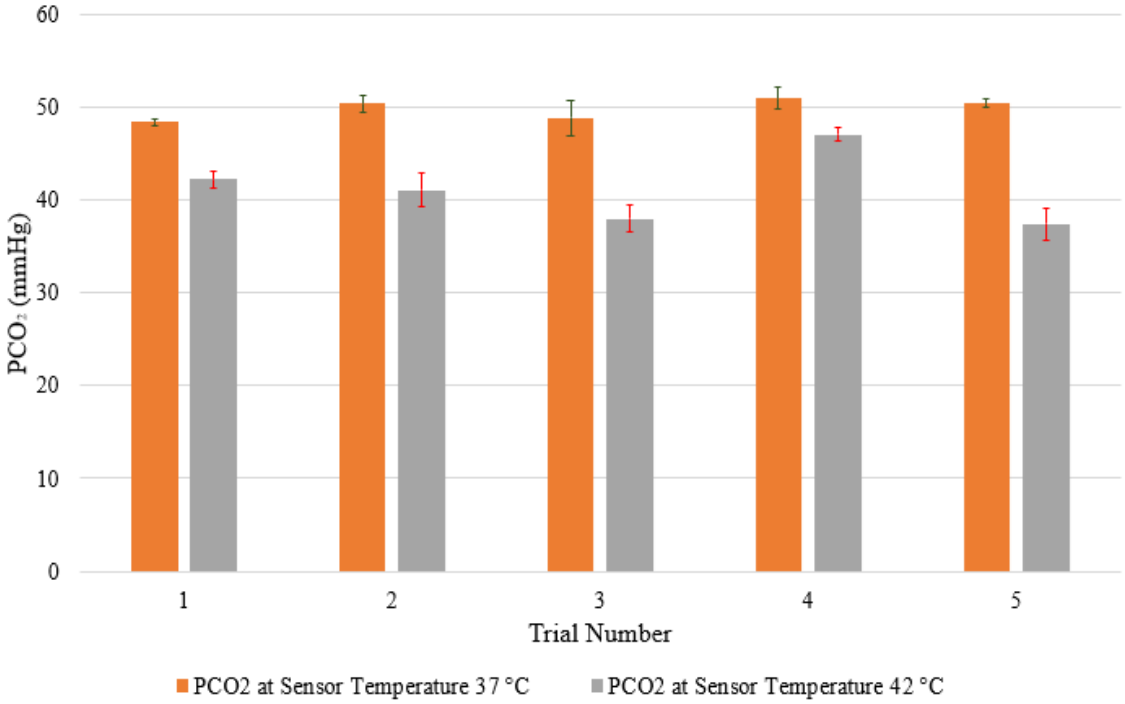


***Figure B.4**: Average PCO_2 measurement using t_C Sensor 92 probe from Volunteer 5's forearm*

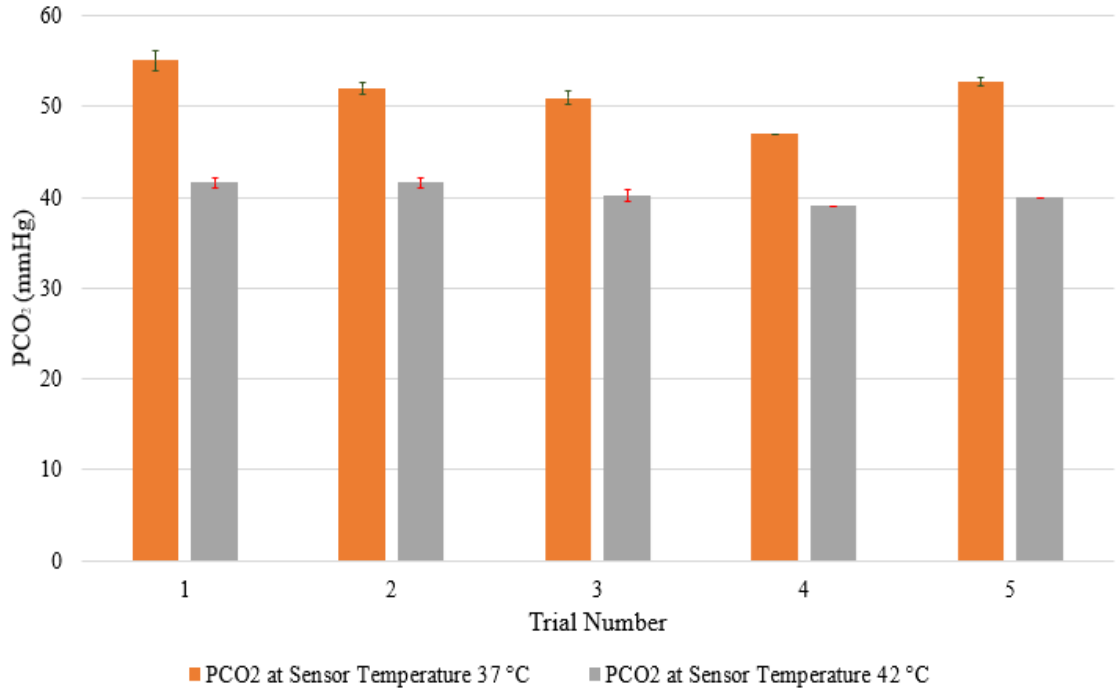


***Figure B.5**: Average PCO_2 measurement using t_C Sensor 92 probe from Volunteer 6's forearm*

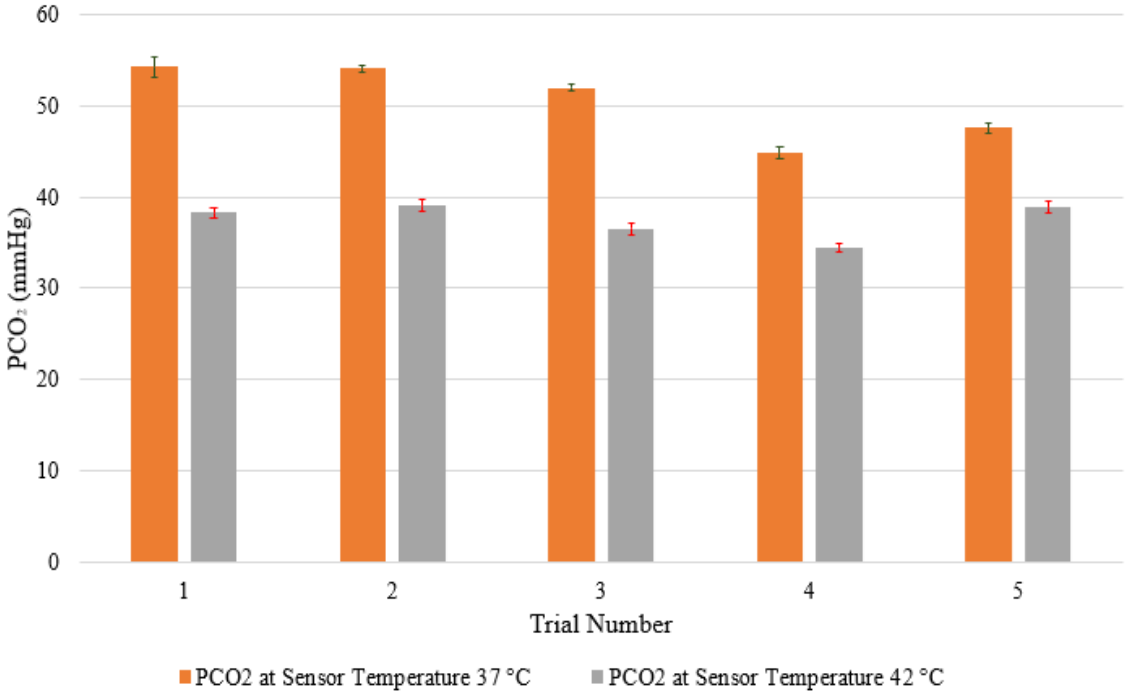


***Figure B.6**: Average PCO_2 measurement using t_C Sensor 92 probe from Volunteer 7's forearm*

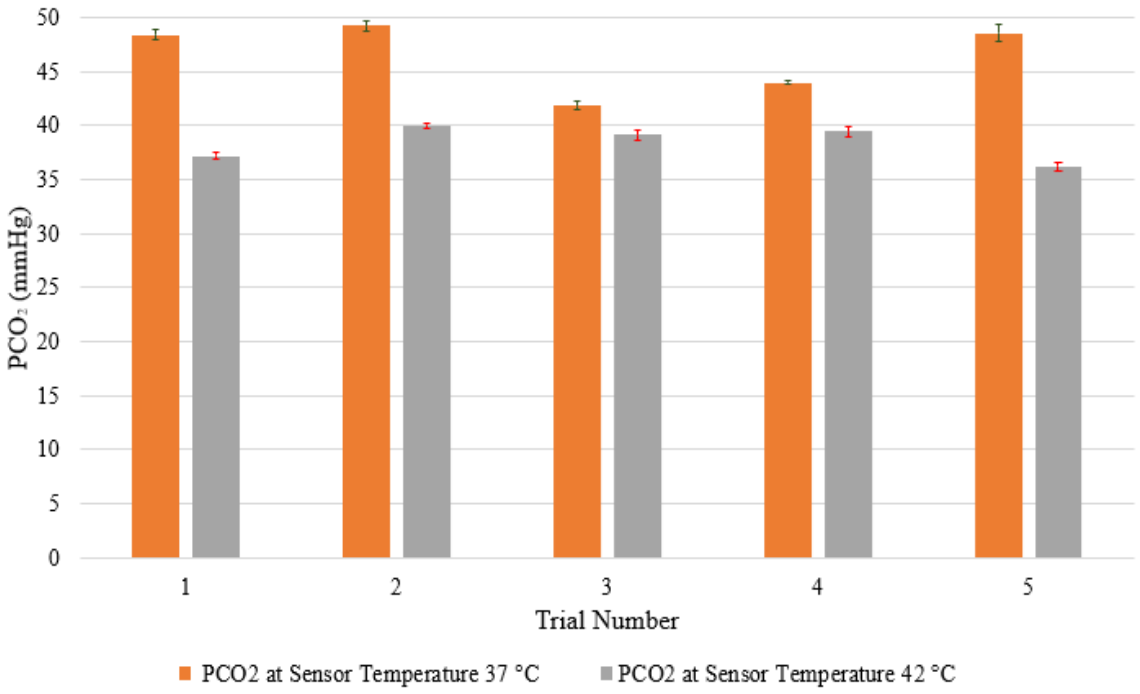


***Figure B.7**: Average PCO_2 measurement using t_C Sensor 92 probe from Volunteer 8's forearm*

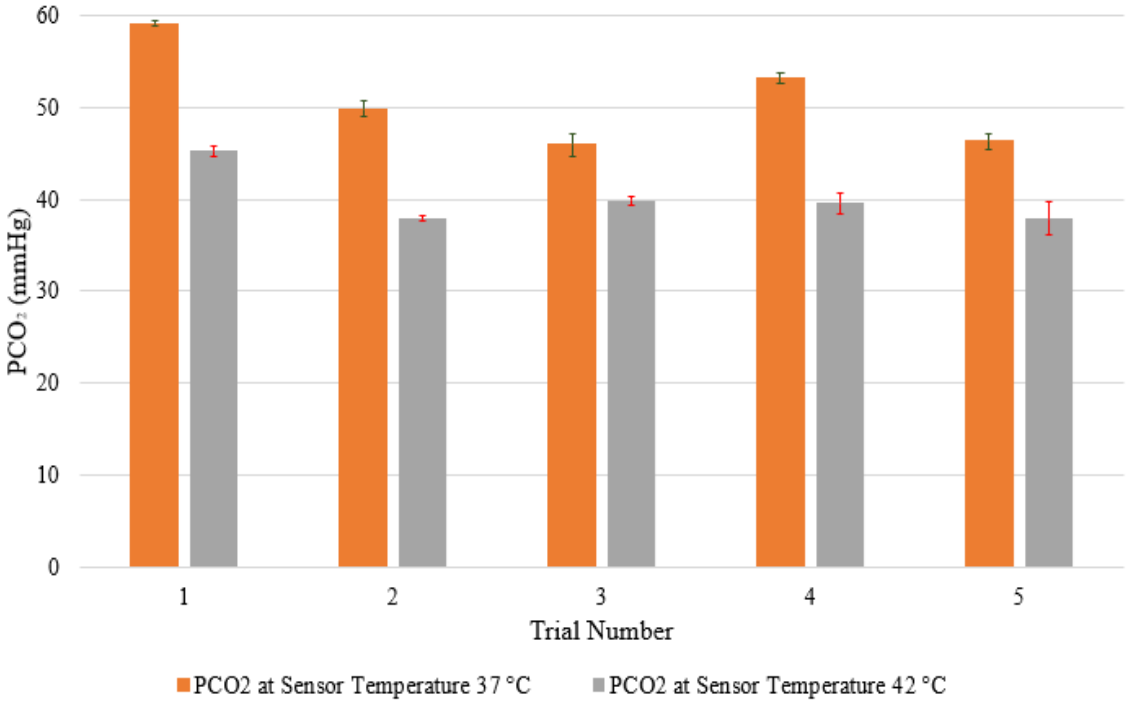


***Figure B.8:** Average PCO_2 measurement using t_C Sensor 92 probe from Volunteer 9's forearm*

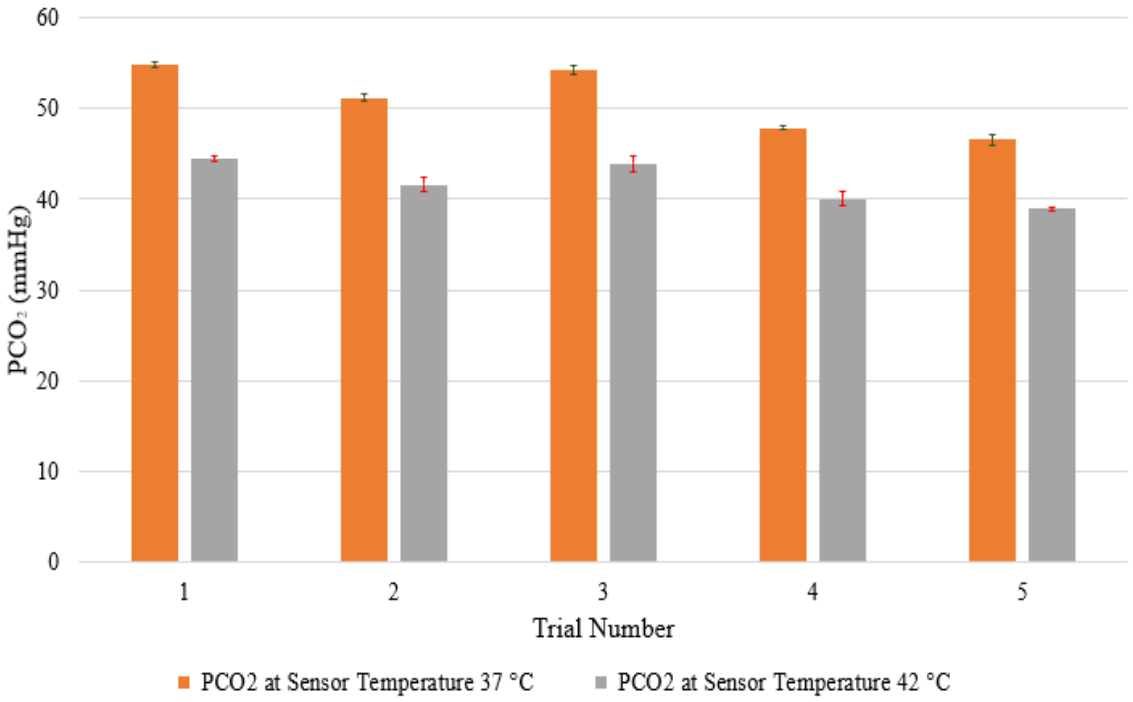


***Figure B.9**: Average PCO_2 measurement using t_C Sensor 92 probe from Volunteer 10's forearm*

C. Appendix C

Results from monitoring CO_2 emitted from human skin during loading using an OFCS and a commercial CO_2 sensor

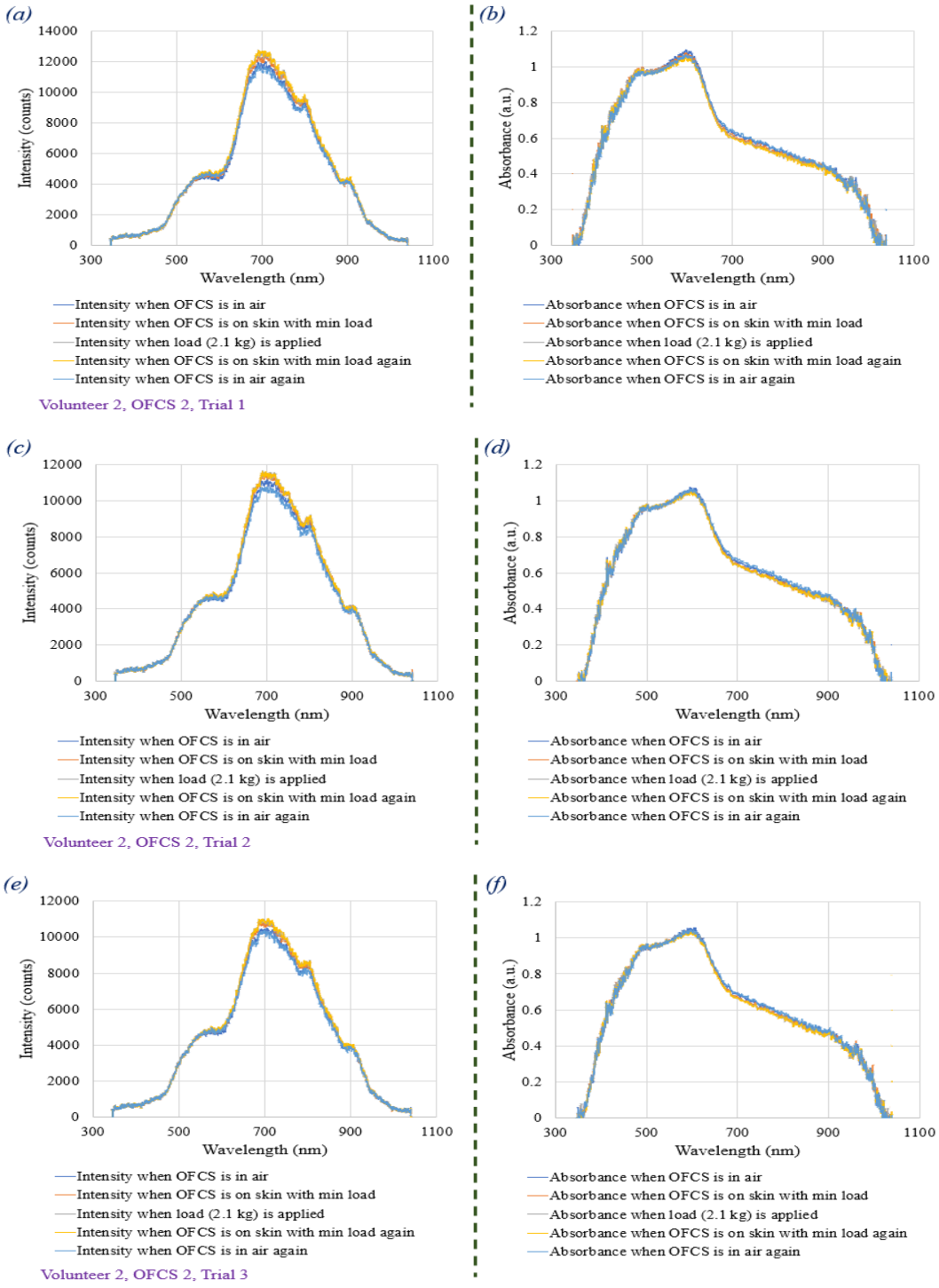


Figure C.1: *(a) (c) (e) Reflection spectra and (b) (d) (f) Absorption spectra of OFCS 2. Each row represents a different Trial 1-3 for Volunteer 2*

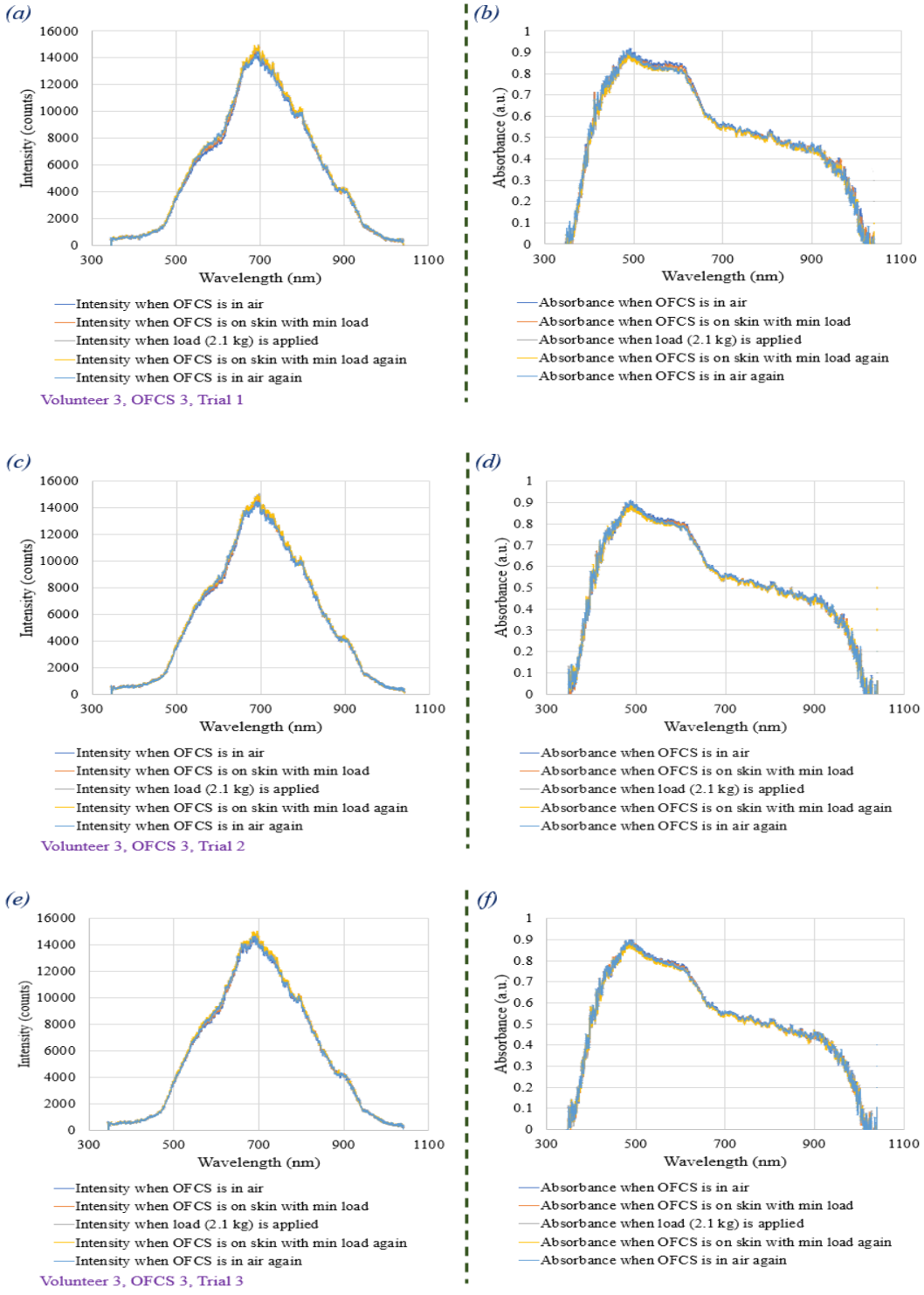


Figure C.2: *(a) (c) (e) Reflection spectra and (b) (d) (f) Absorption spectra of OFCS 3. Each row represents a different Trial 1-3 for Volunteer 3*

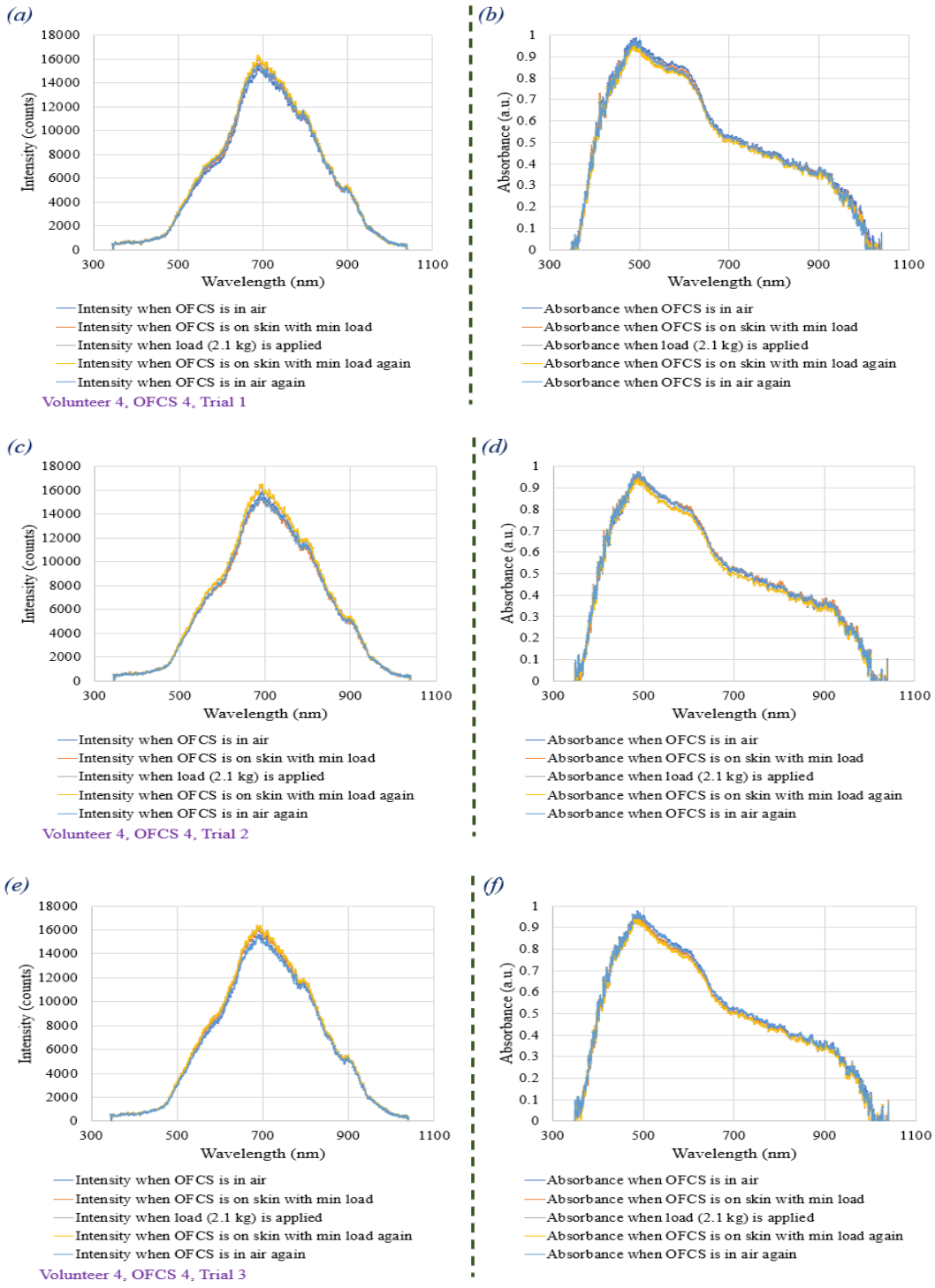


Figure C.3: *(a) (c) (e) Reflection spectra and (b) (d) (f) Absorption spectra of OFCS 4. Each row represents a different Trial 1-3 for Volunteer 4*

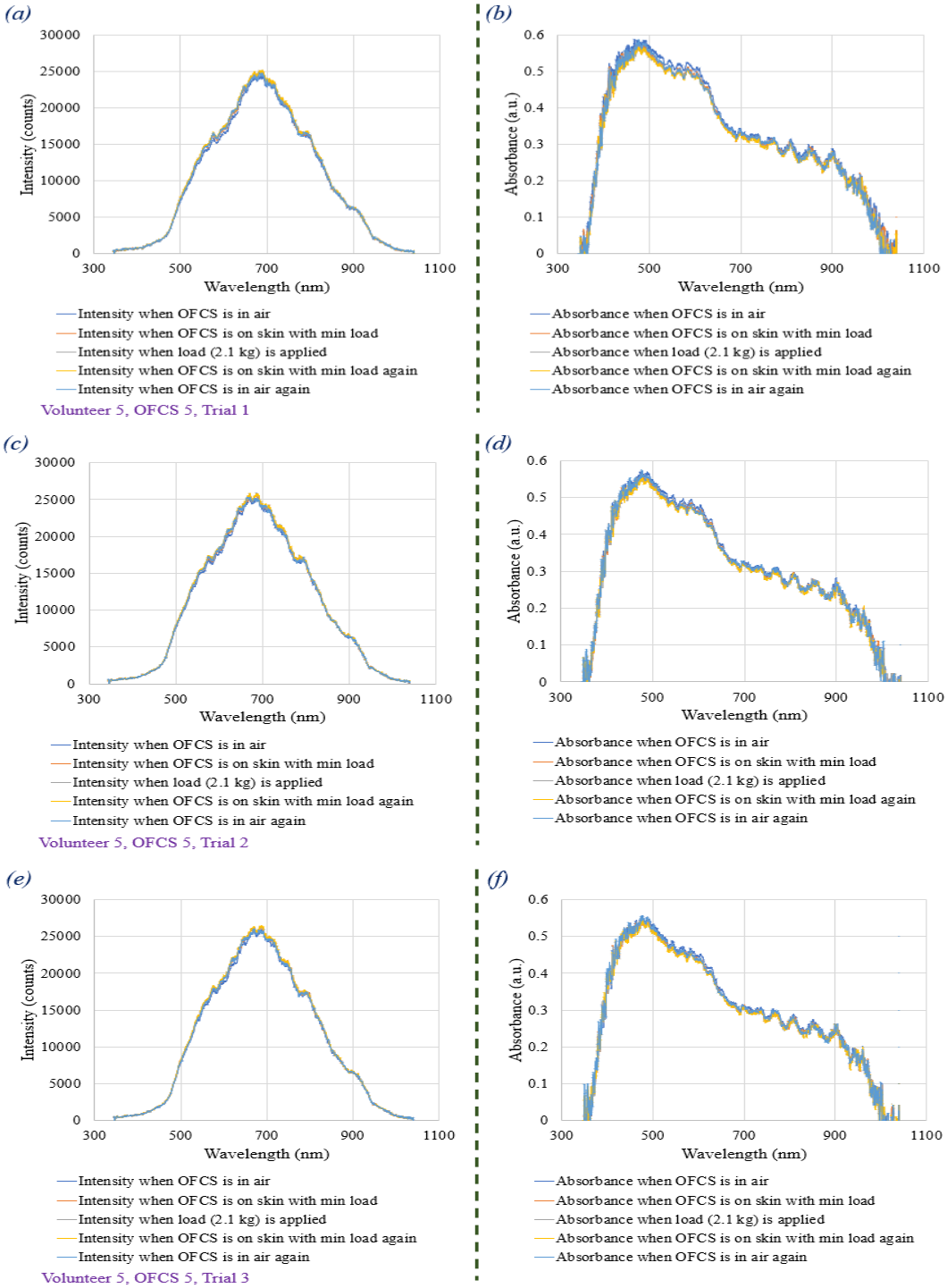


Figure C.4: *(a) (c) (e) Reflection spectra and (b) (d) (f) Absorption spectra of OFCS 5. Each row represents a different Trial 1-3 for Volunteer 5*

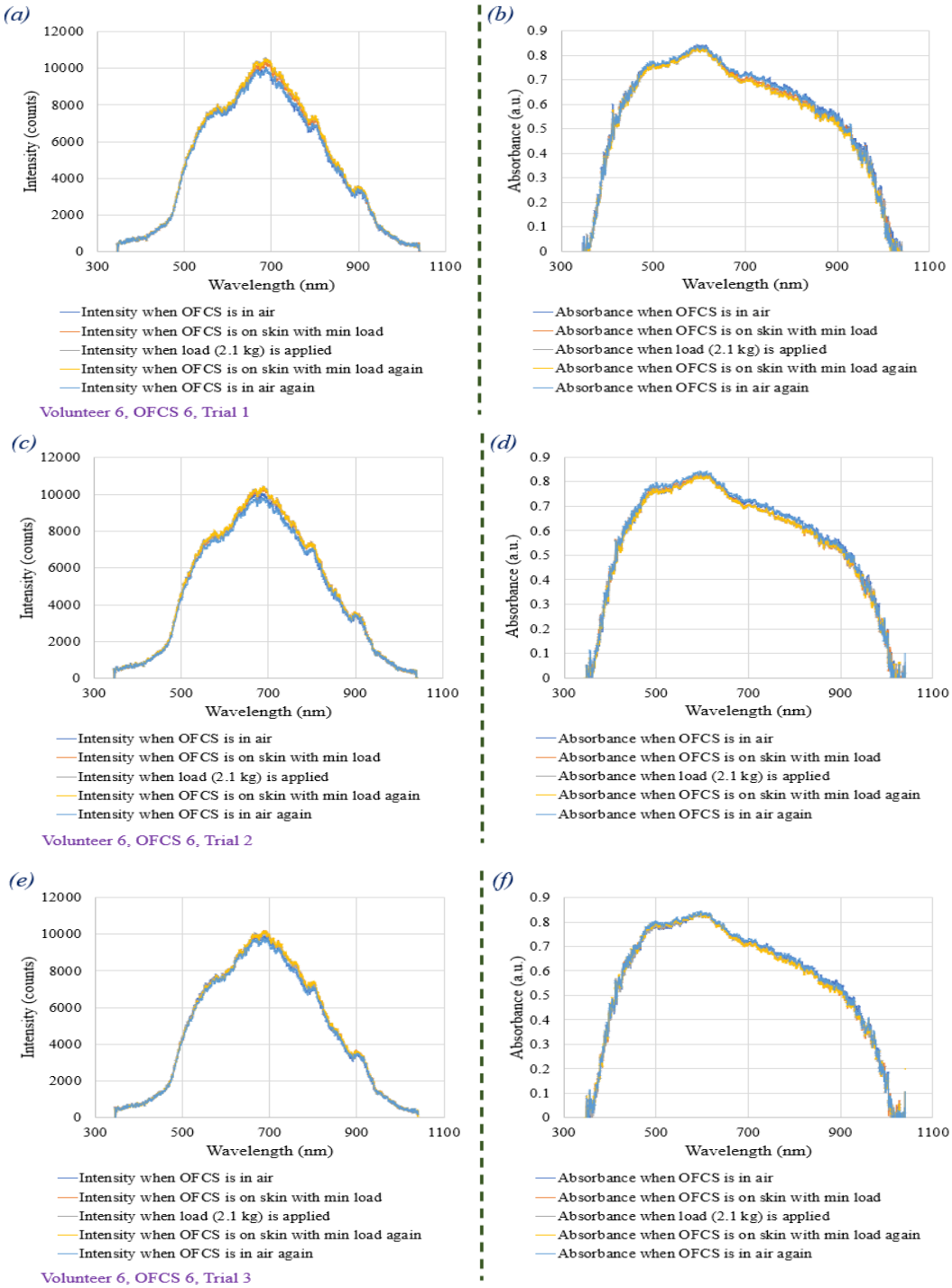


Figure C.5: *(a) (c) (e) Reflection spectra and (b) (d) (f) Absorption spectra of OFCS 6. Each row represents a different Trial 1-3 for Volunteer 6*

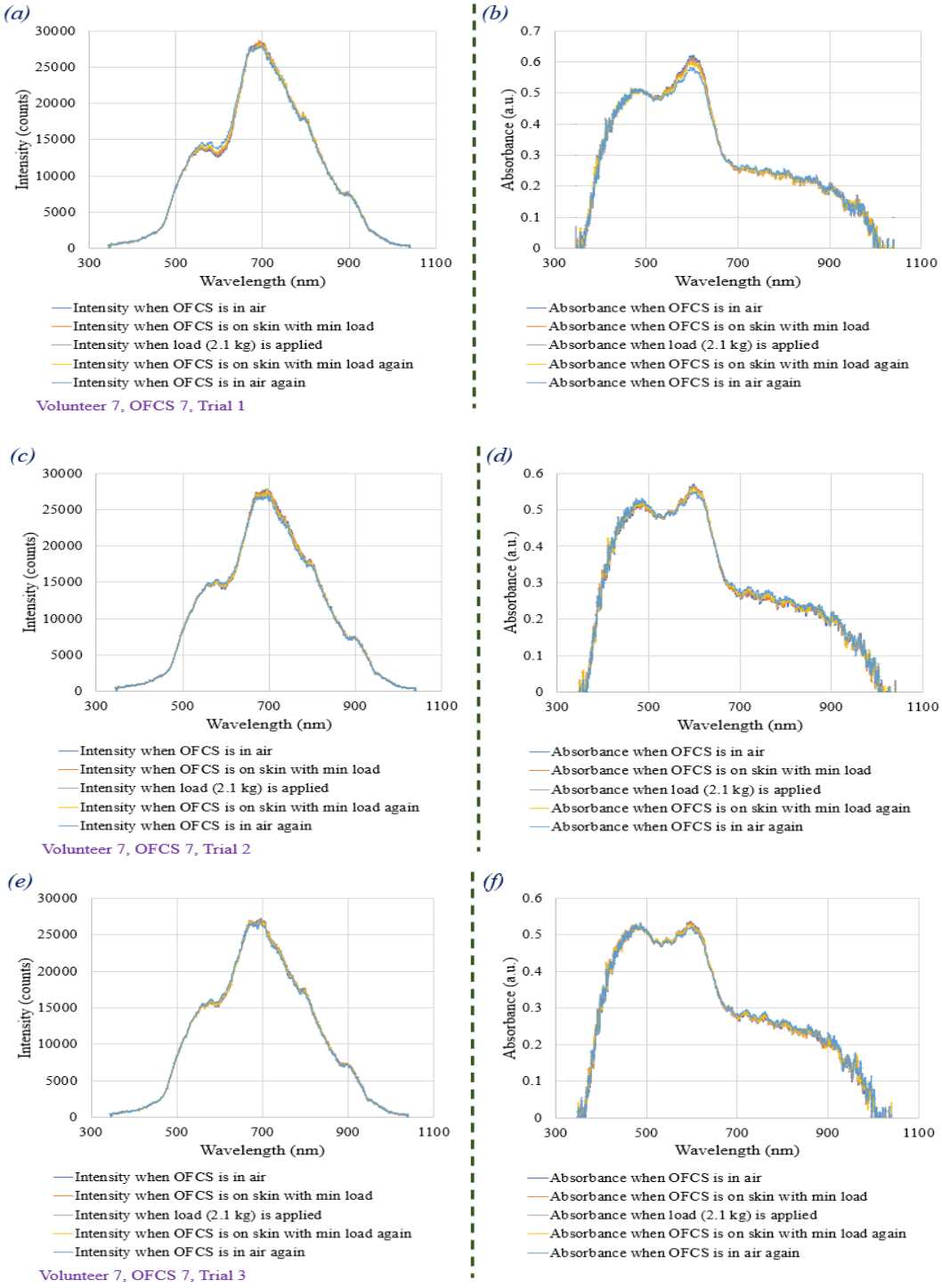


Figure C.6: *(a) (c) (e) Reflection spectra and (b) (d) (f) Absorption spectra of OFCS 7. Each row represents a different Trial 1-3 for Volunteer 7*

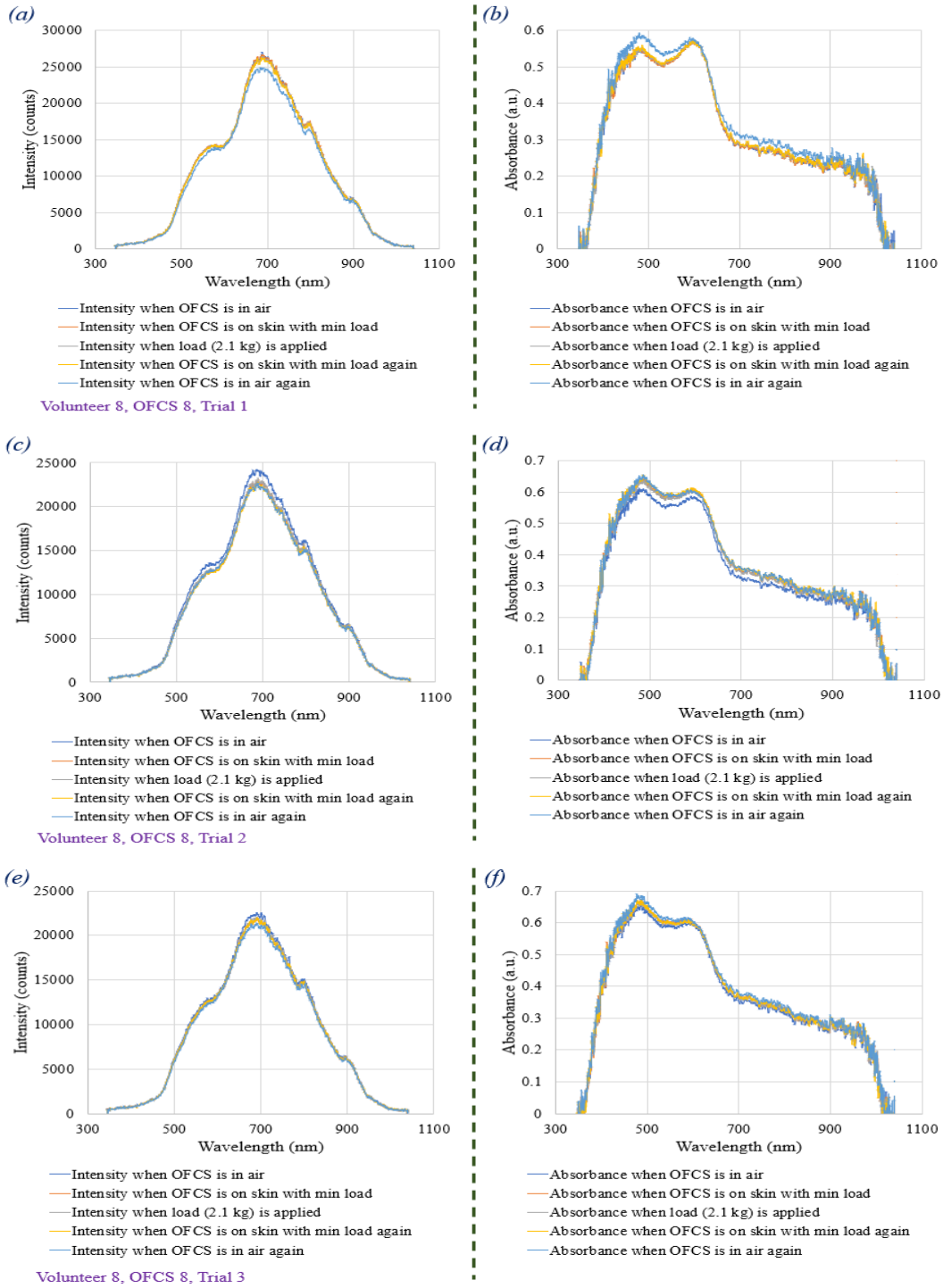


Figure C.7: *(a) (c) (e) Reflection spectra and (b) (d) (f) Absorption spectra of OFCS 8. Each row represents a different Trial 1-3 for Volunteer 8*

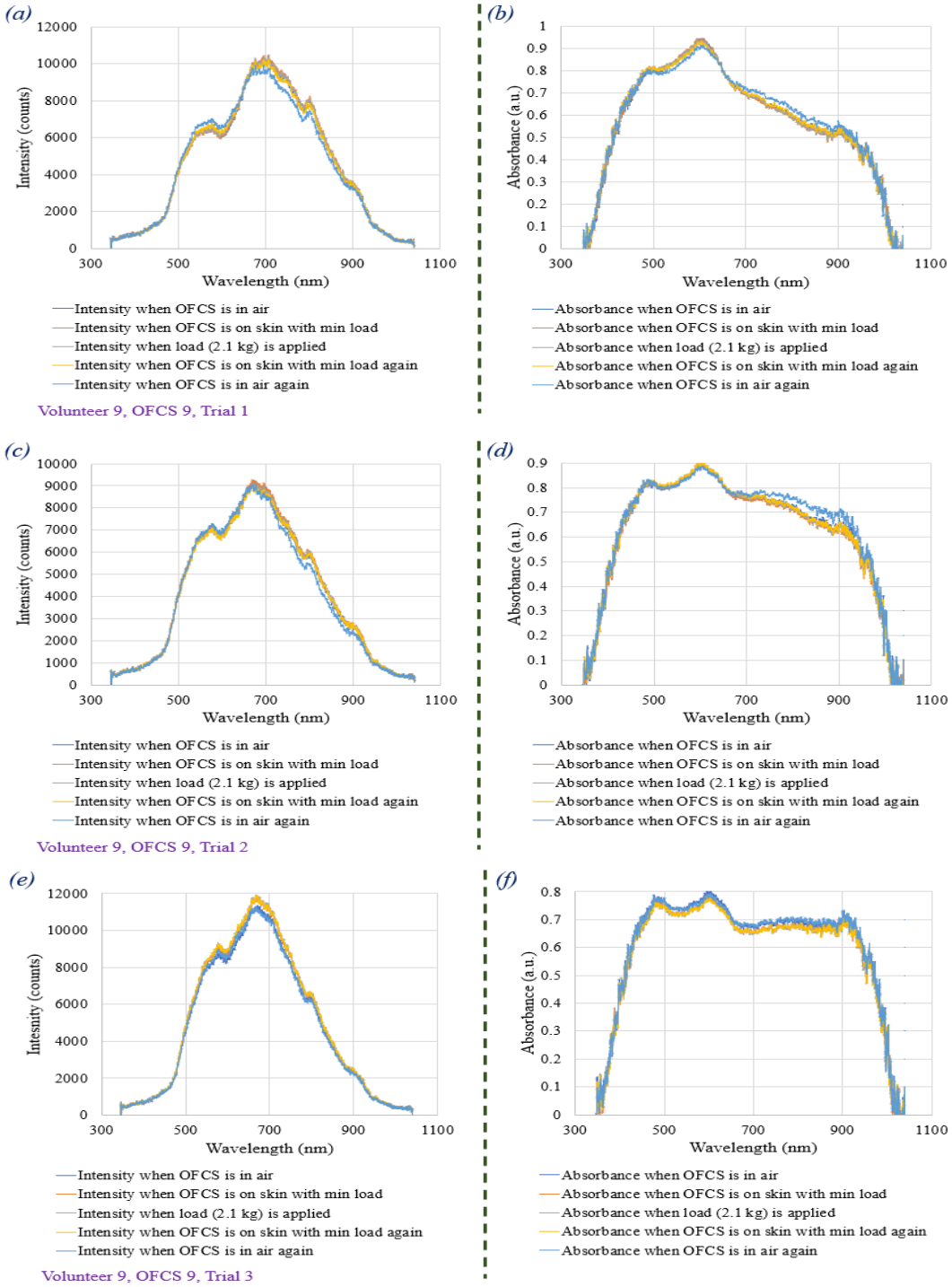


Figure C.8: *(a) (c) (e) Reflection spectra and (b) (d) (f) Absorption spectra of OFCS 9. Each row represents a different Trial 1-3 for Volunteer 9*

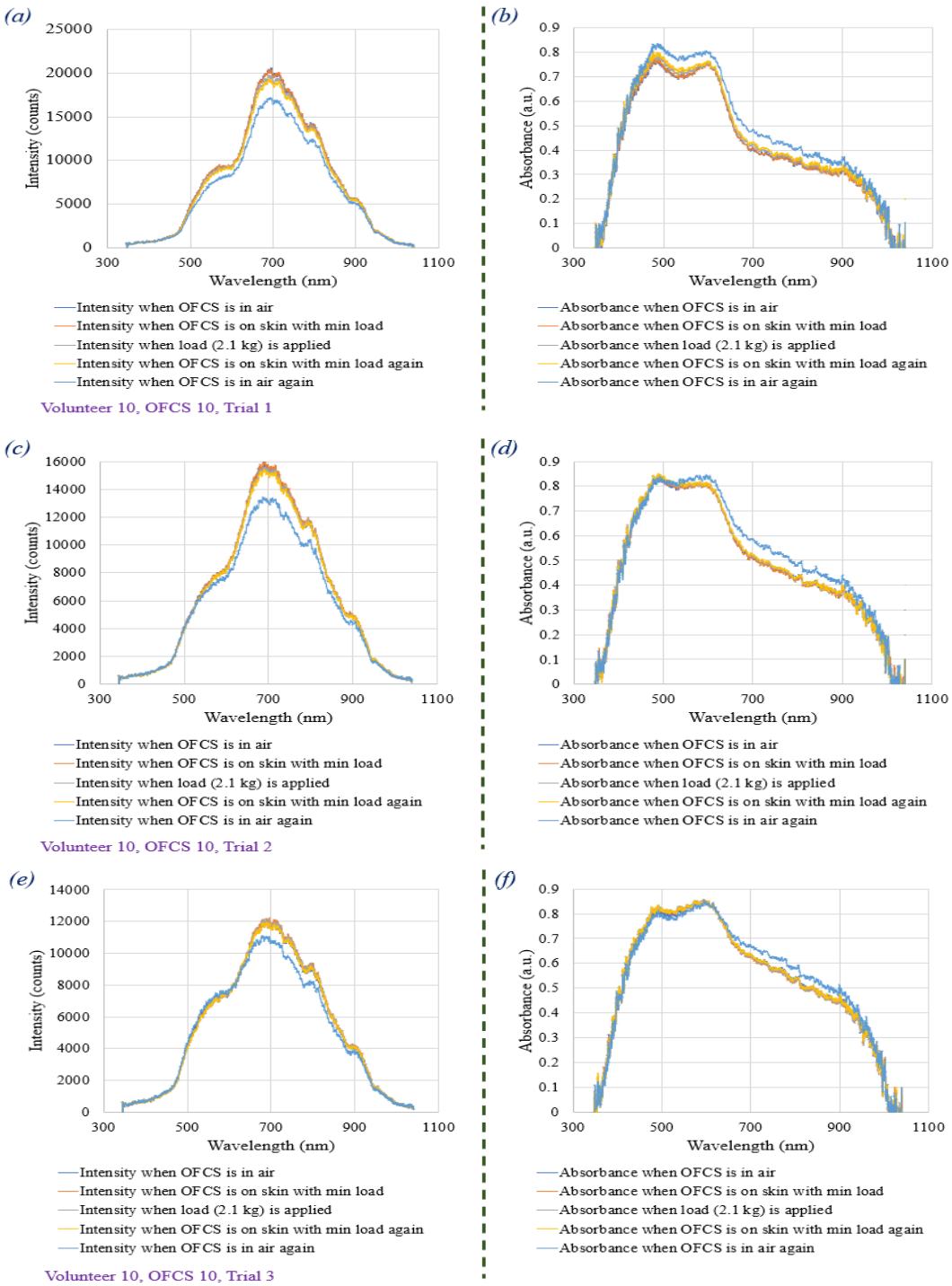


Figure C.9: *(a) (c) (e) Reflection spectra and (b) (d) (f) Absorption spectra of OFCS 10. Each row represents a different Trial 1-3 for Volunteer 10*

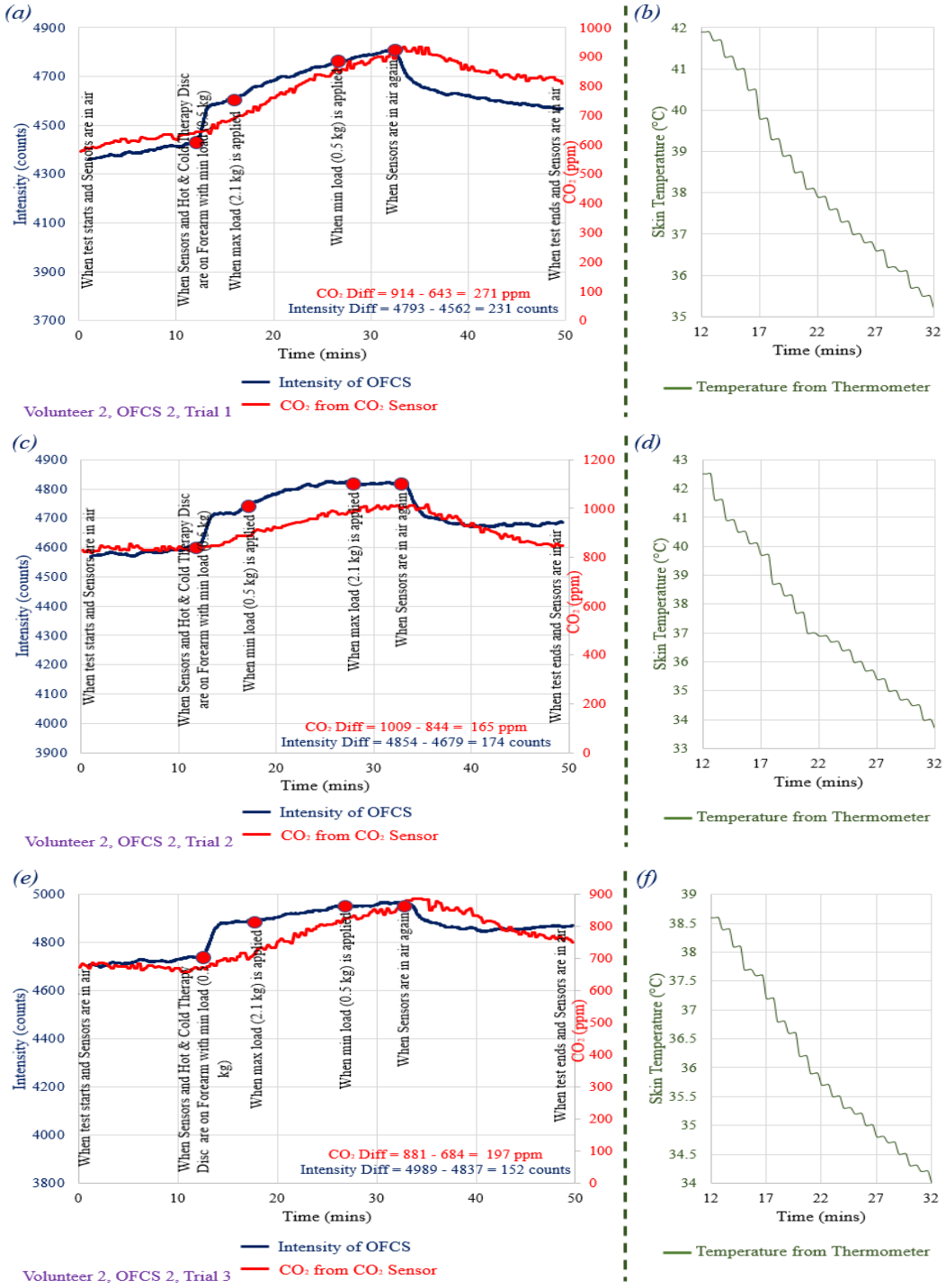


Figure C.10: *(a) (c) (e) Response (Reflection Intensity) of OFCS 2 at wavelength 600 nm and commercial CO_2 sensor on Volunteer 2's forearm (b) (d) (f) Volunteer 2's skin temperature while heated disc is on forearm for Trials 1-3, respectively*

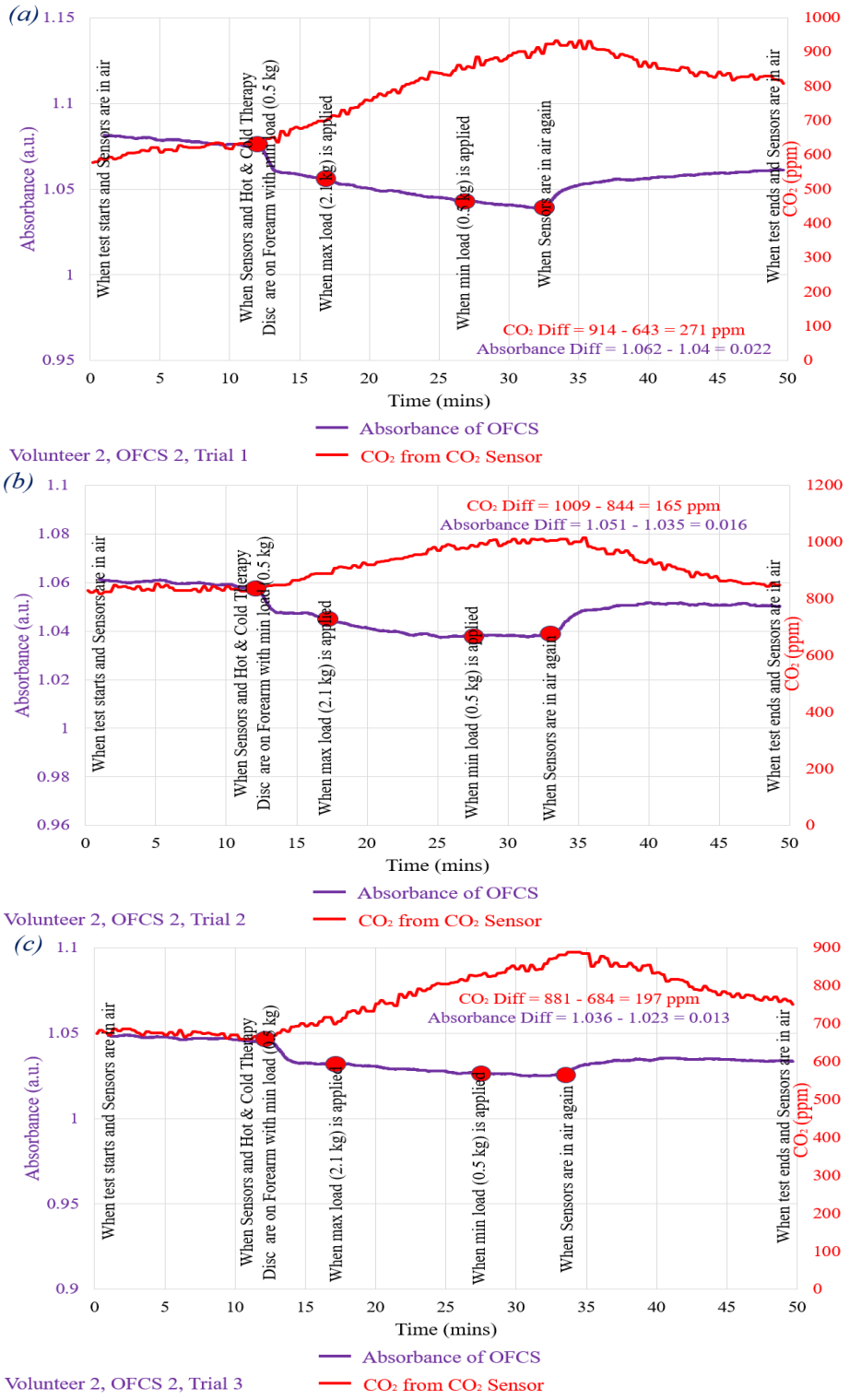


Figure C.11: *(a)-(c) Response (Absorbance) of OFCS 2 at wavelength 600 nm and commercial CO_2 sensor on Volunteer 2's forearm for Trials 1-3, respectively*

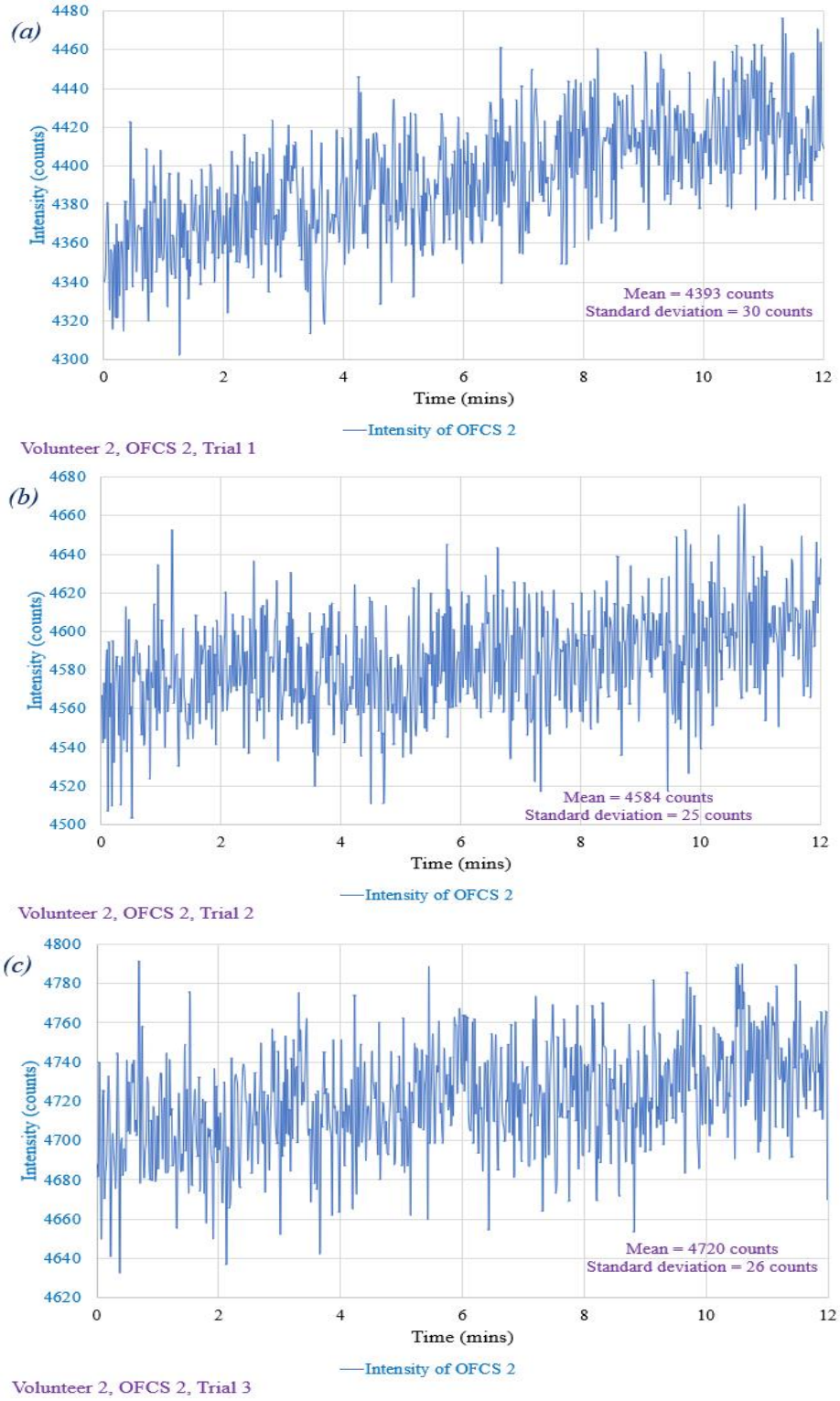


Figure C.12: *(a)-(c) Response (Raw Reflection Intensity) of OFCS 2 at wavelength 600 nm in the air for Trials 1-3, respectively*

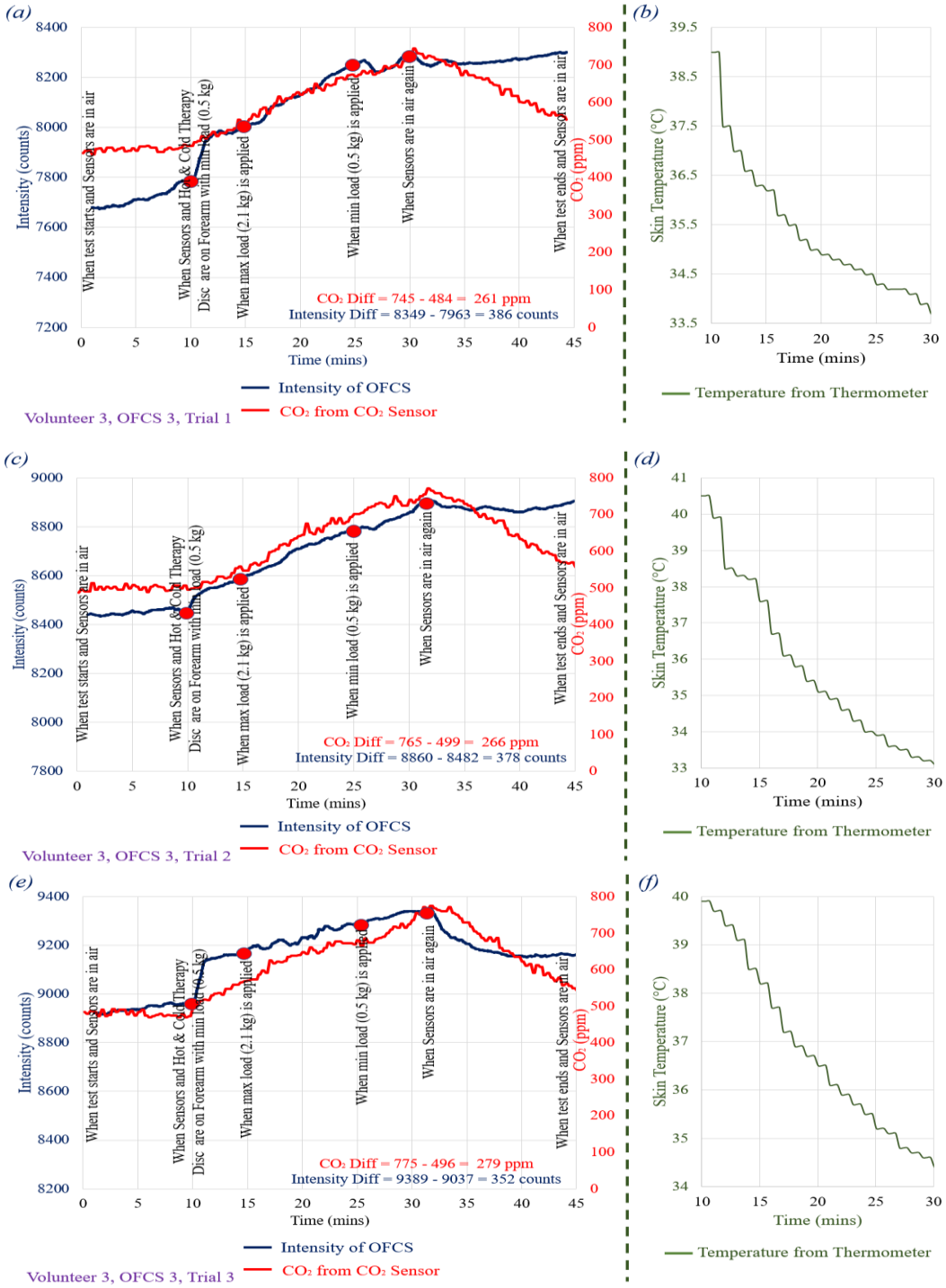


Figure C.13: *(a) (c) (e) Response (Reflection Intensity) of OFCS 3 at wavelength 600 nm and commercial CO_2 sensor on Volunteer 3's forearm (b) (d) (f) Volunteer 3's skin temperature while heated disc is on forearm for Trials 1-3, respectively*

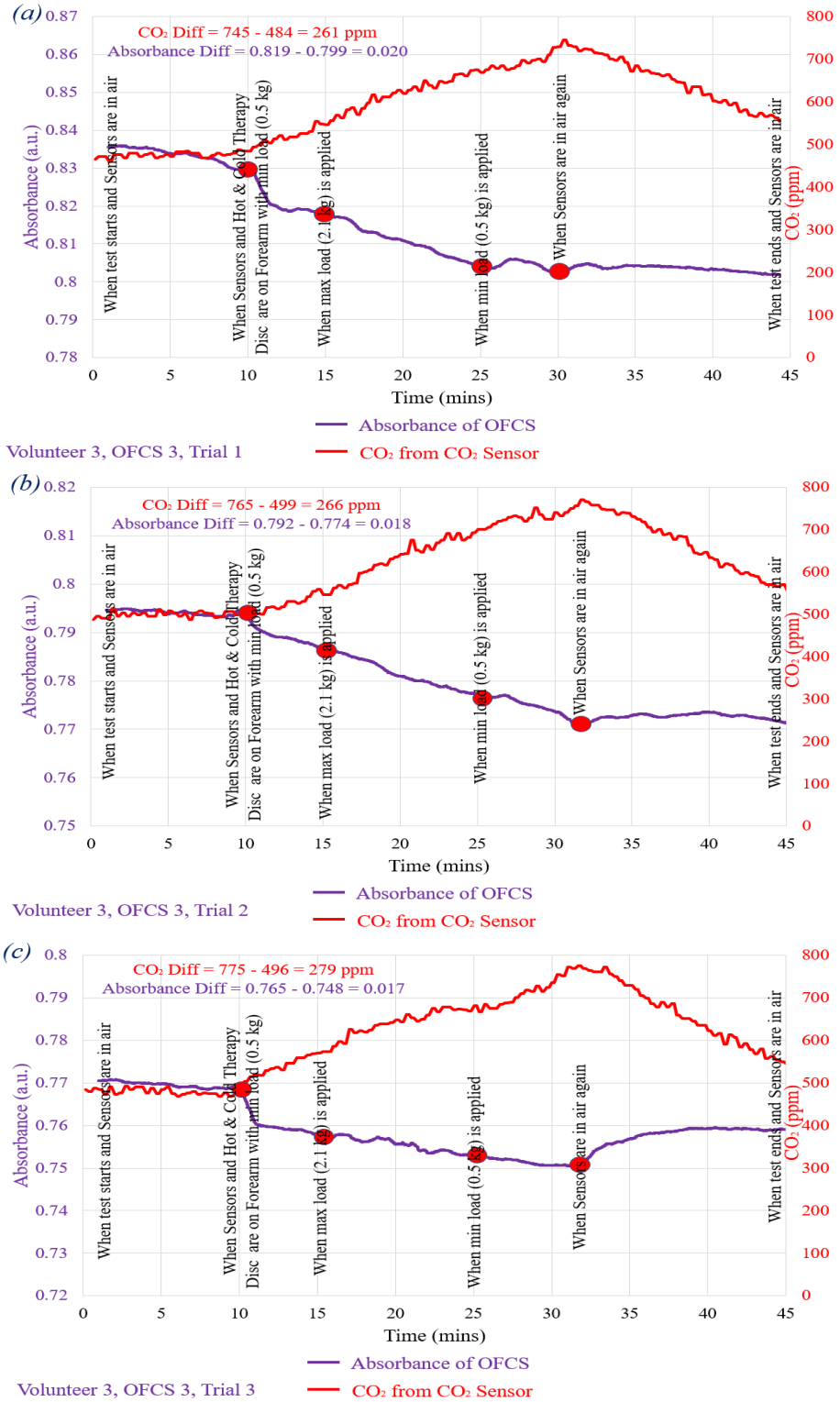


Figure C.14: *(a)-(c) Response (Absorbance) of OFCS 3 at wavelength 600 nm and commercial CO_2 sensor on Volunteer 3's forearm for Trials 1-3, respectively*

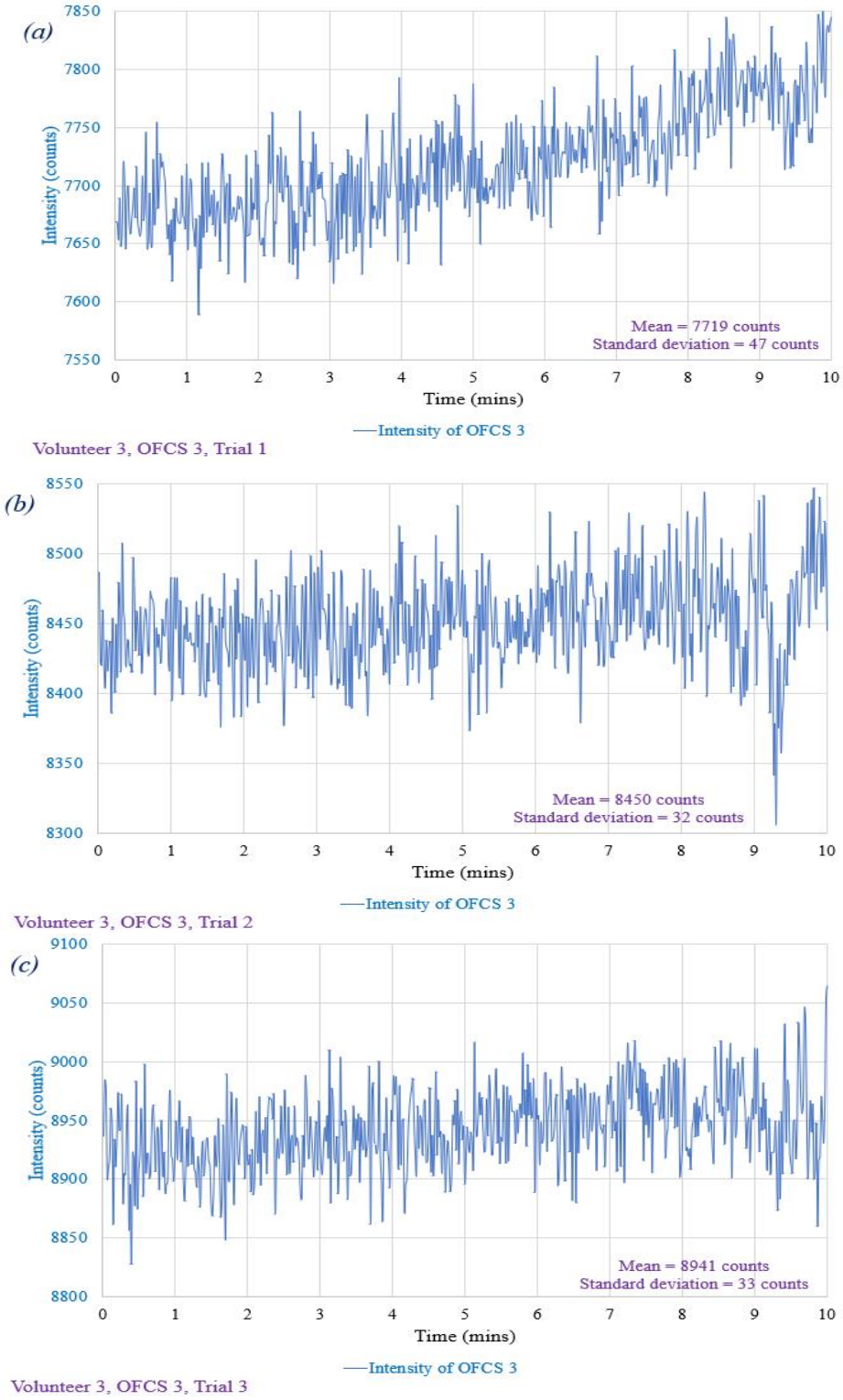


Figure C.15: *(a)-(c) Response (Raw Reflection Intensity) of OFCS 3 at wavelength 600 nm in the air for Trials 1-3, respectively*

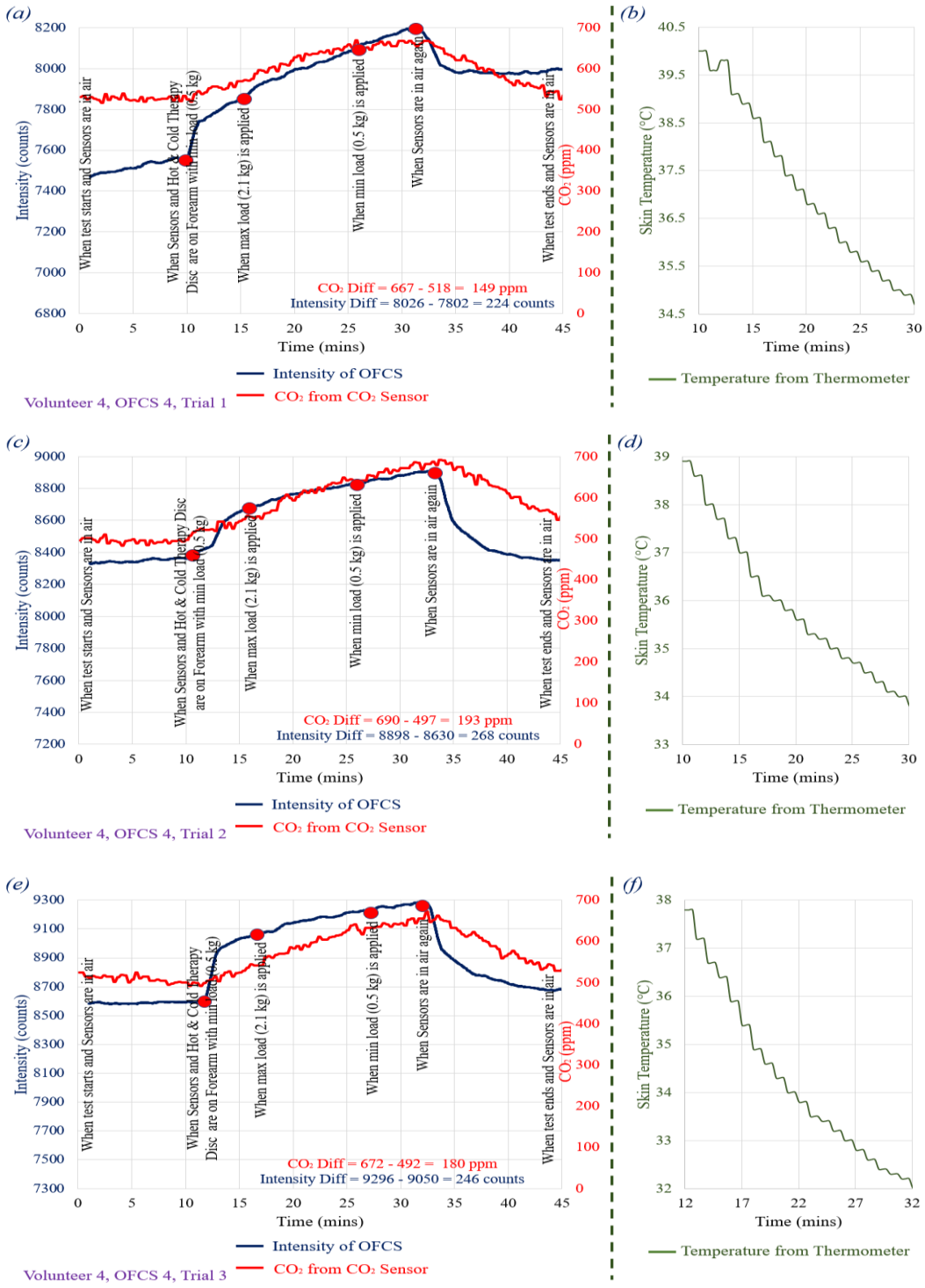


Figure C.16: *(a) (c) (e) Response (Reflection Intensity) of OFCS 4 at wavelength 600 nm and commercial CO_2 sensor on Volunteer 4's forearm (b) (d) (f) Volunteer 4's skin temperature while heated disc is on forearm for Trials 1-3, respectively*

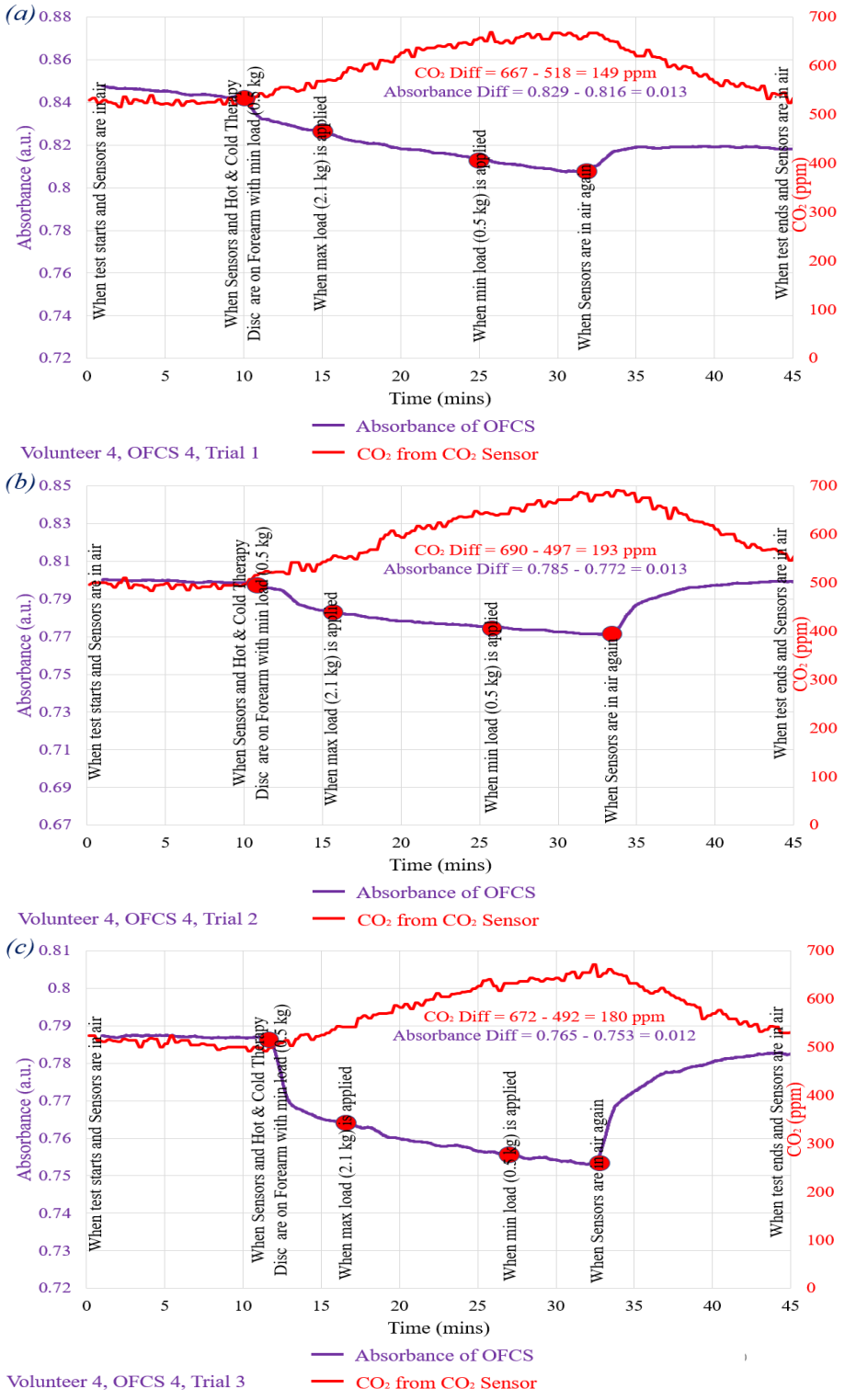


Figure C.17: *(a)-(c) Response (Absorbance) of OFCS 4 at wavelength 600 nm and commercial CO_2 sensor on Volunteer 4's forearm for Trials 1-3, respectively*

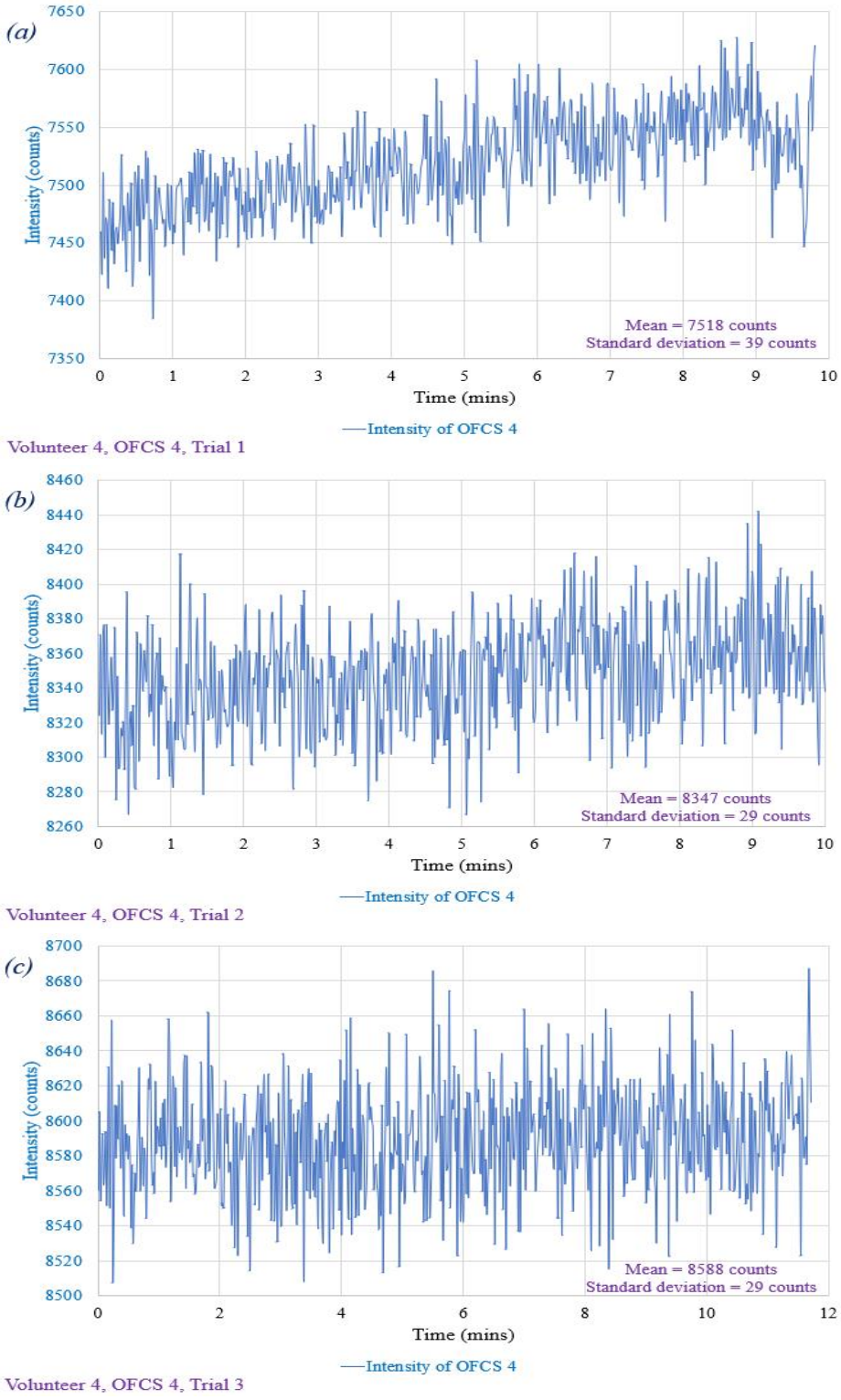


Figure C.18: *(a)-(c) Response (Raw Reflection Intensity) of OFCS 4 at wavelength 600 nm in the air for Trials 1-3, respectively*

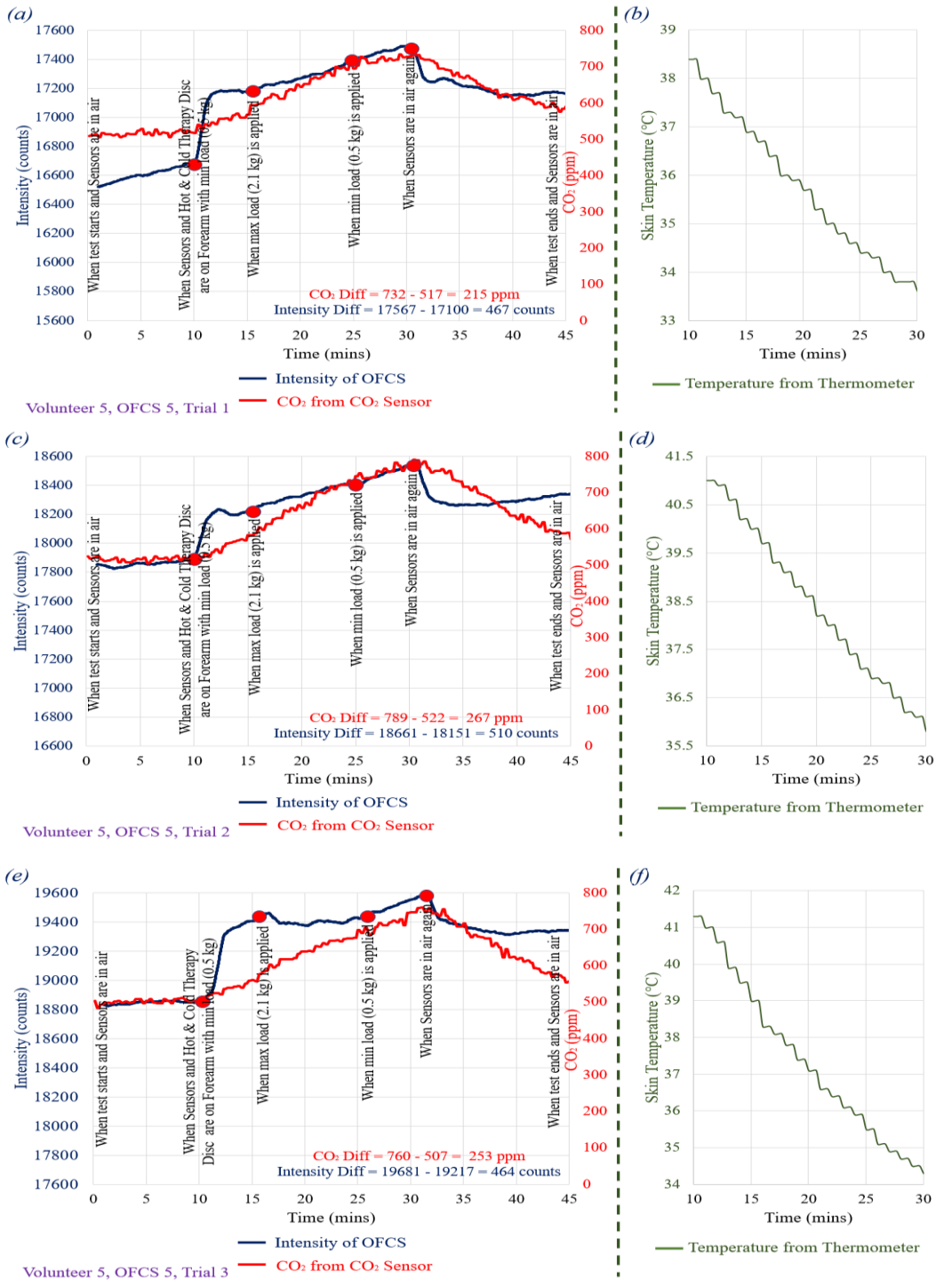


Figure C.19: *(a) (c) (e) Response (Reflection Intensity) of OFCS 5 at wavelength 600 nm and commercial CO_2 sensor on Volunteer 5's forearm (b) (d) (f) Volunteer 5's skin temperature while heated disc is on forearm for Trials 1-3, respectively*

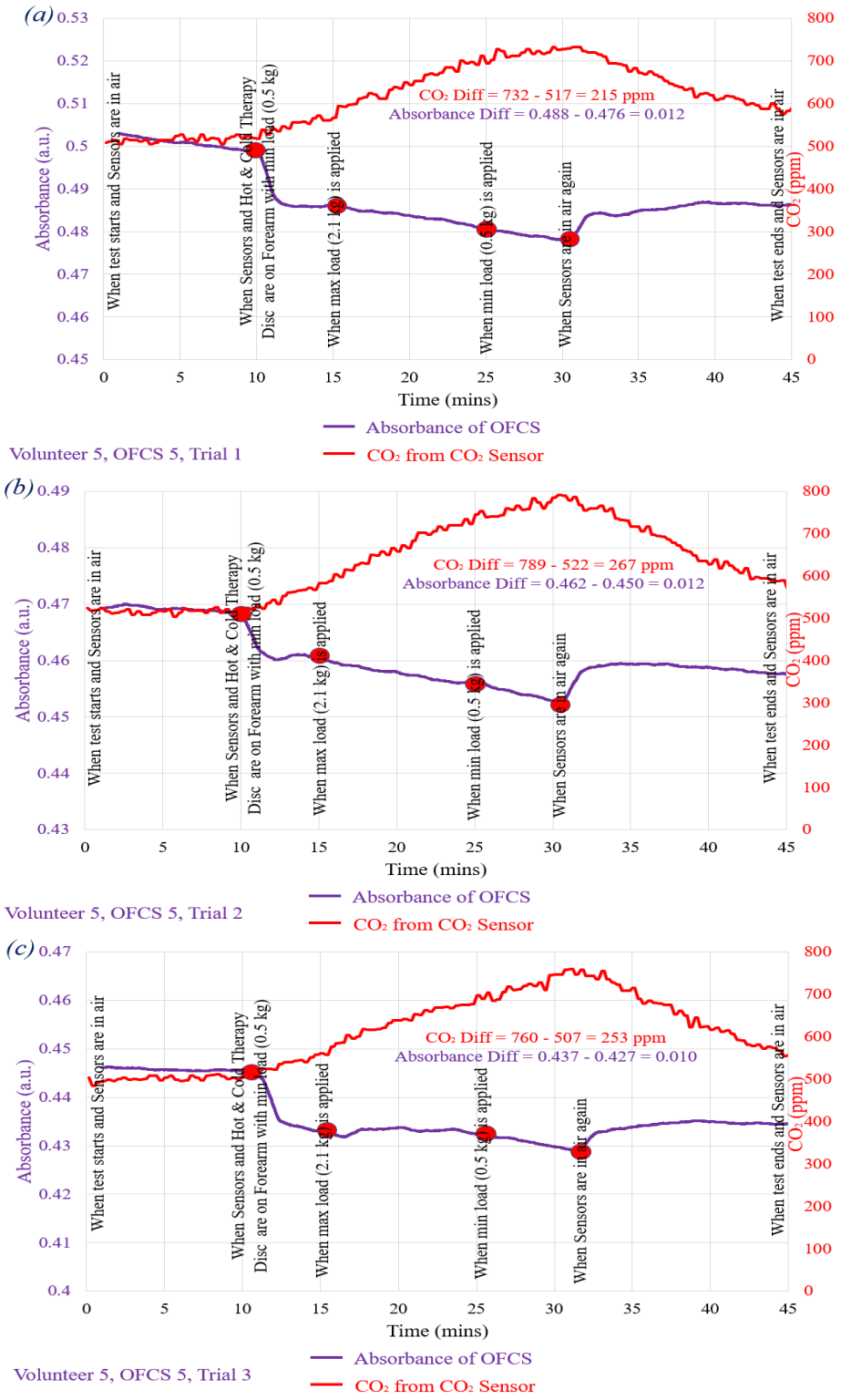


Figure C.20: *(a)-(c) Response (Absorbance) of OFCS 5 at wavelength 600 nm and commercial CO_2 sensor on Volunteer 5's forearm for Trials 1-3, respectively*

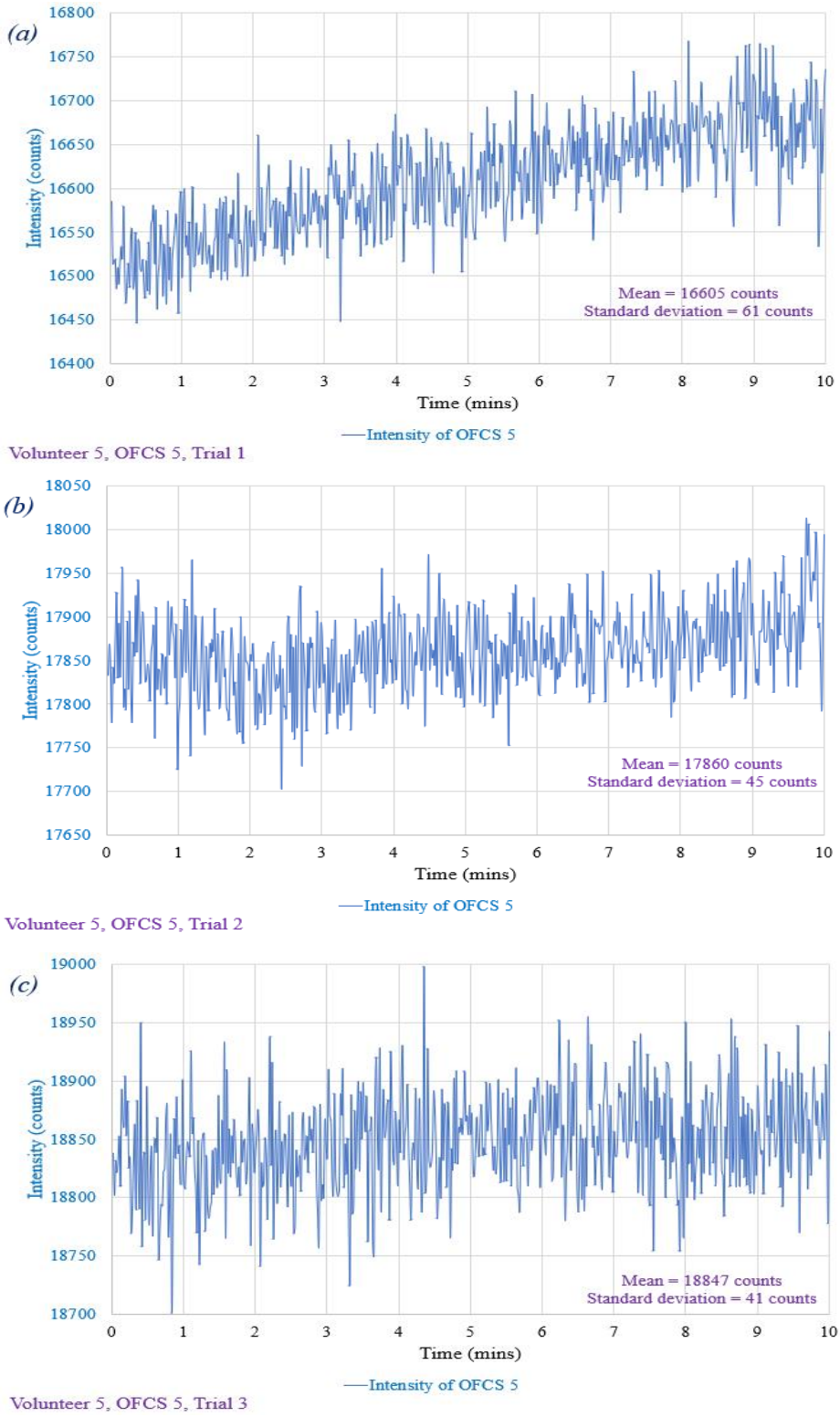


Figure C.21: *(a)-(c) Response (Raw Reflection Intensity) of OFCS 5 at wavelength 600 nm in the air for Trials 1-3, respectively*

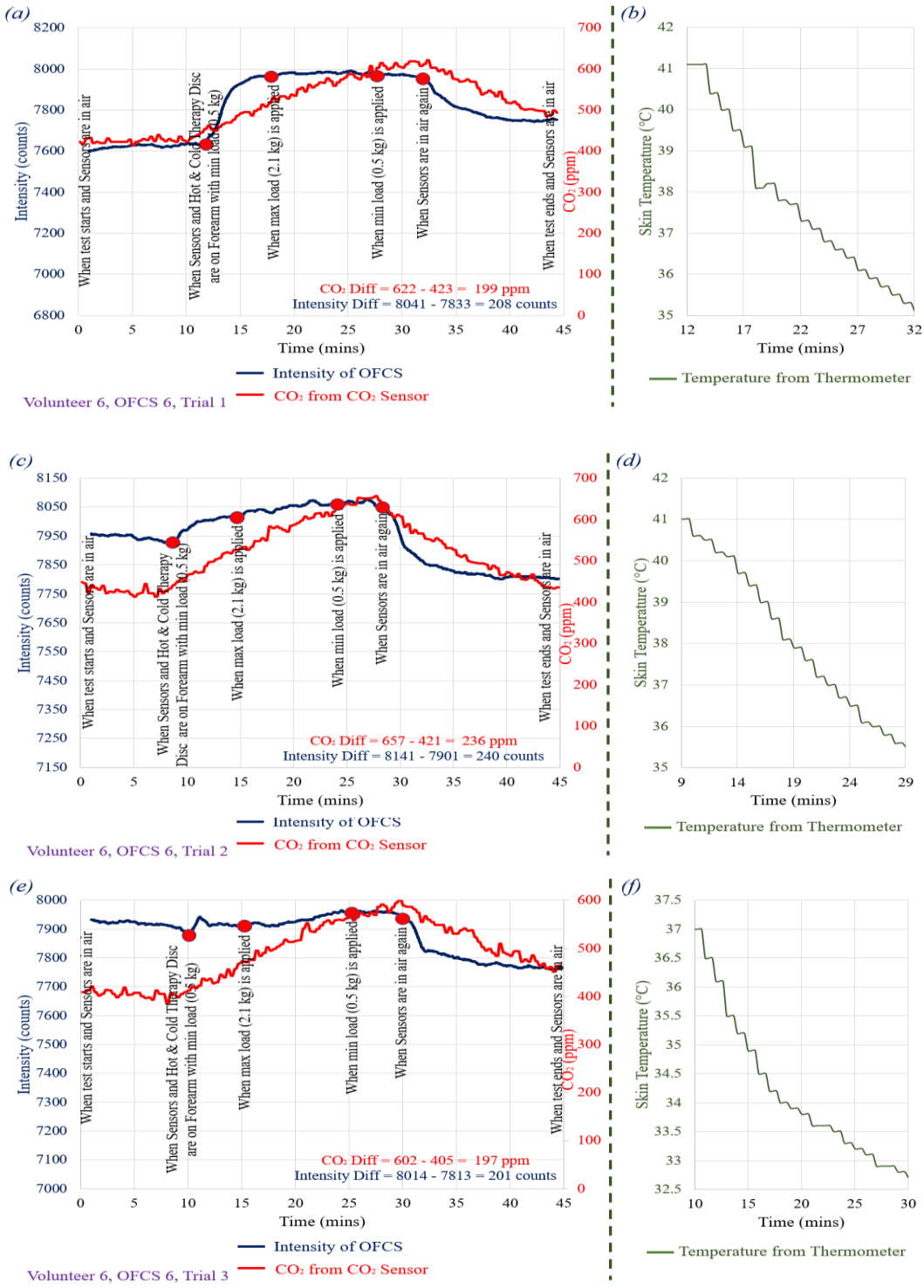


Figure C.22: *(a) (c) (e) Response (Reflection Intensity) of OFCS 6 at wavelength 600 nm and commercial CO_2 sensor on Volunteer 6's forearm (b) (d) (f) Volunteer 6's skin temperature while heated disc is on forearm for Trials 1-3, respectively*

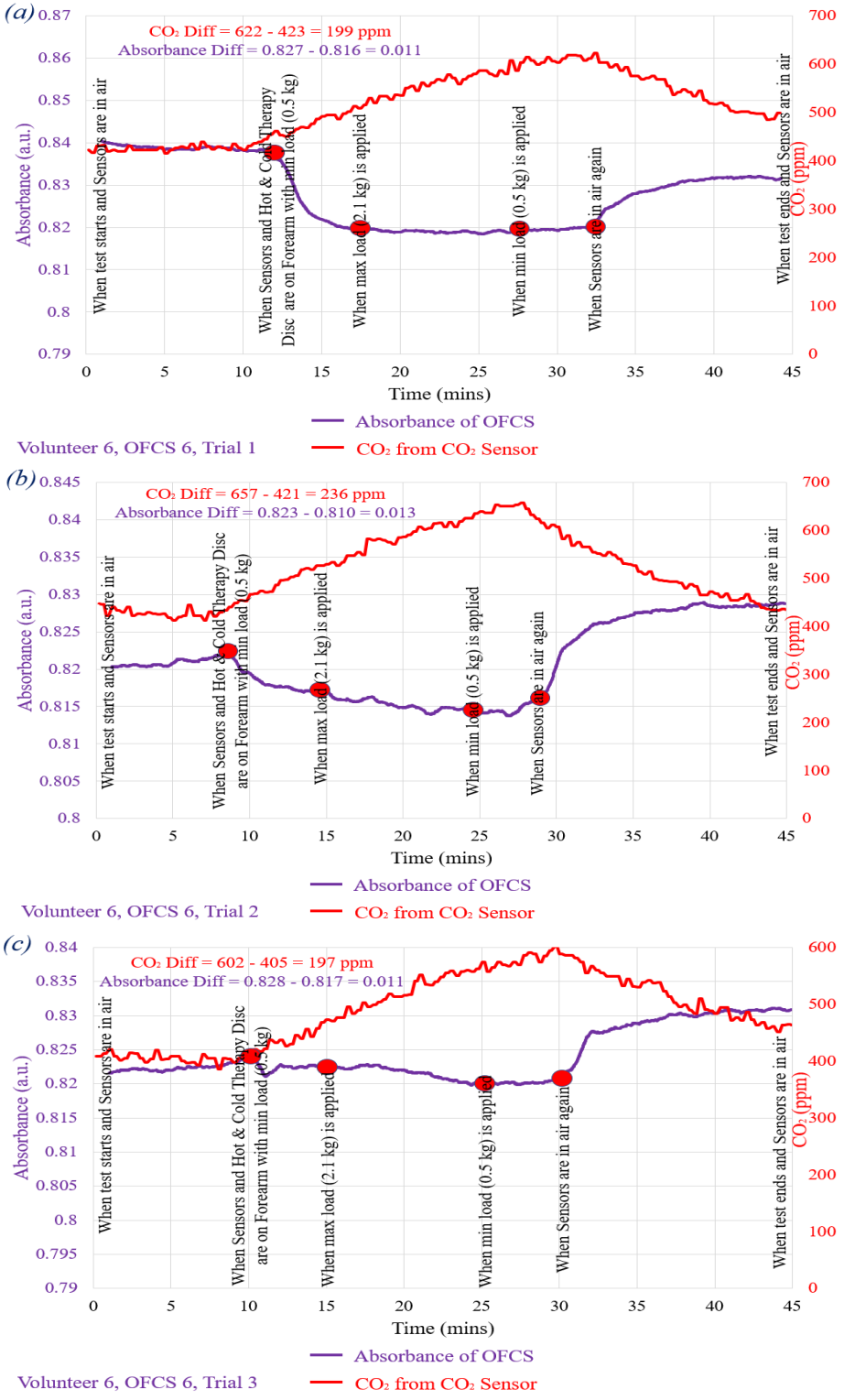


Figure C.23: *(a)-(c) Response (Absorbance) of OFCS 6 at wavelength 600 nm and commercial CO_2 sensor on Volunteer 6's forearm for Trials 1-3, respectively*

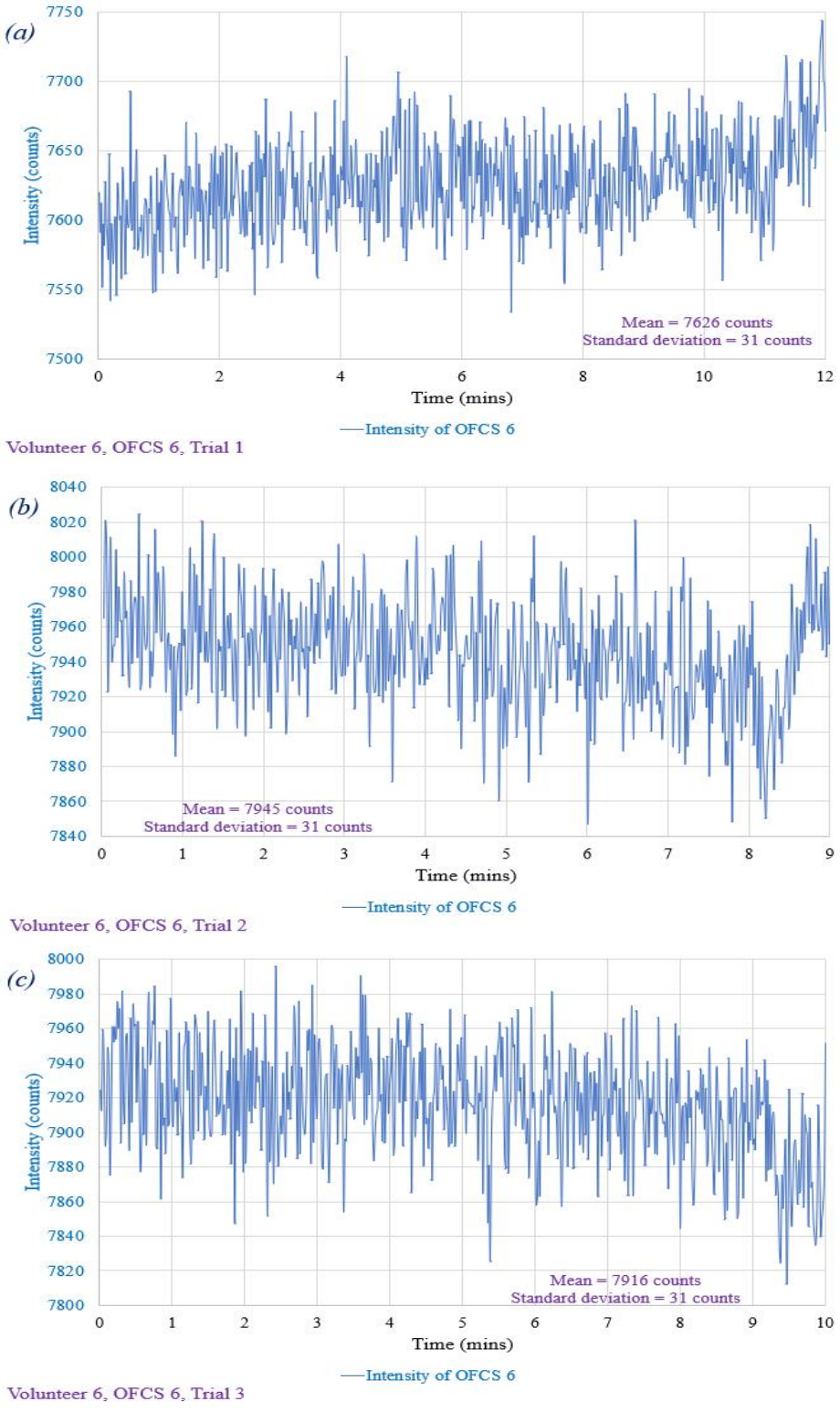


Figure C.24: *(a)-(c) Response (Raw Reflection Intensity) of OFCS 6 at wavelength 600 nm in the air for Trials 1-3, respectively*

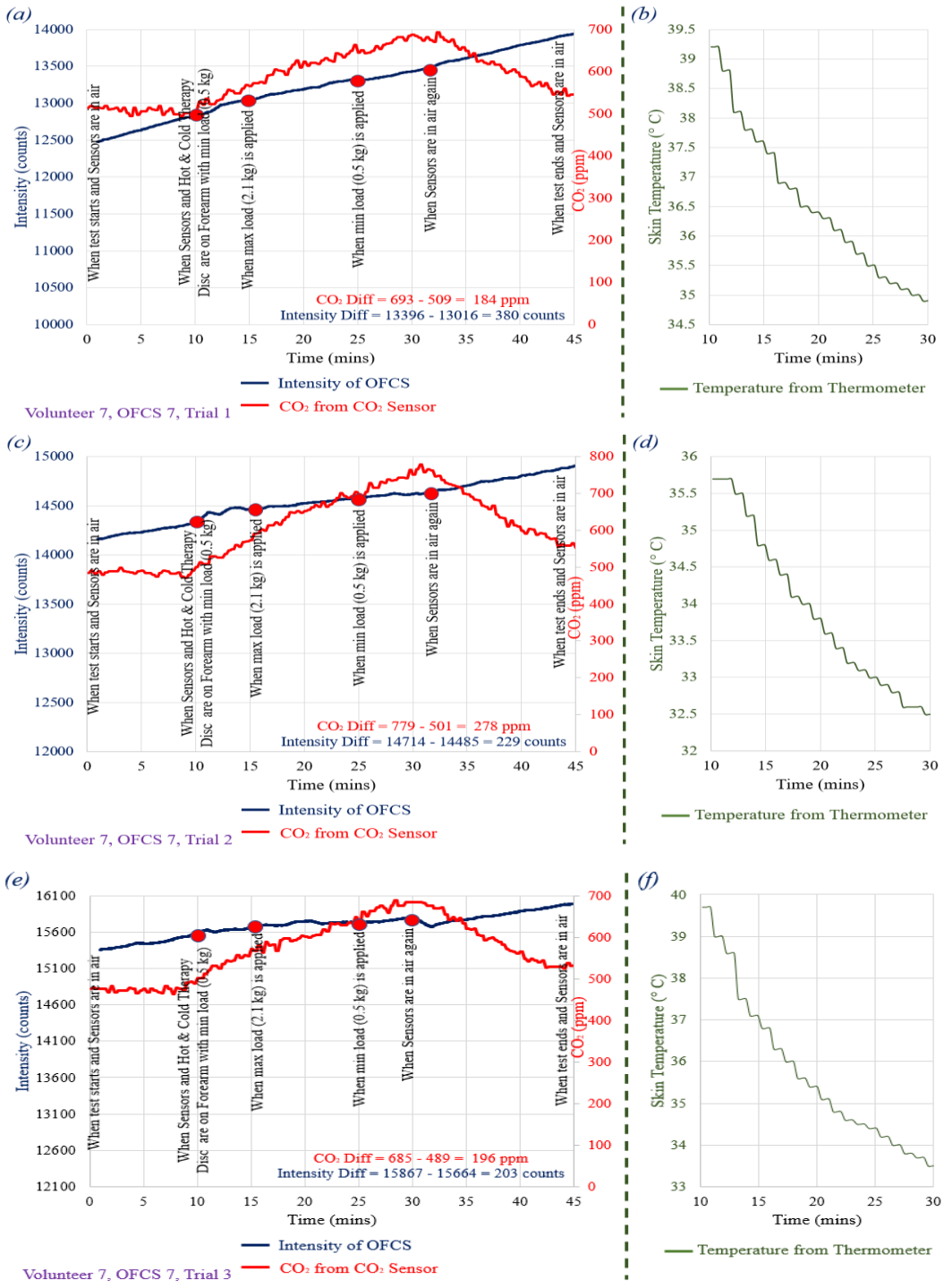


Figure C.25: *(a) (c) (e) Response (Reflection Intensity) of OFCS 7 at wavelength 600 nm and commercial CO_2 sensor on Volunteer 7's forearm (b) (d) (f) Volunteer 7's skin temperature while heated disc is on forearm for Trials 1-3, respectively*

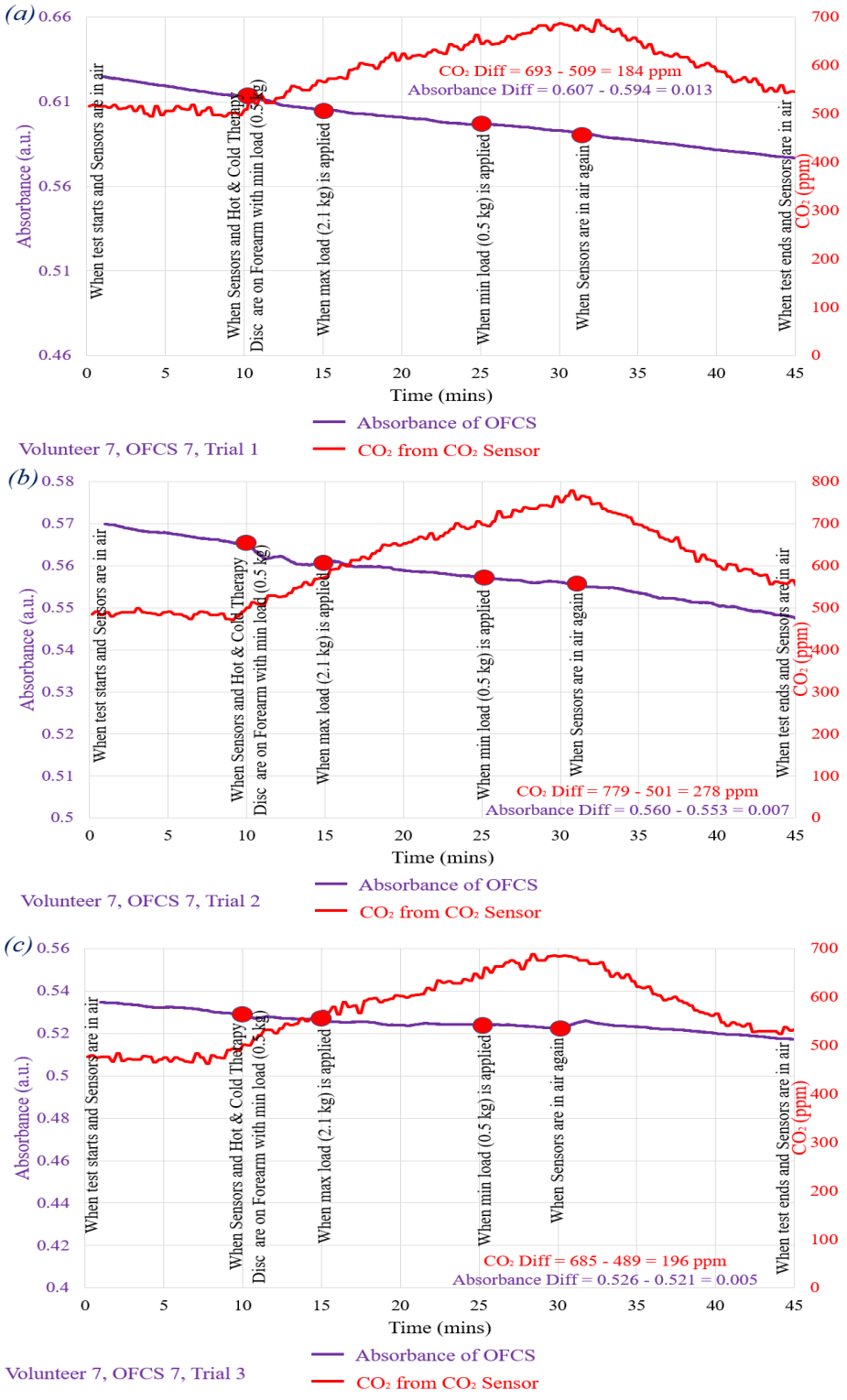


Figure C.26: *(a)-(c) Response (Absorbance) of OFCS 7 at wavelength 600 nm and commercial CO_2 sensor on Volunteer 7's forearm for Trials 1-3, respectively*

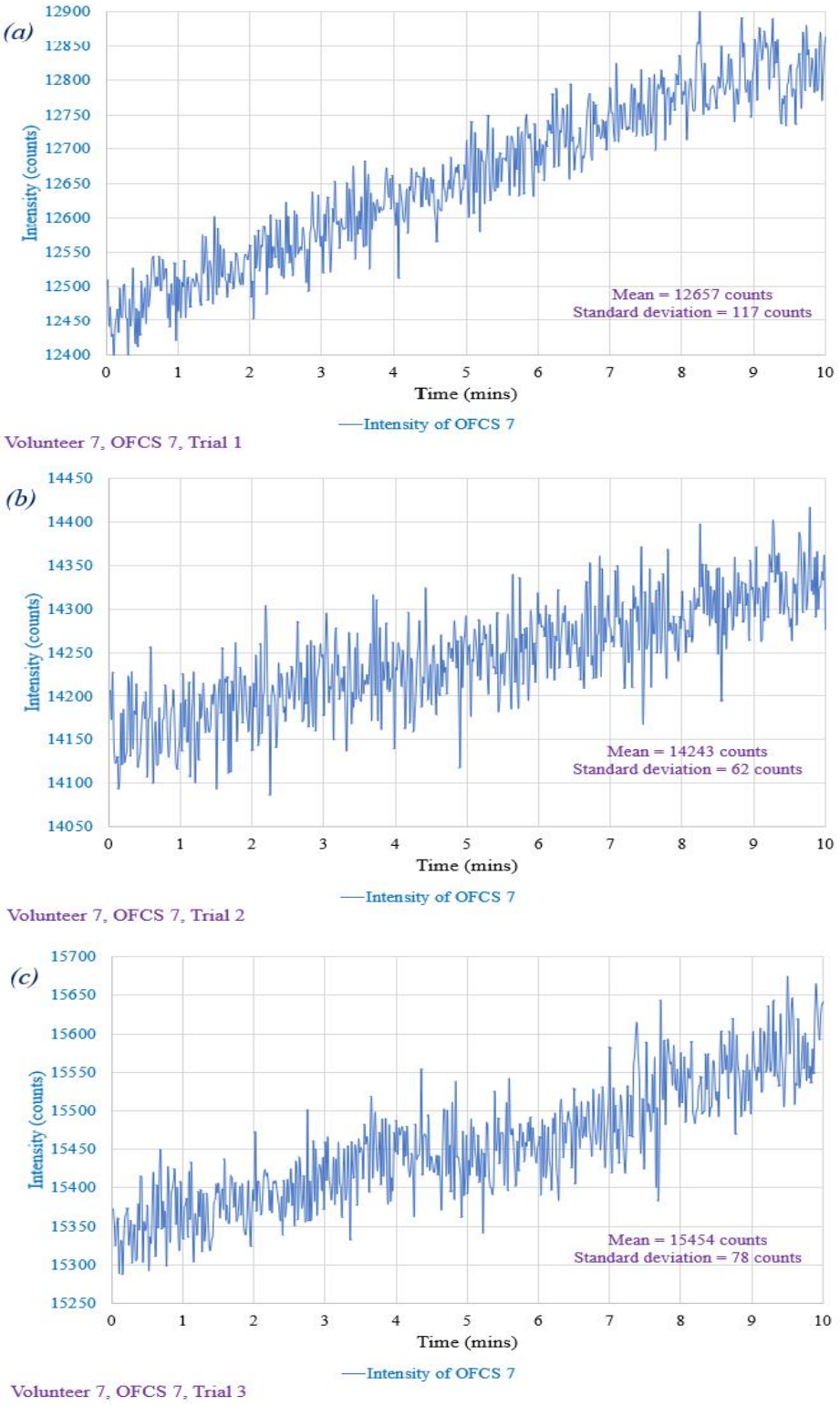


Figure C.27: *(a)-(c) Response (Raw Reflection Intensity) of OFCS 7 at wavelength 600 nm in the air for Trials 1-3, respectively*

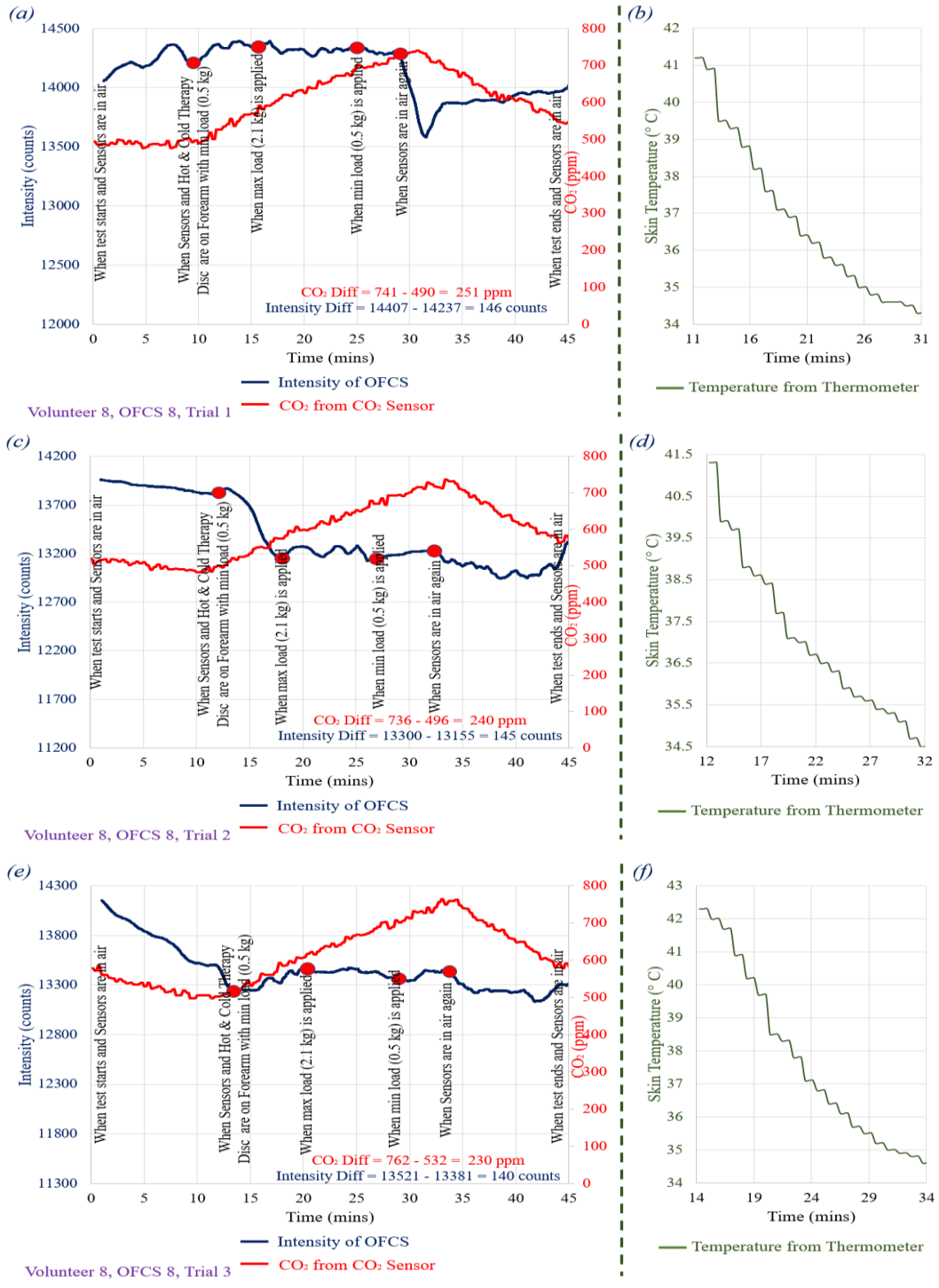


Figure C.28: *(a) (c) (e) Response (Reflection Intensity) of OFCS 8 at wavelength 600 nm and commercial CO_2 sensor on Volunteer 8's forearm (b) (d) (f) Volunteer 8's skin temperature while heated disc is on forearm for Trials 1-3, respectively*

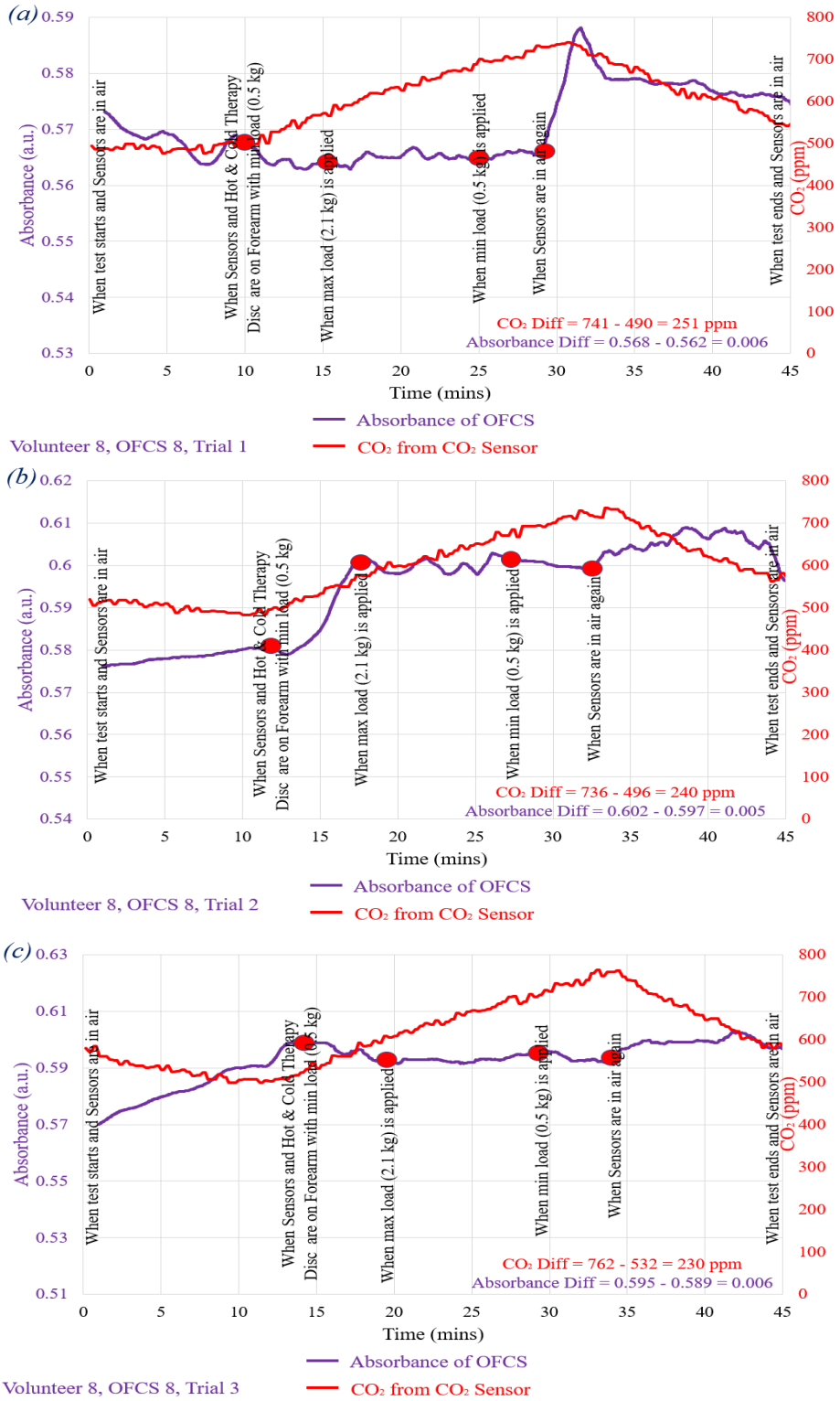


Figure C.29: *(a)-(c) Response (Absorbance) of OFCS 8 at wavelength 600 nm and commercial CO_2 sensor on Volunteer 8's forearm for Trials 1-3, respectively*

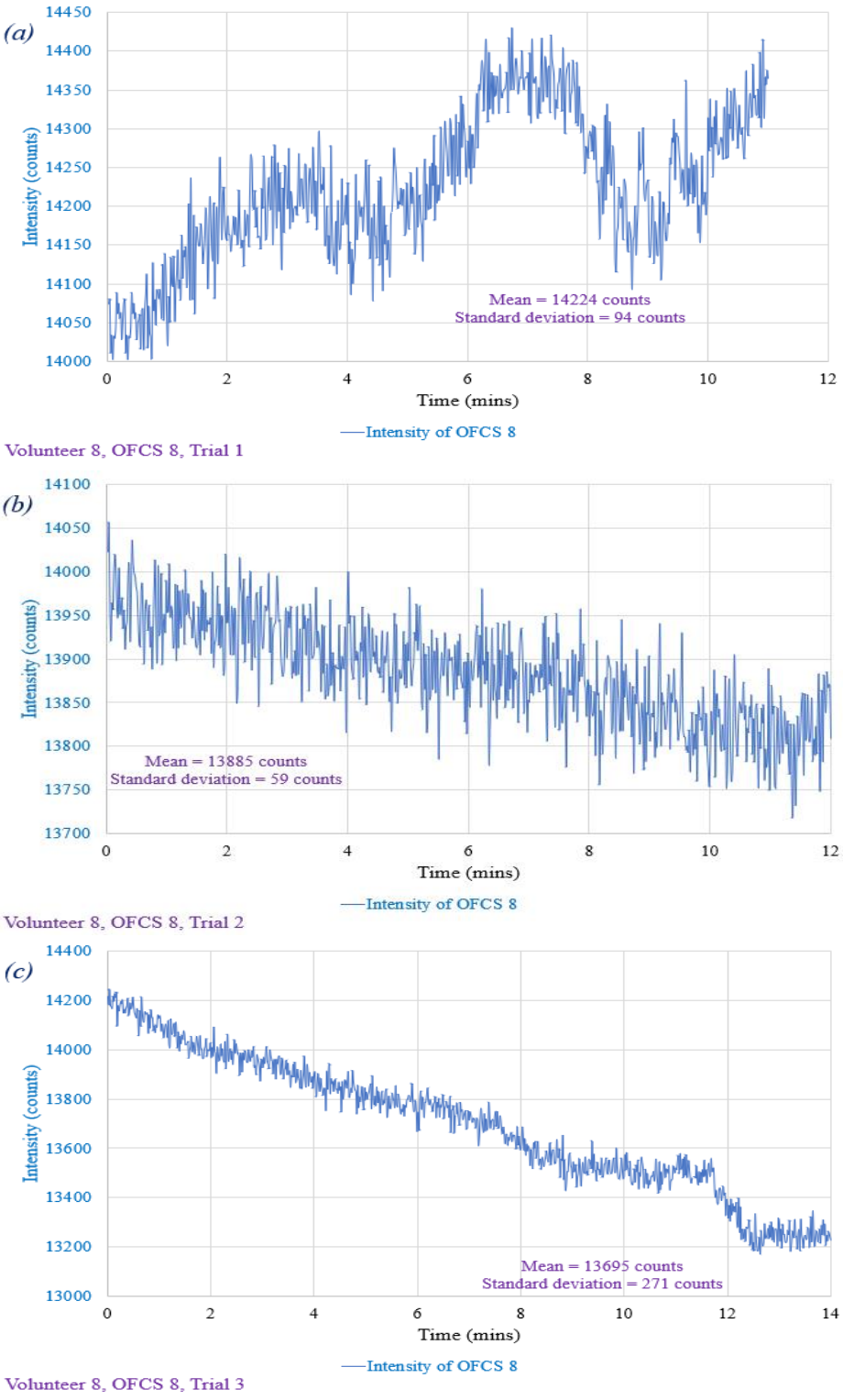


Figure C.30: *(a)-(c) Response (Raw Reflection Intensity) of OFCS 8 at wavelength 600 nm in the air for Trials 1-3, respectively*

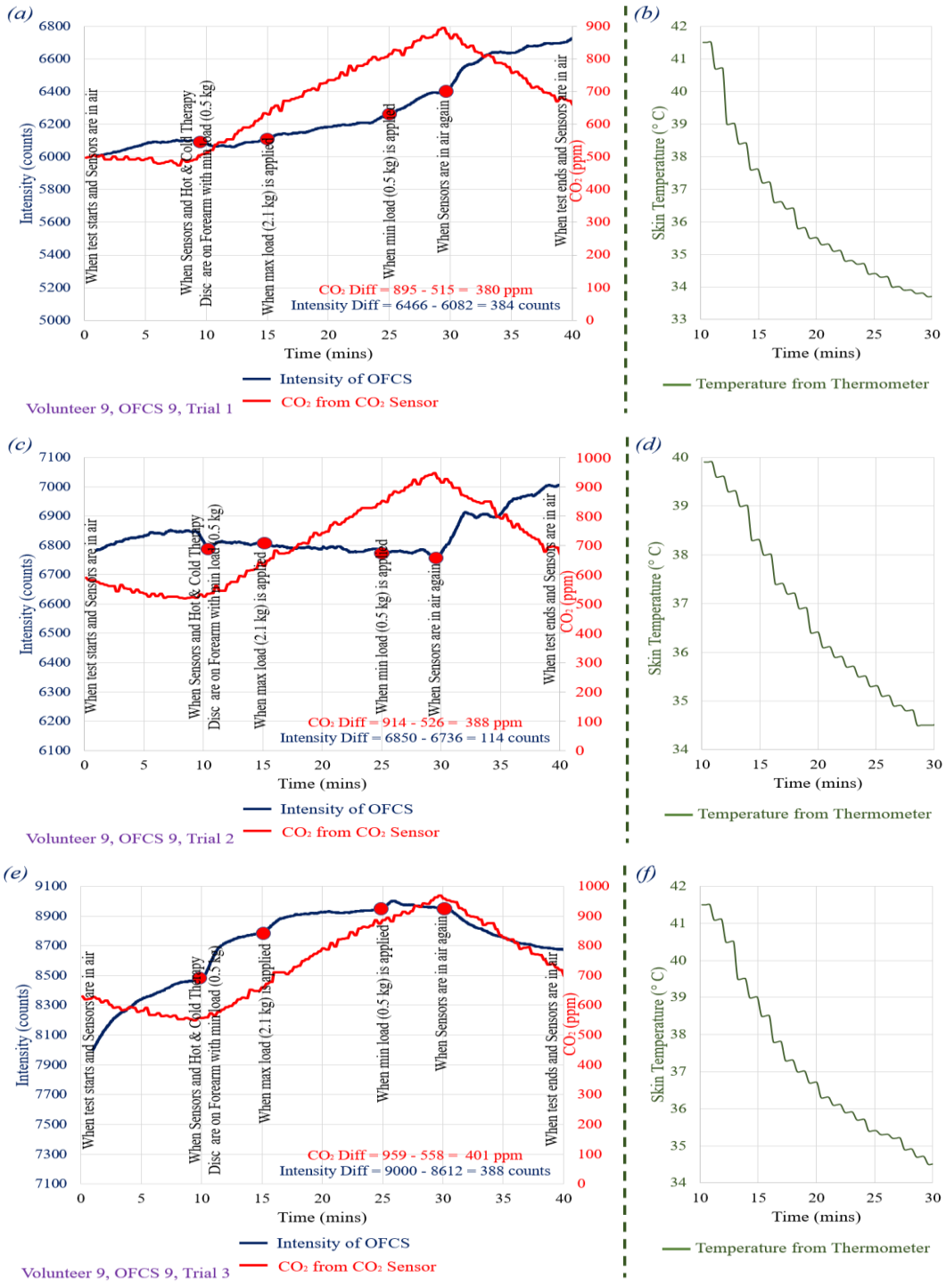


Figure C.31: *(a) (c) (e) Response (Reflection Intensity) of OFCS 9 at wavelength 600 nm and commercial CO_2 sensor on Volunteer 9's forearm (b) (d) (f) Volunteer 9's skin temperature while heated disc is on forearm for Trials 1-3, respectively*

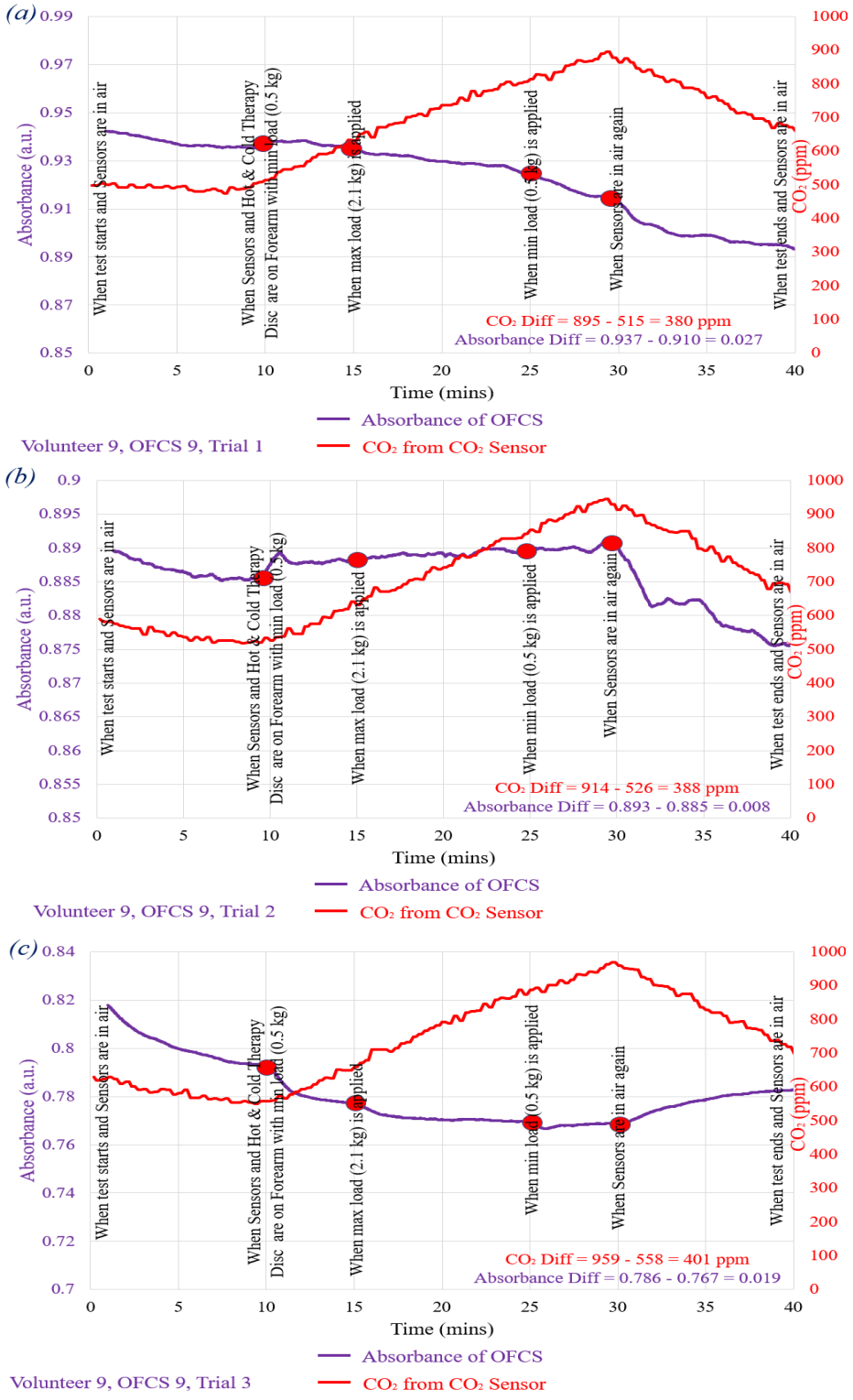


Figure C.32: *(a)-(c) Response (Absorbance) of OFCS 9 at wavelength 600 nm and commercial CO_2 sensor on Volunteer 9's forearm for Trials 1-3, respectively*

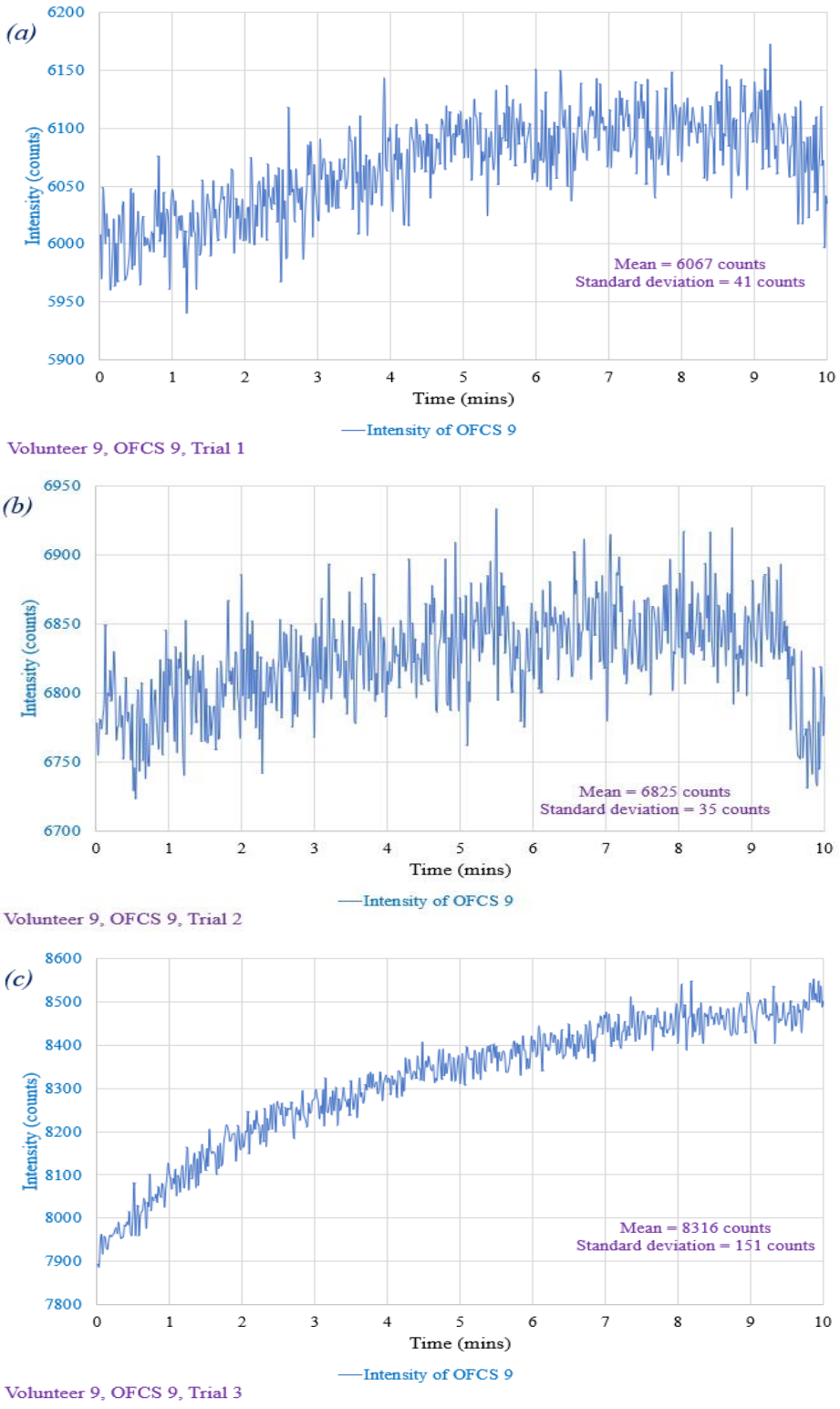


Figure C.33: *(a)-(c) Response (Raw Reflection Intensity) of OFCS 9 at wavelength 600 nm in the air for Trials 1-3, respectively*

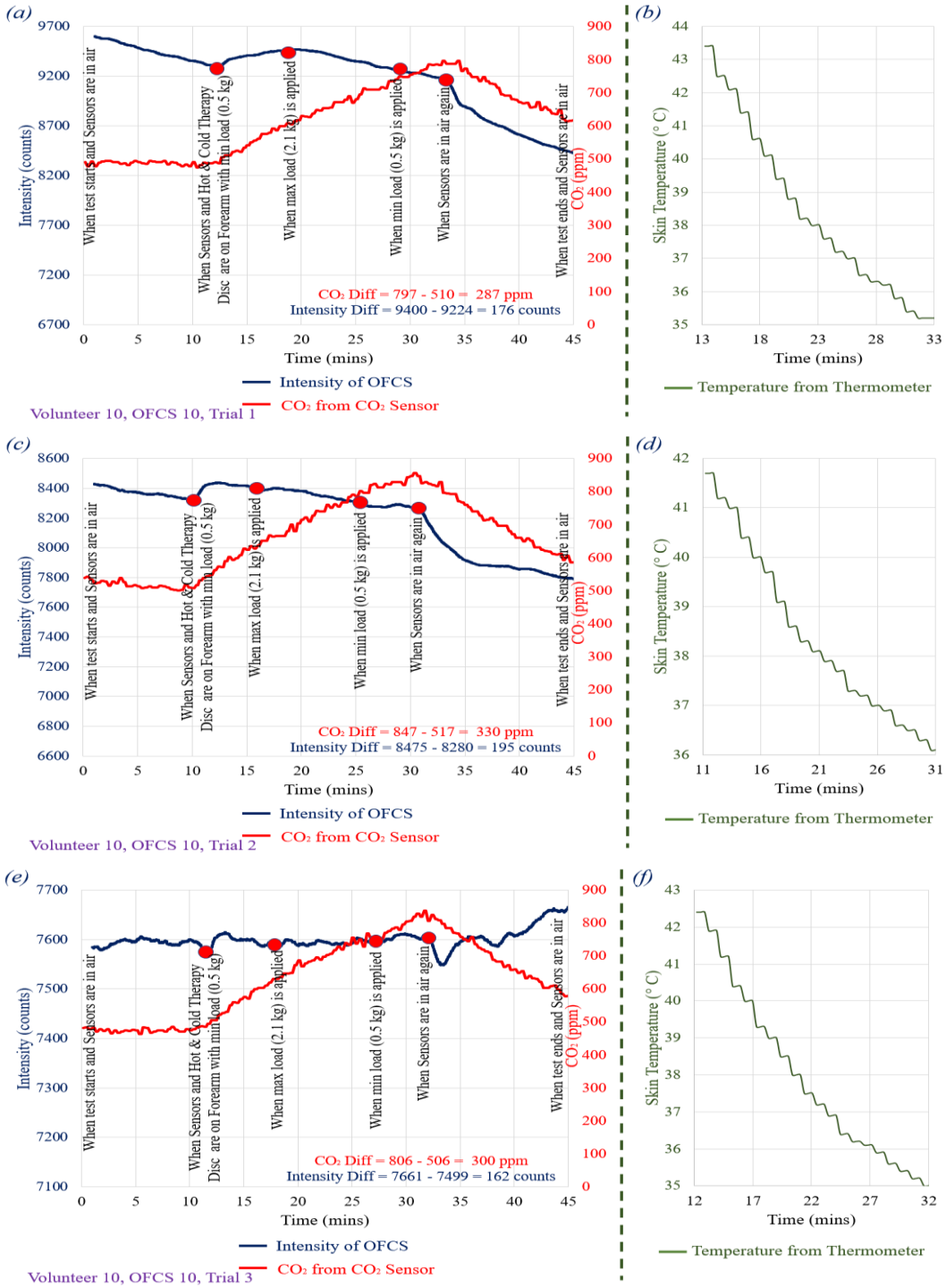


Figure C.34: *(a) (c) (e) Response (Reflection Intensity) of OFCS 10 at wavelength 600 nm and commercial CO_2 sensor on Volunteer 10's forearm (b) (d) (f) Volunteer 10's skin temperature while heated disc is on forearm for Trials 1-3, respectively*

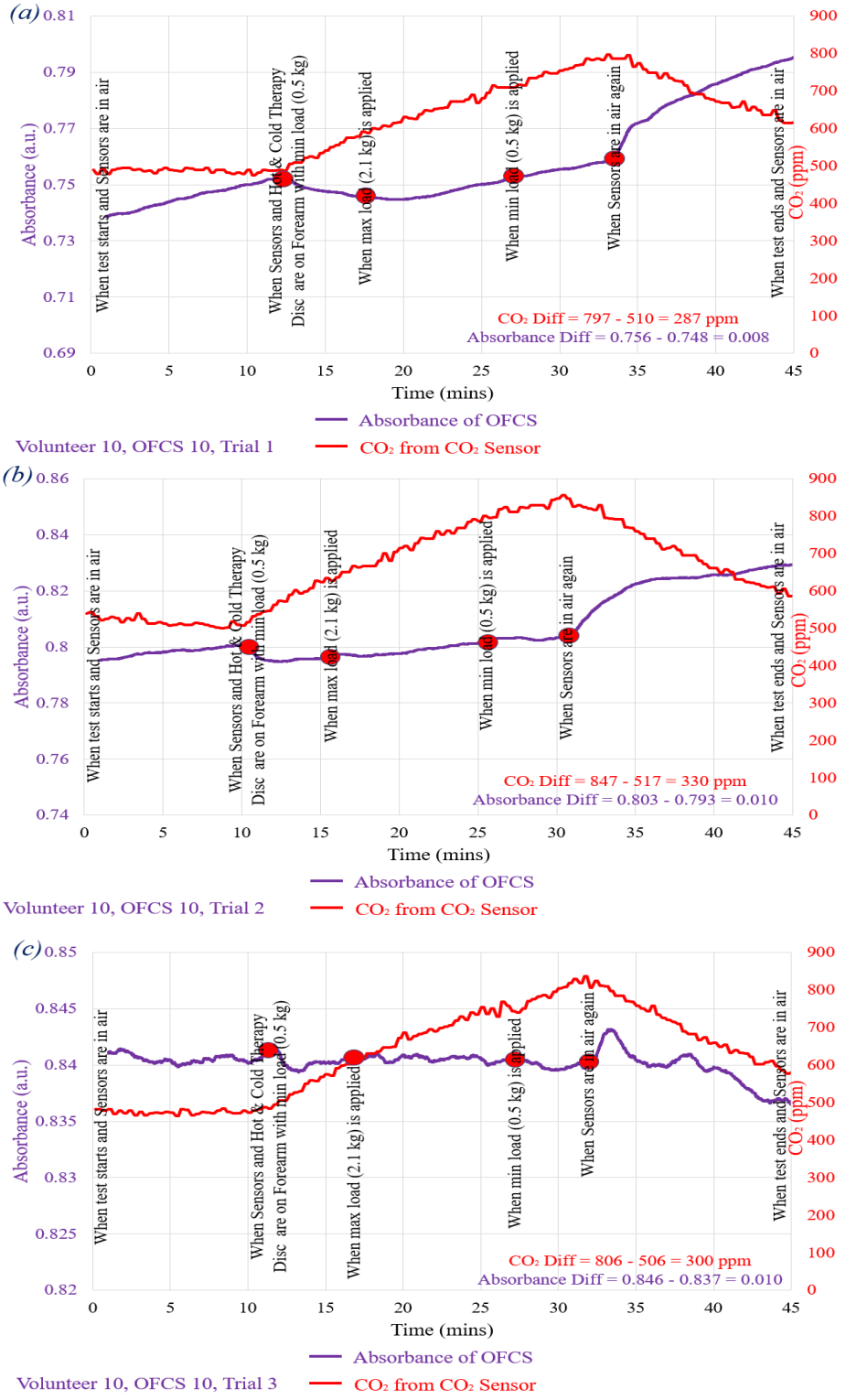


Figure C.35: *(a)-(c) Response (Absorbance) of OFCS 10 at wavelength 600 nm and commercial CO_2 sensor on Volunteer 10's forearm for Trials 1-3, respectively*

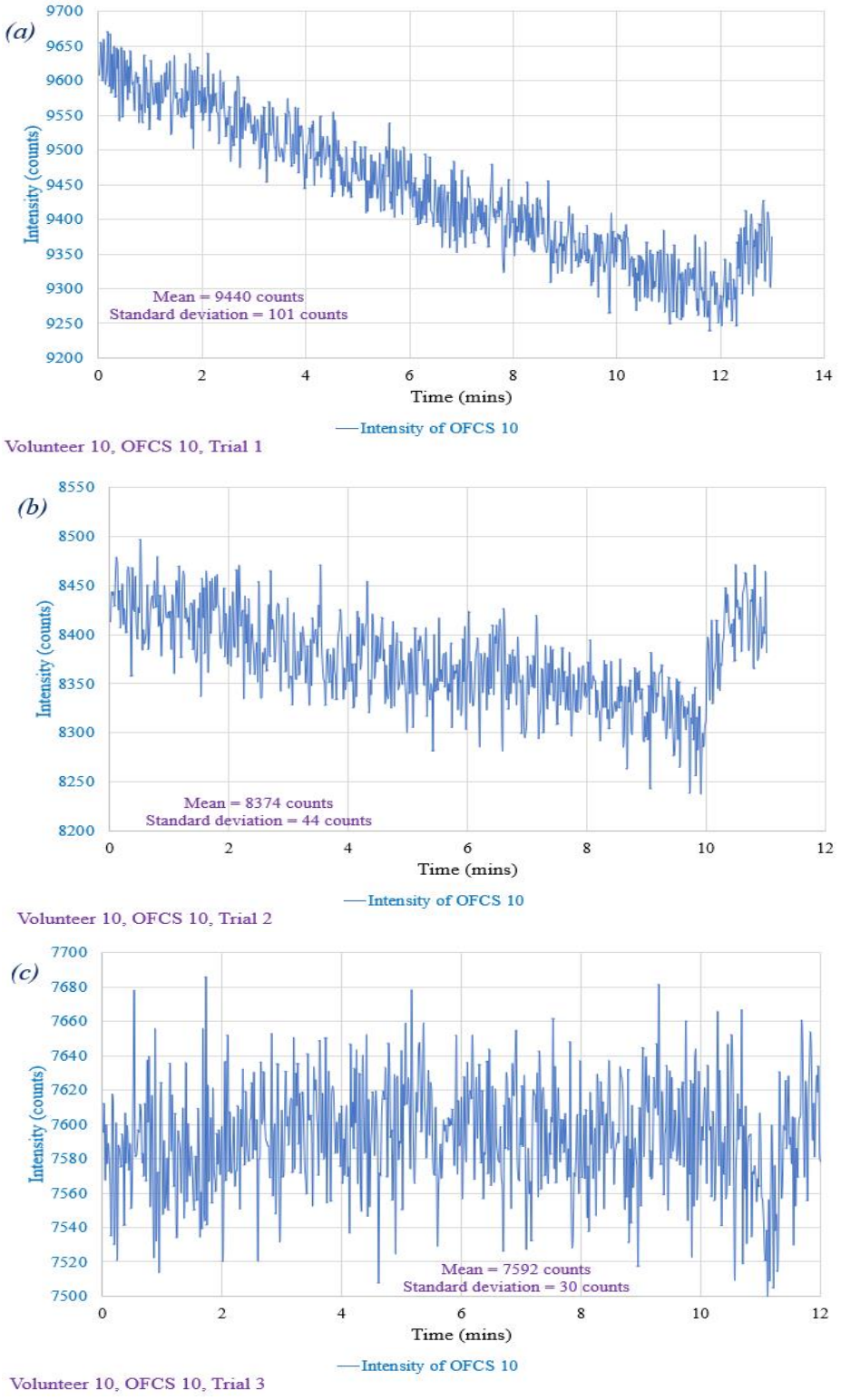


Figure C.36: *(a)-(c) Response (Raw Reflection Intensity) of OFCS 10 at wavelength 600 nm in the air for Trials 1-3, respectively*

D. Appendix D

Experiment Ethics Approval

Monitoring of CO_2 emitted from human skin during loading by using an optical fibre sensor, a commercial CO_2 sensor and a t_C Sensor 92 probe

Participant Information Sheet

You are invited to take part in a study which will detect CO_2 from human skin by using an optical fibre sensor. Before you decide whether to take part it is important for you to understand why the research is being done and what it will involve. If you would like more information or have any questions, please contact Nadia Afroze nadia.afroze@nottingham.ac.uk or Prof Stephen Morgan steve.morgan@nottingham.ac.uk

Background

This study focuses on monitoring CO_2 from human skin during an experiment. Transcutaneous CO_2 pressure (T_CPCO_2) is a measurement of CO_2 released from the skin, which reveals a good correlation with arterial partial pressure of CO_2 (P_aCO_2) [1]. This allows a non-invasive measurement for determining P_aCO_2 for clinical application, such as predicting pressure ulcers (PUs) in ischemic skin tissue. People who experience non-uniform pressure distribution for an extended length of time may develop PUs. However, most PUs starts at the skin's surface and can progress to deeper tissue layers. Deep tissue injury is another classification that develops from deeper muscle layers around bony prominences to the skin. Transcutaneous gas monitoring is a method that was initially created to monitor the respiratory gases of pre-term newborns. Transcutaneous gas monitoring has been modified to measure the CO_2 levels in loaded soft tissues in various research on healthy participants and those thought to be at high risk of developing PUs [2]. CO_2 is a reliable marker for the early detection of PUs. The sensor could make an important contribution to predicting and preventing PUs.

Who are the participants?

Up to 20 healthy volunteers will be recruited primarily from the Optics and Photonics Research Group including researchers/PhD students.

Procedure

There are 2 parts of the experiment: The first part will be done according to set-up as shown in Figure D.1, and the second part will be done according to set-up as shown in Figure D.2.

First procedure:

Before the experiment, the participants will be asked to clean their forearms using alcohol gel (70 % alcohol) provided by the experimenter and allow their skin to adjust to the environment. At the beginning, all participants will be required to sit quietly for 5 minutes before the experiment commences. The participants must wear 2 surgical masks during the experiment because the commercial CO_2 sensor is highly sensitive and can detect breathing CO_2 quickly.

A maximum pressure of 16 kPa (120 mmHg) will be applied to the holder, and the loading effects on the skin tissues will be observed. This has been shown to be a safe level in other studies previously conducted by our collaborators at the University of Southampton [3]. The contact area between the skin and the holder is 1286 mm^2. 16 kPa is equivalent to a 2.1 kg load which is provided by the loading machine. If the participant feels any pain or discomfort during the experiment, the participant should indicate this, and the experiment will be stopped immediately.

a) Volunteers will be asked to place a heated disc with a thermocouple probe on the skin. A foil blanket will be wrapped over the disc, avoiding the hole in the middle of the disc. A compression bandage will be also wrapped around the outer parts of the foil blanket to hold it in place.

b) The holder will be placed through the disc's hole with the PTFE film face down on the volunteer's skin (as shown in Figure D.1) for correct sensor placement.

c) The experiments will run between 37 °C and 42 °C, depending on the heat retention provided by the foil blanket and disc.

d) The holder with the OFCS tip and commercial CO_2 sensor will be placed on the forearm with a minimum load (0.5 kg) for 5 mins to provide a baseline measurement. The 0.5 kg load ensures the sensors remain in place and there is a gas seal between the skin and sensors.

e) A 2.1 kg load will be applied for the next 10 mins.

f) Load will be reduced to 0.5 kg for the next 5 mins.

g) The holder will be removed from the forearm.

The response of the OFCS and commercial CO_2 sensor from a volunteer's skin will be recorded using SpectraSuite Software and GasLab Software, respectively, during the experiment. This experiment will take approximately 20 minutes to complete steps b)-g) for each participant. Each participant will be tested 3 times per day and the measurements will be conducted with at least 30 minutes of break between each test to relax and rest the forearm.

A study has shown that a sensor temperature of 43 °C was well tolerated for 5-8 hours of continuous monitoring [4].

The first experiment will be conducted with the set-up shown in Figure D.1. This is conducted by placing a biocompatible holder (Polylactic acid, PLA, MP002267, Multicomp Pro, Farnell, UK) containing a commercial CO_2 sensor (CM-0120, COZIR-A 10,000 ppm CO_2 Sensor, CO2Meter.com, USA) and an OFCS tip on a volunteer's forearm. The OFCS tip is connected to the PLA based GCC through the channel. The OFCS is not directly in contact with the skin. The holder contains a PTFE cast film layer to prevent humidity from reaching the OFCS tip. The PTFE film acts as a membrane barrier.

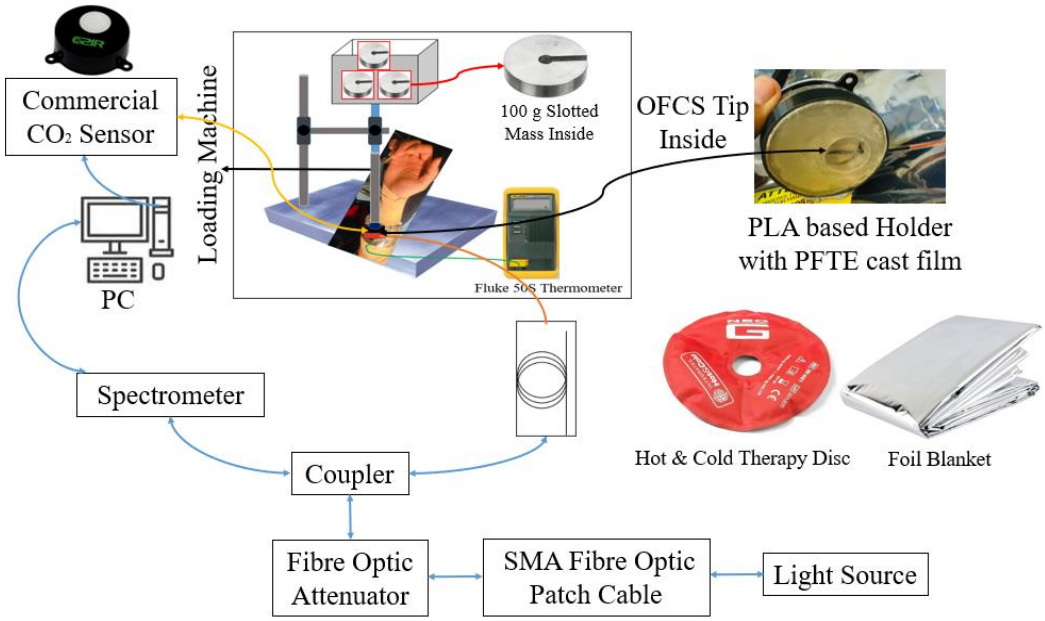


Figure D.1: *Set-up for monitoring CO_2 emitted from wrapped human skin during loading using OFCS and commercial CO_2 Sensor*

Second procedure:

Before the experiment, the participants will be asked to clean the skin under test using alcohol wipe tissue (70 % alcohol) provided by the experimenter and allow their skin to adjust to the environment. At the beginning, all participants will be required to sit quietly for 5 minutes before the experiment commences. The surface of the t_C Sensor 92 will be also cleaned by alcohol wipe tissue (70 % alcohol). The sensor will be calibrated at the temperature at which experiments are conducted (37 °C and 42 °C).

a) Volunteers will be asked to place a fixation ring (as shown in Figure D.2) just on top of the skin (forearm).

b) A small drop of contact gel (as shown in Figure D.2) will be applied to the skin area in the centre of the fixation ring and there is a 2-minute delay.

c) The sensor will be attached to the adhesive layer in the centre of the ring and will be pressed gently against the skin to spread the contact gel.

d) The experiments will run at sensor temperatures of 37 °C or 42 °C, and the duration of the experiment will be 30 minutes.

e) Each participant will be tested 5 times. The measurements will be conducted with at least 2 hours break to avoid prolonged exposure of the skin using the attached probe to the skin.

According to the manufacturer (personal communication), the contact gel (CE marked) has been routinely used in cosmetics and healthcare, and there are no reported allergic reactions. The amount of sensitising substance present in the gel is very small, it contains 36.7 % propylene glycol and 0.125 % cis-1-(3-Chloroallyl)-3, 5, 7-triaza-1-azoniaadamantane chloride (Quaternium-15). Propylene glycol does not contain any hazardous substance or mixture and this ingredient's level of hazard is low. However, there is a tiny quantity of Quaternium-15, which may provoke an allergic reaction among individuals with sensitive skin [5]. Before the experiment, the volunteer will be asked via a questionnaire if they have any allergies that are caused by exposing the skin to certain chemicals. If the volunteer has sensitive skin, they are excluded from this experiment. After 2 minutes of observation, it will be easier to detect if a participant with an unknown sensitivity does react to the chemicals used. If any rash arises after 2 minutes of observation, the volunteer will be excluded from this experiment. It has been noted by the manufacturer (personal communication) that in more than 20 years of routine usage of the TCM probes in clinical practice, no allergic reaction was observed. If the participant feels any pain or discomfort during the experiment, this should be highlighted, and the experiment will be stopped immediately.

The PCO_2 values from a volunteer's skin will be recorded by using the TCM TOSCA monitor. This experiment will take around 30 minutes to complete steps a)-e) for each participant.

The second experiment will be conducted with the set-up shown in Figure D.2. A fixation ring is attached to the volunteer's hand alongside a t_C Sensor 92 probe. The t_C Sensor 92 probe is connected to the monitoring unit (TCM TOSCA monitor, Radiometer, UK) which is used to observe the data and record the results.

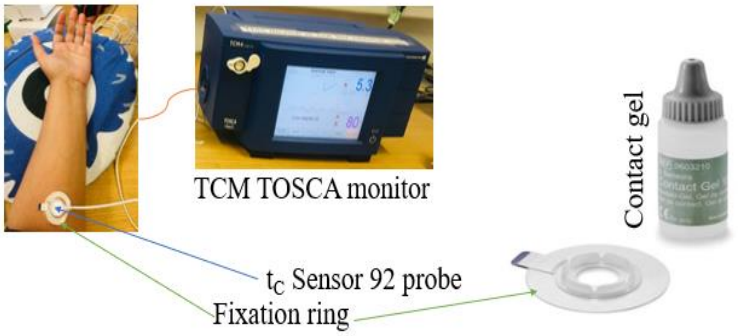


Figure D.2: *Set-up for monitoring PCO_2 from human skin using t_C Sensor 92 probe*

After the experiment, the data from the OFCS, commercial CO_2 sensor, and t_C Sensor 92 probe will be analysed by Microsoft Excel and MATLAB to acquire the value of CO_2 during the experiment.

Part 2: Further Information

Do I have to take part?

No. Participation in the study is entirely voluntary; it is up to you to decide whether or not to take part. If you do decide to take part, you will be given this Participation Information Sheet to keep and be asked to complete a consent form. However, even if you complete the consent form you are still free to withdraw at any time and without giving a reason.

What will happen to me if I take part?

You will be asked to read through the Participant Information Sheet and then asked to complete the Participant Consent Form.

What will happen if I do not want to carry on with the study?

You can withdraw from the study at any time without having to provide a reason. If you do withdraw information that can be attributed to you will not be used in our analysis.

Will I be paid?

No. There is no reward for this research.

Will my taking part in this study be kept confidential?

Yes. All information which is collected about you during the research will be kept strictly confidential and our procedures for handling, processing, storage, and destruction of your data are compliant with the Data Protection Act 1998. The data, including CO_2 signals and PCO_2, will be retained for 7 years following any publication, after this time it will be destroyed. All the data will be stored on password protected computers in the research laboratory of the Optics and Photonics Research Group. Only members of the research group will have access to the data. It is not possible to identify any individuals because any data will be published anonymously.

What will happen to the results of the of the research study?

This result will be used in project reports and in journal publications. The data will be anonymous.

Who has reviewed the study?

The study has been approved by the Faculty of Engineering Ethics Committee and Health and Safety Advisor of the University of Nottingham (UoN), respectively.